



HAL
open science

Green ambient synthesis of robust Metal-Organic Frameworks (MOFs) and Metal Nanoparticles@MOFs Composites

Shan Dai

► **To cite this version:**

Shan Dai. Green ambient synthesis of robust Metal-Organic Frameworks (MOFs) and Metal Nanoparticles@MOFs Composites. Material chemistry. Université Paris sciences et lettres; East China normal university (Shanghai), 2021. English. NNT : 2021UPSLE068 . tel-04086963

HAL Id: tel-04086963

<https://theses.hal.science/tel-04086963>

Submitted on 2 May 2023

HAL is a multi-disciplinary open access archive for the deposit and dissemination of scientific research documents, whether they are published or not. The documents may come from teaching and research institutions in France or abroad, or from public or private research centers.

L'archive ouverte pluridisciplinaire **HAL**, est destinée au dépôt et à la diffusion de documents scientifiques de niveau recherche, publiés ou non, émanant des établissements d'enseignement et de recherche français ou étrangers, des laboratoires publics ou privés.



THÈSE DE DOCTORAT

DE L'UNIVERSITÉ PSL

Préparée à l'École Normale Supérieure de Paris
Dans le cadre d'une cotutelle avec l'East China Normal
University

Synthèse ambiante verte de solides hybrides poreux (MOFs) robustes et de composites nanoparticules métalliques@MOFs

Soutenue par

Shan DAI

Le 10. 11. 2021

Ecole doctorale n° 397

**Physique et Chimie des
Matériaux**

Spécialité

Chimie Matériaux

Composition du jury :

Jerome CANIVET Chargé de recherche CNRS	<i>Rapporteur</i>
Thierry GACOIN Directeur de recherche CNRS	<i>Rapporteur</i>
Anne BLEUZEN Professeur, Université Paris-Saclay	<i>Présidente</i>
Corinne CHANEAC Professeur, Sorbonne université	<i>Examineur</i>
Sergio NAVALON Professeur associé Universitat Politècnica de València	<i>Examineur</i>
Ming HU Chercheur, East China Normal University	<i>Examineur</i>
Christian SERRE Directeur de Recherche CNRS	<i>Directeur de thèse</i>
Antoine TISSOT Chargé de recherche CNRS	<i>Co-encadrant</i>



Acknowledgments

The time finally comes to this day. Four years flew quickly.

First of all, I want to thank all the people who helped me during my PhD thesis at École Normale Supérieure (ENS) and East China Normal University (ECNU). Nothing would have been possible without your help. I would like to thank the Chinese Scholarship Council (CSC), which supported funding for my PhD thesis.

I would like to express my sincere appreciation to **Dr. Antoine Tissot** and **Dr. Christian Serre** for their supervision, useful advices, and patient guidance. Your rigorous attitude, broad scientific views, and humored personality have really impressed me very much. Without your initial permission, I would never have the chance to start my PhD in such a nice MOF group. I am very much grateful for all the discussions, conversations, even some drinking we had together. I believe in that all of your impact will accompany me throughout my life.

I am grateful to all the members of the thesis committee, **Dr. Jérôme Canivet**, **Dr. Thierry Gacoin**, **Prof. Anne Bleuzen**, **Prof. Corinne Chanéac**, **Prof. Sergio Navalón Oltra**, and **Dr. Ming HU**. Special thanks to Dr. Thierry Gacoin and Dr. Jérôme Canivet who are the rapporteurs of my thesis.

I would also like to show my appreciation to my colleagues and supervisors when I was studying in ECNU, Shanghai, China, especially to **Dr. Taiqun Yang**, for the pleasant and nice communications/ learnings with him. I owe my gratitude to **Prof. Sanjun Zhang** for his sustained enthusiasm, strong support, and exemplary guidance in the beginning period of my graduate program.

I wish to show my deepest gratitude with all my heart to all collaborators, **Charlotte Simms**, and **Prof. Tatjana N. Parac-Vogt** from KU Leuven, **Dr. Gilles Patriarche** from Université Paris-Saclay, **Dr. Sergio Navalón Oltra** from Universitat Politècnica de València, **Dr. Sabine Devautour-Vinot** from Université Montpellier, **Dr. Jorge A. Rodriguez Navarro** from Universidad de Granada, **Dr. Ignacio Gascón**, **Dr. Joaquín Coronas** from Universidad de Zaragoza, **Dr. Dan Zhao** from National University of Singapore, **Dr. Takashi Kajiwara**, **Dr. Miyuki Ikeda**, **Dr. Qiang Xu** from National Institute of Advanced Industrial Science and Technology of Japan. I learned a lot from all of you through the discussions with you, which I believe benefits very much for my entire PhD thesis.

I would also take this opportunity to give my profound gratitude to all the kind, nice, excellent colleagues in IMAP: Farid, Vanessa, Mathilde, Georges, Bernard, Iurii, Florian, Oleksii, Shyama, Debanjan, Raquel, Audrey, Asma, Mégane, Angelika, Mathilde Renouard, Joanna, Myan, Anna, Iryna-Romana, Nicolas, Andrea, Ines, Kieu, Johanna, Sarah, Antoine Enel, Hanae for all the pleasant memories we shared during our daily lives in lab or in the bars. Special thanks to the Chinese team in IMAP, I can't stop thinking all of you at this special moment. I wish to write all of your names here: **Bingbing**, **Sujing**, **Lin**, **Heng**, **Wenqing**, **Yuwei**, **Chenchen**, **Yutong**, **Zhihao**, and **Xin**. For those who just joined IMAP, I also want to express my appreciation, Ben,

Soraya, Shaokang, Qingfeng, Jiangliang, and Tobie. I am quite sure you will have very nice time in IMAP.

Finally, I would like to show my deepest love to my family, particularly my parents, old sisters, and cousins. No word can describe my deep sense of gratitude to you. Your endless love, help, faith, and encouragement offered me with confidence and motivation in completing this thesis. I love you.

六年的时光终于走到了今天。

从上海到巴黎，从徘徊到坚定，从彷徨到自信，从过去到未来，不可知而又可期。

心中的感慨千千万，又不知那般叙述。在没有读研之前，我对硕士/博士的学习充满了不自信，我甚至不知道我能否顺利毕业。必须感谢张老师，他给了我很多自信和鼓励，包括在组会和讨论的时候对我的认可。必须感谢杨太群师兄，我们有过很愉快的时光，我在他的身上看到了很多科研工作者的素养和品质。当然，科研起点中遇到的每个人都值得感谢，是你们让我对科研“打起了”兴趣。感谢法国，感谢巴黎。这里自由，友好，宽容的氛围让我倍感舒适，也让我对这座他乡之城有了眷恋，尽管离程将至。

感谢 Christian 和 Antoine，没有你们就没有我在法国的这四年。对你们的感谢溢于言表，宽容，理解，幽默，风度，博学是你们身上的关键字，也是留给我的最大启迪。感谢有你们带我一路走来。

感谢在巴黎的小伙伴们，尤其是 IMAP 组的同事们。我想这么说应该不过分，我的博士阶段是因为你们而更加多彩，更加让人流连，乃至是思念。希望你们博士顺利，前程似锦，也希望我们来日方长，后会有期。

感谢我的家人们，特别是，爸爸妈妈和姐姐，任何时候，你们都是我最坚实的后盾。如今我即将到了而立之年，我想未来做你们的后盾。任时与境变迁，我永远爱你们。

Table of contents

General Introduction	1
Chapter 1 Introduction	9
Metal-Organic Frameworks: from ambient green synthesis to applications	11
1. Introduction	11
2. M(II) MOFs	13
3. M(III) MOFs	18
4. M(IV) MOFs	22
5. Applications of room temperature synthesis strategy	32
6. Perspectives and conclusions	37
References :	38
Recent progresses in metal–organic frameworks based core–shell composites	44
1. Introduction	44
2. Synthetic methods of core-shell MOF-based composites	46
3. Characterizations of core-shell MOF-based composites	58
4. Core-shell composites for catalysis	59
5. Core-shell composites for other applications	77
6. Conclusions and perspectives	80
References	82
Chapter 2 Stepwise room temperature synthesis of MOF-808	87
Contributions to this research	89
Article	90
Supporting information	105
Chapter 3 One-step ambient synthesis of tetravalent MOFs	125
Contributions to this research	127
Article	128
Supporting information	140
Manuscript	156
Supporting information	164

Chapter 4 Investigation of the capping agents removal from Au NPs@MOF-808	171
Contributions to this research.....	173
Manuscript.....	174
Supporting information.....	183
Chapter 5 Core-shell ultra-small Cu NCs@Zr-MOFs for photo-reduction of CO₂.....	192
Contributions to this research.....	194
Manuscript	195
Supporting Information.....	205
General Conclusion and Perspectives	214
Appendix.....	217

Abbreviations

MOFs: Metal-organic frameworks

MIL: Matériaux de l'Institut Lavoisier

PCN: Porous Coordination network

DUT: Technische Universität Dresden

UiO: University of Oslo

ZIF: Zeolitic Imidazolate Framework

MAF: Metal Azolate Framework

NPs: Nanoparticles

NCs: Nanoclusters

PXRD: Powder x-ray diffraction

TEM: Transmission electron microscopy

HRTEM: High-resolution transmission electron microscopy

STEM: Scanning transmission electron microscopy

FT-IR: Fourier-transform infrared spectroscopy

UV-vis: Ultraviolet-visible spectroscopy

TGA: Thermogravimetric analysis

BET: Brunauer-Emmett-Teller

SEM: Scanning electron microscope

DLS: Dynamic light scattering

NMR: Nuclear magnetic resonance spectroscopy

HAADF: High-angle annular dark-field imaging

LTID: Low temperature-induced defect

PVP: Polyvinylpyrrolidone

DMF: N,N-Dimethylformamide

EtOH: Ethanol

MeOH: Methanol

BDC: Benzene-1,4-dicarboxylic acid

BTC: Benzene-1,3,5-dicarboxylic acid

PDA: 1H-Pyrazole-3,5-dicarboxylic acid

TCPP: Tetrakis(4-carboxyphenyl)porphyrin

RT: Room temperature

DFT : Density functional theory

GG : Glycylglycine

cGG : Cyclic glycylglycine

HEWL : Hen egg white lysozyme

STY : Space-time yield

General Introduction

Heterogeneous catalysts frame a cornerstone of the chemical industry and are one of the most crucial technologies for a sustainable future. Catalysis deals with many processes such as production of food, pollution, energy sources, and critical transformation. Even though many works report the increasing efficiency/ selectivity of heterogeneous catalysts, there is no doubt that continuous demand remains for further improvements as the needs are growing in many fields. Inorganic materials and enzymes are the most common heterogeneous catalysts due to their unique catalytic metal sites and robust chemical functionality. Strong motivation recently has emerged in making complex inorganic- organic materials for a more reactive catalytic target. Similar to alloying, organic coordination can modify flexibly the electronic state of inorganic moieties, making them not only more reactive but also more tailorable in figuring out challenging catalysis. With regard to this, developing organic/ inorganic hybrid materials represent a very exciting direction for developing innovative catalysts.

Metal-organic frameworks (MOFs), also named as Porous coordination polymers (PCPs), are a recent class of crystalline organometallic materials. These solids have been drawing massive interest in both academia and industry in the last two decades mainly due to their permanent porosity, as well as tailorable properties. Many potential applications have been demonstrated to be very promising in the field, particularly for heterogeneous catalysis. MOFs as heterogeneous catalysts are in many aspects similar to enzymes in terms of having active metal species in atomic level and a catalytically relevant organic linker environment.

Metal nanoparticles (MNPs) are a sub-class of inorganic nanoparticles, whose sizes range from tens to few nanometers. MNPs have attracted a lot of attention in many research fields due to their unique characteristics and many emerging properties, which are in many ways different compared to their bulk form. Benefitting from the development in the synthetic strategies, better-defined MNPs have been prepared, particularly for those with small size due to their advantages in catalysis. The appealing reactivity enhancement often associated is due to the larger surface-to-volume ratio per unit mass, as well as the higher surface energy. However, regardless of the promises, many challenges still remain in the field, such as the instability of NPs towards harsh conditions like high temperature and high acidity.

Incorporating guest metal NPs into MOFs is another route to prepare highly efficient heterogeneous catalysts, which combines the properties of both the host MOF and guest NPs. The prepared composites present a great potential for several applications apart from catalysis (e.g. sensing, bio-applications), as the encapsulated guest materials can introduce new desired properties that are absent/ poor in the parent material. The most common strategies to encapsulate NPs are called ship-in-a-bottle and bottle-around-ship. The former one represents the introduction of NPs in the pores of preformed MOFs. However, several challenges still remain using this strategy, such as pore blocking by the guest species, NPs leaching during the use, and uncontrollable shape/ composition of NP (the size/ shape of NPs should be compatible with pores of MOFs), etc. These problems can be overcome by using the second strategy, in which MOFs are assembled in a solution containing pre-formed NPs to make core-shell structures. Several studies on the applications of core-shell structures have demonstrated their robust properties, particularly in the field of catalysis due to the close packing between NPs and MOFs, which results in an

interesting synergistic effect. The comparative studies between the core-shell NPs@MOFs and the NPs on the surface of MOFs reveal the advantages of core-shell ones in terms of catalytic activity and selectivity. To construct effective and reproducible core-shell architectures, mild synthesis conditions, e.g., relatively low synthesis temperature, eventually down to room temperature, are usually required but remain still challenging from a synthesis point of view. Many efforts dedicated so far in the field have relied on MOFs constructed from divalent cations (such as ZIF-8, MOF-5, HKUST-1), that can be easily synthesized at ambient conditions. However, these solids strongly suffer from a poor chemical stability, particularly upon exposure to moisture, which prevents their practical applications. MOFs based on high valence cations (e.g., trivalent, tetravalent) and carboxylate linkers are a subclass of MOFs, which often display remarkable chemical stability, especially for tetravalent Zr(IV)-based ones. Unfortunately, the ambient temperature synthesis of tetravalent MOFs is still very challenging, most of the syntheses still relying on traditional heating-based approaches. This is mainly due to the inhibited kinetics of MOF nucleation and growth, which subsequently prevents the effective formation of core-shell composites utilizing Zr-MOFs. Accordingly, preparing tetravalent MOFs at room temperature is one pre-required step for synthesizing core-shell MOF-based composites.

In this thesis, I will, as the first step, develop multiple approaches to prepare robust tetravalent MOFs at room temperature, including conventional stepwise and more facile novel strategies. The ambient synthesis, from a sustainable chemistry point of view, has to be taken into account prior to their future industrial production. Besides, I will exploit this method to the synthesis of several benchmark tetravalent MOFs that have not been yet reported synthesized at ambient conditions. Subsequently, I will use the new room temperature synthesis approaches to incorporate NPs into the MOF to reproducibly form core-shell NPs@MOF composites, prior to address several heterogeneous catalysis challenges.

Summary

This thesis focuses on the development of novel strategies to synthesize tetravalent MOFs at room temperature. These strategies allow us to achieve many different aims, such as tuning the size of MOF to maximize their catalytic efficiency, preparing novel phases that has been long time inaccessible at elevated temperature, and very defective while relatively stable phases. As prerequisite factor for the formation of core-shell MOF based composites, room temperature synthesis of tetravalent metals based MOFs is the first step. Subsequently, the room temperature synthetic methods are applied to form new core-shell structures with ultra-small NPs (<3 nm). The obtained core-shell composites show excellent catalytic efficiency in challenging heterogeneous reactions, such as the photo-reduction of CO₂.

In detail, this thesis is divided into five chapters.

Chapter 1 is composed by two review publications that present an introduction to Metal-organic frameworks and their room temperature synthesis as well as the progress concerning the synthesis and applications of core-shell MOF-based composites. The review papers are untitled “Metal-organic frameworks: from ambient green synthesis to applications” (Adv Energy Mat, 2021), and “Recent Progresses in Metal-Organic Frameworks based core-shell composites”, respectively (Bull Japan Chem Soc, 2021).

In chapter 2, I focus on a 6-connected Zr₆ oxoclusters-based benchmark MOF, namely, MOF-808. In this work, I used pre-synthesized Zr₆ oxoclusters as metal source instead of the commonly used Zr organic/ inorganic salts due to their higher hydrolyzed state. The use of pre-formed Zr₆ oxoclusters enables the use of mild conditions (less acidic than Zr salts) that facilitate the deprotonation of the linkers and the MOF assembly reaction. Additionally, the use of Zr₆ oxoclusters as the metal source bypasses the formation of Zr₆ from Zr(IV) salts, therefore further promoting the MOFs nucleation. As a consequence, MOF-808 is synthesized at room temperature in an aqueous solution. The high reactants concentration makes the ambient synthesis relatively fast (18 h). The synthesis yield reaches almost 100% (calculated according to the ligand). Subsequently, I realize the MOF-808 nanoparticles size has a strong dependence on the concentration of the reactants (from 850 nm to 35 nm), where higher reactants concentration leads to smaller nanoparticles size. The produced nanocrystals exhibit very nice monodispersity while keeping both an excellent crystallinity and porosity. Thanks to the promoted synthesis efficiency due to the high concentration of reactants, the space-time yield for the smallest MOF-808 reaches 2516 kg/ m³/ day. The resulting nanocrystals present a high quality colloidal dispersion of nano-MOF-808, reaching a nearly monodispersed suspension both at various concentrations (from 7 mg/ mL to 0.17 mg/ mL) and long-time-scale (24h). Such kind of ambient/ aqueous solution-based synthesis is very appealing for the encapsulation of temperature-sensitive active NPs using a bottle-around-ship strategy. Furthermore, the nano-MOF-808 series prepared in this work display a remarkable size-dependent catalytic efficiency towards peptide bond selective hydrolysis, both in short Gly-Gly peptide and in a protein substrate consisting of 129 amino acids. The smallest nano-MOFs showed the highest catalytic potential reported so far for Zr-MOFs and the reactivity trend is directly proportional to the external surface area of the MOF particles, thus suggesting that the catalytic reaction most likely occurs on the MOF external surface. Additionally, varying the particle size gives control over the specific protein fragments produced. This shows that MOFs

can be synthesized with a specific particle size to produce desired fragments, proving these MOFs can act as superior artificial protease nanozymes for use in the field of proteomics. The relevant work has been published in *Chem. Mater* (in 2021).

In chapter 3, a new facile and versatile approach is reported for the one-step synthesis of a series of highly porous metal(IV) carboxylate MOFs (M=Zr, Hf, Ce) including five 12-connected and two 8-connected MOFs, using ambient conditions in green solvents. The novel synthesis allows me to produce high-quality crystalline and porous robust metal(IV) carboxylate MOFs with varying metal salts. Moreover, tuning the synthetic parameters allowed me controlling the particle size at the nanoscale, which indicates that this novel synthesis is also applicable to produce nanoMOFs. I subsequently used the 5L pilot-scale system to evaluate the scalability of the synthesis, which allowed me to obtain the highest space-time yield for the room temperature synthesis of MOF-801(Zr). Then, I propose the first insights for the efficient MOF preparation based on *in-situ* kinetics observations. The reactants concentration is found to play a very critical role in determining the reaction efficiency. The high reactants concentration leads to a more acidic solution, which inhibits the MOF growth and slows down the crystallization, while with low concentration, the MOF crystallization significantly decelerated even if the pH is also higher compared to the reference synthesis. Therefore, I have optimized the synthetic conditions, particularly the presence of water and the moderate reactants concentration, in order to facilitate the ambient synthesis. This novel synthesis approach is also applied to synthesize UiO-66-NH₂, UiO-66-COOH, DUT-67, PCN-222 at room temperature in green solvents. This study represents the first one-step, versatile, and template-free room temperature synthesis of many tetravalent MOFs, which, I hope, will guide the future synthesis of tetravalent MOFs at ambient conditions. The relevant work has been published in *Angew. Chem. Int. Ed.* (in 2020). Secondly, I report a similar strategy to synthesize efficiently a series of highly crystalline Ce-UiO-66-X (X= H, Br, NO₂, COOH) in an aqueous solution at room temperature. Ce(IV)-MOFs exhibit very appealing photocatalytic features due to the low-lying 4f orbitals that can conceivably accept electrons from reduced species. In addition, the energy bandgap of the synthesized Ce-UiO-66-X can be tuned by functionalization of the benchmark organic linker (BDC). However, it is of great challenge to synthesize Ce(IV) phases with basic/redox active ligands, such as BDC-NH₂, particularly at elevated temperatures. For the first time, the RT strategy is demonstrated as a useful method to reconcile the contradiction between redox-active metal nodes and redox-active ligands, facilitating the formation of Ce(IV)-MOFs due to the inhibited reduction of Ce(IV) to Ce(III) at room temperature. As a consequence, I obtained a highly crystalline Ce-UiO-66-NH₂ for the first time with a green *de novo* route. I also demonstrated that the novel Ce-UiO-66-NH₂ couldn't be prepared if the reaction temperature is of 60 °C while other synthetic parameters are fixed. To be noted, the product yield of Ce-UiO-66-NH₂ is significantly lower than other Ce-UiO-66-X probably due to the partial inevitable reduction of Ce(IV). This can be tentatively overcome by using more starting Cerium salts, which allows the product yield to reach 86%. The efficient preparation conditions (1-2 h) allow achieving space-time yields (STY) ranging from 300 kg/ m³/ day to 900 kg/ m³/ day, comparable to that of hydro/ solvothermal strategies of other benchmarks MOFs and fulfilling the industrial-scale requirements. Apart from these 12-connected UiO-type Ce-MOFs, I also report other benchmarks Ce(IV) MOFs with varying connectivity modes such as the 8-connected Ce-DUT-67 and 6-connected Ce-MOF-808 using similar aqueous solution-based room temperature

conditions. The catalytic activity of these Ce-MOFs is under investigation. This work is under preparation for publication.

In **chapter 4**, the room temperature synthesis protocol of the Zr trimesate MOF-808 presented in chapter 2 is applied to construct new core-shell Au NPs@MOF-808. The produced Au NPs@MOF-808 displays a uniform Au NPs spatial distribution with a mean size of 3 nm, which could be very interesting for catalysis. However, due to a large amount of capping agent (PVP) used in this study (Au: PVP= 1: 100), PVP shall be removed in order to get an interesting catalytic activity. I show for the first time how the PVP from the core-shell Au NPs@MOF-808 can be removed using various chemical/ physical treatments. The accessibility of Au metal sites has then be evaluated by using a model reaction (oxidation of benzyl alcohol). The double solvent method, which presents the use of the mixture of good/ poor solvent in an appropriate ratio, coupled with hydrochloric acid (HCl) washing showed a promising impact on the removal of PVP, which result in boosted reaction efficiency. I propose then one plausible pathway to explain the efficient removal of capping agent, where hydrochloric acid helps to protonate the PVP, which thus makes the coordinating bonds weaker and increases its solubility. Furthermore, the optimized double solvents (acetone and H₂O) washing plays also an important role for the PVP removal. The mechanism of double solvent washing can be understood as the following: the surface ligands tend to shrink on the surface of NPs to form compact configuration when the poor solvent is added, whilst they can be fully dispersed in the good solvent and therefore easy to detach from the particle surface. I believe these findings may help future studies to achieve better reactivity and selectivity using similar core-shell MOF-based composites. A publication shall be submitted soon.

In the **Chapter 5**, I further take advantage of room temperature synthesis strategy to incorporate for the first time ultra-small Cu nanoclusters (1.6 nm) in three benchmarks microporous Zr-MOFs (MOF-801, UiO-66-NH₂, DUT-67). The formed Cu NCs@MOFs core-shell structures display well-maintained porosity, crystallinity, and product yield compared to their original synthesis without Cu NCs. The mild synthesis conditions, including room temperature and much less acidic solution, are very important factors for successful composites synthesis. Moreover, the low cost of the raw materials and green synthesis conditions enable me to optimize the synthetic parameters to achieve gram-scale catalyst preparation. The prepared composites display high reactivity and selectivity towards the photo-conversion of CO₂ to chemical feedstock at room temperature. In addition, when comparing the catalytic reactivity of Cu NCs on the MOFs, where Cu NCs are mainly on the surface of MOF, a much lower reactivity is observed, demonstrating the advantages of core-shell structures in governing the high reactivity of MOF based catalytic composites. Finally, I study the origin of active sites by using In-situ IR spectroscopy, revealing the contribution of the Cu(I) from the surface of Cu NCs. This work is under preparation for publication.

Finally, the general conclusion and perspectives are discussed.

Overall, the synthesis of tetravalent MOFs at room temperature, as well as the following objectives, including the size tuning of benchmark MOFs, the preparation of high-temperature inaccessible phase, and the construction of core-shell NPs@MOF composites, have been

successfully achieved. The room temperature prepared MOFs/ NPs@MOFs composites show boosted catalytic efficiency for challenging heterogeneous catalysis.

Chapter 1

This chapter is adapted to the following Review publications:

1. Metal-organic frameworks: from ambient green synthesis to applications

Bull. Chem. Soc. Jpn. **2021**, [DOI: 10.1246/bcsj.20210276](https://doi.org/10.1246/bcsj.20210276)

Shan Dai et al.

2. Recent Progresses in Metal-Organic Frameworks based core-shell composites

Adv. Energy. Mater. **2021**, 2100061.

DOI: [10.1002/aenm.202100061](https://doi.org/10.1002/aenm.202100061)

Shan Dai et al.

Table of Contents

Metal-Organic Frameworks: from ambient green synthesis to applications	11
1. Introduction	11
2. M(II) MOFs	13
3. M(III) MOFs	18
4. M(IV) MOFs.....	22
5. Applications of room temperature synthesis strategy.....	32
6. Perspectives and conclusions.....	37
References	38
Recent progresses in metal–organic frameworks based core–shell composites	44
1. Introduction	44
2. Synthetic methods of core-shell MOF-based composites	46
3. Characterizations of core-shell MOF-based composites	58
4. Core-shell composites for catalysis	59
5. Core-shell composites for other applications	77
6. Conclusions and perspectives	80
References	82

Metal-Organic Frameworks: from ambient green synthesis to applications

Abstract: Studies of the room temperature synthesis of Metal-Organic Frameworks (MOFs) are still scarce and mainly focused on divalent metals based MOFs. The development of room temperature synthesis of more chemically robust MOFs is still challenging and therefore lacks of exploration. Here, we review the development of ambient conditions synthesis of MOFs, from the properties of the sole MOF to their related composites. Low temperature green synthesis can not only meet the standards of sustainable chemistry, but also help to achieve a series of property enhancements, including their applications in catalysis, biomedicine, and sensing. Finally, perspectives associated to the synthesis strategies and applications of room temperature methods are discussed.

1. Introduction

Metal-Organic Frameworks (MOFs) have emerged as a promising class of porous materials due to their long-range ordered structure, high specific surface area, tunable composition, as well as almost infinite structural diversity.^[1] All these features make these solids very promising for various applications, including catalysis,^[2] separation,^[3] conductive devices^[4] sensing,^[5] and bio-applications.^[6] In the 1990s, researchers realized the discrete inorganic materials can be interconnected by the organic ligands to form ordered structures.^[7] At the same time, a unique class of crystalline porous materials, namely Metal-Organic Frameworks (MOFs), was defined. Their sometimes extremely high surface area associated with their large chemical and structural diversity makes them appealing and competitive to traditional porous solids (e.g., zeolites, carbons) for a large range of applications, such as gas adsorption/ separation in the early stage.^[8] In particular, the high degree tunability of both the constitutive secondary building units (SBU)^[9] and organic ligands has opened up a rather unique opportunity in the field of porous to tune their properties. In this direction, the efforts have been dedicated to boldly combine almost all kinds of metal cations with varying organic linkers. According to the Cambridge Structural Database (CSD), there are more than 100,000 entries based on the CSD (~10% of the CSD).^[10] Accordingly, the number of relevant publications expanded rapidly in the past two decades (See Figure 1).

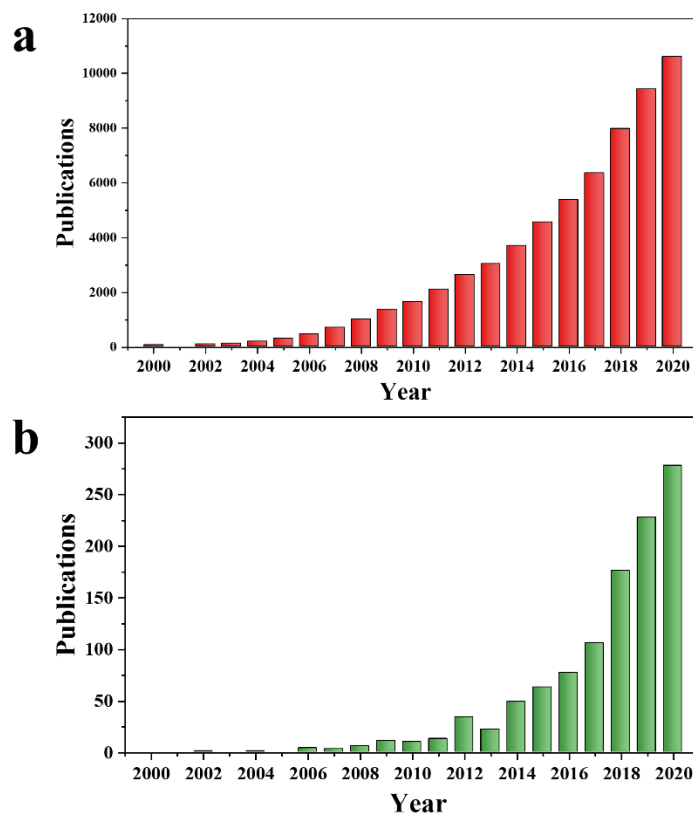


Figure 1. The number of publications of MOF in last two decades, from 2000 to 2020. a) the terms “MOF” or “Metal-Organic Frameworks” b) the terms of “metal-organic frameworks” and “green synthesis” were used to search in Web of Science.

The synthesis of MOFs is often at the origin of many novel properties for various applications. Of these, the most typical preparation route for MOFs is solvothermal/ hydrothermal synthesis, where the metal precursors and organic linkers are mixed and sealed in a Teflon autoclave containing certain solvents (e.g., N,N-dimethylformamide (DMF), N,N-diethylformamide (DEF), sometimes H₂O).^[11] The synthesis temperature is generally between 100 °C and 220 °C. The microwave-assisted hydro/solvothermal synthesis is another method, which is usually used to rapidly rise the temperature of the reaction in order to accelerate the kinetic of crystallisation. As such, microwave-assisted synthesis often combine high efficiency and effective production of nanocrystals due to the shortened synthesis duration.^[12] However, it should be noted that these synthesis methods still requires high temperature combined with autogenous pressure, which therefore limit their upscaling and eventually industrialization.^[13]

Recently, exciting advances have been achieved in the synthesis of MOFs,^[14] including the concept of “green synthesis” that has been applied to prepare MOFs.^[15] Publications grew more significantly in very recent 5 years (see Figure 1b). Depending on the targeted structures and properties, MOFs can be alternatively prepared by using many distinct and “relatively green” approaches, such as electrochemical,^[16] slow diffusion,^[17] spray-drying,^[18] pump flow,^[19] and

mechanochemical^[20] syntheses. However, all these methods are associated with a specific energy cost, which, from a sustainable chemistry point of view, has to be taken into account prior to their future industrial production. Additionally, these methods might also hinder the incorporation of temperature sensitive compounds into core-shell structures.^[21]

Room temperature synthesis (RTS) of MOFs refers to the synthesis in ambient conditions without an external heating procedure. The RTS includes stepwise and direct methods. The former one represents the strategies with multiple steps, including the pre-treatment of organic ligands or inorganic metal cations, and the pre-synthesis of inorganic sub-units (e.g., Fe oxotrimer, Ti oxoclusters, Zr₆ oxoclusters).^[22] This step allows the subsequent ambient construction of the overall MOF. The direct RTS corresponds to a one-pot one-step synthesis without any additional treatment. This method is more interesting compared to stepwise synthesis in terms of synthetic complexity and overall preparation cost. Great progresses have been realized in the field of divalent metals based MOFs RTS within the last years. However, the RTS for high valence MOFs is still challenging due to the higher activation energy needed, which may request external heating to make the reaction start. In all these syntheses, the “space-time yield (SPY)” is rarely calculated regardless of its importance for real applications.

In this review, we summarize the development and the progress of room temperature synthesis methods of MOFs as a function of the charge of the metal cation. We emphasize the importance of RTS of more chemically robust high valence MOFs, such as tri or tetra-valent metals based carboxylate MOFs. The RTS allows a safer and greener synthesis that may be suitable for industrial applications. Additionally, the ambient synthesis that is compatible with the encapsulation of temperature sensitive compounds, could also lead to some property enhancements (e.g., catalysis, gas sorption, biomedicine). We finally discuss the future of the ambient synthesis of chemically robust MOFs and hope this will promote not only novel green synthesis routes but also new applications based on this strategy.

2. M(II) MOFs

Early-stage MOFs were primarily composed of divalent transition metals (Zn²⁺ or Cu²⁺) and polycarboxylate linkers. Divalent MOFs nowadays includes almost all divalent metal cations, such as Ca²⁺, Mg²⁺, Mn²⁺, Fe²⁺, Co²⁺, Ni²⁺, Cu²⁺, Zn²⁺, Cd²⁺ and Ba²⁺.^[23] The typical ligands are based on carboxylates, phosphonates, or N donating linkers. All these options result in a wide range of structure types and porosities, from the micro to mesoscale and with possible functional groups on the organic spacers. The SBUs for M(II)-MOFs contains widely single metal cations, bi/ tri/ tetra-nuclear oxoclusters, and chains (illustrated in Figure 2).^[24] Great efforts were dedicated not only to develop novel M(II)-MOFs but also in to optimize ambient synthesis of these MOFs. For example, in 2008, the rapid, simple, and high-yield room temperature syntheses of various divalent MOFs, including MOF-5, MOF-74/ CPO-27, MOF-177, and Cu-BTC (or HKUST-1) was reported. The extension to a few new structures was also demonstrated by the authors. These examples demonstrated for the first time that heating is not necessary to produce highly crystalline MOFs.^[25] Subsequently, further optimizations of the ambient synthesis of M(II)-carboxylate

MOFs were reported, including efficient ultrasonic synthesis,^[26] aqueous solution-based synthesis with high space-time yield^[27], nanosized MOFs preparation,^[28] mixed divalent metals MOF synthesis^[29] and even mechanochemical syntheses without solvents.^[30] Remarkably, the syntheses of M(II)-carboxylate benchmarks have been optimized and some of them even meet the industry need.^[31] However, the metal–ligand bonds in these MOFs are prone to rapid hydrolysis, often making them not suitable for most practical applications. Moreover, the quality of these room temperature prepared MOFs has been questioned in terms of textural properties.^[32]

Alternatively, using divalent metals and nitrogen containing ligands, such as triazole, tetrazole, imidazole, and pyrazole can lead to more chemically robust MOFs based on M(II)-N bonds.^[33] One typical example is the Zeolitic imidazolate framework (ZIF) series of MOFs. The first example of such structure was reported by Chen's group in 2005 that obtained a MOF with a unique cage-like structure with a large cavity size of 1 nm and a window size of 3.3Å.^[34] Polymorphic structures with imidazolate and Zn(II) subsequently experienced a fast expansion mainly due to their easy crystallization and improved chemical stability and functionality.^[35] Afterwards, the corresponding efficient room temperature synthesis with high crystal quality and different crystal sizes using organic solvents,^[36] aqueous solution,^[37] or even using mechanochemistry,^[38] were reported.^[39] These novel environment-friendly ambient synthesis routes immediately attracted intensive research interest, which subsequently made them the most used synthesis approaches for the synthesis of the ZIF series of MOFs.

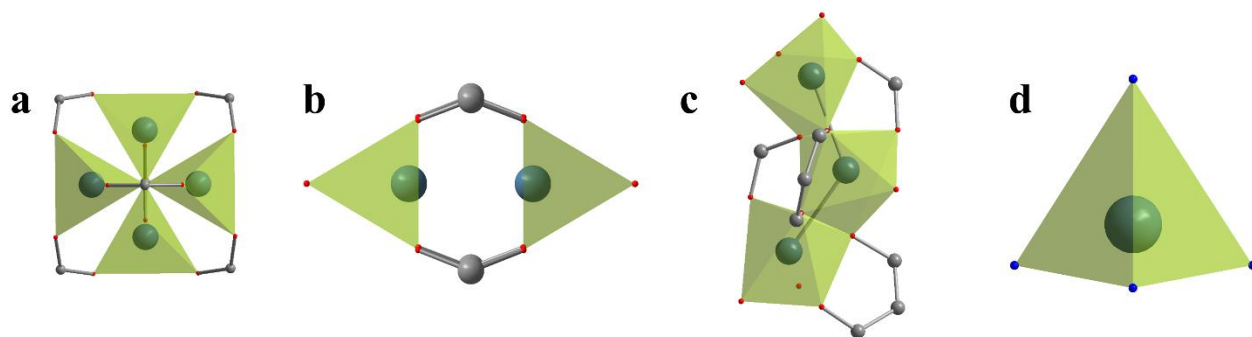


Figure 2. Graphical illustration of common SBUs obtained with divalent MOFs, a) $\text{Zn}_4\text{O}(\text{CO}_2)_6$ oxocluster, b) $\text{Cu}_2(\text{CO}_2)_4$, c) $\text{Ni}_3\text{O}_3(\text{CO}_2)_3$ chain, d) $\text{Zn}(\text{II})$ cation.

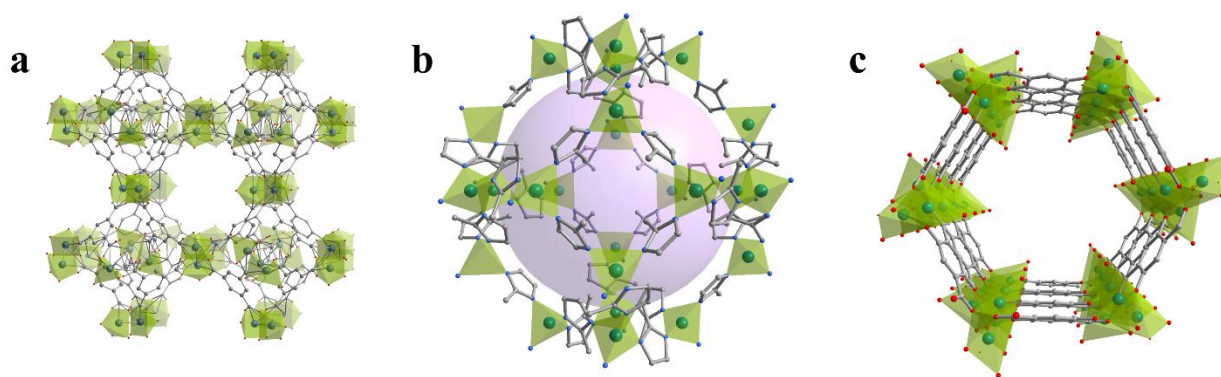


Figure 3. Typical divalent MOFs structures. a) HKUST-1, b) ZIF-8, c) MOF-74/CPO-27. Inorganic node polyhedra in light green with oxygen in red, nitrogen in blue and carbon atoms in grey.

It should be pointed out that even though MAF/ ZIF (MAF stands for Metal Azolate Framework) series of MOFs show improved chemical stability, some of them are still suffering from degradation in pure aqueous solution or slightly acidic conditions.^[40] The use of organic linkers bearing pyrazole groups with a higher pKa (= 19.8) has been applied to prepare even more robust M(II)-N based MOFs, which can be stable not only in boiling aqueous solutions but within a large range of pH, from 2 to 14, for two weeks.^[41] However, the vast majority of divalent MOFs still suffers from degradation in aqueous solution or sometimes even under humid air, which is a clear disadvantage in a view of practical applications.

Table 1. Ambient synthesis examples for M(II) based MOFs.

Materials	Method ^a	SBU	Solvents	Synthesis duration (h)	RTS _{surface} area/ OS _{surface} * area (m ² /g)	Ref
MOF-5	Solution	Zn ₄	DMF	2.5	3909/ 2500-3000 ^[42]	[25]
HKUST-1	Solution	Cu ₂	DMF, EtOH, H ₂ O	23	-	[25]

MOF-177	Solution	Zn ₄	DMF	3	4944/ 4500 ^[43]	[25]
MOF-74	Solution	Ni ₃ chain	DMF	18	1187/ 816 ^[44]	[25]
ZIF-8	Solution	Zn atom	MeOH /DMF	1 /18	962 /1947 ^[35a]	[36]
HKUST-1	Mechanochemical	Cu ₂	-	0.42	758/ 1781 ^[44]	[30]
Cu ₃ (BTB) ₂	Mechanochemical	Cu ₂	-	0.42	628/ 1781 ^[44]	[30]
Cu ₂ (ndc) ₂ (dabco)	Solution	Cu ₂	DMF	24	143	[45]
MOF-74	Solution	Cu ₃ chain	MeOH	0.17	1013/ 816 ^[44]	[46]
Zn ₂ (X) ₂ (DABCO)	Solution	Zn/ Ni/ Co/ Cu atom	MeOH/ DMF	4	2113/ 2104	[47]
Ni ₂ Co ₁ _{1-x} Fe _x	Solution	-	DMF	1	130	[29]
HKUST	Ultrasonic	Cu ₂	DMF	0.08-1	1100/ 1781 ^[44]	[26]
HKUST-1(Cu, Zn), MOF-5 (Cu, Zn)	Salinization	Cu ₂ , Zn ₄ ,	H ₂ O	0.08-2	1721, 687/ 1781 ^[44]	[48]
HKUST-1	Solution	Cu ₂	H ₂ O	1	1749/ 1781 ^[44]	[27a]
HKUST-1	Solution	Cu ₂	DMSO, MeOH	0.17	-	[27b]

HE-MOF	Ultrasonic	Mn/ Fe/ Co/ Ni/ Cu atom	DMF, H ₂ O, EtOH	1	165	[49]
ZIF-8, ZIF-4	Mechanochemical	Zn atom	-	0.5-1	-	[38]
MOF-74	Solution	Zn ₃ , Co ₃ , Mn ₃ , Mg ₃ , Ni ₃ chain	DMF	20	402- 1007/ 816 ^[44]	[28]
ZIF-67	Additive	Co atom	H ₂ O	0.17	868/ 316 ^[50]	[51]
ZIF-93	Additive	Zn atom	H ₂ O	18	604/ 94 ^[52]	[53]
ZIF-8	Solution	Zn atom	MeOH	2-24h	600/ 1947 ^[35a]	[54]
ZIF-8	Additive	Zn atom	MeOH	0.017	1566/ 1947 ^[35a]	[55]
ZIF-61	Additive	Zn atom	MeOH	0.017	-	[55]
ZIF-90	Additive	Zn atom	MeOH	0.017	-	[55]

a: Solution refers to the conventional synthesis that needs solvents. Salinization refers to the synthesis that needs pre-salinization of the organic ligands. Additive represent the using of additional agents in the solution synthesis.

*: OS represents the original synthesis, including solvothermal/ hydrothermal synthesis.

3. M(III) MOFs

In this section, we only focus on the M(III)-carboxylate MOFs due to their higher thermal/chemical stability compared to most divalent MOFs. Trivalent MOFs can be prepared using several transition metal cations including Al^{3+} , Fe^{3+} , Cr^{3+} , V^{3+} , Ga^{3+} , Sc^{3+} , In^{3+} , Bi^{3+} ^[56] and even lanthanide metal cations^[57] combined with most of the conventional di, tri, and other multitopic linkers as organic ligands. Férey and Serre, that pioneers the discovery of trivalent MOFs, developed many well-known benchmark MOFs structures in the MIL-n series : MIL-53,^[58] MIL-101,^[59] MIL-100,^[60] MIL-88,^[61] MIL-127,^[62] etc. So far, two main SBUs constitute the majority of trivalent MOFs.^[63] The first one is the ‘chain’ SBU built from μ_2 -hydroxo corner-sharing M(III) O_6 octahedra (Figure 4a). The second is the M(III) trinuclear unit with a formula of $\text{M}_3(\mu_2\text{-O})(\text{OH})(\text{H}_2\text{O})_2(\text{COO})_6$ (Figure 4b), where the hydroxide groups can be replaced by other anionic species (e.g., F^- , Cl^- ...) depending on the synthesis conditions. The typical synthesis route for trivalent MOFs is the solvothermal synthesis in polar solvents (e.g. water, DMF, alcohols). The large number of available M(III) salts is of great interest to optimize the MOF synthesis in order to meet the demand of the industry. For instance, the first commercially available MOF, Basolite A520,^[64] an analogue of MIL-53-Al solid, was synthesized in water using mild conditions.^[64] The RTS of trivalent MOFs has experienced long-time efforts with limited promising results. For example, Sánchez-Sánchez et al. reported a simple two-steps route for Al-chain based MIL-53-Al (Figure 4c) and its amino- and nitro- functionalized derivatives.^[65] This synthesis method relied on the use of disodium terephthalate as linker salt in sole water due to the poor solubility of terephthalic acid in water (illustrated in Figure 5). The use of linker salt completely changed the solubility of the linker and therefore the kinetics of MOF formation. Several techniques, such as PXRD, 77K nitrogen sorption isotherms and SEM were applied to confirm the quality of the resulting nanocrystals, which was comparable to those synthesized in DMF at high temperature. However, the protonated linker filled up the pores forcing the use of calcination to active MOFs, which is not a friendly method from green chemistry point of view. Apart from the RTS for the MOFs based on inorganic chains, strategies were also reported to deal with aforementioned trimer oxoclusters. MIL-100 is the benchmark ‘trimer’ trivalent carboxylate MOF and is built with M(III) oxotrimers and BTC linkers.^[66] It presents two types of cavities (2.9 nm and 2.5 nm) with a zeolite-like structure (Figure 4d). MIL-100 can be prepared with Cr(III),^[67] Fe(III),^[66] Al(III)^[68] and its synthesis was recently extended to metal(IV) cations such as Ti(IV),^[69] and larger tritopic linkers.^[70] Li and his team reported a RTS strategy by using iron powder and oxidizing radical as starting materials to accelerate the crystallization of MIL-100(Fe) without HF addition.^[71] First, the iron powder was dispersed in aqueous HNO_3 solution under sonication and the BTC linker was mixed in the aqueous solution with *p*-Benzoquinone to form a deprotonated linker. Then, these batches were mixed together under stirring at room temperature for 12 h. The obtained MIL-100(Fe) showed comparable surface area with the conventional synthesis, which indicated its high quality. However, the relatively low product yield, as well as the generated explosive gas (H_2), prevents the use of this synthesis strategy for industry.

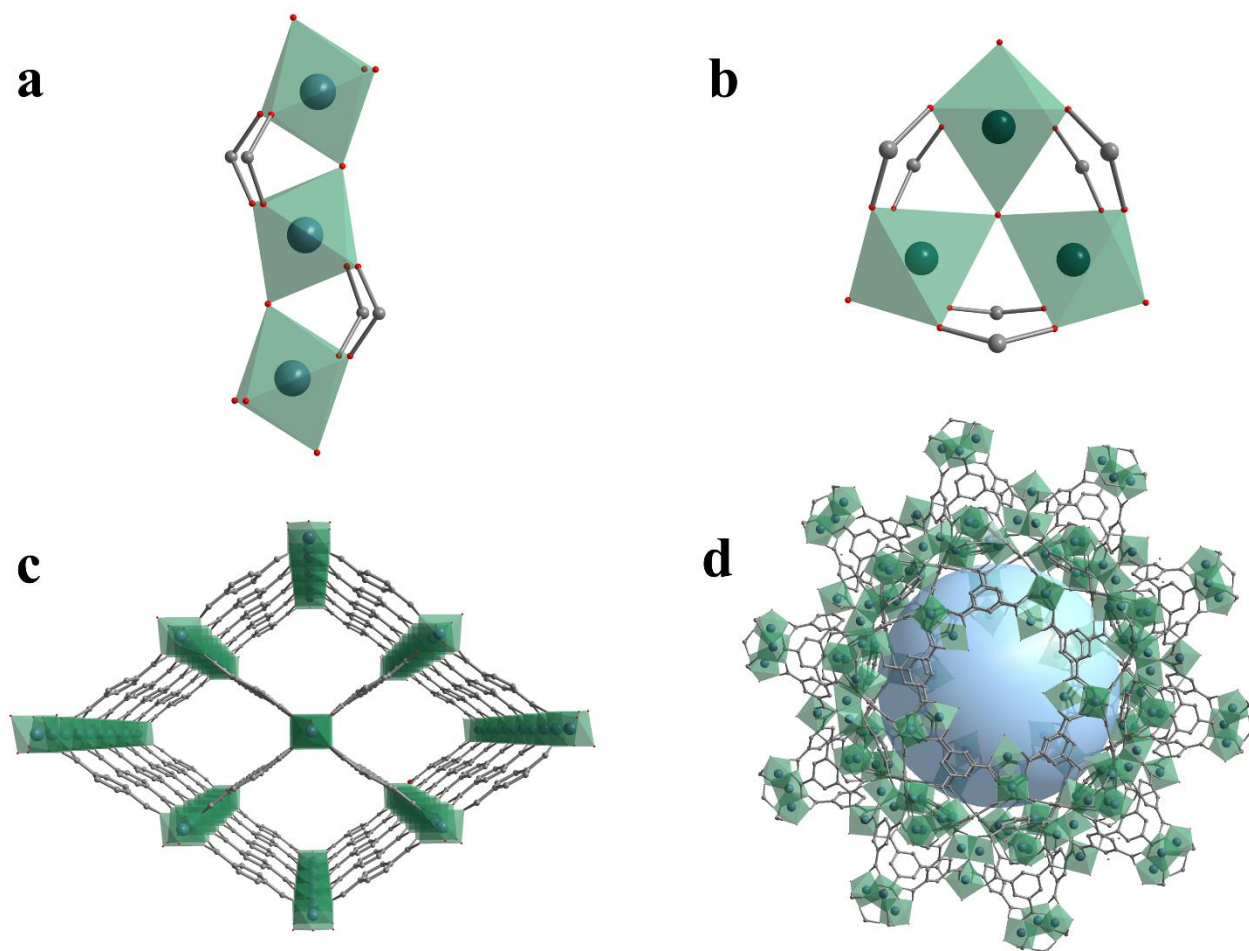


Figure 4. Archetypical SBUs observed in the M(III)-MOFs a) MO_6 chain, and b) M_3 oxo-trimer. c) Structure scheme of MIL-53, d) Structure scheme of MIL-100. Inorganic node polyhedra in green with oxygen atoms in red and carbon atoms in grey.

More recently, $Fe(NO_3)_3$ was directly used as starting metal salt and simply combined with BTC in water. After 48 h stirred at room temperature, an orange solution was obtained. The product was filtered and washed with water to yield an orange-brown solid. No further treatment was needed and therefore, the MOF nanoparticles obtained could be used as such. This is the first example that used directly Fe(III) salt and BTC in a pure aqueous solution to synthesize MIL-100(Fe). The resulting MIL-100 showed high quality, including porosity ($\sim 1800 \text{ m}^2/\text{g}$, BET model), crystallinity, and connectivity. More importantly, the MIL-100 owned a reasonable particle size distribution together with a mean size at around 60 nm, which is very suitable for nanomedicine that rely on bio-compatible nano-MOFs.^[72]

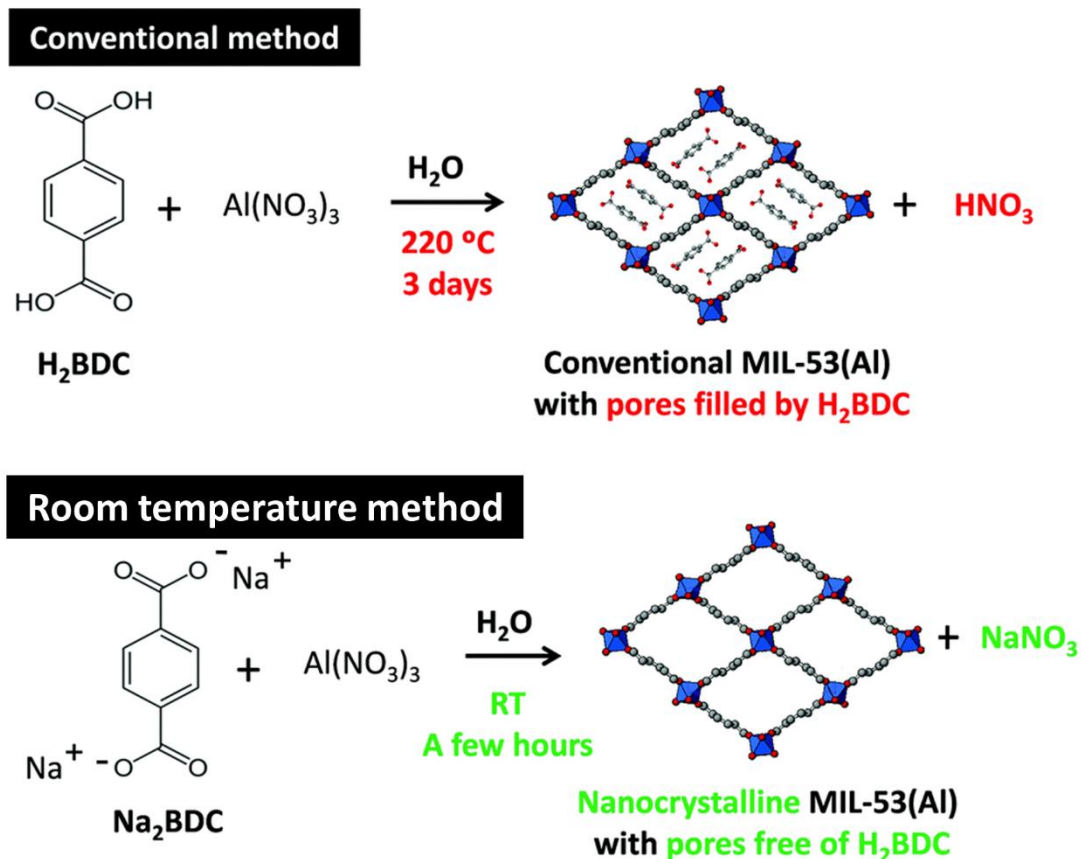


Figure 5. General reaction for the preparation of MIL-53(Al) by conventional (top) and the room temperature green synthesis methods. Produced with permission, RSC 2015.^[65]

Metal(III) oxo-trimers show more diverse structural complexity due to their higher degree of connectivity than metal(III) chains. MIL-88A is a prototypical breathing MOF with trivalent oxo-trimers as SBU. Serre et al reported in 2004 the ambient synthesis in methanol of this MOF relying on preformed trimeric Fe acetate SBU and in 2010 its ambient green synthesis conditions based on various metal sources.^[73] Very recently, Avci-Camur et al. reported RTS of MIL-88A in an aqueous solution through the assistance of acetylacetonate anions. However, the low product yield (25%) makes it hard to prepare at a large scale though it can be alternatively improved to 60% by heating the slurry at 90 °C.^[74]

Apart from the common SBUs observed in the abovementioned examples, more recently, a trivalent Bi(III) phenolate-based MOFs, bismuth ellagate (SU-101), was reported (see Figure 6).^[75] The overall framework is stable in a wide range of pH values. The synthesis was performed through a simple and green pathway, where only water and 6% of acetic acid (by volume) were used as solvent under ambient conditions. High-quality crystals were collected accordingly with a high product yield of 76%. Even though the space-time yield is still not high, only 5 kg m⁻³ day⁻¹, which is significantly lower than many other examples,^[76] one should note the simplicity of the synthesis procedure, carried out at atmospheric pressure and room temperature. To be noted, a very time-consuming synthesis at room temperature could also be problematic due to the many associated costs for an industrial production.

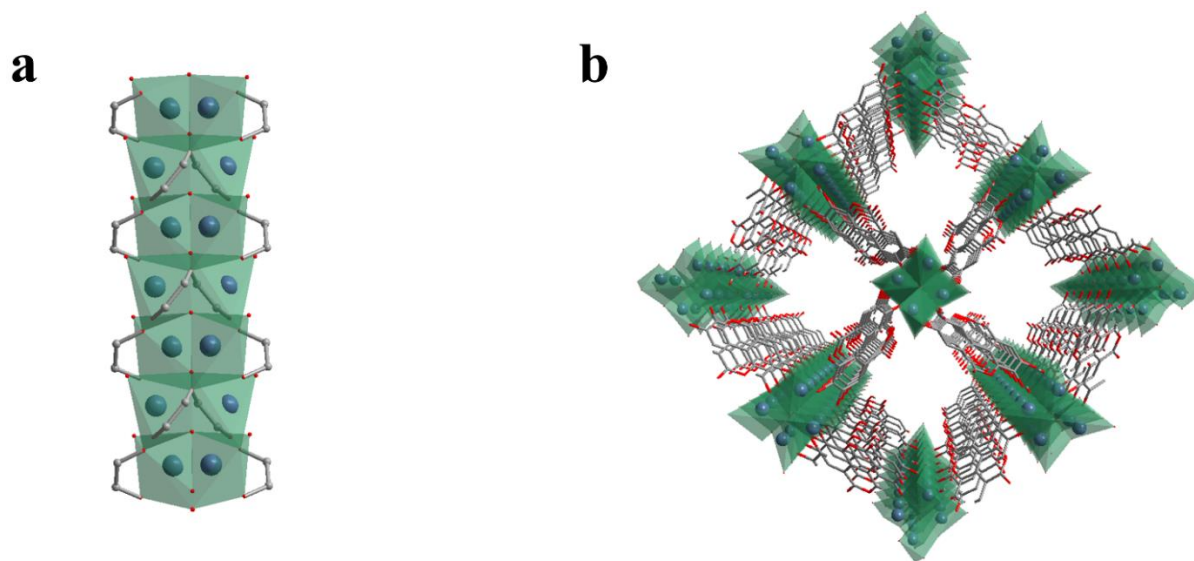


Figure 6. a) binuclear rod-like SBU (Bi₂O), b) the structure of SU-101 as viewed down the *c*-axis. Inorganic node polyhedra in green with oxygen in red, linker molecules in grey.

Table 2. Ambient synthesis examples for M(III) based MOFs.

Materials	Method	SBU	Modulator	Solvents	Synthesis duration (h)	RTS _{surface} area/ OS _{surface} [*] area (m ² /g)	Ref
SU-101	One-step	Bi ₂ O	Acetic acid	H ₂ O	48	412	[75]
MIL-53(Al)	One-step	AlO ₆	-	H ₂ O	24	1144/ 1140 ^[77]	[65]
MIL-100(Fe)	Two-steps	Fe ₃ trimer	-	H ₂ O	12	2482/ 1800 ^[78]	[71]
MIL-100(Fe)	One-step	Fe ₃ trimer	-	H ₂ O	48	1800/ 1800 ^[78]	[72a]
MIL-100(Fe)	Two-steps	Fe ₃ trimer	-	Ethanol H ₂ O	0.08-72	356- 1410/ 1800 ^[78]	[79]

MIL-53(Al)-NH₂	Two-steps	AlO ₆		H ₂ O	14	518/ 1347 ^[80]	[81]
MIL-88A	One-step	Fe ₃ trimer		H ₂ O	72	-	[74]
MIL-88A	One-step	Fe ₃ trimer	-	EtOH H ₂ O	24	-	[82]
MIL-88A	Sonication	Fe ₃ trimer	-	H ₂ O	2	-	[73]

*: OS represents the original synthesis, including solvothermal/ hydrothermal synthesis.

In summary, the room temperature synthesis of crystalline trivalent MOFs is still at its early stage in contrast to divalent ones, mainly due to the higher reactivity of M(III) cations. The appearance of more general and easier synthetic approaches is still required. Besides, the excellent chemical/ thermal stability of trivalent MOFs can allow their doping with several metal cations. Recent publications have demonstrated that these heterometallic MOFs are of importance for emerging applications.^[83] Room-temperature synthesis might facilitate the integration of metals cations with various valences into MOFs structures by preventing their oxidation/ reduction that may occur using higher temperature syntheses. The relevant ambient syntheses of trivalent MOFs are listed in Table 2.

4. M(IV) MOFs

Tetravalent-metal carboxylate based MOFs are another important subclass of MOFs, usually showing a high chemical/ thermal robustness in comparison to other MOFs.^[84] According to Pearson acid-base theory (HSAB), the hard Lewis acids (e.g., metal with high oxidation state) can bond strongly with hard Lewis bases (e.g., carboxylate, phosphonate,^[85] etc.), which thus makes the M(IV)-MOFs robust enough even in some very harsh conditions (boiling water, aqua regia, ammonia vapor).^[84a, 86] Typically, the M(IV) elements in the MOFs chemistry include all the group four elements, which is the second group of transition metals in the periodic table and some lanthanides and actinides. Zr(IV)-MOFs are the most explored tetravalent MOFs due to their appealing properties, including low toxicity, high abundance, excellent stability and their relatively easier crystallisation. For instance, UiO-66 (UiO= University of Oslo) is a benchmark Zr-MOF constructed from Zr(IV) hexanuclear oxoclusters (Figure 7b) connected through 12 terephthalate ligands (typically called 12-connected Zr₆ based phase).^[87] Since the report of UiO-66 in 2008, many promising applications based on this MOF or its analogues have been reported.^[88] This work has also inspired many following discoveries of other Zr-MOFs.^[89] The synthesis of Zr-MOFs was at that time still very challenging due to the high reactivity of Zr(IV) cations with organic linkers, which formed immediately poorly crystalline solids once mixed in solution. In 2011, Schaatte et al. reported that the use of monocarboxylic acids (e.g., formic acid, acetic acid), employed as a

modulator, enable a certain control of the kinetics of coordination between metal and di, tri, or polytopic ligands through competitive effect.^[90] The modulated synthesis of Zr-MOFs led to the rapid discovery of series of Zr-MOFs, in which Zr₆ oxocluster is the most common SBU. As this oxocluster can connect different carboxylate ligands regardless of their difference in topic, size, angle, or functional group, many MOF topologies were obtained.^[91] So far, there are Zr₆ based structures with 12-connected, 10-connected,^[92] 9-connected,^[93] 8-connected,^[86] 6-connected^[94] and 4-connected oxoclusters.^[95] The careful control over the synthesis conditions have also allowed the generation of Zr-MOFs with novel SBUs, such as the ZrO₇ chain found in the MIL-140 series (Figure 7a)^[96] or more recently Zr₁₂ oxoclusters (Figure 7c).^[97]

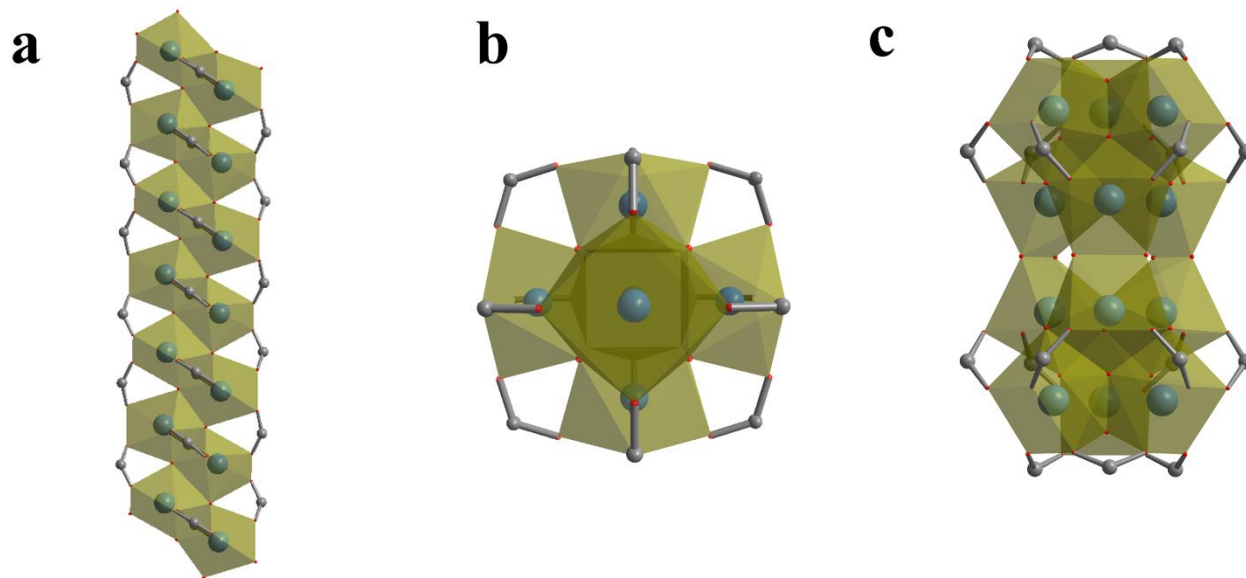


Figure 7. Graphical illustration of common SBUs within Zr(IV)-MOFs, a) ZrO₇ chain, b) Zr₆ oxoclusters, c) Zr₁₂ oxoclusters.

The RTS of Zr-MOFs is complex for many reasons: 1) the high acidity of the solution, which makes difficult the deprotonation of the ligands before the formation of coordination bonds, 2) the exchange reaction between the modulator and organic ligand that needs to be controlled, possibly through heating steps, 3) to the fact that the activation energy for MOF nucleation and growth should be lowered if one wants to work at RT 4) the tendency to form poorly crystalline products. As tetravalent MOFs are relatively recent in comparison to their di/ tri-valent counterparts, the corresponding ambient routes are thus still scarce. In the following, we present several recent strategies that have been successfully applied so far to prepare such materials.

3.1 Stepwise room temperature synthesis

In 2010, Guillerm et al. reported the synthesis of a UiO-type of MOF with *trans*, - *trans*-muconic acid as the organic ligand using pre-formed zirconium methacrylate oxoclusters as the starting material in DMF at room temperature.^[22b] This strategy is called “two-steps synthesis” (illustrated

in Figure 8a) because the commercially unavailable Zr_6 oxoclusters should be pre-synthesized. However, it should be noted that the resulting Muconate-Zr MOF showed relatively low crystallinity even after 4 days of synthesis. Farha and his coworkers more recently used a similar two-steps synthesis to successfully prepare higher quality UiO-66 and its analogues (linker functionalized with $-NO_2$, $-OH$ and $-NH_2$) in DMF at room temperature. They also demonstrated that the defect content of the synthesized UiO-66 decreased when the reaction temperature was increased.^[98] Afterwards, the same group reported that the two-steps synthesis can be also used to synthesize an 8-connected Zr_6 -MOF, NU-901, at room temperature regardless the lower connectivity mode of the oxocluster.^[99] The works involving two-steps RTS are summarized in Table 3. Apart from the two-steps synthesis based on the performed Zr_6 oxoclusters, another two-steps strategy was also proposed recently by Pakamoré et al., where the 2-aminoterephthalic (ATA) acid was pre-treated with NaOH to form Na_2ATA salt at 60 °C. The Na_2ATA solution was then mixed with $ZrOCl_2 \cdot 8H_2O$ in the mixture of H_2O and acetic acid to efficiently form well-crystalline UiO-66- NH_2 (Figure 8b). Notably, authors alternatively used H_2O as solvent instead of the usual toxic and degradable DMF, which will hopefully pave the way towards more sustainable synthesis.^[100] Two-steps room temperature synthesis gives advances for applications, which are discussed in the following part. However, it hinders their use for industrial-level applications due to the relatively complex synthesis procedure. Furthermore, the use of highly toxic solvents, such as DMF and DEF, should be avoided as much as possible. Alternatively, green chemistry, as defined by IUPAC, points out that the chemicals should be non-hazardous to humans.^[101] Therefore, the use of greener solvents, such as H_2O , ethanol, acetone, ethyl acetate, that are commonly accepted in MOFs synthesis is recommended.^[15, 102]

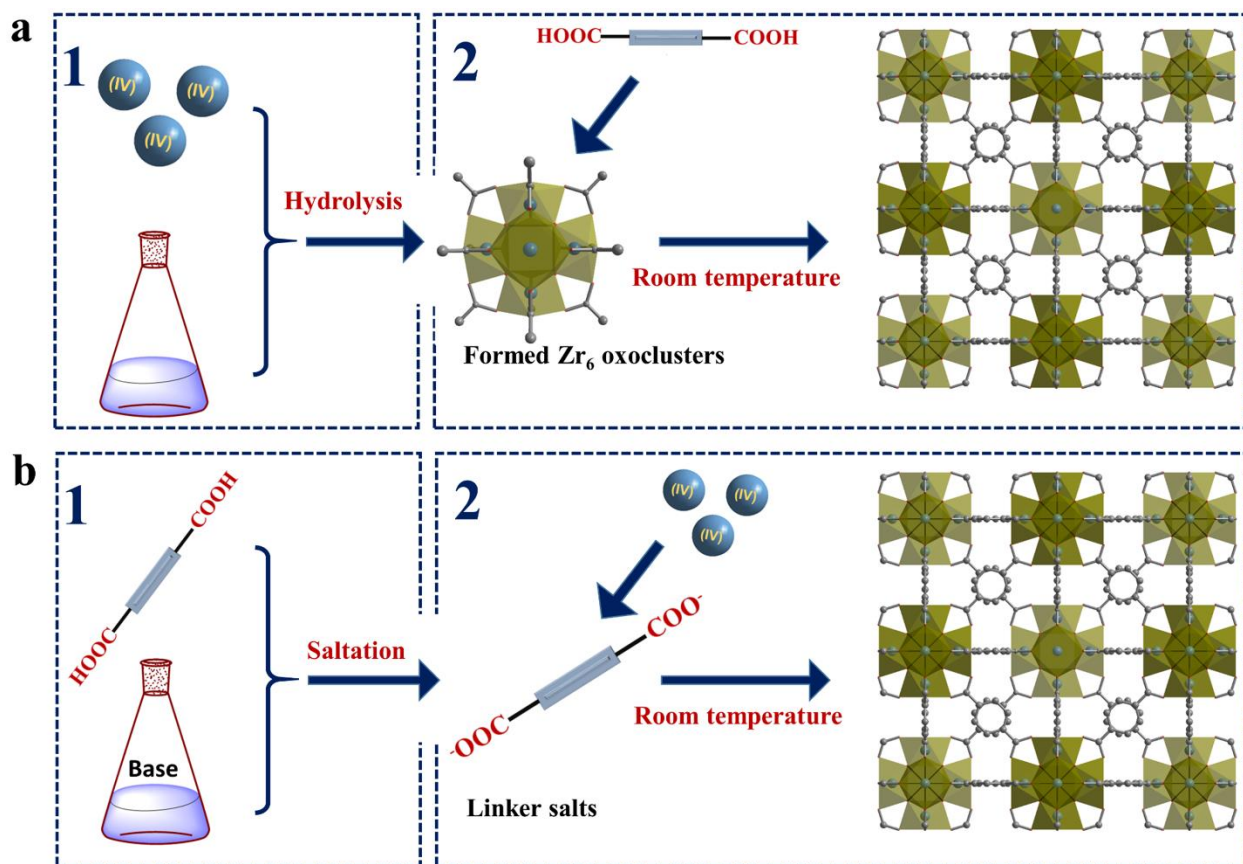


Figure 8. Two-steps room temperature synthetic approaches a) based on performed Zr_6 oxoclusters, b) based on the pre-treated organic linker. the

3.2 Additives-assisted room temperature synthesis

Additive-assisted RTS refers to the synthesis that requires additional species to facilitate the formation of the corresponding MOFs at room temperature. Often, these additives can effectively lower the activation energy of both the MOF nucleation and growth. The room temperature synthesis frequently needs long synthesis duration (>2 days), even when two-steps syntheses are used.^[22b, 98-99] In order to address this, Gu and his team proposed a salting-in species induced self-assembly (SSISA) strategy based on the Hofmeister effect to synthesize a series of MOFs with milder conditions.^[103] Taking advantage of SSISA strategy, they found that a series of pure Ce-UiO-66-X (-H, -CH₃, -Br, -NO₂) can be synthesized at room temperature within 10 min to 6h. Ce(IV)-MOFs are another class of tetravalent MOFs, showing many structural similarities to the well-known Zr-MOFs, in addition to their unique photo-redox properties.^[104] Hofmeister effect describes the influence of anions in the solubility of organic solutes. In that case, BDC was used as a model ligand due to its intensive use in MOFs chemistry. The salting-in ions (the left side in Figure 9a, NO₃⁻, ClO₄⁻, SCN⁻, I⁻) significantly enhance the solubility of BDC in aqueous solution, which therefore decreased the activation energy of MOF nucleation to allow the MOFs formation at room temperature (Figure 9b). However, these RT Ce-UiO-66-X neededs to be well-washed

with DMF after the synthesis, particularly when using pristine BDC, probably due to the incomplete crystallization of MOFs in these conditions.

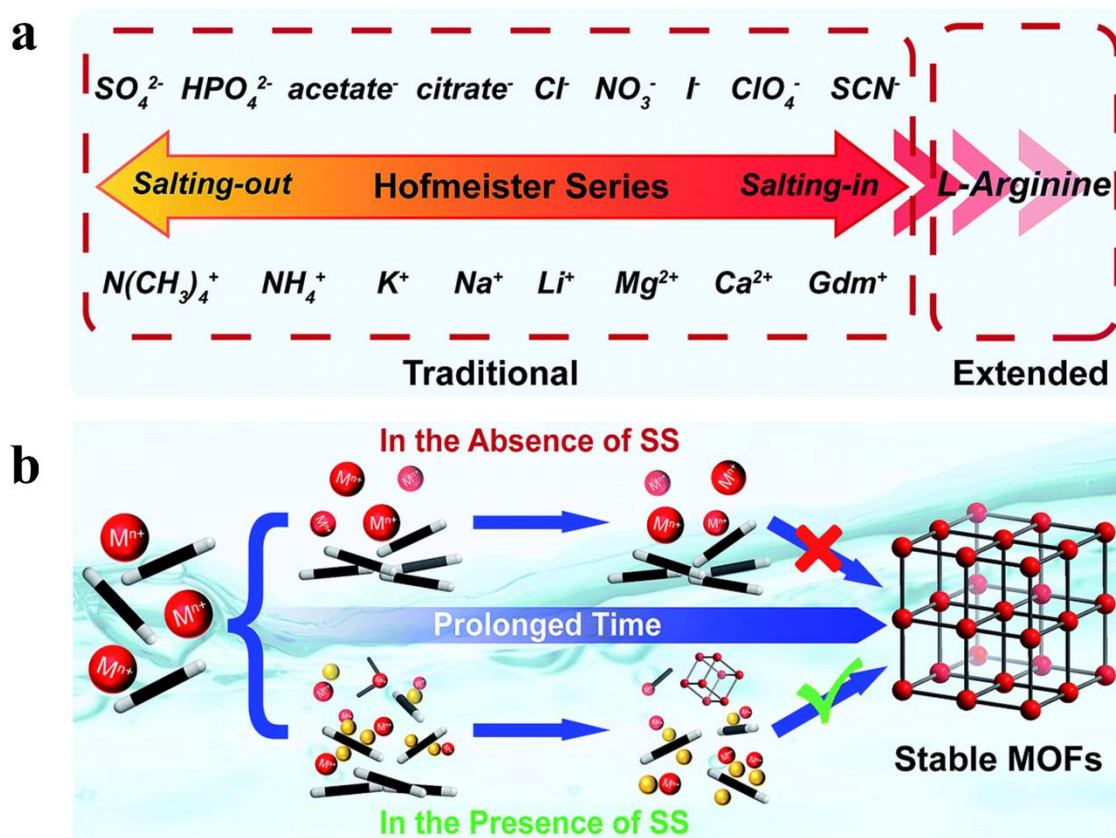


Figure 9. a) Illustration of Hofmeister effect, b) schematic illustration of the SSISA strategy based on Hofmeister effect, SS= Salting-in species. Reproduced with permission, RSC 2019. ^[103]

This promising SSISA strategy could hopefully pave the way for realizing more general RTS. Nevertheless, the introduced additives may rise issues such as sample contamination and additional costs. As such, more straightforward synthetic methods are still desired.

3.3 One-step synthesis

Room temperature direct synthesis stands for the straightforward synthesis without additional additives, multiple steps, or dependence on any salts. In contrast with the above-mentioned strategy relying on additives, using a specific solvent, precursor or synthetic conditions can lead to tetravalent MOFs crystallization. For example, Sang et al. in 2017 reported that using ionic liquids (ILs) as solvent, high-quality UiO-66 can be efficiently prepared in 0.5h at room temperature. In that case, the size of the UiO-66 particles can also be simply controlled from 30 nm to 80 nm by changing the anions and cations of ILs. In-situ small-angle X-ray scattering

(SAXS), X-ray absorption fine structure (XAFS), and ^1H nuclear magnetic resonance (^1H NMR) spectroscopy were applied to dynamically follow the formation of MOF nanoparticles. First, the solvation effect of Zr(IV) precursor $\text{ZrOCl}_2 \cdot 8\text{H}_2\text{O}$ causes hydrolysis and dehydration to yield polymeric hydroxide $\text{Zr}_4(\text{OH})_{12}$ (displayed in Figure 10i). Subsequently, the introduced ILs promote the coordination between the BDC and Zr(IV) through its stronger interaction with acetic acid, which accelerated both the formation of Zr_6 oxoclusters and MOF NPs (Figure 10ii, iii, iv). The resulting UiO-66 showed comparable BET surface area as the examples synthesized using solvothermal strategy, which indicates the excellent removal of the additives.^[105]

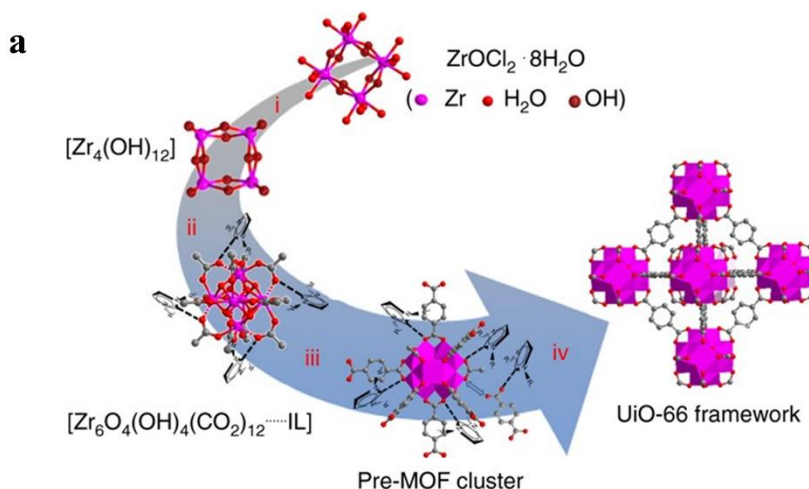


Figure 10. Schematic diagram of the UiO-66 formation in ionic liquid, (i) $\text{ZrOCl}_2 \cdot 8\text{H}_2\text{O}$ hydrolysis to polymeric hydroxide $\text{Zr}_4(\text{OH})_{12}$, (ii) Complexation of zirconium by addition of acetic acid, (iii) IL-assisted linker exchange between acetic acid and BDC to produce pre-MOF oxocluster, (iv) UiO-66 framework formation. Produced with permission. Spring 2017.^[105]

Recently, Avci-Camur et al. showed that metal acetylacetonate complexes can serve as metal sources for the aqueous synthesis of MOFs with good yield (>85%).^[74] Interestingly, by using this approach, a series of UiO-type of MOFs including Fumarate-Zr, UiO-66-(OH)₂, and UiO-66-NH₂ can be facilely prepared at room temperature in an aqueous solution without any additional additives or pre-treatment. Even though this synthesis took around 3 days, this example offered guidance for the following studies, where heating Zr(IV) precursors or ligands is not necessary. However, neither UiO-66-COOH nor UiO-66-(COOH)₂ were synthesized at room temperature and rising the temperature to 90 °C along with increasing reactants concentration were required. This work demonstrated the unique role of metal acetylacetonate complexes in synthesizing UiO-type of MOFs at room temperature. However, no further explanation on the role of acetylacetonate complexes was proposed, while this might be the key to understand the mechanism for future development.

Very recently, we reported the first versatile one-step synthesis at room temperature of tetravalent based MOFs in water using commercial reactants.^[106] As shown in Figure 11a, archetypical MOFs based on either 12-connected phases (MOF-801, UiO-66-NH₂, UiO-66-COOH) and 8-connected (DUT-67, PCN-222) Zr₆ oxoclusters were all simply synthesized at room temperature with the use of water/ ethanol. Furthermore, fumarate-Zr (or MOF-801) was used as a representative example to demonstrate that the synthesis can be performed with different Zr precursors (inorganic/ organic salts) and with several other tetravalent metal cations (Zr, Hf, Ce) and different type of modulators (acetic acid, formic acid). *In-situ* powder diffraction (Figure 11b) was considered to shed light on the nucleation/ growth process, revealing the importance of the concentration on the synthetic efficiency. In addition to the previously investigated synthetic factors, the critical role of the reactants concentration in lowering down the activation energy may guide the future RTS of tetravalent MOFs. This facile synthesis also allowed a modulator-induced size tuning from 220 nm to 45 nm, which will hopefully be useful for applications based on nano-MOFs. Finally, a 5 L pilot-scale system was used (Figure 11c) to evaluate its scalability. The space-time yield (STY) was also determined for the first time with this system, giving a value of 168 kg/ m³/ day. The N₂ isotherms, PXRD measurements, and pilot-scale system demonstrated the high quality of all the prepared MOFs obtained at high yield, which will hopefully pave the way for their future industrial production. To be noted, the low-temperature-induced defect (LTID) was observed among all the synthesized 12-connected MOFs, which made each Zr₆ oxoclusters linked to 8 ligands in average. The very high content of defect for *fcu* phases may also endow many possibilities to the applications that rely on coordination unsaturated sites.

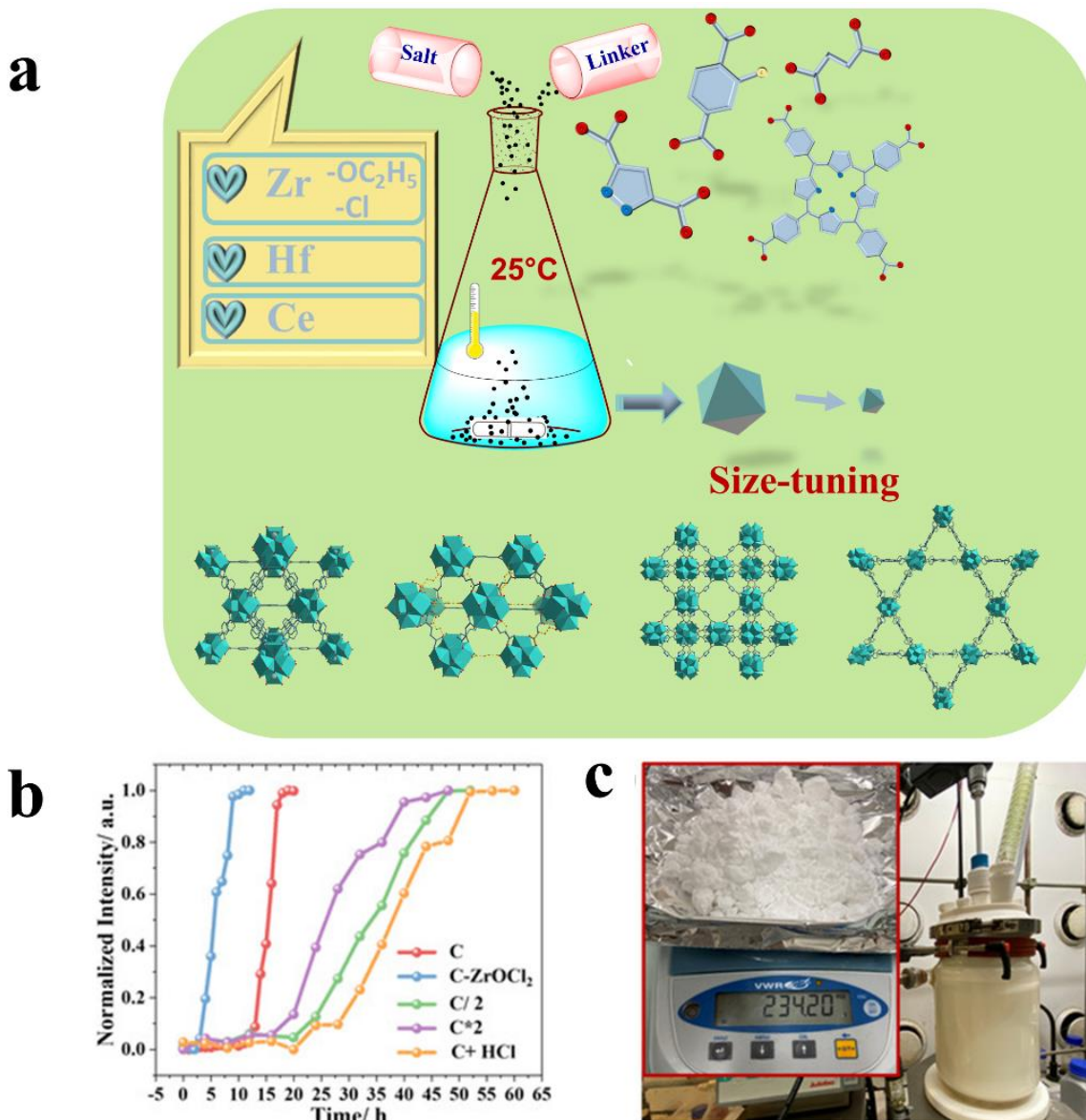


Figure 11. a) Schematic diagram of the room temperature one-step approach, b) plot of the synthesis time versus the intensities of the strongest (1, 1, 1) reflection of MOF-801 with varying precursors concentrations (the reactions were considered saturated when the intensities did not grow significantly), C represented the MOF-801 synthesized in 0.15 mmol/ mL precursors concentration, C*2 represented the 2 times multiple concentration, C/2 represented the 2 times divided concentration, C-ZrOCl₂ represented the MOF-801 synthesized with ZrOCl₂ in 0.15 mmol/ mL concentration, C+ HCl represented the MOF-801 synthesized in 0.15 mmol/ mL reactant with the presence 0.6 mmol/ L of HCl, c) 5L glass reactor laboratory pilot scale system for the upscaling synthesis of MOF-801, inserted picture: mass of product after synthesis, washing and drying. Produced with permission, Wiley 2021.

Table 3. Ambient synthesis examples for M(IV) based MOFs.

Materials	Method^a	Connectivity of Zr₆	Modulator^b	Solvents	Synthesis duration (h)	RTS_{surf} / ST_{surface}[*] (m²/g)	Ref
PCN-224	Two-steps	(4, 6)	AA	DMF	12	2164/ 2600 ^[107]	[108]
UiO-66	Two-steps	12	AA	DMF	18	1450/ 1105 ^[109]	[98]
UiO-66-NH₂	Two-steps	12	AA	DMF	18	1290/ 1123 ^[109]	[98]
UiO-66-OH	Two-steps	12	AA	DMF	18	1140/ 1000 ^[110]	[98]
UiO-66-NO₂	Two-steps	12	AA	DMF	18	960/ 792 ^[109]	[98]
NU-901	Two-steps	(4, 8)	AA	DMF	ON	2130/ 2276 ^[111]	[99]
UiO-66-NH₂	Two-steps	12	AA	H ₂ O	24	888/ 1123 ^[109]	[100]
UiO-66	OS-RD	12	AA	ILs	0.5	1519/ 1105 ^[109]	[105]
UiO-66-NH₂	Two-steps	12	AA	H ₂ O	0.17	717/ 1123 ^[109]	[112]

Muconate-Zr	Two-steps	12	AA	DMF	96	905	[22b]
UiO-66-(COOH)₂	Two-steps	12	TFA	H ₂ O	48	890/ 415 ^[113]	[114]
UIO-66-F₄	Two-steps	12	AA	H ₂ O	48	690/ 680 ^[115]	[114]
Ce-UiO-66	Additive	12	-	H ₂ O	6	968/ 1282 ^[104] b]	[103]
Ce-UiO-66-NO₂	Additive	12	-	H ₂ O	0.08	-	[103]
Ce-UiO-66-Br	Additive	12	-	H ₂ O	0.08	-	[103]
Ce-UiO-66-CH₃	Additive	12	-	H ₂ O	0.08	-	[103]
Fumarate-Zr	OS-RD	12	AA	H ₂ O	72	1249/ 856 ^[116]	[74]
UiO-66-NH₂	OS-RD	12	AA	H ₂ O	72	1106/ 1123 ^[109] l	[74]
UiO-66-(OH)₂	OS-RD	12	AA	H ₂ O	72	733/ 560 ^[110]	[74]
Fumarate-Zr	One-step	12	AA/ FA	H ₂ O	5	1035/ 856 ^[116]	[106]
Hf-MOF-801	One-step	12	AA/ FA	H ₂ O	12	737	[106]
Ce-MOF-801	One-step	12	AA/ FA	H ₂ O	1	781/ 732 ^[104b] l	[106]

UiO-66-NH₂	One-step	12	AA/ FA	H ₂ O EtOH	12	1256/ 1123 ^[109]]	[106]
UiO-66-COOH	One-step	12	AA/ FA	H ₂ O	72	1052/ 551 ^[117]	[106]
DUT-67	One-step	(2, 8)	FA	H ₂ O	48	1018/ 1057 ^[118]]	[106]
PCN-222	One-step	(4, 8)	FA	H ₂ O EtOH	48	1394/ 1728 ^[119]]	[106]

a: OS-RD indicates the direct one-step synthesis while having a reagent-dependent issue.

b: AA, FA represent acetic acid and formic acid, respectively, TFA refers to trifluoroacetic acid.

*: OS represents the original synthesis, including solvothermal/ hydrothermal synthesis.

Tetravalent MOFs have been extensively investigated in the past decade mainly due to their extraordinary chemical robustness. Apart from the interest in discovering new structures, the room temperature synthesis route of M(IV)-MOFs in green solvents offers potential promises for their next-step scale-up synthesis and commercialization. Furthermore, we are convinced that room-temperature synthesis of tetravalent MOFs can not only stimulate their broader fundamental study due to the simplified synthetic threshold, but also promote the exploration of derived new composites in a view of selected applications.

4. Applications of room temperature synthesis strategy

Compared to other porous solids like zeolites, which in most cases still need harsh hydrothermal synthesis conditions,^[120] MOFs can now be synthesized more and more frequently at room temperature. This is of interest not only to meet the requirements of sustainable chemistry and pave the way for their future industrial production but also to develop novel applications. In the following content, we will summarize the main progress in this topic.

4.1 Incorporating temperature-sensitive species through bottle-around-ship

Incorporating guest moieties into MOFs can endow a great potential for several applications such as catalysis^[121] and bio-labeling. The properties of the resulting composites may outperform the one of each single component, particularly for catalysis applications. The concept of catalytically

synergetic effect in MOF-based composites has been well-described and reviewed in many articles.^[122] The bottle-around-ship strategy represents the construction of a core-shell structure, where the core is preformed and then mixed with the MOF precursors solution, which subsequently allows the fabrication of a shell on the surface of the core materials. It enables the incorporation of active species regardless of the differences in size, shape, morphology, and even components between the core and shell.^[21] This strategy differs significantly from the conventional occupancy of MOFs cavity by active guests, which is called ship-in-a-bottle strategy.^[123] However, to successfully prepare core-shell composites, especially when dealing with small inorganic nanoparticles, relatively mild MOF synthesis conditions are requested due to the easy degradation of these temperature-sensitive guests.^[124]

In an early stage contribution, Lu et al. reported a versatile approach using ambient synthesis to fabricate a series of core-shell Au/ Pt NPs@ZIFs structures (Figure 12a).^[125] The subsequent catalytic/ photonic property enhancement was observed. Subsequent works using ZIF series prepared at room temperature led to even more exciting achievements.^[126] The ambient synthesis of chemically stable Zr-MOFs is also interesting for the construction of inorganic nanoparticles based core-shell architecture. For instance, a very recent paper from Jiang's group reported the successful fabrication of core-shell Pt NCs@PCN-224 through RTS (Figure 12b). The same fabrication while using the conventional solvothermal method led to core-shell structure too, but with a pronounced aggregation of Pt NPs, which is a drawback for catalytic applications.^[127] In addition to the small inorganic nanoparticles, another temperature-sensitive biomolecules have also been incorporated in MOFs using RTS (e.g., protein, Figure 12c).^[128] The formed protein@ZIF-8 showed a retained bioactivity even after being treated at 80 °C and boiled in DMF. Another study revealed the encapsulation of enzymes within ZIF-8 that led to not only stability improvement but also bioactivity enhancement.^[129]

These results illustrate the premises of core-shell composites in many applications regardless of their difficulty in synthesis.^[130] The RTS approach provides optimized synthetic parameters for this goal. Nevertheless, the most investigated MOFs so far are divalent MOFs, which are in most cases not robust enough against humidity or water for some applications. The recent developments of ambient synthesis strategies on more chemically robust tri/ tetra-valent MOFs may however pave the way for the future expansion of this field.

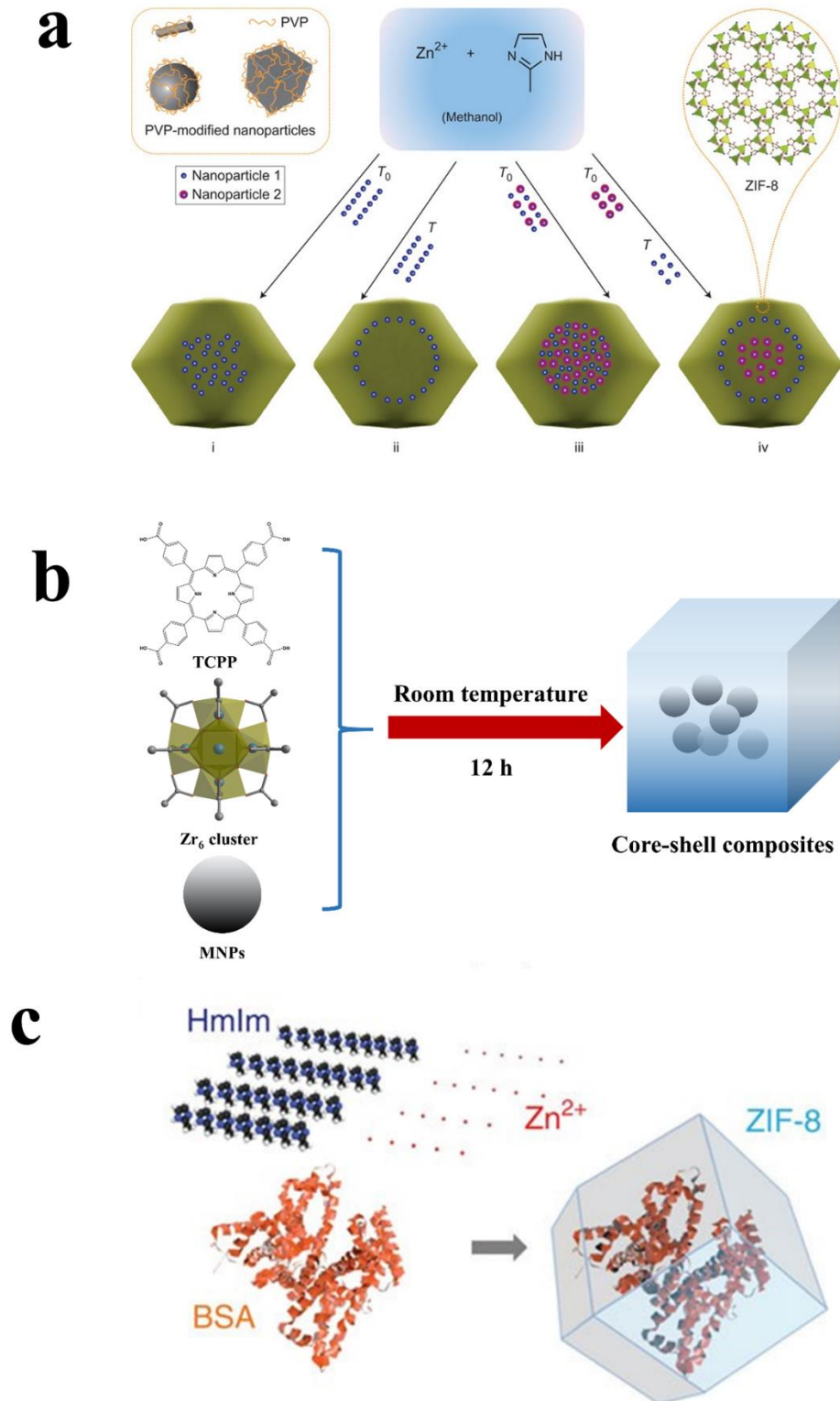


Figure 12. a) Scheme of the controlled encapsulation of inorganic nanoparticles in ZIF-8, the spatial distribution of incorporated PVP-modified nanoparticles within ZIF-8 crystals can also be controlled by their different addition sequence, b) Scheme of the strategy to form core-shell Pt

NPs@PCN-224, c) Schematic proposing the fabrication of protein@ZIF-8 composite. Produced with permission, Springer 2012,^[125] Springer 2015.^[128]

4.2 Room temperature assisted defect-engineered MOFs

Low-temperature synthesis method has been realized as a useful tool to manipulate the defect content in Zr-MOFs in 2010.^[22b] Farha and co-workers found similar results in the cases of 12-connected UiO-66 and 8-connected NU-901, both synthesized at room temperature.^[99, 131] It has been well-documented that the presence of defect sites in given MOF is of particular interest for their properties modulation, such as catalytic reactivity mainly due to the more exposed metal sites. Our recent findings revealed that RTS in the aqueous solution can effectively generate highly defective UiO-type MOFs. The synthesized fumarate-Zr displayed 8-fold connectivity for each Zr_6 instead of 12, which is among the most defective UiO-type of MOF. Consequently, the water vapor isotherm on the defective fumarate-Zr indicated the high adsorption capacity, as well as high affinity with H_2O of these very defective MOFs due to the increased Coulomb interaction from –OH group at the defect sites.^[106] Kang et al. recently found that the rapid and ambient electrosynthesis of a Cu-carboxylate MOF (MFM-100) led to more defective MFM-100(c, d) (Figure 13c, d) than MFM-100 (a, b) from solvothermal batch (Figure 13a, b),^[132] making them more reactive for the selective oxidation of benzyl alcohol (Figure 13e). More importantly, the produced defective mesoporous MFM-100 can be reused for at least five cycles, indicating there is no much compromising in the MOF stability when defect are presents (Figure 13f). This example revealed the ambient synthesis can not only lead to a larger pore size material but also facilitate catalytic oxidation with excellent cycling performance.

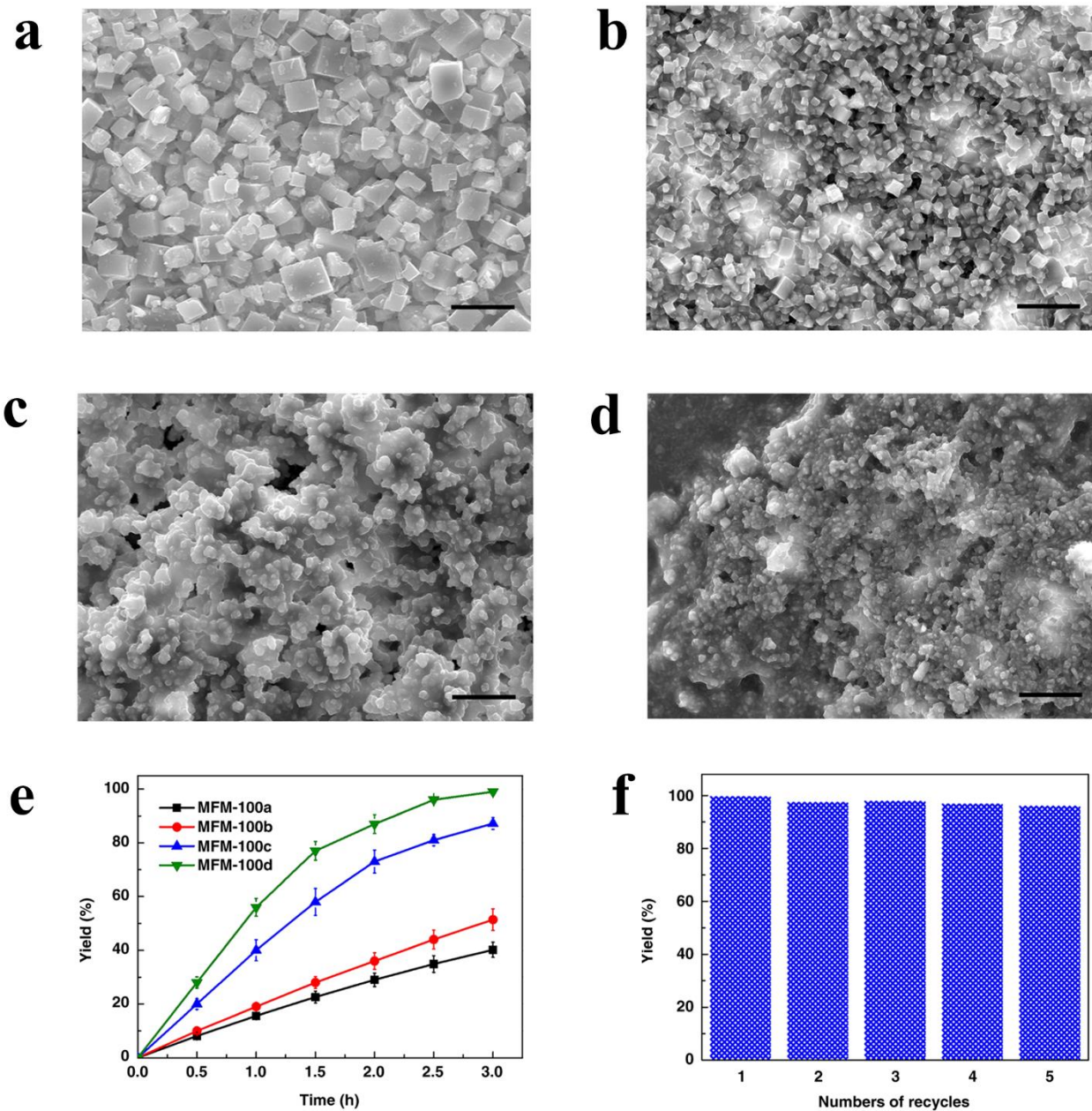


Figure 13. SEM images of a) MFM-100a, b) MFM-100b, c) MFM-100c, d) MFM-100d. e) Time-dependent yields of aldehydes from selected substrates catalyzed over MFM-100. f) Reusability of MFM-100d. Produced with permission, Springer 2019.^[132]

RTS can be regarded as a useful platform to stretch the applications of the corresponding MOFs, such as the aforementioned ones. However, synthesizing MOFs in mild conditions has also been demonstrated as an interesting way to allow many *in-situ* techniques that are only operational in very mild conditions, such as *in-situ* Transmission electron microscopy,^[133] *in-situ* Static light scattering,^[134] and laboratory *in-situ* Powder X-ray diffraction.^[106] For instance, in order to get an insight on the crystallization process of any given MOF, *in-situ* PXRD is often the best technique.

However, most of MOFs syntheses rely on solvothermal/ hydrothermal conditions to form crystals and can therefore only be studied using synchrotron-based X-Ray radiation combined with pressure-resistant systems. The ambient synthesis conditions can allow researchers to investigate the MOF synthesis kinetics using a laboratory X-ray diffractometer. From a fundamental understanding point of view, having an insight on nucleation and growth processes, as well as the existence of possible intermediates, is of critical importance, as it may lead to a better understanding of the synthesis processes and even to new synthetic concepts.

5. Perspectives and conclusions

Developing the room temperature synthesis (RTS) under green conditions of a MOF of interest, has become nowadays pre-requisite in parallel to the investigation of its potential applications. In this review, we have summarized the development of MOFs RTS with a special emphasis on the most chemically stable MOFs. Even though some promising synthesis routes have been reported to date, many challenges still remain. In terms of sustainable synthesis, RTS is of interest when compared to the conventional heating methods. However the limited product yield, as well as the prolonged synthesis duration, still need to be circumvented prior to their utilization in industry. The space-time yield, although by far not the sole parameter to be considered to assess the technico-economic production of a solid, is still not taken into account systematically in most studies. Moreover, the use of highly toxic organic solvents or corrosive metal salts is still common, while it is not favorable for industrial applications. One can alternatively consider the use of greener organic solvents, such as ethanol, acetone, or ethyl acetate if the organic ligands are insoluble in pure water at room temperature. The extension of RTS to more chemically robust MOFs has been recently preliminary achieved, but the mechanism behind still needs further understanding, particularly for the nucleation-growth kinetics.

Regarding the potential applications, the room temperature synthesis of divalent MOFs, particularly ZIFs, has already intensively been used for the incorporation of temperature-sensitive compounds. The room temperature efficient synthesis procedure and ideal crystallinity make especially ZIF-8 very suitable for achieving this goal. However, the ultra-small aperture size (3.4Å), limited chemical stability and deficient functions of ZIF-8 are in some cases important drawbacks for this MOF. The application of high-valence MOFs might hopefully address these limitations although their range of stability and properties often differs. Additionally, room temperature synthesis routes allow high throughput parametric investigation, possibly assisted by fluidics, which is more desired in the stage of materials optimization. Finally, we hope this review article will facilitate the development of new energy-saving green synthesis routes of MOFs, their potential applications, and even new concepts in a near future.

References :

- [1] R. Freund, S. Canossa, S. M. Cohen, W. Yan, H. Deng, V. Guillerme, M. Eddaoudi, D. G. Madden, D. Fairen-Jimenez, H. Lyu, *Angew. Chem., Int. Ed.* **2021**. DOI: 10.1002/anie.202101644.
- [2] A. Bavykina, N. Kolobov, I. S. Khan, J. A. Bau, A. Ramirez, J. Gascon, *Chem. Rev.* **2020**, 120, 8468.
- [3] R. B. Lin, S. C. Xiang, W. Zhou, B. L. Chen, *Chem* **2020**, 6, 337.
- [4] L. S. Xie, G. Skorupskii, M. Dinca, *Chem. Rev.* **2020**, 120, 8536.
- [5] a) J. Q. Liu, Z. D. Luo, Y. Pan, A. K. Singh, M. Trivedi, A. Kumar, *Coord. Chem. Rev.* **2020**, 406; b) H. Q. Yin, X. B. Yin, *Acc. Chem. Res.* **2020**, 53, 485.
- [6] T. Simon-Yarza, A. Mielcarek, P. Couvreur, C. Serre, *Adv. Mater.* **2018**, 30, 1707365.
- [7] a) S. Drumel, P. Janvier, P. Barboux, M. Bujolideuff, B. Bujoli, *Inorg. Chem.* **1995**, 34, 148; b) O. M. Yaghi, H. L. Li, *J. Am. Chem. Soc.* **1995**, 117, 10401; c) A. K. Cheetham, G. Ferey, T. Loiseau, *Angew. Chem., Int. Ed.* **1999**, 38, 3268; d) M. Kondo, T. Yoshitomi, K. Seki, H. Matsuzaka, S. Kitagawa, *Angew. Chem., Int. Ed.* **1997**, 36, 1725.
- [8] M. Eddaoudi, J. Kim, N. Rosi, D. Vodak, J. Wachter, M. O'Keeffe, O. M. Yaghi, *Science* **2002**, 295, 469.
- [9] M. Eddaoudi, D. B. Moler, H. L. Li, B. L. Chen, T. M. Reineke, M. O'Keeffe, O. M. Yaghi, *Acc. Chem. Res.* **2001**, 34, 319.
- [10] a) P. Z. Moghadam, A. Li, S. B. Wiggin, A. Tao, A. G. P. Maloney, P. A. Wood, S. C. Ward, D. Fairen-Jimenez, *Chem. Mater.* **2017**, 29, 2618; b) How many MOFs are there in the CSD?, <https://www.ccdc.cam.ac.uk/support-and-resources/support/case/?caseid=9833bd2c-27f9-4ff7-8186-71a9b415f012>, accessed.
- [11] N. Stock, S. Biswas, *Chem. Rev.* **2012**, 112, 933.
- [12] a) J. Klinowski, F. A. A. Paz, P. Silva, J. Rocha, *Dalton Trans.* **2011**, 40, 321; b) I. Thomas-Hillman, A. Laybourn, C. Dodds, S. W. Kingman, *J. Mat. Chem. A* **2018**, 6, 11564.
- [13] M. I. S. Neves, E. Gkaniatsou, F. Nouar, M. L. Pinto, C. Serre, *Faraday Discuss.* **2021**, Advance Article. DOI: 10.1039/D1FD00018G.
- [14] a) S. Wang, C. Serre, *ACS Sustain. Chem. Eng.* **2019**, 7, 14, 11911-11927; b) S. Geng, E. Lin, X. Li, W. Liu, T. Wang, Z. Wang, D. Sensharma, S. Darwish, Y. H. Andaloussi, T. Pham, *J. Am. Chem. Soc.* **2021**. DOI: 10.1021/jacs.1c02108 ; c) Y. Xiao, A. N. Hong, Y. Wang, X. Bu, P. Feng, *Chem. Eur. J.* **2019**, 25, 16358.
- [15] H. Reinsch, *Eur. J. Inorg. Chem.* **2016**, 27, 4290.
- [16] N. Campagnol, E. R. Souza, D. E. De Vos, K. Binnemans, J. Fransaer, *Chem. Commun.* **2014**, 50, 12545.
- [17] X.-Y. Chen, B. Zhao, W. Shi, J. Xia, P. Cheng, D.-Z. Liao, S.-P. Yan, Z.-H. Jiang, *Chem. Mater.* **2005**, 17, 2866.
- [18] J. Troyano, C. Çamur, L. Garzón-Tovar, A. Carné-Sánchez, I. Imaz, D. MasPOCH, *Acc. Chem. Res.* **2020**, 53, 1206.
- [19] Y. Xin, S. Peng, J. Chen, Z. Yang, J. Zhang, *Chin. Chem. Lett.* **2020**, 31, 1448.
- [20] T. Stolar, K. Uzarevic, *Crystengcomm* **2020**, 22, 4511.
- [21] S. Dai, A. Tissot, C. Serre, *Adv. Energy Mater.* **2021**, 2100061. DOI: 10.1002/aenm.202100061
- [22] a) M. Bosch, S. Yuan, W. Rutledge, H.-C. Zhou, *Acc. Chem. Res.* **2017**, 50, 857; b) V. Guillerme, S. Gross, C. Serre, T. Devic, M. Bauer, G. Ferey, *Chem. Commun.* **2010**, 46, 767.
- [23] a) P. Pachfule, T. Panda, C. Dey, R. Banerjee, *CrystEngComm* **2010**, 12, 2381; b) L. Maserati, S. M. Meckler, C. Li, B. A. Helms, *Chem. Mater.* **2016**, 28, 1581.

- [24] a) N. L. Rosi, M. Eddaoudi, J. Kim, M. O'Keeffe, O. M. Yaghi, *Angew. Chem., Int. Ed.* **2002**, 41, 284; b) M. J. Kalmutzki, N. Hanikel, O. M. Yaghi, *Sci. Adv.* **2018**, 4, eaat9180.
- [25] D. J. Tranchemontagne, J. R. Hunt, O. M. Yaghi, *Tetrahedron* **2008**, 64, 8553.
- [26] Z.-Q. Li, L.-G. Qiu, T. Xu, Y. Wu, W. Wang, Z.-Y. Wu, X. Jiang, *Mater. Lett.* **2009**, 63, 78.
- [27] a) J. Huo, M. Brightwell, S. El Hankari, A. Garai, D. Bradshaw, *J. Mat. Chem. A* **2013**, 1; b) J.-L. Zhuang, D. Ceglarek, S. Pethuraj, A. Terfort, *Adv. Func. Mater.* **2011**, 21, 1442.
- [28] M. Diaz-Garcia, A. Mayoral, I. Diaz, M. Sanchez-Sanchez, *Cryst. Growth Des.* **2014**, 14, 2479.
- [29] Q. Qian, Y. Li, Y. Liu, L. Yu, G. Zhang, *Adv Mater* **2019**, 31, e1901139.
- [30] M. Klimakow, P. Klobes, A. F. Thünemann, K. Rademann, F. Emmerling, *Chem. Mater.* **2010**, 22, 5216.
- [31] P. Silva, S. M. F. Vilela, J. P. C. Tome, F. A. A. Paz, *Chem. Soc. Rev.* **2015**, 44, 6774.
- [32] a) G. Calleja, J. A. Botas, M. G. Orcajo, M. Sánchez-Sánchez, *Journal of Porous Materials* **2010**, 17, 91; b) S. S. Kaye, A. Dailly, O. M. Yaghi, J. R. Long, *J. Am. Chem. Soc.* **2007**, 129, 14176.
- [33] J. C. Tan, T. D. Bennett, A. K. Cheetham, *Proc. Natl. Acad. Sci. U.S.A.* **2010**, 107, 9938.
- [34] X. C. Huang, Y. Y. Lin, J. P. Zhang, X. M. Chen, *Angew. Chem., Int. Ed.* **2006**, 45, 1557.
- [35] a) K. S. Park, Z. Ni, A. P. Cote, J. Y. Choi, R. D. Huang, F. J. Uribe-Romo, H. K. Chae, M. O'Keeffe, O. M. Yaghi, *Proc. Natl. Acad. Sci. U.S.A.* **2006**, 103, 10186; b) C. T. He, L. Jiang, Z. M. Ye, R. Krishna, Z. S. Zhong, P. Q. Liao, J. Xu, G. Ouyang, J. P. Zhang, X. M. Chen, *J. Am. Chem. Soc.* **2015**, 137, 7217.
- [36] J. Cravillon, S. Munzer, S. J. Lohmeier, A. Feldhoff, K. Huber, M. Wiebcke, *Chem. Mater.* **2009**, 21, 1410.
- [37] Y. C. Pan, Y. Y. Liu, G. F. Zeng, L. Zhao, Z. P. Lai, *Chem. Commun.* **2011**, 47, 2071.
- [38] P. J. Beldon, L. Fabian, R. S. Stein, A. Thirumurugan, A. K. Cheetham, T. Friscic, *Angew. Chem., Int. Ed.* **2010**, 49, 9640.
- [39] J. P. Zhang, Y. B. Zhang, J. B. Lin, X. M. Chen, *Chem. Rev.* **2012**, 112, 1001.
- [40] a) X. L. Liu, Y. S. Li, Y. J. Ban, Y. Peng, H. Jin, H. Bux, L. Y. Xu, J. Caro, W. S. Yang, *Chem. Commun.* **2013**, 49, 9140; b) D. Ge, H. K. Lee, *J. Chromatogr. A* **2011**, 1218, 8490; c) K. Leus, T. Bogaerts, J. De Decker, H. Depauw, K. Hendrickx, H. Vrielinck, V. Van Speybroeck, P. Van Der Voort, *Microporous Mesoporous Mat.* **2016**, 226, 110; d) H. F. Zhang, D. F. Liu, Y. Yao, B. Q. Zhang, Y. S. Lin, *J. Membr. Sci.* **2015**, 485, 103.
- [41] V. Colombo, S. Galli, H. J. Choi, G. D. Han, A. Maspero, G. Palmisano, N. Masciocchi, J. R. Long, *Chemical Science* **2011**, 2, 1311-1319.
- [42] N. L. Rosi, J. Eckert, M. Eddaoudi, D. T. Vodak, J. Kim, M. O'Keeffe, O. M. Yaghi, *Science* **2003**, 300, 1127.
- [43] H. K. Chae, D. Y. Siberio-Perez, J. Kim, Y. Go, M. Eddaoudi, A. J. Matzger, M. O'Keeffe, O. M. Yaghi, *Nature* **2004**, 427, 523.
- [44] A. R. Millward, O. M. Yaghi, *J. Am. Chem. Soc.* **2005**, 127, 17998.
- [45] J. Zha, X. Zhang, *Cryst. Growth Des.* **2018**, 18, 3209.
- [46] J. G. Flores, E. Sanchez-Gonzalez, A. Gutierrez-Alejandre, J. Aguilar-Pliego, A. Martinez, T. Jurado-Vazquez, E. Lima, E. Gonzalez-Zamora, M. Diaz-Garcia, M. Sanchez-Sanchez, I. A. Ibarra, *Dalton Trans.* **2018**, 47, 4639.
- [47] J. Hungerford, K. S. Walton, *Inorg. Chem.* **2019**, 58, 7690.
- [48] W. Xu, G. Li, W. Li, H. Zhang, *RSC Adv.* **2016**, 6, 37530.
- [49] X. Zhao, Z. Xue, W. Chen, X. Bai, R. Shi, T. Mu, *J. Mat. Chem. A* **2019**, 7, 26238.

- [50] J. Qian, F. Sun, L. Qin, *Mater. Lett.* **2012**, 82, 220.
- [51] A. F. Gross, E. Sherman, J. J. Vajo, *Dalton Trans.* **2012**, 41, 5458.
- [52] W. Morris, N. He, K. G. Ray, P. Klonowski, H. Furukawa, I. N. Daniels, Y. A. Houndonougbo, M. Asta, O. M. Yaghi, B. B. Laird, *J. Phys. Chem. C* **2012**, 116, 24084.
- [53] E. V. Ramos-Fernandez, A. Grau-Atienza, D. Farrusseng, S. Aguado, *J. Mat. Chem. A* **2018**, 6, 5598.
- [54] M. Zhu, S. R. Venna, J. B. Jasinski, M. A. Carreon, *Chem. Mater.* **2011**, 23, 3590.
- [55] C. Duan, F. Li, J. Xiao, Z. Liu, C. Li, H. Xi, *China Mater.* **2017**, 60, 1205.
- [56] L. Hamon, C. Serre, T. Devic, T. Loiseau, F. Millange, G. Férey, G. De Weireld, *J. Am. Chem. Soc.* **2009**, 131, 8775.
- [57] a) Y.-P. Wu, G.-W. Xu, W.-W. Dong, J. Zhao, D.-S. Li, J. Zhang, X. Bu, *Inorg. Chem.* **2017**, 56, 1402; b) S.-N. Zhao, G. Wang, D. Poelman, P. V. D. Voort, *Materials* **2018**, 11, 572.
- [58] C. Serre, F. Millange, C. Thouvenot, M. Nogues, G. Marsolier, D. Louër, G. Férey, *J. Am. Chem. Soc.* **2002**, 124, 13519.
- [59] G. Férey, C. Mellot-Draznieks, C. Serre, F. Millange, J. Dutour, S. Surblé, I. Margiolaki, *Science* **2005**, 309, 2040.
- [60] M. Latroche, S. Surblé, C. Serre, C. Mellot-Draznieks, P. L. Llewellyn, J. H. Lee, J. S. Chang, S. H. Jhung, G. Férey, *Angew. Chem.* **2006**, 118, 8407.
- [61] C. Serre, C. Mellot-Draznieks, S. Surblé, N. Audebrand, Y. Filinchuk, G. Férey, *Science* **2007**, 315, 1828.
- [62] D. Cunha, M. Ben Yahia, S. Hall, S. R. Miller, H. Chevreau, E. Elkaïm, G. Maurin, P. Horcajada, C. Serre, *Chem. Mater.* **2013**, 25, 2767.
- [63] a) H. Reinsch, M. A. van der Veen, B. Gil, B. Marszalek, T. Verbiest, D. De Vos, N. Stock, *Chem. Mater.* **2013**, 25, 17; b) C. Volkringer, D. Popov, T. Loiseau, N. Guillou, G. Férey, M. Haouas, F. Taulelle, C. Mellot-Draznieks, M. Burghammer, C. Riekel, *Nat. Mater.* **2007**, 6, 760; c) M. O’Keeffe, O. M. Yaghi, *Chem. Rev.* **2012**, 112, 675.
- [64] E. Alvarez, N. Guillou, C. Martineau, B. Bueken, B. Van de Voorde, C. Le Guillouzer, P. Fabry, F. Nouar, F. Taulelle, D. de Vos, J. S. Chang, K. H. Cho, N. Ramsahye, T. Devic, M. Daturi, G. Maurin, C. Serre, *Angew. Chem., Int. Ed.* **2015**, 54, 3664.
- [65] M. Sánchez-Sánchez, N. Getachew, K. Díaz, M. Díaz-García, Y. Chebude, I. Díaz, *Green Chem.* **2015**, 17, 1500.
- [66] P. Horcajada, S. Surble, C. Serre, D. Y. Hong, Y. K. Seo, J. S. Chang, J. M. Greneche, I. Margiolaki, G. Férey, *Chem. Commun.* **2007**, 27, 2820-2822.
- [67] a) P. L. Llewellyn, S. Bourrelly, C. Serre, A. Vimont, M. Daturi, L. Hamon, G. De Weireld, J. S. Chang, D. Y. Hong, Y. K. Hwang, S. H. Jhung, G. Férey, *Langmuir* **2008**, 24, 7245; b) A. Vimont, J. M. Goupil, J. C. Lavalley, M. Daturi, S. Surble, C. Serre, F. Millange, G. Férey, N. Audebrand, *J. Am. Chem. Soc.* **2006**, 128, 3218.
- [68] G. Férey, C. Serre, C. Mellot-Draznieks, F. Millange, S. Surble, J. Dutour, I. Margiolaki, *Angew. Chem., Int. Ed.* **2004**, 43, 6296.
- [69] J. Castells-Gil, M. P. N, N. Almora-Barrios, I. da Silva, D. Mateo, J. Albero, H. Garcia, C. Marti-Gastaldo, *Chem. Sci.* **2019**, 10, 4313.
- [70] D. Feng, T. F. Liu, J. Su, M. Bosch, Z. Wei, W. Wan, D. Yuan, Y. P. Chen, X. Wang, K. Wang, X. Lian, Z. Y. Gu, J. Park, X. Zou, H. C. Zhou, *Nat. Commun.* **2015**, 6, 5979.
- [71] B. Yuan, X. Wang, X. Zhou, J. Xiao, Z. Li, *Chem. Eng. J.* **2019**, 355, 679.

- [72] a) M. Panchal, F. Nouar, C. Serre, M. Benzaqui, S. Sene, N. Steunou, M.G. Marques, EP 17305119.4, **2017**; b) X. Li, L. Lachmanski, S. Safi, S. Sene, C. Serre, J.-M. Greneche, J. Zhang, R. Gref, *Sci. Rep.* **2017**, 7, 1.
- [73] T. Chalati, P. Horcajada, R. Gref, P. Couvreur, C. Serre, *J. Mat. Chem.* **2011**, 21, 2220.
- [74] C. Avci-Camur, J. Perez-Carvajal, I. Imaz, D. MasPOCH, *ACS Sustainable Chem. Eng.* **2018**, 6, 14554.
- [75] E. S. Grape, J. G. Flores, T. Hidalgo, E. Martinez-Ahumada, A. Gutierrez-Alejandre, A. Hautier, D. R. Williams, M. O'Keeffe, L. Ohrstrom, T. Willhammar, P. Horcajada, I. A. Ibarra, A. K. Inge, *J. Am. Chem. Soc.* **2020**, 142, 16795.
- [76] a) F. Li, C. Duan, H. Zhang, X. Yan, J. Li, H. Xi, *Ind. Eng. Chem. Res.* **2018**, 57, 9136; b) J. Huo, M. Brightwell, S. El Hankari, A. Garai, D. Bradshaw, *J. Mat. Chem. A* **2013**, 1, 15220.
- [77] T. Loiseau, C. Serre, C. Huguenard, G. Fink, F. Taulelle, M. Henry, T. Bataille, G. Férey, *Chem. Eur. J* **2004**, 10, 1373.
- [78] Y.-K. Seo, J. W. Yoon, J. S. Lee, U.-H. Lee, Y. K. Hwang, C.-H. Jun, P. Horcajada, C. Serre, J.-S. Chang, *Micropor. Mesopor. Mat.* **2012**, 157, 137.
- [79] G. Majano, O. Ingold, M. Yulikov, G. Jeschke, J. Pérez-Ramírez, *CrystEngComm* **2013**, 15, 9885.
- [80] L. Zhang, J. Wang, T. Du, W. Zhang, W. Zhu, C. Yang, T. Yue, J. Sun, T. Li, J. Wang, *Inorg. Chem.* **2019**, 58, 12573.
- [81] L. Huang, J. Cai, M. He, B. Chen, B. Hu, *Ind. Eng. Chem. Res.* **2018**, 57, 6201.
- [82] H. Fu, X.-X. Song, L. Wu, C. Zhao, P. Wang, C.-C. Wang, *Mater. Res. Bull.* **2020**, 125, 110806.
- [83] H. Yang, Y. Wang, R. Krishna, X. Jia, Y. Wang, A. N. Hong, C. Dang, H. E. Castillo, X. Bu, P. Feng, *J. Am. Chem. Soc.* **2020**, 142, 2222.
- [84] a) S. Wang, T. Kitao, N. Guillou, M. Wahiduzzaman, C. Martineau-Corcoc, F. Nouar, A. Tissot, L. Binet, N. Ramsahye, S. Devautour-Vinot, *Nat. Commun.* **2018**, 9, 1; b) G. Mouchaham, F. S. Cui, F. Nouar, V. Pimenta, J.-S. Chang, C. Serre, *Trends Chem.* **2020**, 2, 990.
- [85] a) A. Clearfield, Z. K. Wang, *J. Chem. Soc., Dalton Trans.* **2002**, 15, 2937-2947; b) Z. K. Wang, J. M. Heising, A. Clearfield, *J. Am. Chem. Soc.* **2003**, 125, 10375; c) A. Clearfield, Z. K. Wang, P. Bellinghausen, *J. Solid State Chem.* **2002**, 167, 376.
- [86] S. Wang, J. S. Lee, M. Wahiduzzaman, J. Park, M. Muschi, C. Martineau-Corcoc, A. Tissot, K. H. Cho, J. Marrot, W. Shepard, G. Maurin, J. S. Chang, C. Serre, *Nat. Energy* **2018**, 3, 985.
- [87] J. H. Cavka, S. Jakobsen, U. Olsbye, N. Guillou, C. Lamberti, S. Bordiga, K. P. Lillerud, *J. Am. Chem. Soc.* **2008**, 130, 13850.
- [88] a) Z. Chen, S. L. Hanna, L. R. Redfern, D. Alezi, T. Islamoglu, O. K. Farha, *Coord. Chem. Rev.* **2019**, 386, 32; b) I. A. Lazaro, R. S. Forgan, *Coord. Chem. Rev.* **2019**, 380, 230; c) X. D. Zhang, Y. Yang, X. T. Lv, Y. X. Wang, N. Liu, D. Chen, L. F. Cui, *J. Hazard. Mater.* **2019**, 366, 140.
- [89] J. F. Lyu, X. Zhang, K. Otake, X. J. Wang, P. Li, Z. Y. Li, Z. J. Chen, Y. Y. Zhang, M. C. Wasson, Y. Yang, P. Bai, X. H. Guo, T. Islamoglu, O. K. Farha, *Chem. Sci.* **2019**, 10, 1186.
- [90] A. Schaate, P. Roy, A. Godt, J. Lippke, F. Waltz, M. Wiebcke, P. Behrens, *Chemistry* **2011**, 17, 6643.
- [91] V. Bon, I. Senkovska, I. A. Baburin, S. Kaskel, *Cryst. Growth Des.* **2013**, 13, 1231.
- [92] S. J. Wang, N. Khaferaj, M. Wahiduzzaman, K. Oyekan, X. Li, K. Wei, B. Zheng, A. Tissot, J. Marrot, W. Shepard, C. Martineau-Corcoc, Y. Filinchuk, K. Tan, G. Maurin, C. Serre, *J. Am. Chem. Soc.* **2019**, 141, 17207.

- [93] Y. M. Zhao, S. B. Qi, Z. Niu, Y. L. Peng, C. Shan, G. Verma, L. Wojtas, Z. J. Zhang, B. Zhang, Y. Q. Feng, Y. S. Chen, S. Q. Ma, *J. Am. Chem. Soc.* **2019**, 141, 14443.
- [94] H. Furukawa, F. Gandara, Y. B. Zhang, J. Jiang, W. L. Queen, M. R. Hudson, O. M. Yaghi, *J. Am. Chem. Soc.* **2014**, 136, 4369.
- [95] H. Wang, X. L. Dong, J. Z. Lin, S. J. Teat, S. Jensen, J. Cure, E. V. Alexandrov, Q. B. Xia, K. Tan, Q. N. Wang, D. H. Olson, D. M. Proserpio, Y. J. Chabal, T. Thonhauser, J. L. Sun, Y. Han, J. Li, *Nat. Commun.* **2018**, 9, 1.
- [96] V. Guillerm, F. Ragon, M. Dan-Hardi, T. Devic, M. Vishnuvarthan, B. Campo, A. Vimont, G. Clet, Q. Yang, G. Maurin, G. Ferey, A. Vittadini, S. Gross, C. Serre, *Angew. Chem., Int. Ed.* **2012**, 51, 9267.
- [97] a) P. F. Ji, K. Manna, Z. Lin, X. Y. Feng, A. Urban, Y. Song, W. B. Lin, *J. Am. Chem. Soc.* **2017**, 139, 7004; b) S. Wang, L. Chen, M. Wahiduzzaman, A. Tissot, L. Zhou, I. A. Ibarra, A. Gutierrez-Alejandre, J. S. Lee, J.-S. Chang, Z. Liu, J. Marrot, W. Shepard, G. Maurin, Q. Xu, C. Serre, *Matter* **2021**, 4, 182.
- [98] M. R. DeStefano, T. Islamoglu, J. T. Hupp, O. K. Farha, *Chem. Mater.* **2017**, 29, 1357.
- [99] H. Noh, C.-W. Kung, T. Islamoglu, A. W. Peters, Y. Liao, P. Li, S. J. Garibay, X. Zhang, M. R. DeStefano, J. T. Hupp, O. K. Farha, *Chem. Mater.* **2018**, 30, 2193.
- [100] I. Pakamore, J. Rousseau, C. Rousseau, E. Monflier, P. A. Szilagy, *Green Chem.* **2018**, 20, 5292.
- [101] A. E. Marteel, J. A. Davies, W. W. Olson, M. A. Abraham, *Annu. Rev. Environ. Resour.* **2003**, 28, 401.
- [102] C. Duan, Y. Yu, J. Xiao, Y. Li, P. Yang, F. Hu, H. Xi, *Green Energy Environ.* **2021**, 6, 33.
- [103] K. Li, J. Yang, J. Gu, *Chem. Sci.* **2019**, 10, 5743.
- [104] a) J. Jacobsen, A. Ienco, R. D'Amato, F. Costantino, N. Stock, *Dalton Trans.* **2020**, 49, 16551; b) M. Lammert, M. T. Wharmby, S. Smolders, B. Bueken, A. Lieb, K. A. Lomachenko, D. D. Vos, N. Stock, *Chem. Commun.* **2015**, 51, 12578.
- [105] X. Sang, J. Zhang, J. Xiang, J. Cui, L. Zheng, J. Zhang, Z. Wu, Z. Li, G. Mo, Y. Xu, J. Song, C. Liu, X. Tan, T. Luo, B. Zhang, B. Han, *Nat. Commun.* **2017**, 8, 175.
- [106] S. Dai, F. Nouar, S. Zhang, A. Tissot, C. Serre, *Angew. Chem., Int. Ed.* **2021**, 60, 4282.
- [107] D. Feng, W.-C. Chung, Z. Wei, Z.-Y. Gu, H.-L. Jiang, Y.-P. Chen, D. J. Darensbourg, H.-C. Zhou, *J. Am. Chem. Soc.* **2013**, 135, 17105.
- [108] H. He, L. Li, Y. Liu, M. Kassymova, D. Li, L. Zhang, H.-L. Jiang, *Nano Res.* **2020**, 14, 444.
- [109] G. E. Cmarik, M. Kim, S. M. Cohen, K. S. Walton, *Langmuir* **2012**, 28, 15606.
- [110] M. J. Katz, Z. J. Brown, Y. J. Colón, P. W. Siu, K. A. Scheidt, R. Q. Snurr, J. T. Hupp, O. K. Farha, *Chem. Commun.* **2013**, 49, 9449.
- [111] S. J. Garibay, I. Iordanov, T. Islamoglu, J. B. DeCoste, O. K. Farha, *CrystEngComm* **2018**, 20, 7066.
- [112] L. Huelsenbeck, H. Luo, P. Verma, J. Dane, R. Ho, E. Beyer, H. Hall, G. M. Geise, G. Giri, *Cryst. Growth Des.* **2020**, 20, 6787.
- [113] Q. Yang, S. Vaesen, F. Ragon, A. D. Wiersum, D. Wu, A. Lago, T. Devic, C. Martineau, F. Taulelle, P. L. Llewellyn, *Angew. Chem.* **2013**, 125, 10506.
- [114] Z. Chen, X. Wang, H. Noh, G. Ayoub, G. W. Peterson, C. T. Buru, T. Islamoglu, O. K. Farha, *CrystEngComm* **2019**, 21, 2409.
- [115] R. N. Amador, L. Cirre, M. Carboni, D. Meyer, *J. Environ. Manage.* **2018**, 214, 17.

- [116] G. Wißmann, A. Schaate, S. Lilienthal, I. Bremer, A. M. Schneider, P. Behrens, *Micropor. Mesopor. Mat.* **2012**, 152, 64.
- [117] F. Ragon, B. Campo, Q. Yang, C. Martineau, A. D. Wiersum, A. Lago, V. Guillermin, C. Hemsley, J. F. Eubank, M. Vishnuvarthan, *J. Mat. Chem. A* **2015**, 3, 3294.
- [118] J. Jacobsen, H. Reinsch, N. Stock, *Inorg. Chem.* **2018**, 57, 12820.
- [119] H.-Q. Xu, J. Hu, D. Wang, Z. Li, Q. Zhang, Y. Luo, S.-H. Yu, H.-L. Jiang, *J. Am. Chem. Soc.* **2015**, 137, 13440.
- [120] C. S. Cundy, P. A. Cox, *Chem. Rev.* **2003**, 103, 663.
- [121] Y. Liu, Z. Tang, *Adv. Mater.* **2013**, 25, 5819.
- [122] a) Q. Yang, Q. Xu, H.-L. Jiang, *Chem. Soc. Rev.* **2017**, 46, 4774; b) Z. Xia, J. Fang, X. Zhang, L. Fan, A. J. Barlow, T. Lin, S. Wang, G. G. Wallace, G. Sun, X. Wang, *Appl. Catal. B* **2019**, 245, 389.
- [123] A. Aijaz, A. Karkamkar, Y. J. Choi, N. Tsumori, E. Rönnebro, T. Autrey, H. Shioyama, Q. Xu, *J. Am. Chem. Soc.* **2012**, 134, 13926.
- [124] B. F. Johnson, *Top. Catal.* **2003**, 24, 147.
- [125] G. Lu, S. Li, Z. Guo, O. K. Farha, B. G. Hauser, X. Qi, Y. Wang, X. Wang, S. Han, X. Liu, J. S. DuChene, H. Zhang, Q. Zhang, X. Chen, J. Ma, S. C. J. Loo, W. D. Wei, Y. Yang, J. T. Hupp, F. Huo, *Nat. Chem.* **2012**, 4, 310.
- [126] a) C. H. Kuo, Y. Tang, L. Y. Chou, B. T. Sneed, C. N. Brodsky, Z. P. Zhao, C. K. Tsung, *J. Am. Chem. Soc.* **2012**, 134, 14345; b) B. L. Chen, Z. X. Yang, Y. Q. Zhu, Y. D. Xia, *J. Mat. Chem. A* **2014**, 2, 16811; c) Q. H. Yang, Q. Xu, S. H. Yu, H. L. Jiang, *Angew. Chem., Int. Ed.* **2016**, 55, 3685; d) H. Q. Zheng, Y. N. Zhang, L. F. Liu, W. Wan, P. Guo, A. M. Nystrom, X. D. Zou, *J. Am. Chem. Soc.* **2016**, 138, 962.
- [127] H. H. He, L. Y. Li, Y. Liu, M. Kassymova, D. D. Li, L. L. Zhang, H. L. Jiang, *Nano Res.* **2021**, 14, 444.
- [128] K. Liang, R. Ricco, C. M. Doherty, M. J. Styles, S. Bell, N. Kirby, S. Mudie, D. Haylock, A. J. Hill, C. J. Doonan, P. Falcaro, *Nat. Commun.* **2015**, 6, 1.
- [129] F. Lyu, Y. Zhang, R. N. Zare, J. Ge, Z. Liu, *Nano Lett.* **2014**, 14, 5761.
- [130] a) M. Zhao, K. Yuan, Y. Wang, G. Li, J. Guo, L. Gu, W. Hu, H. Zhao, Z. Tang, *Nature* **2016**, 539, 76; b) A. Kumar, A. Sharma, Y. Chen, M. M. Jones, S. T. Vanyo, C. Li, M. B. Visser, S. D. Mahajan, R. K. Sharma, M. T. Swihart, *Adv. Func. Mater.* **2021**, 31, 2008054; c) X. Liu, L. He, J. Zheng, J. Guo, F. Bi, X. Ma, K. Zhao, Y. Liu, R. Song, Z. Tang, *Adv. Mater.* **2015**, 27, 3273.
- [131] M. Kalaj, K. L. Prosser, S. M. Cohen, *Dalton Trans.* **2020**, 49, 8841.
- [132] X. Kang, K. Lyu, L. Li, J. Li, L. Kimberley, B. Wang, L. Liu, Y. Cheng, M. D. Frogley, S. Rudic, A. J. Ramirez-Cuesta, R. A. W. Dryfe, B. Han, S. Yang, M. Schroder, *Nat. Commun.* **2019**, 10, 4466.
- [133] J. P. Patterson, P. Abellan, M. S. Denny Jr, C. Park, N. D. Browning, S. M. Cohen, J. E. Evans, N. C. Gianneschi, *J. Am. Chem. Soc.* **2015**, 137, 7322.
- [134] J. Cravillon, R. Nayuk, S. Springer, A. Feldhoff, K. Huber, M. Wiebcke, *Chem. Mater.* **2011**, 23, 2130.

Recent progresses in metal–organic frameworks based core–shell composites

Abstract: Encapsulation of active guest compounds inside Metal-Organic Frameworks (MOFs) architectures is one of the most promising routes to reach properties beyond those of the bare MOFs and/or guest species. In contrast with the conventional host/guest composites that rely on the encapsulation of guest species into MOF cavities, core-shell composites display a better accessibility to the pores ensuring an optimal diffusion of the substrate while presenting a unique structure that prevents from the aggregation and the runoff of the active guests and ensures a tight interaction between core and shell, leading to synergistic effects. Herein, this progress report summarizes the recent advances in this field. The main synthetic strategies are first discussed before highlighting few potential applications, such as heterogeneous environmental catalysis, gas separation and sensing, while others (bio-applications...) will be briefly mentioned. We conclude this review by a critical perspective in order to promote new generations of MOFs based composites for energy-related applications.

1. Introduction

Metal-organic frameworks (MOFs) are a class of crystalline porous hybrid materials with varying dimensionality that has been widely studied in the past two decades.^[1] MOFs properties mainly derive from the structural arrangements of their inorganic part (metal cations, eventually assembled in secondary building units (SBUs)) with organic ligands.^[2] The high degree of tuneability of these solids, including pre-design and post-modification approaches, makes MOFs appealing for various potential applications,^[3] particularly in the field of energy.^[4] Compared to conventional porous solids (e.g. Metal oxides, Zeolites, Carbon materials. etc), MOFs can exhibit an unprecedented diversity in terms of pore sizes and shapes, associated in some cases to remarkable surface areas (up to 7000 m²/g,^[5] BET model) and/or redox or Lewis open metal sites (OMS).^[7] Noteworthy MOFs can also benefit from an easy ligand functionalization towards the enhancement of their catalytic properties, including the concepts of “multivariate MOFs”.^[6]

Incorporating guest moieties into MOFs presents a great potential for several applications (e.g. catalysis, gas separation), as the encapsulated guest materials can introduce new requested properties that are absent in the parent material. In addition, the properties of the composite may outperform the one of each single component.^[7, 8] Well-documented synthetic strategies have been reported, including pre- and post-synthetic guest incorporation, depending on the interaction

between the host and the guest.^[9] For example, a wide range of functional materials (e.g. inorganic metal nanoparticles, coordination complexes, quantum dots, polyoxometalates, enzymes, and polymers...) have been introduced post-synthetically into the pores of MOFs.^[10, 11] Among them, inorganic metal nanoparticles (NPs) have been widely studied due to their remarkable properties in energy and environmentally-related applications.^[4] The features of these MOF-based composites make them appealing to address prominent issues in catalysis.^[12] Nevertheless, there are still several limitations that still need to be considered: (1) the confined nanoparticles can block the pores during their growth, therefore preventing the substrate from diffusing inside the solid; (2) only guest species smaller than the pore dimensions can be loaded; (3) in some cases, the shape/morphology of the guest species cannot be controlled due to constraints imposed by the host (pore shape/size/interactions...); (4) the precise control of the guest location is in most cases not possible and depositing guests on the MOF external surface is unavoidable, regardless of very limited tentative studies;^[13, 14] (5) guests may leach in liquid phase, leading to unwanted homogeneous catalysis. In order to overcome these problems, the preparation of core-shell compounds using MOFs was first proposed in 2012.^[10, 15] This so-called “bottle-around-ship” strategy is based on the construction of a stratified structure, where the “core” (that can be inorganic nanoparticles,^[16] MOFs,^[17] Metal oxides,^[18] Silica,^[19] Polymers,^[20] Carbon nanotubes,^[21] etc) is encased in a MOF “shell”. It allows an effective encapsulation regardless the shape, size, morphology, and composition of the “core”. For example, one MOF can cover a second MOF, forming a MOF@MOF architecture, which greatly expands the accessible structural complexity.^[8, 22, 23] Notably, thanks to complementary chemical/physical properties, the combination of two distinct materials might lead to the synergetic effect, where the resulting core-shell structure behaves beyond each single material.^[24, 25] The almost infinite categories of MOFs and “core” materials make their combinations becoming indeed diverse. Lately, researchers have started to pay attention to the derived composites that based on the core-shell MOF-based architectures for advanced applications. Of those, carbonized core-shell composites and hollow structures (yolk-shell,^[26] hollow multi-shelled structures^[27, 28]) particularly exhibited broad research interest due to their facilitated properties (conductivity,^[29] hierarchical porosity,^[30] diffusion,^[31] etc). Note that, even though the thermolysis at high temperature often completely/ partially destroy the MOFs, the overall remaining porosity and the sequence of active sites can relatively maintain by controllable thermodynamics. Another effective strategy to prepare yolk-shell or hollow structures relies on the pre-formed well-defined core-shell structures. The differences in the chemical/ physical stability between core and shell provide the opportunity to a controllable etching of the core materials to form hollow structures.^[32] However, due to the recently published reviews and limited scope of this review,^[33] we will not particularly emphasize on the derived materials based on core-shell composites.

In this report, we summarize the most significant recent progresses in the development of core-shell NPs@MOF and MOF@MOF, with a particular emphasis on the synthetic strategies and synergistic effects. In the first case, MOFs are not only playing the role of supports to host NPs, which effectively prevents their aggregation during the material preparation and use, but also give a fully available pore space required for an optimal diffusion of the substrates. In the second case, whose development is even more recent, most studies refer to gas separation, probably due to the

possibility to combine the properties of the two materials (e.g. uptake and selectivity) in order to get optimized sorption behaviour. Finally, we will propose perspectives for the design of new generations of advanced core-shell composites for diverse applications such as energy-related catalysis and gas separation.



Scheme 1. Illustration of the synthesis methods (CAAS = Capping agent-assisted synthesis; ITAS = Inorganic template-assisted synthesis; EGS = Epitaxial growth synthesis) and the main applications of core-shell MOFs based composites.

2. Synthetic methods of core-shell MOF-based composites

2.1. Capping agent-assisted synthesis

The capping agent-assisted synthesis (CAAS) usually involves two steps, where the pre-synthesized core material is first prepared prior to the growth of MOF shell around, resulting in discrete species within the ordered MOF framework. However, the preparation of core-shell MOF-based composites still remains challenging due to the risk of aggregation of active NPs and/or of self-nucleation of MOF particles. Capping agents/surfactants can to some extent prevent this, on one hand inhibiting the aggregation of small NPs and on the other hand compensating the lattice mismatch between the MOF and the NPs. In a pioneering work, Lu et al. reported a versatile polyvinylpyrrolidone (PVP) assisted approach to encapsulate several inorganic materials with distinct sizes and shapes in ZIF-8 (ZIF stands for Zeolitic Imidazolate Frameworks), which subsequently led to a catalytic/physical properties enhancement. Transmission electron microscopy (TEM) suggested that the encapsulation process does not rely on the heterogeneous nucleation mechanism, but instead is based on the continuous growth of a MOF shell around the particles. In the synthesis process, PVP not only contributes to the stability of the inorganic nanoparticles but also enhances its affinity with the coordination-polymer through weak interactions, either between pyrrolidone rings (C=O) and Zn(II) ions from ZIF nodes and/or between apolar groups of PVP and the organic linkers of the MOF.^[10]

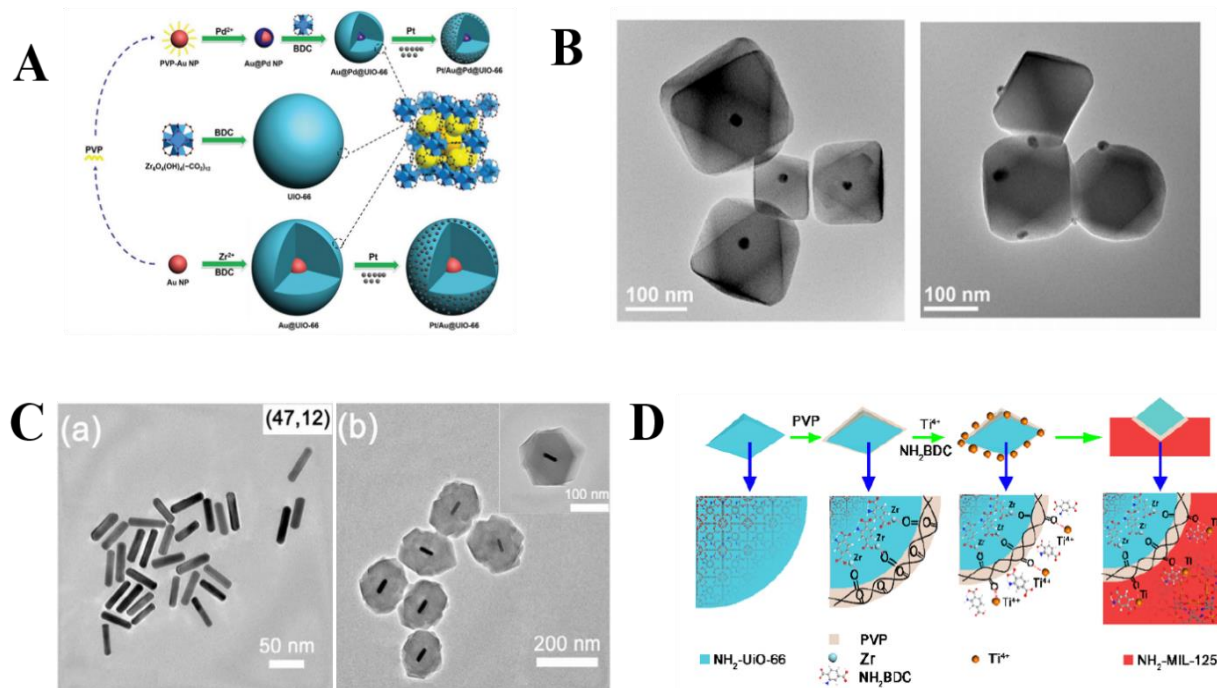


Figure 1. A) Synthetic route for the synthesis of Au@Pd NPs and other composites. B) TEM images of Cu nanocrystals embedded into UiO-66 and Cu nanocrystals on the external surface of UiO-66. C) TEM images of CTAB-stabilized Au NRs (a) and TEM image of Au NRs@ZIF-8 core-shell nanostructure (b). D) Schematic representations of the coordination phenomenon associated with the systematic growth of the MOF-on-MOF hybrid structure. A-D) Reproduced with permission.^[34-37] Copyright 2018, Wiley-VCH. Copyright 2016, American Chemical Society. Copyright 2018, Springer.

Since then, CAAS method have been used with a broad range of compounds, including bimetallic alloys, non-noble metal NPs, NPs with various shapes/ sizes, as well as using MOF as core. PVP, an amphiphilic non-ionic polymer of a low toxicity, is one of the most common capping agent for encapsulation of inorganic materials in MOFs. For example, Hu et al. used PVP protected Au NPs and Au@Pd bimetallic NPs to fabricate monodisperse spherical core-shell architectures with UiO-66 (Figure 1A).^[34] The accessible pore space enabled an additional encapsulation of Pt NPs through conventional ship-in-a-bottle strategy. In addition to noble metal NPs, Yaghi et al. reported single 18 nm PVP coated Cu nanocrystals encapsulated within UiO-66 single crystals and 18 nm Cu nanocrystals anchored on the external surface of UiO-66 crystals (Figure 1B).^[35] The resulting Cu nanocrystal@UiO-66 exhibited a superior catalytic activity in comparison with the Cu nanocrystals deposited on the outer surface of the MOF. In addition, the use of Zr(OiPr)₄ as precursor for the MOF synthesis led to a better core-shell structure compared with the use of acidic salts such as ZrCl₄ and ZrOCl₂ due to the possible dissolution of Cu nanocrystals under acidic conditions. Similarly, Tang et al. encapsulated PVP-stabilized Au Nanorods (Au NRs) in ZIF-8 using a two steps method (Figure 1C). The well-defined single Au NRs@ZIF-8 particles showed preserved porosity and high purity, paving the way for optical studies on these anisotropic objects.^[36] Other works also reported the encapsulation of other inorganic materials with distinct morphologies,^[27] shapes^[38] and sizes^[39]. Apart from inorganic nanomaterials, Kitagawa et al. proposed a general strategy for the synthesis of MOF@MOF hetero-architectures where PVP was used to overcome the limitation of the lattice matching rule (Figure 1D).^[37] The PVP played a role like glue, interacting with the core metal (Zr⁴⁺) in the first step via electrostatic attraction and then coordinating to the shell metal cations (Ti⁴⁺), therefore giving a chance to combine 3D MOFs that have distinct topologies. In addition, the authors demonstrated that the sizes and morphologies of MOF crystals can be well controlled by changing the amount of PVP and of core MOF particles.

In addition to polymers, CAAS was also intensively applied using other kinds of small molecules / surfactants depending on the capping agent requested in the design process of core materials.^[40] For example, cetyltrimethylammonium bromide (CTAB) is a surfactant that enables individual encasement and controlled alignment of several nanomaterials.^[41, 42] Yang et al. applied CTAB as a bridging layer to construct a series of MOF-based core-shell/yolk-shell structures on the surface of Pt-Ni nanoframes through the sequence of encasement, overgrowth, and dissociation of the sacrificed shell.^[43] The sizes and shapes of the final composite could be tuned by changing the growth time and the quantity of CTAB in solution. In another example, the hydrophobic tail of CTAB was used to control the interaction between Pd particles and ZIF-8 in order to align the (100) planes of Pd structure with the (110) planes of ZIF-8.^[44] Tsung et al. also reported a core-shell UiO-66@ZIF-8 structure using CTAB as a surfactant. The CTAB was proven to be the optimal surfactant in terms of shape/overgrowth control in comparison with other micelle forming surfactants, such as tetradecyltrimethylammonium bromide (TTAB), cetylpyridinium bromide (CPB), and sodium dodecyl sulfate (SDS), as well as with PVP. It is worth noticing (Figure 2E) that the thickness of the MOF shell can be tuned down to 40 nm depending on the amount of reactants used.^[45] Dang et al. presented a facile LYZ (self-assembled lysozymes)-based strategy (Figure 2B) for fabricating well-defined core-shell nanocomposites consisting of a NP core and a MOF shell. The LYZs could spontaneously form a robust layer with abundant functional groups on the surfaces of NPs such as 14 nm Au NPs, Au nanostars, CdTe quantum dots, CuO, β -FeOOH,

magnetic NPs (Figure 2C), which makes them handy to mediate the MOFs heterogeneous nucleation and growth at their surface.^[46] Hence, use of a stronger capping agent can be a useful approach to create core-shell NP@MOF nanocomposites due to its high affinity with both NPs and MOF

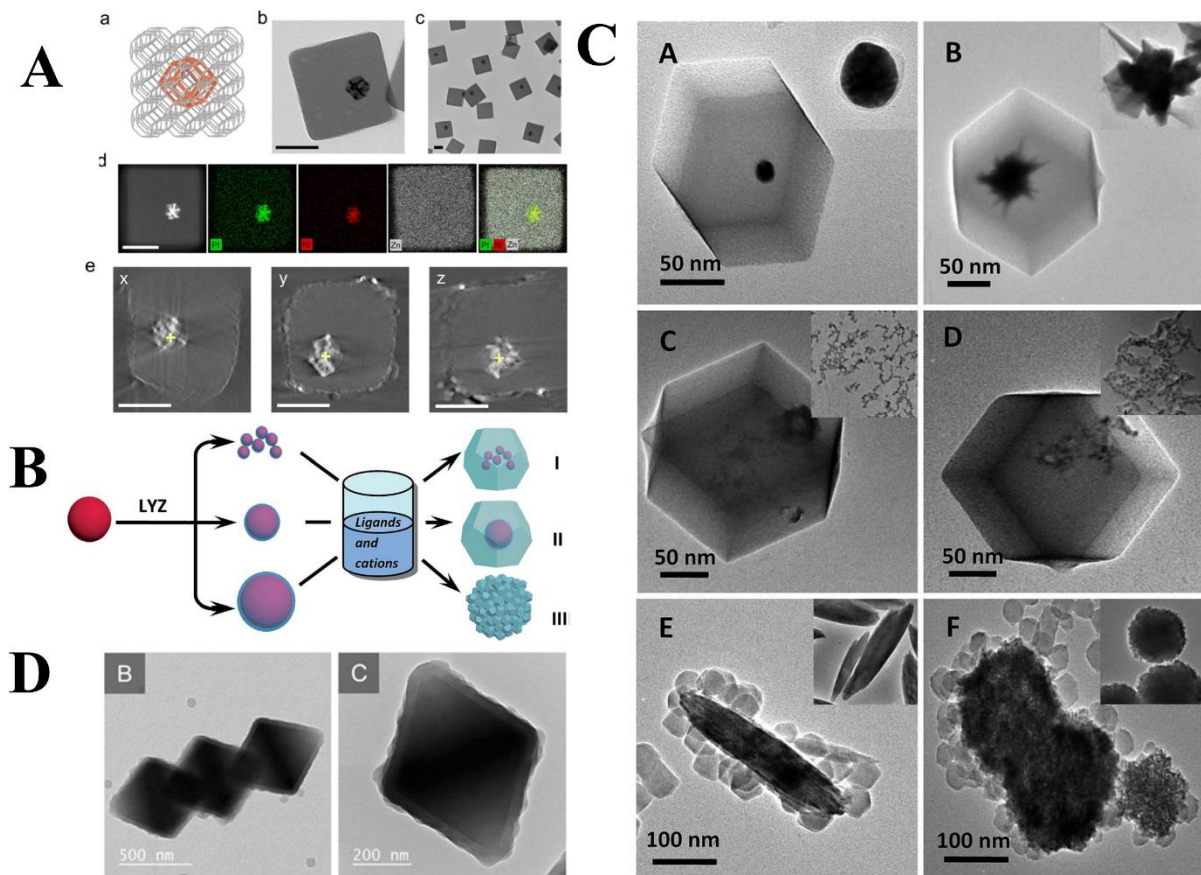


Figure 2. A) Scheme of the Pt-Ni@ZIF-8 core-shell composites (a), TEM images of the obtained composites (b-c), HAADF-STEM image and EDX maps (d), tomographic reconstruction images of single core-shell frame-in-frame structure, the yellow plus marker shows the same position in all three orthogonal slices (e). B) Illustration of the stepwise strategy of the controlled encapsulation of NPs in ZIF-8 to form multiple- (I) or single-core-monocrystalline-shell (II) or single-core-polycrystalline-shell (III) structures. C) TEM images of Nanoparticles@ZIF-8 ((a-f) with various core materials (14 nm Au NPs, Au nanostar, CdTe, CuO, β -FeOOH, MNP) D) TEM images of UiO-66@ZIF-8. Reproduced with permission.^[43, 45, 46] Copyright 2020, American Chemical Society. Copyright 2017, Royal Society of Chemistry. Wiley-VCH. Copyright 2015, Wiley-VCH.

2.2. Inorganic template-assisted synthesis

Inorganic template-assisted synthesis (ITAS) is a core-shell fabrication process that involves two steps: the binding of inorganic materials with core materials, such as coating with SiO₂ (serving as binding sites for shell MOF) or metal oxide (subsequently be used as the metal source for the

shell MOF growth) and the MOF synthesis.^[47] The preparation of such core-shell composites has few manifest advantages: 1) the template metal oxide can be directly used as the metal source of shell MOF; 2) in the case of reactive NPs, the particles can be protected by an oxide shell during the synthesis and might be accessible to catalytic substrates when the shell is fully dissolved. Even though the ITAS method looks appealing, it exhibits some disadvantages in comparison with CAAS method such as the limited designability of the wrapped NPs (size, shape, morphology, etc.) associated with the necessary shell MOF chemical stability when the etching of the sacrificing metal oxide is needed as well as the request of an easy to dissolve sacrificing metal oxide. Pioneering works have used ZnO,^[48] Cu₂O,^[49] Al₂O₃,^[50] Silica^[51] as a template for the construction of core-shell composites. Recently, Cheng et al. coated Cu₂O particles with silica, which were further encapsulated into ZIF-8, representing the first room temperature incorporation of unstable active Cu₂O nanocubes within a MOF (Figure 3A-C). A blue slurry was obtained instead of yellow one when SiO₂ was not used as protective layer (Figure 3C), confirming the role of SiO₂ to avoid Cu(I) oxidation. In addition to being a useful protective layer, SiO₂ can also play a role as sacrificial template to form a hollow structure (40nm in size) when selective etching of SiO₂ is performed using NaOH under inert atmosphere.^[52] Metal oxide/ Metal(0) nanoparticles have also been used as sacrificing agents to form core-shell architectures.^[53, 54] For example, Che et al. synthesized nanostructures of the octahedron and flower Pt-Cu@HKUST-1, where Pt-Cu alloys acted as a template for the subsequent MOF shell growth in-situ via the consumption of Cu(0). In a typical synthesis, Pt-Cu alloy with various morphologies were pre-synthesized (Figure 3D, schematic illustration) and PVP was used as capping agent for protecting active Pt-Cu alloy while Fe(III) was used in order to oxidize Cu(0) in Cu(II). Pt-Cu with different morphologies were encapsulated in HKUST particles (Figure 3E (a-b)), evidencing the versatility of the ITAS method. The obtained octahedron and flower Pt-Cu@HKUST-1 both presented a very thin shell thickness of ca. 21- 25 nm and almost unchanged Pt-Cu alloy size (ca. 43nm).^[54]

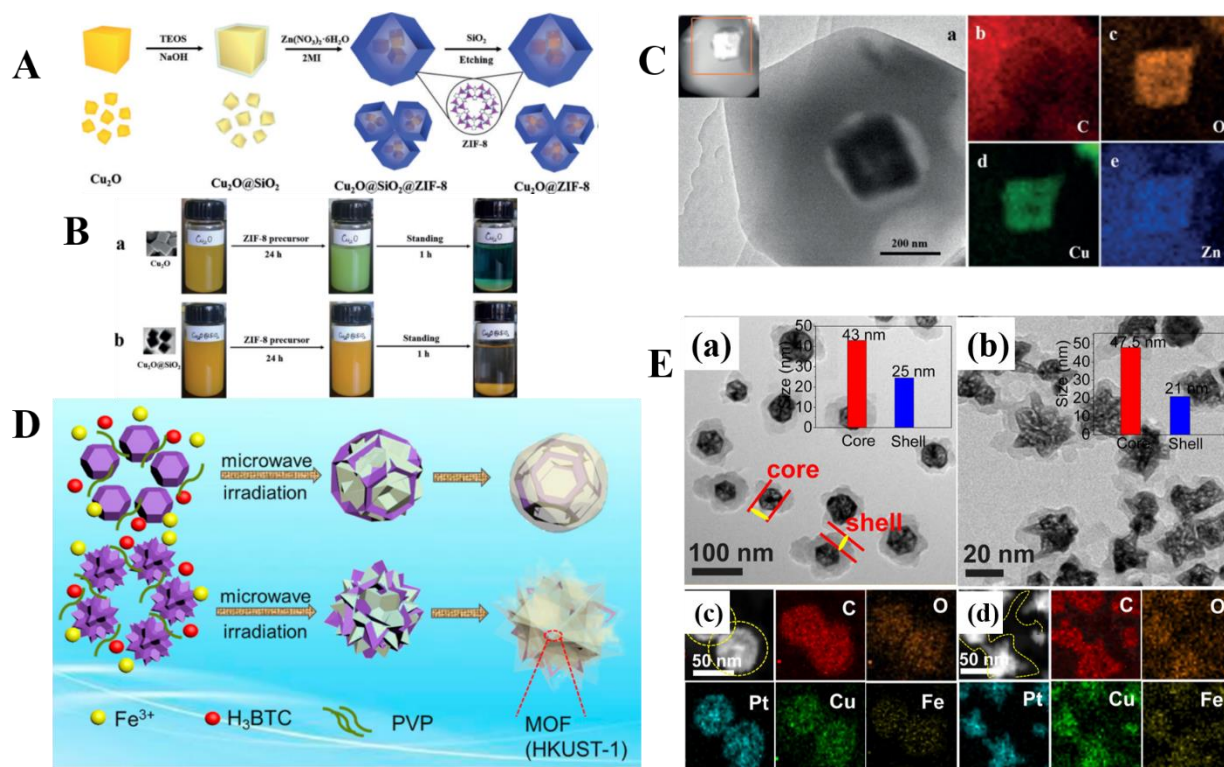


Figure 3. A) Schematic illustration for the synthesis of $\text{Cu}_2\text{O}@ZIF-8$ composites. B) Comparative experiment for the stability of (a) Cu_2O and (b) $\text{Cu}_2\text{O}@SiO_2$. C) (a) TEM image of $\text{Cu}_2\text{O}@ZIF-8$, (b-e) elemental distribution for $\text{Cu}_2\text{O}@ZIF-8$. D) Illustration of the in-situ synthesis of Pt-Cu frame@HKUST-1 under the Microwave irradiation TSS method. E) (a-b) TEM images of octahedron Pt-Cu frame@HKUST-1 and flower Pt-Cu frame@HKUST-1 (insert: size distribution histogram). Reproduced with permission.^[52, 54] Copyright 2018, Wiley-VCH. Copyright 2017, American Chemical Society.

2.3. One-pot synthesis

One-pot synthesis consists in a direct mixing of both MOFs and NPs precursors in one pot.^[55] It exhibits serious advantages such as high efficiency, low complexity, and upscaling ability. It should be pointed out that the active cation for the NPs synthesis should undergo few steps in the presence of MOF precursors in solution (metal source, ligand) that are, the reduction into metal particle, the protection of the NPs, followed by the MOF growth around the NPs. Therefore, solvothermal conditions for MOFs synthesis are usually not compatible with this strategy due to a lack of control of the formation of the inorganic NPs. This raises additional challenges for the MOF chemists. Li's group reported first the one-step synthesis of Pt NPs@UiO-66 where H_2 and DMF were used as reducing and bridging agents, respectively. The specific interactions between Pt° and -C-N groups and between C=O moieties and Zr^{4+} favored the growth of the MOF on the surface of Pt NPs rather than in solution.^[14] More recently, Wang et al. reported a one-pot PVP microwave irradiation-assisted strategy to fabricate Ag NPs@IRMOF-3 (illustrated in Figure 4A).^[56] This facile synthesis procedure allowed a fine control of the shell thickness (Figure 4B (a-c)) from 24 nm to 175 nm simply through a control of the reaction time. The size of Ag NPs could also be tuned by decreasing the initial concentration of AgNO_3 (Figure 4B (b, d, e)) and increasing

the amount of PVP, leading to a size down to 5.2 nm with the lowest Ag loading. Indeed, PVP acted as a stabilizer of Ag NPs as well as provided interactions to adsorb IRMOF-3 precursors onto the Ag NPs surfaces via coordination interaction between the pyrrolidone rings (C=O) and Zn^{2+} . In this work, the heating method seemed to be key point, as the use of solvothermal heating led to self-depositing of small Ag NPs rather than to a core-shell structure.

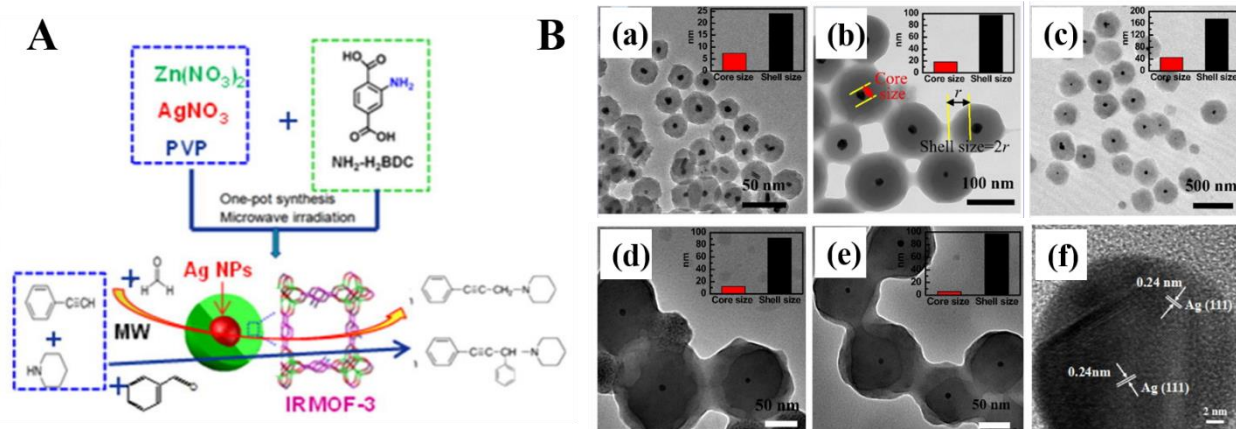


Figure 4. A) Schematic illustration for the synthesis of one-pot Ag NPs@IRMOF-3. B) TEM images and average sizes of core and shell (inset) of Ag@IRMOF-3 nanostructures under MW heating at 120 °C with 0.014 mmol $AgNO_3$ at crystallization time of (A) 5 min, (B) 15 min, (C) 30 min, and with (D) 0.0014 mmol, (E) 0.0005 mmol $AgNO_3$ at crystallization time of 15 min, (F) HRTEM image of the represented core. Reproduced with permission.^[56] Copyright 2017, Elsevier Inc.

2.4. Epitaxial growth synthesis

Epitaxial growth synthesis (EGS) involves the synthesis of the core MOF particle followed by the fabrication of the second layer of MOF around the core.^[17, 57] It should be noted that the shell “MOF” usually have to exhibit a similar topology than core one. In addition, active NPs can be deposited/ adsorbed at the interface of the two layers before the epitaxial growth. The compounds MOFs@NPs@MOFs are also called sandwich structures. Such composites have many similarities to conventional core-shell structures, while the control of the shell thickness in the super-thin range (<10 nm) is easier due to the great synthetic flexibility accessible for the shell synthesis (tuning the concentration of precursors, reactants ratio...). Tang et al. reported a series of sandwich structures based on MIL-101 and Pt NPs in 2016, which represent a proof of concept to design highly efficient and selective catalysts.^[58] Recently, this group synthesized a series of sandwich structures UiO-67@Pd NPs@UiO-X (X=66, 67(N) (N = 2,2'-bipyridine-5,5'-dicarboxylic acid), 67, 68) to study the contribution of organic linkers in catalytic efficiency via a similar epitaxial growth method (Figure 5 (A)). Micron-scale UiO-67 was chosen as the core and pre-synthesized in DMF through a conventional method (Figure 5 (B, C)). In a second step, H_2PdCl_4 was added to UiO-67 dispersed in methanol and reduced by $NaBH_4$. Figure 5 (D, E) demonstrated that the ultra-small Pd NPs were deposited on the surface of the MOF crystals. Subsequently, the precursors of the shell were mixed with the UiO-67@Pd suspension and the core-shell structure was formed

after solvothermal synthesis. Figure 5 (F, G) evidences the ideal spatial distribution of Pd NPs, with a shell thickness that is controllable from 35 to 50 nm by optimizing the precursor concentration and coating time. Additionally, other shells including UiO-66, UiO-67(N), and UiO-68 were also produced.^[59] Similarly, in order to overcome the ill-defined MNPs and blurred interactions at the interface, Zhu et al. reported a sandwich MOFs@APNPs@MOFs (APNCs= monodisperse atomically precise nanoclusters) structure, in which the encapsulated Au NCs are $\text{Au}_{25}(\text{L-Cys})_{18}$ clusters.^[60]

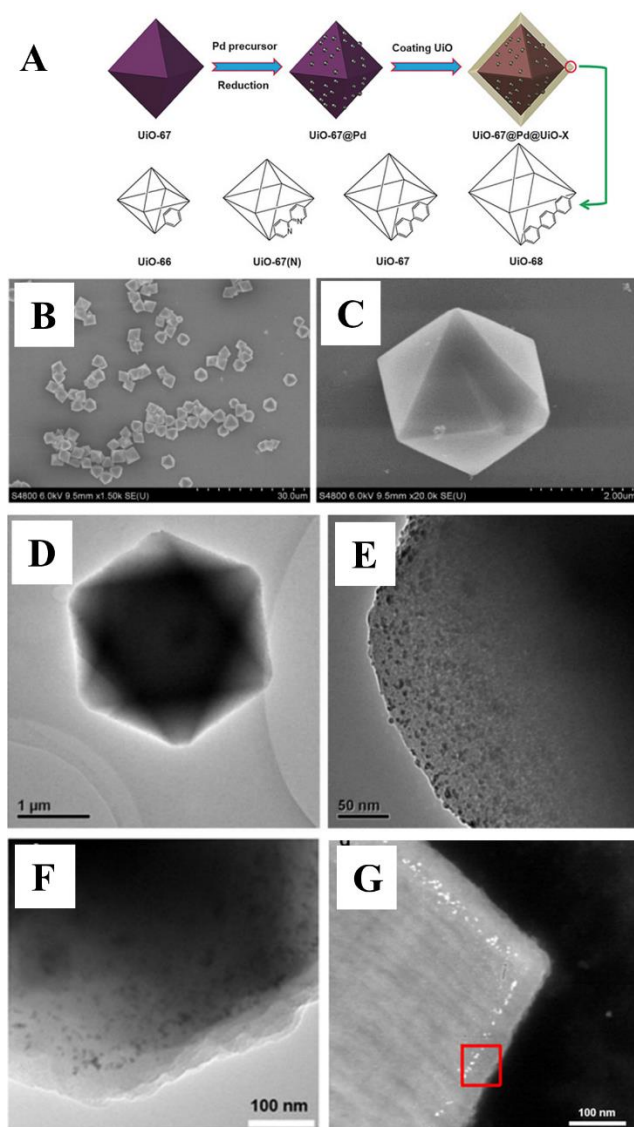


Figure 5. A) Synthetic route of Pd NPs sandwiched by a UiO core and shell with different pore apertures and wettability, UiO@Pd@UiO-X (X=66, 67(N), and 68). B, C) SEM images of UiO-67. D, E) TEM images of single UiO-67@Pd. F) TEM image of UiO-67@Pd@UiO-67 (50 nm). G) HAADF-STEM image of the cross-section of UiO-67@Pd@UiO-67 (50 nm). Reproduced with permission.^[59] Copyright 2019, Wiley-VCH.

Apart from the examples loaded with active NPs, strategies to prepare bare MOFs@MOFs (also called MOF-on-MOF) have also been investigated recently.^[61] In that case, overcoming the large mismatched lattices (for example Fe-MIL-88B@Fe-MIL-88C, illustrated in Figure 6(A)) is challenging, despite the use of isorecticular core and shell. Moonhyun et al. reported the synthesis of core-shell hybrid MOFs with the use of tip-to-middle anisotropic growth method, where the growth of the MOF shell (Fe-MIL-88C) started selectively at the tips of the template and effectively propagated along the *c* direction of core MOF. As shown in Figure 6(B), the pre-synthesized Fe-MIL-88B core exhibits a 3D hexagonal structure with a particle length at $0.88 \pm 0.10 \mu\text{m}$. The MOF growth process was monitored by SEM after 50 s, 80 s, and 600 s (Figure 6 (C-E)), corresponding to the intermediates and final product, respectively. X-ray powder diffraction proved that due to the highly flexible nature of MIL-88's, the cell parameters of Fe-MIL-88C could be self-adjusted according to the template for the effective growth, especially on the *ab* planes exposed at the particles tips. In a control experiment, the solvothermal reaction of 4, 4'- biphenyldicarboxylic acid (H₂BPDC), and Fe(NO₃)₃ in the presence of pre-formed Fe-MIL-88B particles was performed in order to obtain Fe-MIL-88B@Fe-MIL-88D. However, only independent MOF crystals were formed, indicating this epitaxial growth synthesis may not be suitable for compounds presenting too large lattice mismatches. Nevertheless, a more complex well-defined core-shell of Fe-MIL-88B@Ga-MIL-88B@Fe-MIL-88C was successfully formed (Figure 6(F)), demonstrating the large scope of this anisotropic growth method.^[62] However, the large scale construction of perfect core-shell MOF@MOF is not the same concept as the one in small scale due to the possible problematic encasement (e.g., incomplete covering, heterogeneous nucleation), which might significantly influence the following applications (e.g., gas separation).

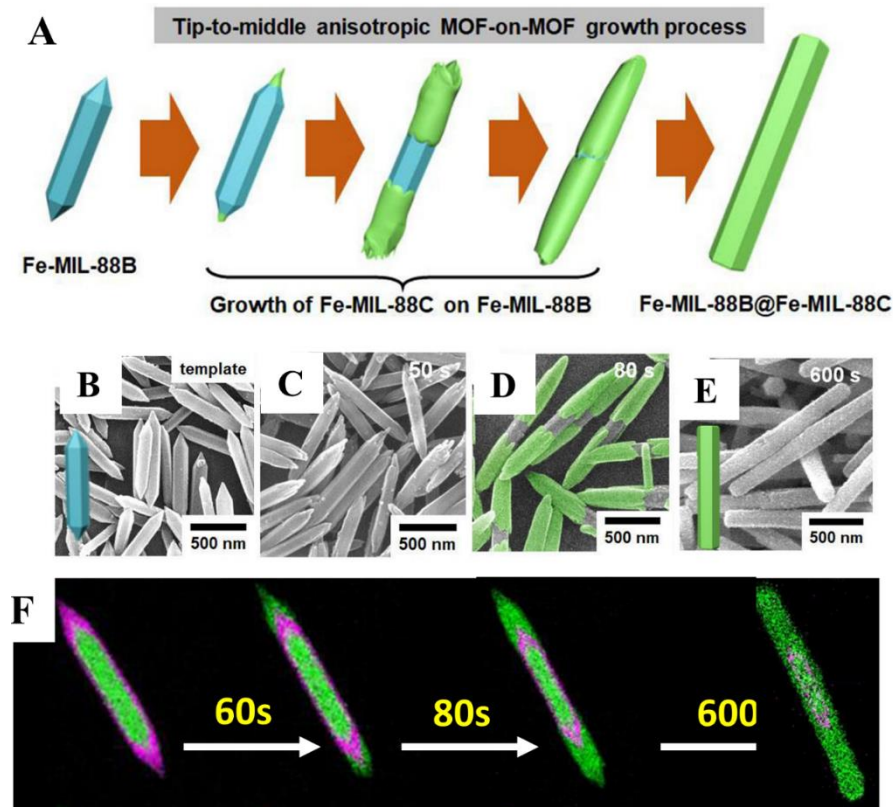


Figure 6. A) Schematic representation for the proposed tip-to-middle anisotropic MOF-on-MOF growth process with mismatched cell lattices for the production of well-defined core-shell hybrid Fe-MIL-88B@Fe-MIL-88C. SEM images monitoring the MOF-on-MOF growth process during the formation of core-shell hybrid Fe-MIL-88B@Fe-MIL-88C, at B) 0 s, C) 50 s, D) 80 s, E) 600 s. Newly grown shells in the intermediates are highlighted in green in D). F) Elemental mapping images monitoring the tip-to-middle anisotropic MOF-on-MOF growth process for the formation of doubly shelled core-shell Fe-MIL-88B@Ga-MIL-88B@Fe-MIL-88C, green color represents Fe, purple color represents Ga. Reproduced with permission^[62]. Copyright 2020, American Chemical Society.

2.5. Discussion

The synthesis of core-shell architectures has experienced a rapid development during last years due to their high potential for applications in catalysis, sensing etc. Among the various strategies, ITAS method is a facile route however facing disadvantages such as the compromise in structure robustness that is needed in order to extract metal ions from the core. Therefore, most studies were focused on divalent-based MOFs and implementing them with more robust metal(III, IV) MOFs remains an important challenge. CAAS appears as the strategy with the broadest range of utilization due to its ease in controlling the shape, size, and chemical nature of the encapsulated core. However, the presence of multiple steps as well as the use of capping agents might limit its practical use. EGS is a more recent approach that exhibits many similarities to CAAS but can allow the synthesis of super-thin shell thickness, therefore improving the diffusion of the substrates. Recently, work reported by Kwon et al. showed the MOFs that share similar 2D lattice parameters can be used for epitaxial growth, which might help to explore other composites.^[63] Although the above-mentioned methods are considered as more rational approaches and therefore have been commonly used so far, there is still a need to devote more effort to develop one-pot synthesis which, from a practical point of view, looks quite promising due to its lower cost and easier up-scaling.^[64] As a pre-requisite for the incorporation of functional but fragile compounds in chemically stable MOFs, mild synthesis conditions, e.g., relatively low synthesis temperature, eventually down to room temperature, were explored but remain challenging.^[10, 35, 65, 66] For instance, we have reported very recently a versatile one-step room-temperature environmentally-friendly approach for the syntheses of 12-connected (MOF-801, UiO-66-NH₂, UiO-66-COOH) and 8-connected (DUT-67, PCN-222) M₆ oxoclusters (M=Zr, Hf, Ce) based MOFs (Figure 7). The efficient synthetic strategy allows us not only to tune the MOF particles size but also to achieve a high space time yield that could pave the way towards the more effective and efficient construction of core-shell composites.^[67]

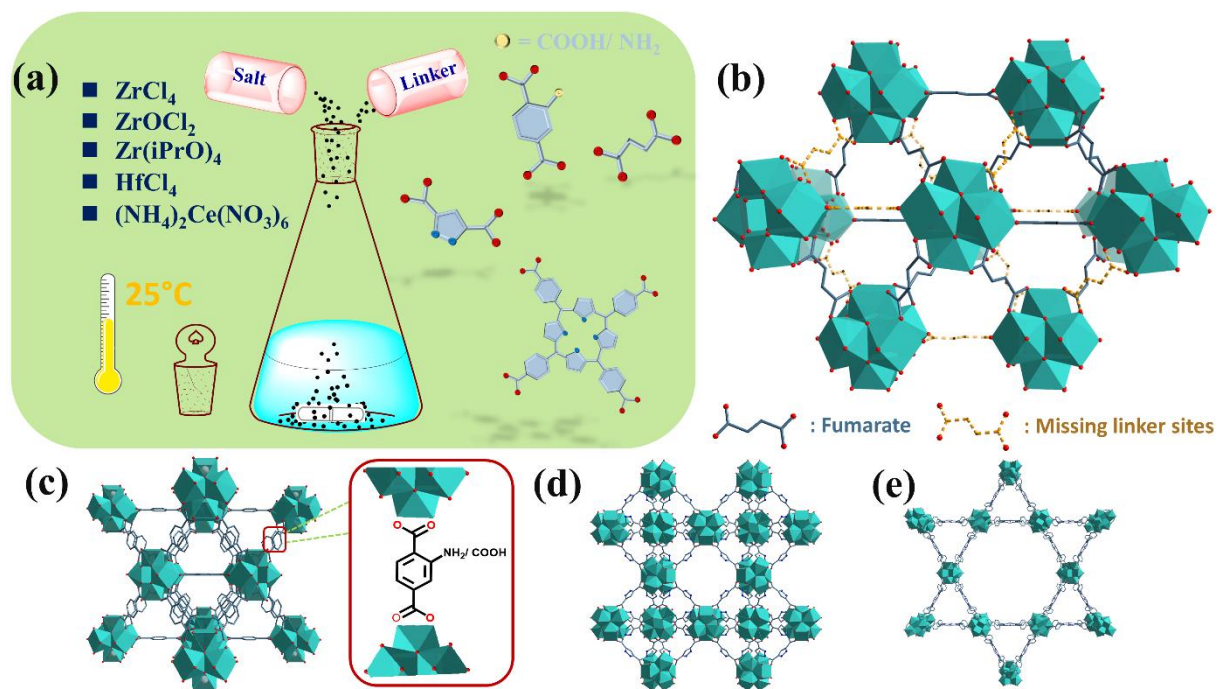


Figure 7. Schematic diagram of the room temperature one-step synthesis approach (a). Representative of the crystal structures of MOF-801 (Zr, Hf, Ce) viewed along (101) plane and the illustration of existing defects (b), UiO-66- $COOH/NH_2$ (c), DUT-67 (PDA) (d) and PCN-222 (e). Metal polyhedra, carbon and oxygen atoms are in cyan, black and red, respectively (hydrogen atoms have been omitted for the sake of clarity). Reproduced with permission.^[57] Copyright 2020, Wiley-VCH.

Table 1. Comparison of the different synthetic methods.

	CAAS (Capping agent-assisted synthesis)	ITAS (Inorganic template-assisted synthesis)	One-pot	EGS (Epitaxial growth synthesis)
Advantages	<ul style="list-style-type: none"> • Most versatile method • Tunable synthetic parameters • Allow large lattice mismatches 	<ul style="list-style-type: none"> • “Clean” surface of NPs 	<ul style="list-style-type: none"> • Direct • Potentially scalable 	<ul style="list-style-type: none"> • “Clean” surface of NPs (sandwich composites) • Tunable shell thickness
Disadvantages	<ul style="list-style-type: none"> • Remaining bridging agent that may block the active sites • Multiple-steps synthesis 	<ul style="list-style-type: none"> • Remaining capping agent • Challenging synthesis • Lack of properties control 	<ul style="list-style-type: none"> • Similar structure needed for core and shell (MOF@MOF) • More complex synthesis (sandwich composites) 	

3. Characterizations of core-shell MOF-based composites

One important challenge for the core-shell MOFs materials is to precisely determine the location and spatial distribution of the core materials, particularly in the following cases: 1) ultra-small NPs (diameter ≤ 3 nm) where it is often hard to distinguish if the NPs are located inside or on the MOF surface; 2) light metal NPs (such as Cu NPs, Fe/ Fe_xO_y NPs. etc) that suffer from a lack of electron density contrast when combined with heavy metal-based MOF shells (e.g. Zr, Hf, etc.)^[68,69]; 3) when the interface between core and shell is hard to distinguish because they contain the same metal (e.g. small CoFeO_x @Co-MOF, MOF-801@UiO-66).^[22,70] In other words, when the core nano-objects are ultrasmall or have similar lattice parameters and/or composition than the shell, the conventional characterization methods (SEM, TEM...) are not providing sufficient information about the interface between core and shell matrix, which drive the properties of the core-shell compound. The development of advanced characterization techniques is therefore needed in order to have a better understanding of the properties of the solids and will be presented in this section of the review.^[71]

HRTEM (High-resolution TEM): HRTEM is a key technique to determine the structural and spatial properties of core and shell, such as size/thickness of core and shell, lattice constants, atomic variations, chemical environment... Recently, STEM (Scanning transmission electron microscopy) has been intensively used for its ultra-high resolution (down to sub-50 pm resolutions for aberration correction STEM). It can provide high-quality incoherent images using high-angle scattered electrons in both dark and bright-field modes because of the different Z value of atoms in the core NPs compared with the metal atom of the shell MOF. Therefore, it is usually easy to get meaningful images when the encapsulated NPs are relatively big or containing heavier atoms than the shell. Researchers were able to use aberration-corrected STEM to observe ultra-small nanoparticles (or nanoclusters, size ≤ 2 nm) encapsulated in MOF shell, particularly when the shell is thick.^[69] Energy-dispersive X-ray spectroscopy (called EDS or EDX, usually coupled with TEM/ SEM) is a complementary technique that enables an element distribution mapping within core-shell particles, particularly when the core and shell cannot be easily distinguished from bright/ dark field images,^[68] giving access to information on the loading quantity and distribution of each element. For example, Rogach et al. were not able to identify Cu Nanoclusters (less than 2nm) within the framework of ZIF-8 using conventional STEM image (Figure 8A (a-b)), while EDX mapping (Figure 8A (c-f)) allowed to locate N, Cu and Zn respectively. The uniform loading of Cu evidences the incorporation and homogeneous distribution of Cu NCs through the entire ZIF-8 structure.^[72] In another example, Rosi et al. confirmed a series of multivariate stratified MOF@MOF structure using EDX.^[61] In their case, the core-shell UiO-67(Hf)@UiO-67(Zr) was characterized by EDX line-scan data across single MOF particles that clearly showed the formation of a binary domain stratified MOF with a core-shell structure (Figure 8B). The co-existence of two domains was further confirmed by EDX mapping, where Hf was detected in the entire area of a particle while Zr was only detected in the center. For both STEM and EDS techniques, it should be mentioned that the highly energetic electron beam can damage the MOF structure, as already observed with more robust zeolites, which limits the imaging under typical working conditions. Thus, a careful control the beam intensity as well as the exposure time is required.

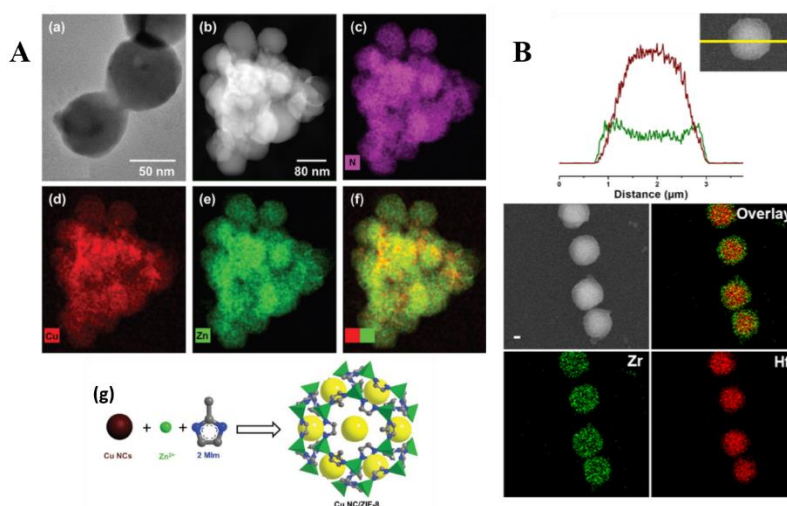


Figure 8. A) (a-b) HRTEM and HAADF-STEM images of Cu NC/ ZIF-8, (c-f) EDS elemental mapping of N, Cu, Zn, and Cu/ Zn, (g) Schematic diagram of the synthesis of Cu NC/ ZIF-8 composites. B) SEM-EDS characterization of stratified UiO-67(Hf)@UiO-67(Zr). Reproduced with permission.^[61, 72] Copyright 2017, Wiley-VCH. Copyright 2019, American Chemical Society.

Other techniques: To determine with a high degree of accuracy the structure of complex core-shell composites, other techniques are usually required. TEM Tomography was rarely used so far regardless of its ability to confirm the 3D architecture probably due to the low stability of MOFs during the long beam exposure time required. Even though, Yang et al. reported recently the utilization of 3D tomography to localize encased Pt-Ni nanoparticles, leading to a reconstructed 3D morphology evidencing that Pt-Ni NPs are located inside ZIF-8 crystals in all three orthogonal slices (Figure 2A (e)).^[43] In addition, indirect characterization techniques can be used in order to verify the respective positions of core and shell. For instance, one of the main features of core-shell NPs@MOF is that active nanoparticles do not occupy the pore space of MOF, and thus do not affect too much its porosity as well as its pore size. To verify this, one typically uses N₂ adsorption porosimetry and checks the total sorption capacity and pore size distribution. However, this method is sometimes not relevant when the loading content is low and cannot be applicable when the NPs are deposited on the MOF surface or when dealing with MOF@MOF core-shells. In the case of the EGS method, the fabrication of the second layer of MOF on the surface of core MOF can lead to an expansion of the crystalline domain size. Therefore, SEM measurements together with the particle size estimation based on the PXRD Bragg peaks width might be combined to get information on the core-shell structure.

4. Core-shell composites for catalysis

Incorporating active “core objects” into a MOF shell is of particular interest for catalysis, due to the broad scope of available encapsulated species, including single and multiple components. It could sometimes lead to a synergistic catalytic effect due to the interaction between active compounds and inorganic nodes/organic ligand of the MOF.^[35, 58, 73, 74] Moreover, the tailorable/functionalizable porosity of MOF endows the designed composites with tunable sorption selectivity and stability, which are key factors for catalysis.^[59, 75, 76] In the following section, we will discuss the advances of core-shell MOF-based composites in selective, efficient energy-related catalytic reactions.

4.1 Core-shell Inorganic Nanoparticles (NPs)@MOFs for energy-related applications

4.1.1 CO₂ reduction

The heavy reliance on fossil fuels has led to a significant rise in atmospheric CO₂, which is generally considered as the culprit for global climate change.^[77] The conversion of CO₂ to valuable products, such as CO, CH₄, C₁ or C₂ oxygenated compounds is extremely attractive, but scientifically highly challenging due to the strength of the C=O double bond (806 kJ/mol), which is significantly higher than C-C (336 kJ/mol), C-H (411 kJ/mol), or C-O (327 kJ/mol) bonds.^[78] Accordingly, the catalytic reactivity of core-shell NPs@MOF towards CO₂ reduction was explored due to the possible synergistic effect between metal NPs with the pore functionality of the MOF.

Xu et al reported a series of multi-layered noble metal/ alloy nanoparticles encapsulated in Zn/ Co based-MOFs for CO₂ reduction.^[79, 80] As shown in Figure 9(A), monodispersed core-shell Au@Pd bimetallic nanoparticles (size=17 nm) were successfully incorporated in the center of a Co-MOF and Pt NPs were subsequently loaded on the outer surface of Au@Pd@1Co architecture to build Pt/Au@Pd@1Co composites (Figure 9(B-C)). The CO₂ reduction tests in Figure 9(D) suggested that 8-Pt/Au@Pd@1Co (4, 8, or 12 represent the volume of the Pt NPs solution) owned the best conversion among all the analogs due to their relatively high Pt NPs content, and an excellent selectivity in comparison with Au@Pd@1Co and 4-Pt/1Co. These results (Figure 9(F)) revealed that the loaded Pt NPs enhanced the conversion of CO₂, while Au@Pd NPs dramatically changed the proportion of CO to CH₄ in the products. The authors also found that the temperature had a positive impact on the CO₂ conversion and CO selectivity. When increasing the temperature from 300 to 400 °C (Fig 9(E)), the conversion of 4-Pt/Au@Pd@1Co increased from 4.38% to 15.6%, and the CO selectivity increased from 73.4% to 87.5%. This may be attributed to the opposite processes of CO generation (endothermic) and CH₄ generation (exothermic). The mechanism for the formation of CO was attributed to the redox properties of active metal centers ($\text{CO}_2 + \text{M}^{n+} \rightarrow \text{MO}_x + \text{CO}$, $\text{H}_2 + \text{MO}_x \rightarrow \text{M}^{n+} + \text{H}_2\text{O}$), while the MOF enabled an enhanced adsorption of CO₂ molecules near the catalyst. The bimetallic Au@Pd are indeed active for C=O bond hydrogenation and decomposition of oxygenated molecules while Pt NPs serves as additional active sites for conversion due to the limited pore volume of MOF and low content of Au@Pd. In contrast, the formate decomposition mechanism for the reverse Water-Gas Shift Reaction (WGSR indicates the reaction of carbon monoxide and water vapor to form carbon dioxide and hydrogen) is unlikely to occur due to the narrow pores of the host MOF, which may also contribute for the high selectivity towards CO production (tetrahedron CH₄ is larger than linear CO).^[80]

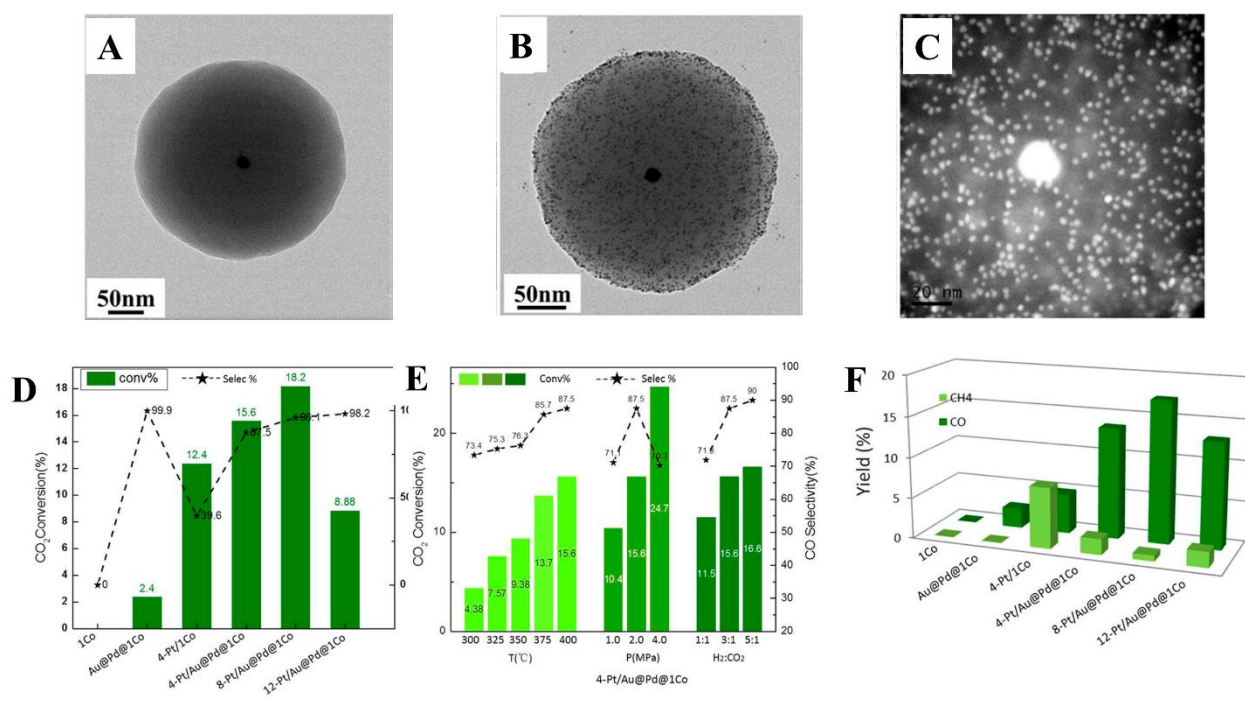


Figure 9. A) HRTEM images of Au@Pd@1Co. B) HRTEM images of Pt/Au@Pd@1Co. C) HADDF-STEM image of the detail of Pt/Au@Pd@1Co particle. D) CO₂ conversion and CO selectivity of the different catalysts for RWGS (reverse water-gas shift). E) CO₂ conversion and CO selectivity at different reaction conditions for RWGS. F) Yield of the different catalysts for RWGS. Reproduced with permission.^[80] Copyright 2018, ACS.

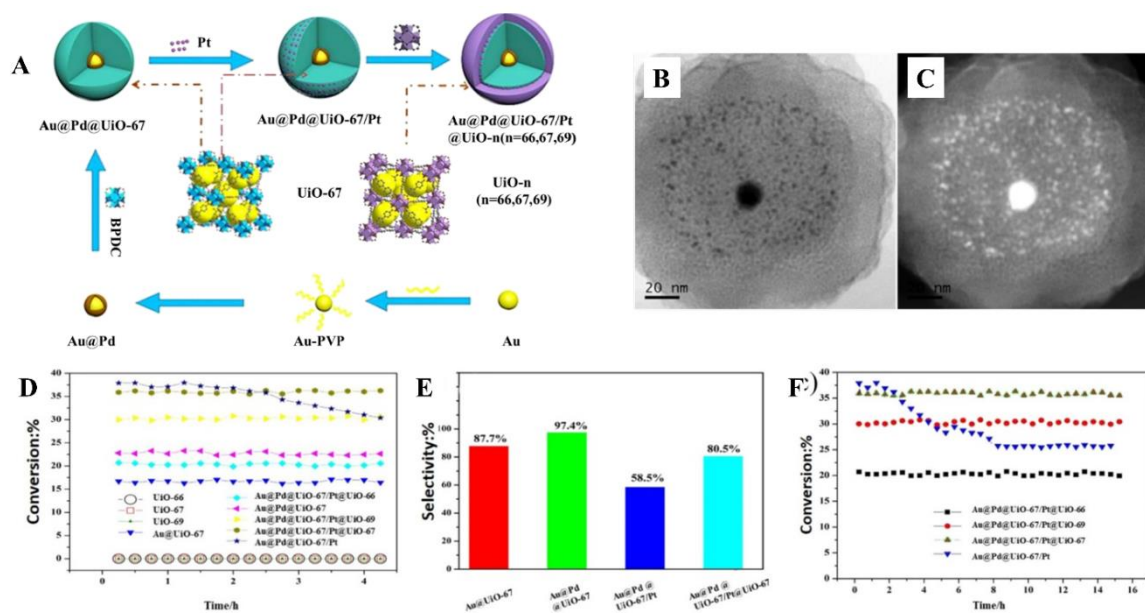


Figure 10. A) Synthetic route for sandwich Au@Pd@UiO-67/Pt@UiO-n and their nanocomposites. B-C) HAADF-STEM images of Au@Pd@UiO-67/Pt@UiO-67. CO₂ conversion and CO selectivity D) CO₂ conversion for the catalysts at 400 °C, E) CO selectivity for the catalysts at 400 °C, F) stability for the catalysts at 400 °C by a longevity test. Reproduced with permission.^[81] Copyright 2019, ACS.

Similarly, the authors recently reported other spherical sandwich core-shell structures Au@Pd@UiO-67/Pt@UiO-n (n=66, 67, 69) for efficient CO₂ conversion. The synthetic

schematic diagram for the sandwich core-shell structure is shown in Figure 10(A). The monodispersed Au@Pd alloy and well-localized Pt NPs were characterized by STEM (Figure 10(B-C)). The size of the encased Au@Pd NPs was 16.6 nm and the one of Pt NPs of 3.3 nm. The catalytic results in Figure 10(D-E) demonstrated that 1) even though Au@Pd@UiO-67/Pt (Pt on the surface of Au@Pd@UiO-67) exhibited an increased conversion, the selectivity for CO decreased due to the further hydrogenating of CO to form CH₄; 2) Au@Pd@UiO-67/Pt@UiO-66 showed the lowest conversion efficiency but highest selectivity in Au@Pd@UiO-67/Pt@UiO-*n* (*n* = 66, 67, 69), highlighting the impact of the porosity of the outer shell on the conversion and selectivity; 3) the thicker the outer shell is, the higher selectivity but a lower conversion was observed because the shell thickness slowed down the reactant and product diffusion. As seen in Figure 10(F), long-term catalytic tests suggested the superior stability of Au@Pd@UiO-67/Pt@UiO-*n* (*n* = 66, 67, 69) compared to Au@Pd@UiO-67/Pt due to the lack of outer MOF preventing the Pt NPs from migration and agglomeration in the second compound.^[81]

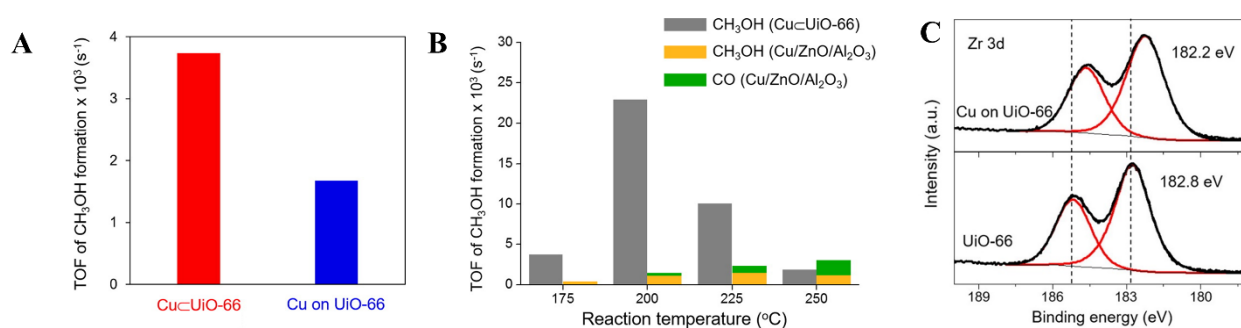


Figure 11. A) Initial turnover frequency (TOF) of methanol formation over Cu@UiO-66 and Cu on UiO-66. B) TOFs of product formation over Cu@UiO-66 catalyst and Cu/ZnO/Al₂O₃ catalyst at various reaction temperatures. C) XPS Zr 3d spectra of UiO-66 and Cu on UiO-66. Reproduced with permission.^[35] Copyright 2016, ACS.

Apart from the use of noble metal nanoparticles as active centers, non-noble nanoparticles driving CO₂ reduction catalysts are of strong interest due to their much lower cost and higher availability. Notably, Cu-based catalysts showed remarkable reactivity.^[82] Yaghi et al. synthesized 18 nm Cu nanocrystals encapsulated within or outside UiO-66 particles to give Cu@UiO-66 (core-shell structure) or Cu on UiO-66, (Figure 1B)), with 1 and 1.4 % of loaded according to ICP-AES analysis, respectively. A series of benchmark supports (UiO-66, MIL-101(Cr), ZIF-8, mesoporous silica MCF-26, ZrO₂, Al₂O₃) were also selected to encapsulate Cu. However, when performing catalytic evaluation (T=175°C, gas flow of CO₂/H₂ (1/3) at 10 bar), neither Cu@MIL-101(Cr) nor Cu@ZIF-8 showed reactivity towards methanol unlike the Zr-O and Zn-O based supports. By comparing the reactivity between Cu@UiO-66 and Cu on UiO-66, the authors found that the location of the Cu nanocrystals did not affect the catalytic activity (Figure 11(A)). Cu@UiO-66 showed however more than a 2-fold improved TOF value ($3.7 \times 10^{-3} \text{ s}^{-1}$ versus $1.7 \times 10^{-3} \text{ s}^{-1}$) and an enhanced stability in working conditions. The authors assumed that the higher number of contact points between Zr₆ oxo-clusters and the surface of the Cu NPs did lead to an increase of the reactivity. Notably, Figure 11(B) showed that despite the increased content of CO when elevating the temperature in the benchmark Cu/ZnO and Zn/Al₂O₃, no CO was generated in the Cu@UiO-66 catalyst whatever the temperature. The high selectivity is associated to the fact that the reverse water-gas shift reaction is endothermic, which means the CO product is favored at a higher temperature. XPS analysis was performed

to shed light on the high selectivity of Cu on UiO-66. The Zr 3d spectrum of catalyst (Fig. 11(C)), particularly the Zr 3d_{5/2} peak shift from 182.8 to 182.2 eV in comparison with pristine UiO-66, indicated that the Zr(IV) is reduced when in close interaction with Cu nanocrystals. This finding will hopefully promote the discovery of other more efficient and cheap Cu@MOFs catalysts.^[35]

Selective CO₂ reduction reaction has so far been tentatively explored via the use of core-shell composites. Nevertheless, from a practical application point of view, strong efforts are still required to develop more efficient core-shell catalysts in CO₂ reduction particularly through the use of cheaper core and shell materials. One can imagine enhancing the efficiency by either optimizing the host-guest interactions or the relative ratio of incorporated active sites, or by decreasing the size of the active nanoparticles, while a better understanding of the impact of the interaction between the MOF and the Cu nanoparticles is needed.

4.1.2 H₂ Production

H₂ is considered as the most promising new generation sustainable fuel due to the escalating depletion of traditional fossil fuel resources and the growing threat of environmental pollution. Series of emerging heterogeneous catalysts started to draw scientists' attention in recent years. However, the generation of H₂ from H₂O still faces massive challenges and MOFs-based composites (with active NPs) showed interesting properties for this reaction due to their possible combination with a large amount of guest active materials.

Nie et al. followed a template-sacrificing synthesis strategy to encapsulate a series of noble-metal sensitized semiconductors (ZnO@M, M= Au, Pt, Ag) in ZIF-67 for photoelectrochemical (PEC) water splitting.^[83] Since ZnO@Au@ZIF-67 showed remarkably improved photoconversion efficiency and photocurrent density, this example is discussed in detail. As displayed in Figure 12(A-B), a core-shell structure with 85 nm core and 18 nm shell was prepared. The catalyst was applied as photo-anode for PEC water splitting under UV-visible spectrum illumination. The current intensity of ZnO@Au@ZIF-67 was largely boosted (to 1.93 mA.cm⁻²) by using Au NPs in comparison with the pure ZnO (0.38 mA.cm⁻²), which can be attributed to the enhanced visible-light absorption offered by the Au SPR (Surface Plasmon Resonance) effect (Figure 12(C)). Subsequently, both the O₂-evolution rate and the photocurrent were monitored simultaneously to evaluate the efficiencies and stabilities of PEC water splitting. As shown in Figure 12(E), the ZnO@Au@ZIF-67 showed the highest average O₂-evolution rate among all catalysts (ZnO@ZIF-67, ZnO@Au@ZIF-8, ZnO@Au, and ZnO), which was 4.9 times higher than the one of ZnO. Notably, the PXRD patterns and SEM images confirmed the excellent stability of ZnO@Au@ZIF-67 in PEC water splitting after several catalytic cycles. As a proof-of-concept, the strategy was extended to other active nanoparticles, including Ag, Pt and both of them showed comparable reactivity towards water splitting. Even though the moderate catalytic efficiency is still far from real application in comparison to benchmarks (e.g., BiVO₄, perovskite), it can nevertheless give useful indications to further improve the overall efficiency of such composites.

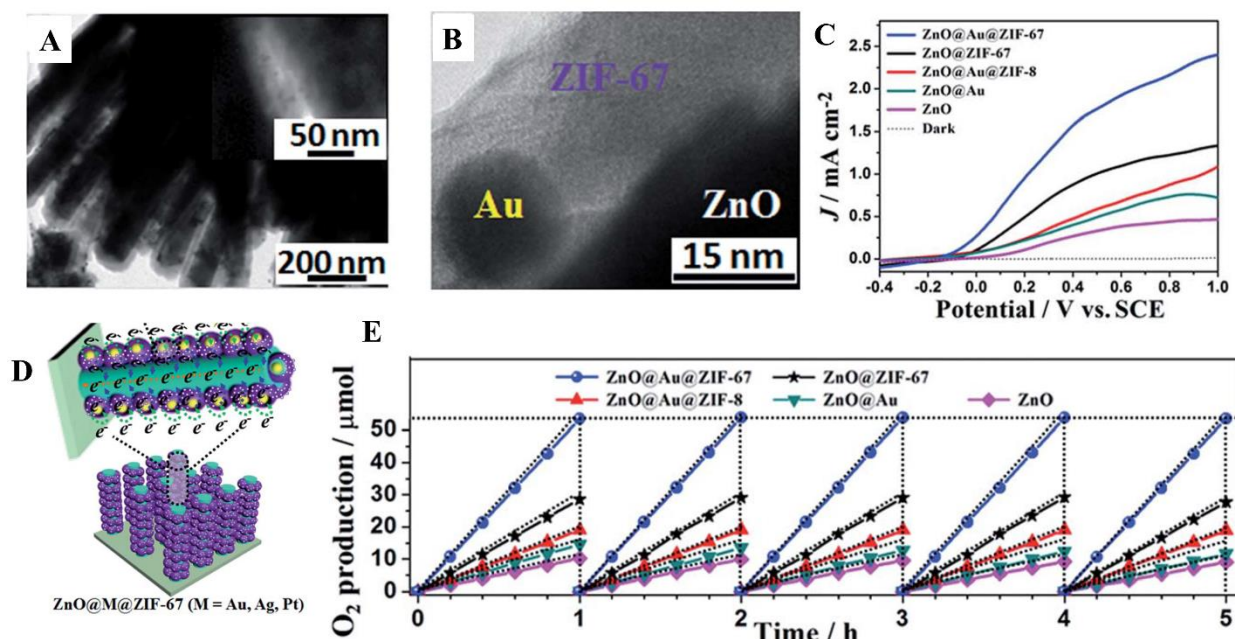


Figure 12. A) TEM image of ZnO@Au@ZIF-67. B) HRTEM image of ZnO@Au@ZIF-67. C) J - V curves for several compounds. D) Schematic illustration of the fabrication of the ZnO@M@ZIF-67 photo-anode for PEC water splitting. E) O₂-production performance under full-spectrum illumination ($\lambda > 200$ nm) over five cycles on ZnO@Au@ZIF-67. Reproduced with permission.^[83] Copyright 2017, Royal Society of Chemistry.

The water-gas shift (WGS) reaction ($\text{H}_2\text{O} + \text{CO} \rightarrow \text{H}_2 + \text{CO}_2$) is a promising way to produce H₂ that is however rate-limited by the activation of H₂O.^[84] To address this, Kitagawa et al. proposed the use of highly hydrophilic UiO-66 as support for Pt Nanocrystals (Pt NCs) with distinct spatial distribution, that is, Pt NCs on the surface of UiO-66 (Pt on UiO-66) and core-shell structure (Pt@UiO-66) (Figure 13(A-B)). The H₂O sorption isotherms (Figure 13C) confirmed the maintained porosity of the composites. As shown in Figure 13(D), the conversion of CO into CO₂ increased with temperature for both the composites and Pt deposited on ZrO₂. The Pt@UiO-66 owned the highest conversion at 340°C (10.8%), compared with that of Pt on UiO-66 (8.1%) and of Pt on ZrO₂ (6.4%). *In-situ* Infrared-mass spectra (IR-MS) measurements demonstrated that Pt@UiO-66 owns a better H₂O adsorption, therefore enhancing the formation of Pt-OH bonds compared to Pt on UiO-66 and Pt on ZrO₂. As additional evidence, when the thickness of the MOF shell decreased from 80 to 40 nm, the reactivity of Pt@UiO-66 exhibited higher WGS reaction activity than both Pt@UiO-66-80nm and Pt on UiO-66 (Figure 13(F)). Furthermore, after 5 cycles, the catalytic activity of Pt@UiO-66-40nm did not change, confirming the high stability of Pt@UiO-66-40nm.^[73] This example clearly revealed that hydrophilicity, tight host-guest interaction, as well as shell thickness all affect the reactivity of MOF-based core-shell WGS catalysts, which give insights for the development of catalysts with higher activity.

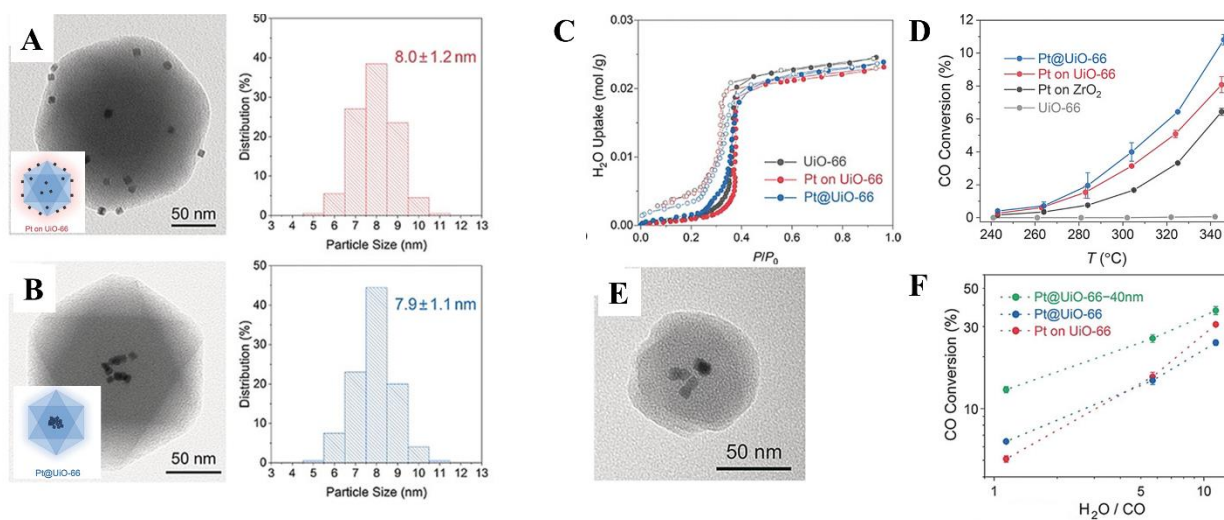


Figure 13. TEM images and particle size distribution (insert: schematic images) of A) Pt on UiO-66 and B) Pt@UiO-66. C) H₂O adsorption isotherms at 298K with adsorption represented by closed circles and desorption by open circles. (P/P_0 : relative pressure). D) Temperature dependence of CO conversion on WGS reaction. The flow rate was H₂O/ CO/ Ar = 11/ 10/ 50 sccm (standard cubic centimeters per minute), and the pressure was 0.65 MPa. E) TEM images of Pt@UiO-66-40nm. F) a) CO conversion versus H₂O/CO ratio for WGS reaction over Pt on UiO-66 (red), Pt@UiO-66 (blue), and Pt@UiO-66-40nm (green). Reaction conditions: 11.4, 57.0, or 114 sccm of H₂O, 10 sccm of CO, 50 sccm of Ar, 0.65 MPa and 320 °C. Reproduced with permission.^[73] Copyright 2019, Wiley-VCH.

Subsequently, the same group studied the influence of ligand functionalization on the H₂O activation. As illustrated in Figure 14 (A-D), the Pt NCs were encapsulated in several functionalized UiO-66 frameworks. The ligand functionalization significantly affected the catalytic activity of the WGS reaction (Pt@UiO-66-Me₂ > Pt@UiO-66-H > Pt@UiO-66-Br) (Figure 14 (E)). These differences in reactivity were attributed to the different chemical states of H₂O in UiO-66 as –Br functional groups could provide relatively hydrophilic pores with a higher affinity to H₂O while –Me₂ functional groups could lead to more hydrophobic pores with a lower affinity to H₂O. The chemical shifts of the adsorbed H₂O obtained by ¹H NMR (Figure 14(F) revealed that the adsorbed H₂O and Zr-OH are relatively mobile and exchangeable (3.5, 3.8, and 3.3 ppm for Pt@UiO-66-H, Pt@UiO-66-Br, and Pt@UiO-66-Me₂, respectively), while the signals from aromatic rings are not affected by water sorption. The highest H₂O chemical shift observed for Pt@UiO-66-Br indicates a decrease in electron density of proton compared to pristine Pt@UiO-66-H. Moreover, *In-situ* IR was applied to confirm the formation of OH species resulting from H₂O activation (Figure 14G). With Pt@UiO-66-Me₂, intense IR bands at 3734-3765 cm⁻¹ and 3533 cm⁻¹ could be attributed to the Pt-OH and Pt-COOH bands, the former one being an active intermediate in WGS reaction and the latter one corresponding to an intermediate species formed from Pt-CO and Pt-OH. This revealed that apart from the core-shell encapsulation, the direct MOF functionalization is a convenient strategy to improve the catalytic properties.^[75]

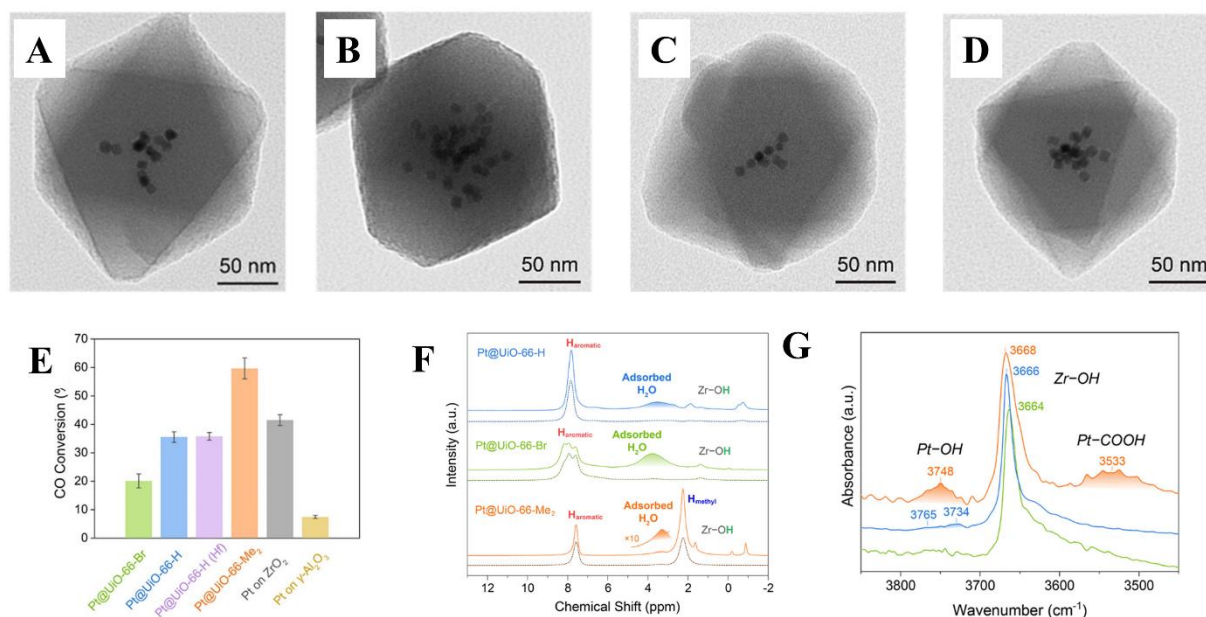


Figure 14. A) Pt@UiO-66-H. B) Pt@UiO-66-H(Hf). C) Pt@UiO-66-Br. and D) Pt@UiO-66-Me₂ nanoparticles observed by TEM; E) CO conversion in the WGS reaction at 340 °C. Reaction conditions: 114 sccm of H₂O, 10 sccm of CO, 50 sccm of Ar, and 0.65 MPa. F) ¹H ultrafast (70 kHz) MAS NMR spectra (top, solid lines) and the corresponding ¹H DQNMNMR spectra (bottom, dashed lines) of Pt@UiO-66 analogues at room temperature, where the peaks attributed to adsorbed H₂O are highlighted. The unlabeled peak around 6.5 ppm corresponds to the residual ligand. G) *In situ* IR spectra during WGS reaction at 300 °C for Pt@UiO-66-H (blue), Pt@UiO-66-Br (green), and Pt@UiO-66-Me₂ (orange) under a mixed gas flow (H₂O/CO/N₂ = 4.5/0.4/15.1 sccm). Reproduced with permission.^[75] Copyright 2019, ACS.

With the incorporated active nanoparticles and the photo-responsive components of the MOF, the NPs@MOFs often show an enhanced UV and even visible light absorption, making them promising for photocatalytic H₂ generation. The highly designable pore/channel space provides a wide range of possibilities in order to tune the transport distance of charge carriers to the MOF, which therefore may effectively suppress the fast recombination of electron-hole pairs that is one of the main parameters limiting the photocatalytic efficiency of semiconductors.^[85] For example, Jiang et al. reported that ca. 3nm Pt nanoparticles could be encapsulated inside (Pt@UiO-66-NH₂) or supported (Pt/UiO-66-NH₂) on UiO-66-NH₂ (Figure 15 (A-D)). Interestingly, the difference in the NPs spatial position led to a distinct catalytic reactivity. As displayed in Figure 15 (E-F), compared to the poor hydrogen production efficiency (1.72 μmol.g⁻¹.h⁻¹) of pristine UiO-66-NH₂, the Pt/UiO-66-NH₂ and Pt@UiO-66-NH₂ showed around 30 times (50.26 μmol.g⁻¹.h⁻¹) and 150 times (257.38 μmol.g⁻¹.h⁻¹) higher reactivity, respectively, suggesting that the charge separation between MOF and Pt plays an important role in catalytic efficiency. These results evidenced that, all other parameters being fixed, the NPs incorporated in UiO-66-NH₂ present a higher photo-catalytic efficiency than the one located at the MOF surface, probably due to the shorter distance between Pt NPs and the host MOF. In this study, the authors applied ultrafast transient absorption (TA) spectroscopy and transient luminescence spectroscopy to analyze the photo-excited carrier dynamics of nanocomposites systems (Figure 15G-H). The mean excited state and PL lifetimes (Figure 15H-I) decrease from UiO-66-NH₂ to Pt/UiO-66-NH₂, and Pt@UiO-66-NH₂, respectively, which can be attributed to the opening of an additional electron transfer channel from UiO-66-NH₂ to Pt NPs in Pt@UiO-

66-NH₂ due to the shortened electron-transport distance, in line with a suppression of the photo-excited charge recombination in these materials.^[74]

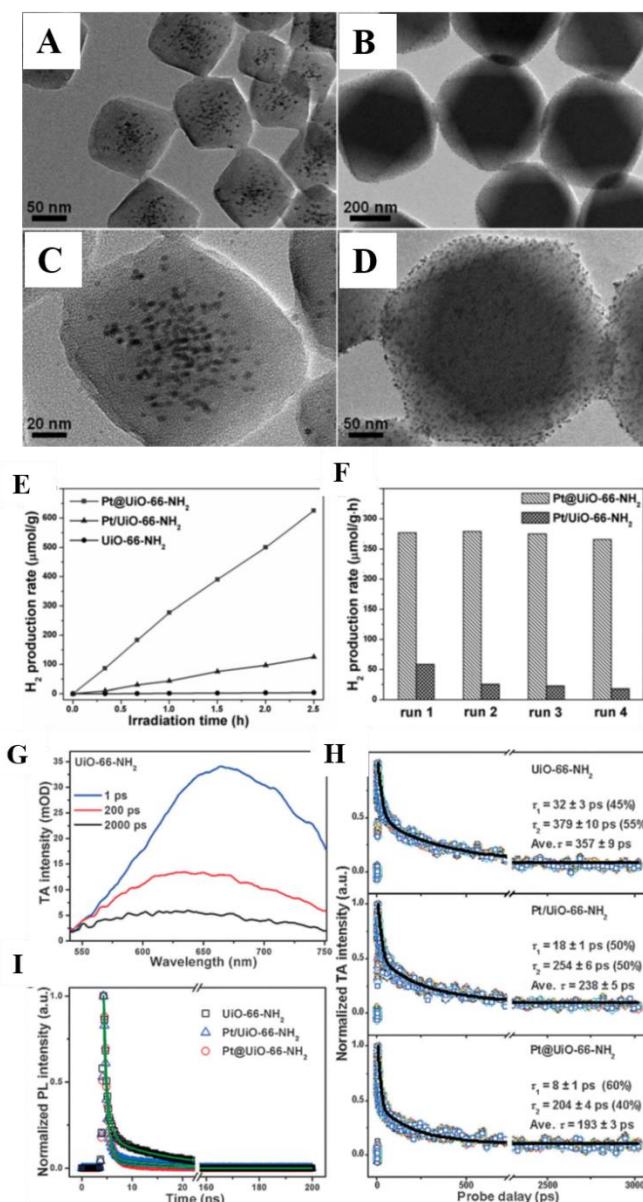


Figure 15. Typical TEM images of A), C) Pt@UiO-66-NH₂ and B), D) Pt/UiO-66-NH₂. E) Photocatalytic hydrogen-production rates of UiO-66-NH₂, Pt@UiO-66-NH₂ and Pt/UiO-66-NH₂. F) Recycling performance comparison between Pt@UiO-66-NH₂ and Pt/UiO-66-NH₂. G) TA spectra of UiO-66-NH₂ with TA signal given in mOD (OD: optical density). H) TA kinetics, and I) Time-resolved PL decay profiles for UiO-66-NH₂, Pt@UiO-66-NH₂, and Pt/UiO-66-NH₂, respectively ($\lambda_{\text{ex}}=400$ nm, $\lambda_{\text{em}}=455$ nm). Reproduced with permission.^[74] Copyright 2016, Wiley-VCH.

Other studies demonstrated that the preparation of core-shell structures could provide unprecedented chemical designability, unexpected catalytic reactivity, and open up more opportunities for energy-related applications.^[35, 73] It is doubtless that this domain will continue to draw intensive attention in a near future, particularly to design more efficient non-noble metal containing MOF catalysts with better photophysical properties, durability, visible light

absorption with the ultimate ambition to develop efficient noble metal free overall water splitting photocatalysts.

4.2 Core-shell Nanoparticles (NPs)@ MOFs structures for organic synthesis

MOFs comprising several types of active sites are of interest as multifunctional heterogeneous organic catalysts. Incorporating additional active species in MOF could not only endow a synergistic effect but also give rise to unprecedented high selectivity due to the contribution of the well-defined pore size and chemical nature of the MOF. Thus, in this section, we summarize the recent progresses in heterogeneous organic catalysis relying on core-shell MOF based composites.

The selective hydrogenation of the carbon-oxygen group from α , β -unsaturated alcohols is a widely studied but highly challenging catalytic reaction due to the thermodynamically favored carbon-carbon hydrogenation. Therefore, the selectivity/ conversion/ reusability obtained using pure noble metal Nanoparticles based catalysts (e.g., Pt NPs,^[86] Au NPs^[87]). To this end, Tang et al. showed that MOFs coupled with Pt NPs forming sandwich structures can be effective selectivity regulators for the hydrogenation of α , β -unsaturated aldehydes. The heterogeneous catalysts were developed by epitaxial growth of a mesoporous MIL-101(Cr, Fe) shell on the Pt NPs@MIL-101(Cr) core (Figure 16(A)). The shell thickness and the nature of the metal nodes were optimized and the compound MIL-101(Cr)@Pt@MIL-101(Fe)^{2.9} (2.9 refers to the shell thickness expressed in nm) was finally selected. Figure 16(B) shows the well-defined Pt NPs spatial distribution as well as the highly ordered structure of the compound, which presents an excellent selectivity along with almost full conversion for the transformation of cinnamaldehyde to cinnyl alcohol (Figure 16(E)). The reusability tests evidenced the unaltered high conversion, high selectivity and also maintained crystallinity during five successive catalytic cycles (Figure 16(C, D)). Density functional theory calculations indicated that the preferential interaction of the C=O bond of cinnamaldehyde with the Coordinatively Unsaturated Sites (CUS) of the MOF was thermodynamically favored and that at the same time, the formation of cinnyl alcohol was more energetically favored than other byproducts.^[58] This example evidences that high activity can be obtained using MOF-based core-shell particles. However, attention should be paid in developing highly selective catalysts using less expensive and/or toxic active centers.

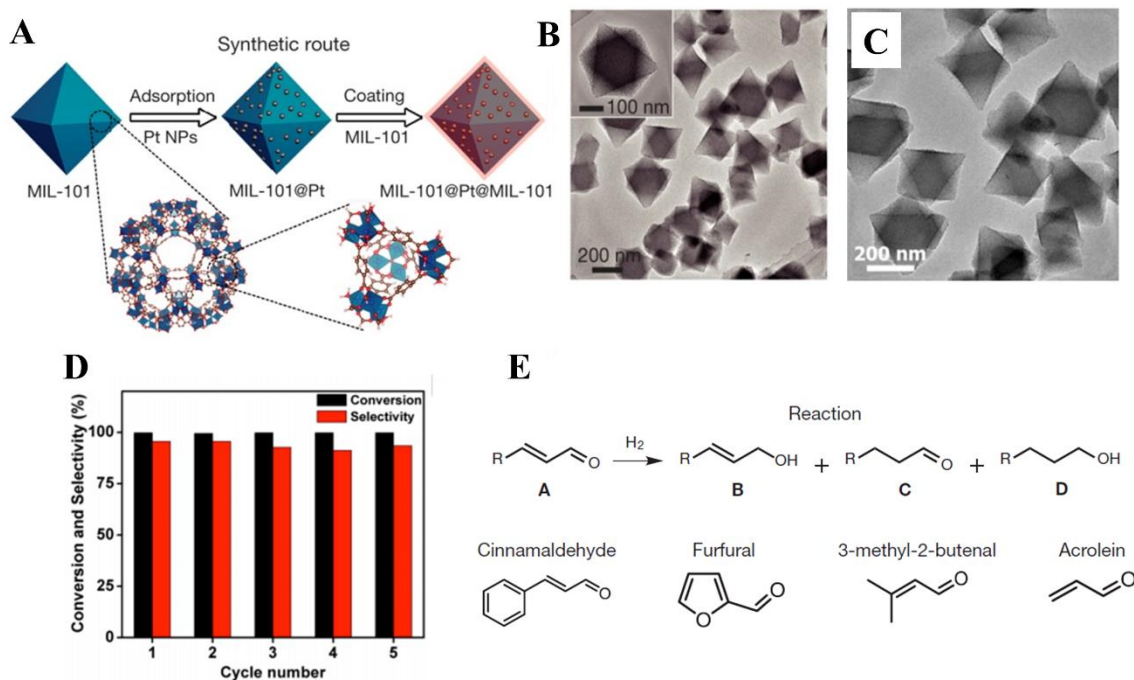


Figure 16. A) Illustration of the synthetic route to generate MIL-101@Pt@MIL-101, comprising Pt nanoparticles (NPs) sandwiched between a core and a shell of MIL-101. B) TEM image of MIL-101(Cr)@Pt@MIL-101(Fe)^{2.9} C) TEM image of MIL-101(Cr)@Pt@MIL-101(Fe)^{2.9} after cycling catalytic tests. D) Stability tests of MIL-101(Cr)@Pt@MIL-101(Fe)^{2.9} for hydrogenation of cinnamaldehyde to cinnyl alcohol. E) Schematic diagram of hydrogenation of α , β -unsaturated aldehydes. Reproduced with permission.^[58] Copyright 2016, Nature Publishing Group.

In another example, Huang et al. *in-situ* grew MOF-74 on preformed uniform bimetallic Pt-Ni nanowires (NWs) using the MOF's ligands to capture the dissolved Ni²⁺ during the dealloying process. TEM images and EDS mapping in Figure 17(A-B) evidenced that the Pt-Ni NWs were well encapsulated in a MOF-74 shell. The shell thickness could be readily adjusted by tuning the amount of Ni from the initial Pt-Ni NWs as well as the amount of introduced reactants during the MOF growth (Figure 17(C-D)). The hydrogenation of cinnamaldehyde (CAL) (Figure 17(E)) was used to investigate the reactivity and conversions close to 100% were reported for Pt-Ni_(1.6, 2.09, 2.20) NWs@Ni/Fe_x-MOF ($x=2, 3, 4, 5$ mg, corresponding to the mass of introduced FeCl₃·6H₂O) with different Ni and Fe contents.^[88]

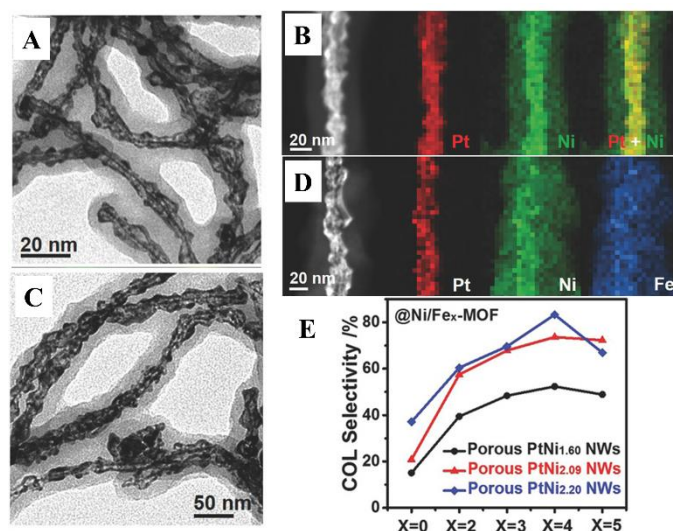


Figure 17. A) TEM image of PtNi_{2.20} NWs@Ni-MOF. B) HAADF-STEM image and EDS mappings of PtNi_{2.20} NWs@Ni-MOF. C) TEM image of PtNi_{2.20} NWs@Ni/Fe₄-MOF. D) HAADF-STEM image and EDS mappings of PtNi_{2.20} NWs@Ni/Fe₄-MOF. E) Catalytic performance of the different catalysts. Reproduced with permission.^[88] Copyright 2018, Wiley-VCH.

Similarly, MOF can serve as support not only to prevent active nanoparticles from aggregation but also to contribute to the enhancement of the selectivity and/or conversion for several organic reactions. Other recent progresses are listed in Table 2.

Even though the combination of active NPs and MOFs can be achieved using alternative methods such as impregnation, deposition-precipitation, surface grafting or chemical vapor deposition, these techniques can lead to leaching or aggregation of active NPs during the course of the heterogeneous catalytic reaction. Core-shell structures can solve this issue by immobilizing the NPs that are embedded within the MOF particles. Apart from the confinement effect of core-shell composites, remarkable synergetic effects leading to promising catalytic performance (e.g., Ref 29, 66, 67, 53) also lead to significant improvements in selectivity, conversion and sometimes both have been described. Indeed, the in-situ growth of shell on the surface of the core objects leads to a close packing between NPs and MOFs, which enables efficient energy/charge transfer between the MOF and the active NPs, similar to Schottky junctions observed in the metal-semiconductor materials.^[89] This interesting synergetic function has been widely observed in both gas and liquid based catalysis. (see Table 1.) Very recently, the strengthening of the interaction between active NPs and MOFs has been alternatively achieved by partial deligandation of metal/ MOF composites.^[90] This controlled deligandation of the MOF induces much more accessible Cr-O metal sites while relatively maintaining the MOF porosity. This enables a stronger interaction with the guest active NPs, achieving similar synergetic effects as the core-shell composites. This example evidenced that the strong interaction between NPs and MOFs is one of the key for overall catalytic performance, even though the authors prepared such composites based on metal NPs loaded in the pores of MOFs.

Table 2. Summary of the catalytic applications based on core-shell composites.

Core	Shell	Shell role	Synthesis method	Core size (nm)	Shell thickness (nm)	Content (wt %)	Applications	Refs
Pd NPs	UiO-66/ 67/ 68	Synergy*	EGS	3.5	35-50	0.59-0.66	Semihydrogenation	[59]
Pd NPs	UiO-66(Hf)	Synergy	CAAS	7.6	NA	5.2	Hydrogenation	[91]
Fe ₃ O ₄	Cu ₃ (BTC) ₂	Synergy	CAAS	230	60	NA	Aerobic oxidation	[92]
Copper hydroxysulfates	HKUST-1	Synergy	TSS	NA	NA	NA	Acetalization	[93]
Au@Pt Nanotubes	ZIFs	Synergy	CAAS	52	250	0.84-2.5	Semihydrogenation	[94]
Pt-Pd NCs	UiO-67	Synergy	CAAS	49-60	120	1.93 Pt 0.055 Pd	Reverse water-gas shift reaction	[95]
Au@Pd NPs	UiO-66	Synergy	CAAS	16-17	98	NA	CO ₂ hydrogenation	[34]

UiO-66	UiO-66-F ₄	Synergy	EGS	50-80	NA	NA	Dye adsorption Sulfide Oxidation	[96]
Pt NPs	UiO-66-NH ₂	Synergy	CAAS	3	NA	2.87	Photocatalytic Hydrogen- production	[74]
Pd NPs	ZIF-8	-	TSS	4.5	NA	1.1	Hydrogenation of olefins	[97]
Au@Pd, Pt NPs	UiO-67	Synergy	CAAS, EGS	16.6 Au@Pd NPs 3.3 Pt NPs	9.1-18.3	0.64 Pt, 0.36 Au, 0.074 Pd	Reverse water-gas shift reaction	[81]
Au@Pd, Pt NPs	1Co	Synergy	CAAS	17 Au@Pd	130	NA	CO ₂ to CO	[80]
Au ₂₅ NCs, ZIF-8	ZIF-67	Synergy	EGS	1.2	2-25	1	Carboxylation of phenylacetylene	[60]
ZnO@Au	ZIF-67	Synergy	CAAS	85	18	1.08	Photoelectrochemic al water splitting	[83]
Pt NPs	UiO-66-NH ₂	Synergy	CAAS	NA	NA	NA	H ₂ generation	[98]
CdS	ZIF-8	Synergy	CAAS	70	13.6-102	NA	Photocatalytic H ₂ generation	[99]

UiO-66	UiO-67-BPY	Synergy	EGS	150	50	NA	Knoevenagel condensation	[100]
ZIF-67	Co-MOF-74	Synergy	TSS	450-490	10-50	NA	Water oxidation reaction	[23]
Au@Pd	MOF-74	Immobilization*	CAAS	14	NA	0.095 Au 0.035 Pd	CO ₂ conversion	[79]
Au@Pd	Co ₂ (oba) ₄ (3-bpdh) ₂	Immobilization	CAAS	17	135	NA	CO ₂ conversion	[80]
PtNiNWs	Ni/Fe ₄ -MOF	Synergy	CAAS	20	NA	NA	Cinnamaldehyde hydrogenation	[88]
Pt NPs	Ni/ Zn-MOF	Immobilization	CAAS	5	NA	0.15	Cinnamaldehyde hydrogenation	[101]
UiO-66	UiO-67-BPY/ Ag	Synergy	EGS	150	50	0.73 Ag	CO ₂ fixation via carboxylation	[102]
Cu@ Pd	ZIF-8	Synergy	CAAS	61	600-1000	5.5 mol% Cu 0.1 mon% Pd	Selective Hydrogenation of different Alkynes	[103]
Fe ₃ O ₄ @PDA-Pd	Cu-BTC	Synergy	CAAS	530	10	2.27 Pd	Reduction of 4-nitrophenol	[104]

Pd NCs	MIL-101(Fe)	Synergy	CAAS	12.3	NA	59.5	Hydrogenation of α , β -unsaturated carbonyl compounds	[25]
Pt NPs	ZIF-8, ZIF-71	Immobilization	CAAS	4.3	NA	3	Hydrogenation of cinnamaldehyde	[105]
Pt-CeO ₂	UiO-66-NH ₂	Synergy	CAAS	50-180	8-30	1 Pt	Hydrogenation of Furfural	[106]
Rh-Ni	MOF-74(Ni)	Synergy	TSS	NA	2-50	NA	Hydrogenation of Alkyne	[107]
Pt NCs	UiO-66-H	Synergy	CAAS	7.9-8.0	NA	6.7	Water-gas shift reaction	[75]
	UiO-66-H(Hf)					4.6		
	UiO-66-Br					5.3		
	UiO-66-Me ₂					5.9		
Ni ₂ P/ Ni ₁₂ P ₅	UiO-66-NH ₂	Synergy	CAAS	10	NA	0.512 0.559	Photocatalytic H ₂ production	[108]
Pt NPs	UiO-66	Immobilization	CAAS	7.9	80	6.7	Water-gas shift reaction	[73]

Cu NCs	UiO-66	Immobilization	CAAS	18	NA	1.4	CO ₂ reduction	[35]
TS-SnO ₂ - HoMSs	MIL- 100(Fe)	Synergy	CAAS	>500	50	97	Lithium Storage	[27]

NA: Not Available

Table 3: Summary of the other applications based on core-shell composites.

Core	Shell	Shell function	Synthesis method	Core size (nm)	Shell thickness (nm)	Content (wt %)	Applications	Refs
Zns QDs	ZIF-67	Immobilization	CAAS	5	NA	NA	Cu ²⁺ detection	[109]
NaYF ₄ : Yb, Er	MIL-101- NH ₂ (Fe)	Immobilization	CAAS	40	NA	NA	Bio-imaging	[110]
Au Nanorod	MIL- 88(Fe)	Immobilization	CAAS	40	NA	NA	Bio-diagnosis	[111]
HKUST-1	MOF-5	Improved adsorption capacity	NA	100	NA	10	CH ₄ storage	[112]
MIL-101- NH ₂ (Al)	ZIF-8	Enrichment	CAAS	NA	NA	15%	Detection and removal of Cu ²⁺	[113]

Au NRs	Zr-Porphyrinic	Immobilization	CAAS	53.8*25.2	8.1-13.2	NA	Photodynamic/ Photothermal/ Chemotherapy of Tumor	[41]
Zn ₃ (BPD C) ₃ (BiPY)	Zn(BPDC)(BPP)	Improving selectivity	TSS	NA	NA	40.1	CO ₂ / N ₂ separation	[114]
ZIF-8	ZIF-67	Improved capacitance	CAAS	50-4000	170	NA	Supercapacitors	[115]
Au Nanostar	ZIF-8	Immobilization	CAAS	NA	NA	NA	Drug release	[116]

*: Synergy indicates the enhancement either in the selectivity or the reactivity. Immobilization indicates that the main role of MOF is to be a stabilizer, which is also the case for the other roles.

5. Core-shell composites for other applications

5.1 Gas separation

MOFs have been employed intensively for applications in separation mainly due to the high diversity of accessible pore size/shape, along with the possible presence of open metal sites and the possibility to functionalize the ligand.^[117] However, some MOFs suffer from drawbacks such as poor chemical/ physical stability, high capacity but low selectivity or the opposite. Therefore, it would be very useful to combine the functionalities of different MOFs simultaneously. Pioneering works reported by Kitagawa et al. and Rosi et al. on the design of MOF@MOF architectures evidenced the applicability of this strategy.^[8, 118]

Very recently, Shang et al. synthesized a core-shell MOF@MOF structure, in which a Zn-based MOF with 3D structure was chosen as the core (MOF-C) and another Zn-based 2D layered MOF as shell, grown through a competitive ligand exchange method (same concept as ITAS). The structure and morphology of the compound are shown in Figure 18(A-B). Synchrotron X-ray powder diffraction was used to quantify the formation of the core-shell composite as well as the structure conversion from MOF-C (core MOF) to MOF-S (shell MOF). The calculated content of shell could be tuned from 59.9 wt% to 90.2 wt% (Figure 18(C)) upon increase of the ligand exchange time. N₂ sorption isotherms (Figure 18(D)) confirmed the successful fabrication of the core-shell structure. Indeed, the pristine MOF-C showed a typical Type-I isotherm due to its inherent microporosity, while MOF-S and MOF-C@MOF-S both showed a nonporous structure, suggesting the well-formed core-shell structure. CO₂ and N₂ adsorption revealed that the adsorption capacities decreased with the exchange time, in agreement with an increase in the shell thickness that exhibit a much lower N₂ adsorption capacity (Figure 18(E)). Figure 18(F) showed the adsorption selectivity for CO₂ was higher for the core-shell structure than for both the core and the shell, evidencing the synergetic effect of the core-shell architecture.^[114]

In addition, Urban et al. prepared a core-shell structure with a larger pore MOF (UiO-66-NH₂, 0.7nm) as core and smaller pore one (ZIF-8) as shell. The material was used to prepare hybrid membranes presenting a remarkably improved CO₂ separation performance compared to a polysulfone membrane. In this work, the larger pore MOF acted as a molecular transport highway and the small pore MOF shell worked as a molecular filter. This example demonstrated, despite its enhanced complexity compared to single MOF mixed matrix membrane, that the development of MOF-based core-shell could provide new avenues for

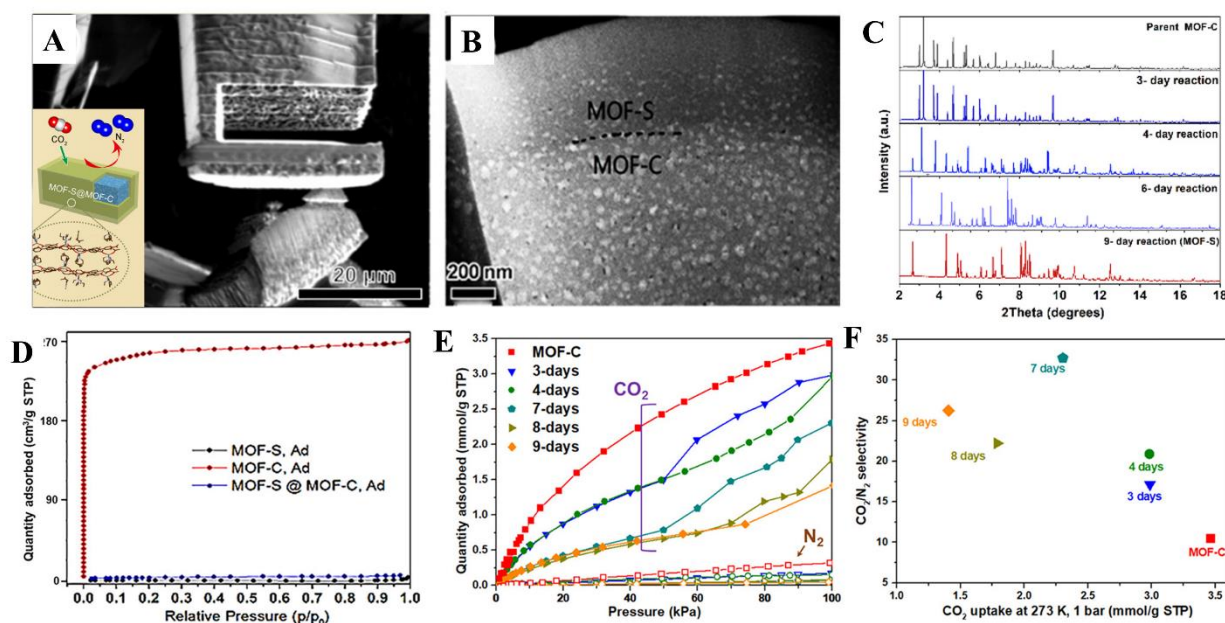


Figure 18. A) SEM image of MOF-C@MOF-S, B) TEM image of a cross section of MOF-C@MOF-S composite. C) Synchrotron X-ray powder diffraction patterns of pristine parent MOF-C and samples with 3-, 4-, 6- (MOF-C@MOF-S) and 9-days (MOF-S) exchange time. D) CO₂ and N₂ adsorption/desorption isotherms and (b) CO₂/N₂ selectivity and CO₂ uptakes (273 K, 1 bar) of MOF-C@MOF-S with 0- (MOF-C), 3-, 4-, 7-, 8- and 9-days (MOF-S) exchange (N₂, hollow symbols; CO₂, solid symbols). Reproduced with permission.^[114] Copyright 2019, ACS.

Due to the remaining challenges in synthesizing and characterizing well-defined core-shell MOF@MOF architectures, most works reported so far have been barely focused on the synthesis strategies.^[22, 61, 62] However, one can consider gas separation applications using MOF@MOF structures as a promising research domain.

5.2 Sensing

MOFs have been recognized as ideal porous materials for sensing applications, mainly for their tunable physicochemical properties (e.g., optical,^[3] magnetic,^[108] absorptive,^[109] electrical features^[120]). The incorporation of guest species within the MOFs endows wider possibilities for their applications in sensing, such as the enhancement of the optical properties, improvement of the stability of the wrapped species, boosted selectivity towards complex sensing systems, etc. However, core-shell architectures applied in sensing applications are still at their infancy with only few articles reported so far, in which anisotropic or low dimension nano-materials were used.

Fairen-Jimenez et al reported a room temperature strategy to encapsulate thermally sensitive PEG protected plasmonic Au Nanorods (AuNR@PEG-SH) in NU-901, a Zr-based MOF (Figure 19(A-B)). Selective surface-enhanced Raman spectroscopy (SERS) technique was applied to detect 4-mercaptobiphenylcarbonitrile (BPTCN) from varying analyte environments. As shown in Figure 19(C), when separately incubating AuNR@NU-901 in a mixed solution of PST (thiolated polystyrene), PST-BPTCN, BPTCN, and BPT (biphenyl-thiol), the Raman

spectra contains both the MOF peaks and the targeted analyte peaks in the case of BPTCN and MOF, revealing the selective adsorption of BPTCN due to the appropriate size of the molecular and strong affinity of thiols for AuNRs. In an aqueous environment, the characteristic modes at 1091, 1189, and 1588 cm^{-1} appear in the spectrum immediately after injection of BPTCN and saturated in 125 s (Figure 19(D)), further evidencing the effective adsorption, as well as the sensitive probing of BPTCN. This work demonstrated the potential of core-shell architecture for Raman-based sensing applications.^[65]

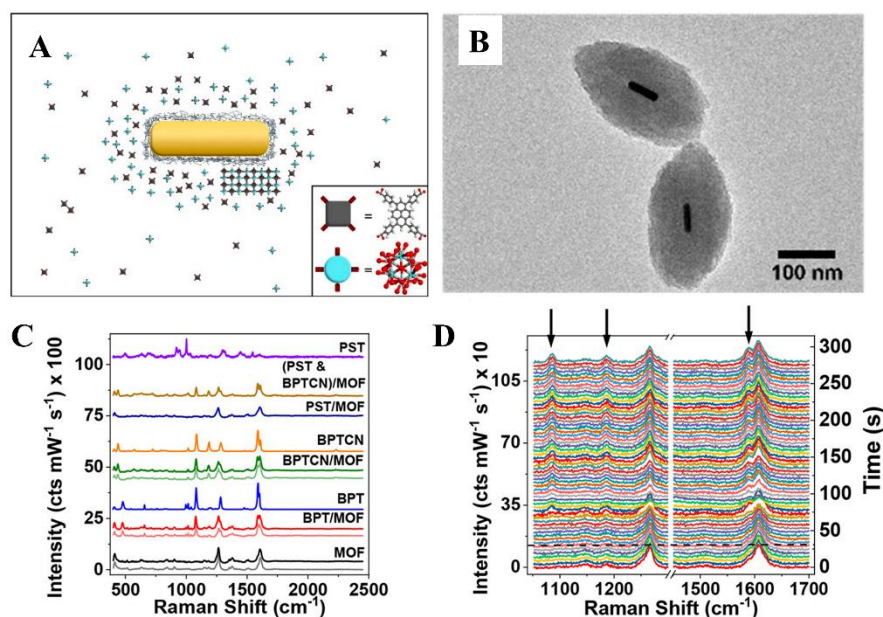


Figure 19. A) Schematic of PEG protected Au nanorods and MOF precursors. B) TEM image of AuNR@NU-901. C) SERS spectra of AuNR@NU-901 before and after incubation with various analytes. D) In situ SERS measurements of BPTCN infiltration in an aqueous environment containing AuNR@NU-901. Reproduced with permission.^[65] Copyright 2019, ACS.

Luminescence is considered as one of the most promising optical properties in sensing applications and several works have reported luminescent species@MOF structures using quantum dots,^[109, 121] or luminescent nanoclusters.^[69, 72] Due to the satisfying bio-compatibility of ultra-small nanoclusters, studies already demonstrated their potential in the bio-sensing field.^[122] However, the poor thermal stability of luminescent nanoclusters often hinders the development of this kind of composites as heating is usually needed for the synthesis of most of MOFs. ZIFs appear as an appealing platform for this application due to their chemical robustness and very mild synthesis conditions (e.g., room temperature^[123]). For example, Wang et al. reported the fabrication of a highly luminescent Au Nanoclusters@ZIF-8 composite. The effective encapsulation led to a significant luminescence enhancement in comparison to bare Au nanoclusters (Figure 20A). The obtained luminescent composites showed an interesting selective (Figure 20D, E) and sensitive (Figure 20B, C) detection of H_2S both in liquid and gas phase, although one could point out the risk, upon long term exposure, to disrupt these Zn MOFs through formation of ZnS or to dissolve them through acidification of the media upon formation of H_2SO_4 . This example was successfully extended to other luminescent nanoclusters (Ag) and other MOF support (ZIF-7)^[69], which demonstrate the potential of luminescent species@MOF

structures for sensing applications. However, we believe there are still a lot of works to perform in order to understand how the host-guest interaction influence the optical properties of the solids and to shape the compounds into sensing devices.

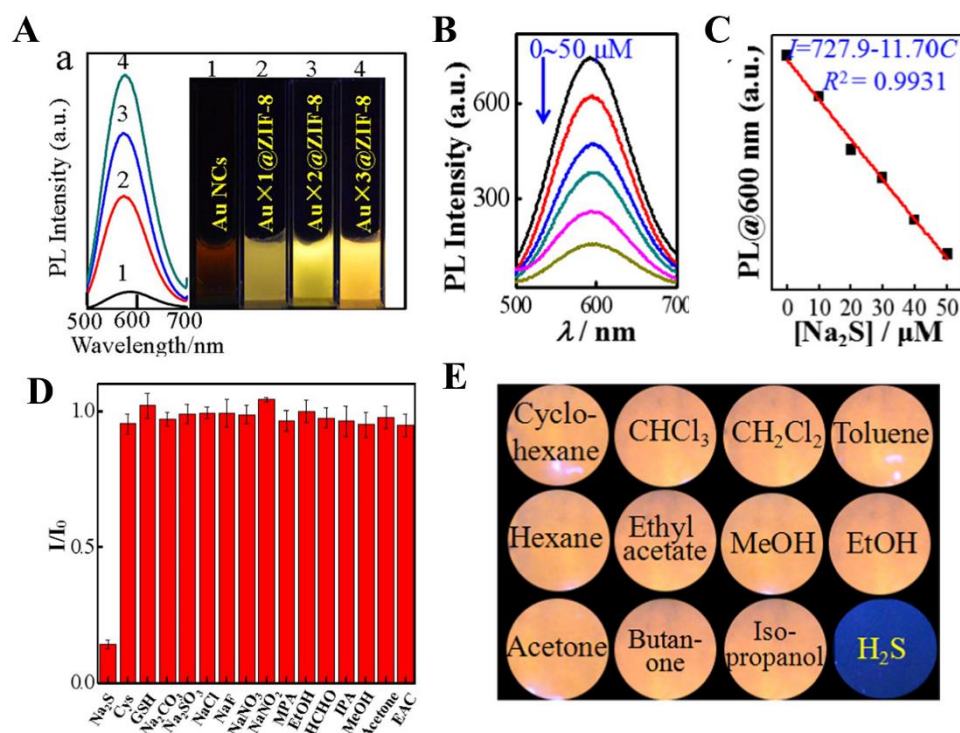


Figure 20. A) Photoluminescence spectra and corresponding photographs of AuNCs, AuNCs \times 1@ZIF-8, AuNCs \times 2@ZIF-8, and AuNCs \times 3@ZIF-8 under 365 nm light. Selective fluorescence sensing of H₂S. B) Photoluminescence intensity evolution, C) and corresponding linear plot of AuNCs \times 3@ZIF-8 in the presence of different concentrations of Na₂S. D) Selectivity tests in the presence of various interferents. E) Photographs of paper sensors exposing to different volatile organic compounds (VOCs) under 365 nm light. Reproduced with permission.^[69] Copyright 2018, ACS.

Other possible applications of MOF-based core-shell architectures are summarized in Table 3.

6. Conclusions and perspectives

In this review, we summarized the recent progresses in the field of MOF-based core-shell composites, mainly including encapsulated inorganic nanoparticles, metal oxides, and MOFs in MOFs. The almost infinite possible combinations, afforded by the massive library of MOFs shells and inorganic materials cores, make these compounds appealing for a wide range of applications. These core-shell composites can combine the advantages of the core materials (properties not present in the shell MOF) and the shell MOFs (designable aperture size/morphologies, physical/ chemical properties), which can ultimately lead to synergetic effects.

Despite the great achievements that have been accomplished to date in this domain, several challenges/ disadvantages still exist. For instance, the use of MOFs with a limited chemical stability as shell is a clear limitation to meet the requirements of practical applications, especially when exposed to water and/or corrosive species. Thus, one important challenge is to

further extend these core-shells architectures to more chemically/ thermally robust MOFs, which requires to venture into more complex chemistries that in some cases are not compatible with fragile active species. In addition, the synthetic parameters governing the core-shell formation often remain unclear, even though few reports identified the key roles of some of them (e.g. capping agent,^[44] anions,^[35] ratio of metal/ ligand,^[65] etc). Systematic explorations of synthetic parameters are still lacking, therefore limiting the successful fabrication of ideal core-shell structures. Indeed, the control of the shell thickness, of the spatial distribution / content of the core remains really challenging, while this is a key parameter in most cases. In addition, the incomplete covering of the core object is sometimes unavoidable, which can negatively influence the overall properties of the core-shell structures.

Moreover, the incorporation of small (more active) core materials in a shell framework requires the size of active NPs to be larger than the windows of the shell MOF to prevent from leaching, particularly when dealing with applications in liquid phase. Thus, such MOFs with narrow pores shall thus be non-porous to large molecules, which however as a potential drawback will limit the size of the reaction substrates. The removal of capping agent is also a key point for more efficient catalysis when performing capping agent-assisted synthesis. However, this step remains almost unexplored due to the difficulty in fully removing the capping agent while maintaining the framework integrity. In addition, it can be quite challenging to characterize the signature of the capping molecule overlapping usually with the signals from the ligand.

In terms of catalytic applications, the charge transfer behavior between metal nodes and NPs can be regarded as a remarkable feature that associated with synergetic effects. However, maximizing this interface interaction still requires many efforts. For example, the control of the quantity of guests is not as straightforward in the case of the ship-in-a-bottle synthetic strategy. In addition, the structural parameters allowing an efficient synergy between host and guest remain unclear and additional computational and experimental works are requested to build-up structure-activity correlations that may guide the design of solids with “improved” properties. Finally, the use of a one-pot synthesis strategy should be more developed, as it presents an obvious interest for upscaling the synthesis of such materials. Concomitantly, developing advanced characterization techniques to understand synergetic effects between active NPs and MOF in catalysis is still required in order to better understand the materials’ properties and to guide the design of next generation of solids.

We hope this progress report will shed some light on the current synthesis and characterization of MOF-based core-shell structures that are expanding fast for a broad range of potential applications. It also ambitions to demonstrate that, in order to meet the emerging and challenging demands in various practical applications, developing more facile synthesis strategies and more efficient core-shell composites is still highly desirable.

References

- [1] T. Devic, C. Serre, *Chem. Soc. Rev.* **2014**, 43, 6097; S. Yuan, L. Feng, K. C. Wang, J. D. Pang, M. Bosch, C. Lollar, Y. J. Sun, J. S. Qin, X. Y. Yang, P. Zhang, Q. Wang, L. F. Zou, Y. M. Zhang, L. L. Zhang, Y. Fang, J. L. Li, H. C. Zhou, *Adv. Mater.* **2018**, 30, 1704303; T. Kitao, Y. Y. Zhang, S. Kitagawa, B. Wang, T. Uemura, *Chem. Soc. Rev.* **2017**, 46, 3108.
- [2] M. J. Kalmutzki, N. Hanikel, O. M. Yaghi, *Sci. Adv.* **2018**, 4, eaat9180; H. X. Deng, C. J. Doonan, H. Furukawa, R. B. Ferreira, J. Towne, C. B. Knobler, B. Wang, O. M. Yaghi, *Science* **2010**, 327, 846.
- [3] W. P. Lustig, S. Mukherjee, N. D. Rudd, A. V. Desai, J. Li, S. K. Ghosh, *Chem. Soc. Rev.* **2017**, 46, 3242; H. L. Wang, Q. L. Zhu, R. Q. Zou, Q. Xu, *Chem* **2017**, 2, 52; J. M. Yu, L. H. Xie, J. R. Li, Y. G. Ma, J. M. Seminario, P. B. Balbuena, *Chem. Rev.* **2017**, 117, 9674; T. Simon-Yarza, A. Mielcarek, P. Couvreur, C. Serre, *Adv. Mater.* **2018**, 30, 1870281.
- [4] Q. H. Yang, Q. Xu, H. L. Jiang, *Chem. Soc. Rev.* **2017**, 46, 4774.
- [5] O. K. Farha, I. Eryazici, N. C. Jeong, B. G. Hauser, C. E. Wilmer, A. A. Sarjeant, R. Q. Snurr, S. T. Nguyen, A. O. Yazaydin, J. T. Hupp, *J. Am. Chem. Soc.* **2012**, 134, 15016.
- [6] A. Helal, Z. H. Yamani, K. E. Cordova, O. M. Yaghi, *Nat. Sci. Rev.* **2017**, 4, 296; C. D. Wu, M. Zhao, *Adv. Mater.* **2017**, 29; N. L. Strutt, D. Fairen-Jimenez, J. Iehl, M. B. Lalonde, R. Q. Snurr, O. K. Farha, J. T. Hupp, J. F. Stoddart, *J. Am. Chem. Soc.* **2012**, 134, 17436; T. M. McDonald, D. M. D'Alessandro, R. Krishna, J. R. Long, *Chem. Sci.* **2011**, 2, 2022.
- [7] A. Dhakshinamoorthy, H. Garcia, *Chem. Soc. Rev.* **2012**, 41, 5262; J. Guo, Y. Wan, Y. Zhu, M. Zhao, Z. Tang, *Nano Res.* **2020**, pp.1-16.
- [8] T. Li, J. E. Sullivan, N. L. Rosi, *J. Am. Chem. Soc.* **2013**, 135, 9984.
- [9] A. Aijaz, A. Karkamkar, Y. J. Choi, N. Tsumori, E. Ronnebro, T. Autrey, H. Shioyama, Q. Xu, *J. Am. Chem. Soc.* **2012**, 134, 13926; D. Feng, Z. Y. Gu, J. R. Li, H. L. Jiang, Z. Wei, H. C. Zhou, *Angew. Chem., Int. Ed. Engl.* **2012**, 51, 10307.
- [10] G. Lu, S. Li, Z. Guo, O. K. Farha, B. G. Hauser, X. Qi, Y. Wang, X. Wang, S. Han, X. Liu, J. S. DuChene, H. Zhang, Q. Zhang, X. Chen, J. Ma, S. C. Loo, W. D. Wei, Y. Yang, J. T. Hupp, F. Huo, *Nat. Chem.* **2012**, 4, 310.
- [11] X. Z. Lian, Y. Fang, E. Joseph, Q. Wang, J. L. Li, S. Banerjee, C. Lollar, X. Wang, H. C. Zhou, *Chem. Soc. Rev.* **2017**, 46, 3386; R. R. Salunkhe, J. Tang, N. Kobayashi, J. Kim, Y. Ide, S. Tominaka, J. H. Kim, Y. Yamauchi, *Chem. Sci.* **2016**, 7, 5704; R. Canioni, C. Roch-Marchal, F. Secheresse, P. Horcajada, C. Serre, M. Hardi-Dan, G. Ferey, J. M. Greneche, F. Lefebvre, J. S. Chang, Y. K. Hwang, O. Lebedev, S. Turner, G. Van Tendeloo, *J. Mat. Chem.* **2011**, 21, 1226; Y. X. Ye, W. G. Guo, L. H. Wan, Z. Y. Li, Z. J. Song, J. Chen, Z. J. Zhang, S. C. Xiang, B. L. Chen, *J. Am. Chem. Soc.* **2017**, 139, 15604; H. R. Moon, D. W. Lim, M. P. Suh, *Chem. Soc. Rev.* **2013**, 42, 1807.
- [12] A. Aijaz, A. Karkamkar, Y. J. Choi, N. Tsumori, E. Ronnebro, T. Autrey, H. Shioyama, Q. Xu, *J. Am. Chem. Soc.* **2012**, 134, 13926.
- [13] Q. Yang, W. Liu, B. Wang, W. Zhang, X. Zeng, C. Zhang, Y. Qin, X. Sun, T. Wu, J. Liu, F. Huo, J. Lu, *Nat. Commun.* **2017**, 8, 14429.
- [14] H. L. Liu, L. N. Chang, C. H. Bai, L. Y. Chen, R. Luque, Y. W. Li, *Angew. Chem., Int. Ed.* **2016**, 55, 5019.
- [15] T. Tsuruoka, H. Kawasaki, H. Nawafune, K. Akamatsu, *ACS Appl. Mater. Interfaces* **2011**, 3, 3788.
- [16] K. Sugikawa, Y. Furukawa, K. Sada, *Chem. Mater.* **2011**, 23, 3132.
- [17] K. Koh, A. G. Wong-Foy, A. J. Matzger, *Chem. Comm.* **2009**, 6162.
- [18] W. Xia, R. Q. Zou, L. An, D. G. Xia, S. J. Guo, *Energy Environ. Sci.* **2015**, 8, 568.
- [19] S. Ehrling, C. Kutzscher, P. Freund, P. Muller, I. Senkovska, S. Kaskel, *Micropor. Mesopor. Mater.* **2018**, 263, 268.
- [20] K. Shen, L. Zhang, X. Chen, L. Liu, D. Zhang, Y. Han, J. Chen, J. Long, R. Luque, Y. Li, B. *Chem. Sci.* **2018**, 359, 206.

- [21] S. J. Yang, J. Y. Choi, H. K. Chae, J. H. Cho, K. S. Nahm, C. R. Park, *Chem. Mater.* **2009**, 21, 1893.
- [22] F. Wang, S. F. He, H. L. Wang, S. W. Zhang, C. H. Wu, H. X. Huang, Y. Q. Pang, C. K. Tsung, T. Li, *Chem. Sci.* **2019**, 10, 7755.
- [23] C. Y. Guo, J. Guo, Y. H. Zhang, D. Wang, L. Zhang, Y. Guo, W. L. Ma, J. D. Wang, *CrystEngComm* **2018**, 20, 7659.
- [24] H. Kobayashi, Y. Mitsuka, H. Kitagawa, *Inorg. Chem.* **2016**, 55, 7301; Y. Liu, Z. Tang, *Adv. Mater.* **2013**, 25, 5819.
- [25] V. R. Bakuru, S. B. Kalidindi, *Chem. Eur. J.* **2017**, 23, 16456.
- [26] W. Liu, J. Huang, Q. Yang, S. Wang, X. Sun, W. Zhang, J. Liu, F. Huo, *Angew. Chem., Int. Ed. Engl.* **2017**, 56, 5512; X. Deng, S. Liang, X. Cai, S. Huang, Z. Cheng, Y. Shi, M. Pang, P. Ma, J. Lin, *Nano Lett.* **2019**, 19, 6772.
- [27] J. Zhang, J. Wan, J. Wang, H. Ren, R. Yu, L. Gu, Y. Liu, S. Feng, D. Wang, *Angew. Chem., Int. Ed. Engl.* **2019**, 58, 5266.
- [28] L. Wang, J. Wan, Y. Zhao, N. Yang, D. Wang, *J. Am. Chem. Soc.* **2019**, 141, 2238.
- [29] H. Xu, Z. X. Shi, Y. X. Tong, G. R. Li, *Adv. Mater.* **2018**, 30, e1705442.
- [30] F. Meng, S. Zhang, L. Ma, W. Zhang, M. Li, T. Wu, H. Li, T. Zhang, X. Lu, F. Huo, J. Lu, *Adv. Mater.* **2018**, 30, e1803263.
- [31] H. Sheng, D. Chen, N. Li, Q. Xu, H. Li, J. He, J. Lu, *Chem. Mater.* **2017**, 29, 5612.
- [32] X. Zhang, C. Y. Chuah, P. Dong, Y. H. Cha, T. H. Bae, M. K. Song, *ACS Appl. Mater. Interfaces* **2018**, 10, 43316; W. Zhang, Y. Liu, G. Lu, Y. Wang, S. Li, C. Cui, J. Wu, Z. Xu, D. Tian, W. Huang, J. S. DuCheneu, W. D. Wei, H. Chen, Y. Yang, F. Huo, *Adv. Mater.* **2015**, 27, 2923.
- [33] Z. Wang, N. Yang, D. Wang, *Chem. Sci.* **2020**, 11, 5359; Z. Zhao, J. Ding, R. Zhu, H. Pang, *J. Mater. Chem. A* **2019**, 7, 15519; T. Qiu, S. Gao, Z. Liang, D. G. Wang, H. Tabassum, R. Zhong, R. Zou, *Angew. Chem., Int. Ed. Engl.* **2020**.
- [34] Z. Zheng, H. Xu, Z. Xu, J. Ge, *Small* **2018**, 14, 1702812.
- [35] B. Rungtaweeworanit, J. Baek, J. R. Araujo, B. S. Archanjo, K. M. Choi, O. M. Yaghi, G. A. Somorjai, *Nano Lett.* **2016**, 16, 7645.
- [36] Y. Li, J. Jin, D. Wang, J. Lv, K. Hou, Y. Liu, C. Chen, Z. Tang, *Nano Res.* **2018**, 11, 3294.
- [37] Y. Gu, Y. N. Wu, L. Li, W. Chen, F. Li, S. Kitagawa, *Angew. Chem., Int. Ed. Engl.* **2017**, 56, 15658.
- [38] H. D. Mai, V. C. T. Le, T. M. T. Pham, J.-H. Ko, H. Yoo, *ChemNanoMat* **2017**, 3, 857.
- [39] Z. H. Zhou, M. Y. Li, J. Zhao, Z. G. Di, C. Z. Di, B. Liu, C. Zhang, C. H. Yan, L. L. Li, *Chem. Comm.* **2018**, 54, 8182-8185.
- [40] J. He, R. C. C. Yap, S. Yee Wong, Y. Zhang, Y. Hu, C. Chen, X. Zhang, J. Wang, X. Li, *CrystEngComm* **2016**, 18, 5262; J. J. Zhou, P. Wang, C. X. Wang, Y. T. Goh, Z. Fang, P. B. Messersmith, H. W. Duan, *Acs Nano* **2015**, 9, 6951.
- [41] J.-Y. Zeng, M.-K. Zhang, M.-Y. Peng, D. Gong, X.-Z. Zhang, *Adv. Funct. Mater.* **2018**, 28, 1705451.
- [42] N. R. Jana, L. Gearheart, C. J. Murphy, *Adv. Mater.* **2001**, 13, 1389; T. K. Sau, C. J. Murphy, *J. Am. Chem. Soc.* **2004**, 126, 8648.
- [43] S. Chen, X.-Y. Liu, J. Jin, M. Gao, C. Chen, Q. Kong, Z. Ji, G. A. Somorjai, O. M. Yaghi, P. Yang, *ACS Mater. Lett.* **2020**, 2, 685.
- [44] P. Hu, J. Zhuang, L. Y. Chou, H. K. Lee, X. Y. Ling, Y. C. Chuang, C. K. Tsung, *J. Am. Chem. Soc.* **2014**, 136, 10561.
- [45] J. Zhuang, L. Y. Chou, B. T. Sneed, Y. Cao, P. Hu, L. Feng, C. K. Tsung, *Small* **2015**, 11, 5551.
- [46] K. Wang, N. Li, X. Hai, F. Dang, *J. Mater. Chem. A* **2017**, 5, 20765.

- [47] C. Young, J. Wang, J. Kim, Y. Sugahara, J. Henzie, Y. Yamauchi, *Chem. Mater.* **2018**, 30, 3379.
- [48] W. W. Zhan, Q. Kuang, J. Z. Zhou, X. J. Kong, Z. X. Xie, L. S. Zheng, *J. Am. Chem. Soc.* **2013**, 135, 1926.
- [49] Y. Liu, W. Zhang, S. Li, C. Cui, J. Wu, H. Chen, F. Huo, *Chem. Mater.* **2014**, 26, 1119.
- [50] Y. Zhao, N. Kornienko, Z. Liu, C. Zhu, S. Asahina, T. R. Kuo, W. Bao, C. Xie, A. Hexemer, O. Terasaki, P. Yang, O. M. Yaghi, *J. Am. Chem. Soc.* **2015**, 137, 2199.
- [51] Y. Y. Fu, C. X. Yang, X. P. Yan, *Chemistry* **2013**, 19, 13484.
- [52] B. Li, J. G. Ma, P. Cheng, *Angew. Chem., Int. Edi.* **2018**, 57, 6834.
- [53] M. H. Hassan, D. Andreescu, S. Andreescu, *ACS Appl. Nano Mater.* **2020**, 3, 3288; X. Chen, Y. Zhang, Y. Zhao, S. Wang, L. Liu, W. Xu, Z. Guo, S. Wang, Y. Liu, J. Zhang, *Inorg. Chem.* **2019**, 58, 12433.
- [54] Y. Jiang, X. Zhang, X. Dai, Q. Sheng, H. Zhuo, J. Yong, Y. Wang, K. Yu, L. Yu, C. Luan, H. Wang, Y. Zhu, X. Duan, P. Che, *Chem. Mater.* **2017**, 29, 6336.
- [55] L. He, Y. Liu, J. Liu, Y. Xiong, J. Zheng, Y. Liu, Z. Tang, *Angew. Chem., Int. Ed. Engl.* **2013**, 52, 3741; L. Y. Chen, H. R. Chen, Y. W. Li, *Chem. Comm.* **2014**, 50, 14752.
- [56] D. Li, X. Dai, X. Zhang, H. Zhuo, Y. Jiang, Y.-B. Yu, P. Zhang, X. Huang, H. Wang, *J. Catal.* **2017**, 348, 276.
- [57] P. Á. Szilágyi, M. Lutz, J. Gascon, J. Juan-Alcañiz, J. van Esch, F. Kapteijn, H. Geerlings, B. Dam, R. van de Krol, *CrystEngComm* **2013**, 15; M. Pan, Y. X. Zhu, K. Wu, L. Chen, Y. J. Hou, S. Y. Yin, H. P. Wang, Y. N. Fan, C. Y. Su, *Angew. Chem., Int. Ed. Engl.* **2017**, 56, 14582.
- [58] M. Zhao, K. Yuan, Y. Wang, G. Li, J. Guo, L. Gu, W. Hu, H. Zhao, Z. Tang, *Nature* **2016**, 539, 76.
- [59] K. Choe, F. Zheng, H. Wang, Y. Yuan, W. Zhao, G. Xue, X. Qiu, M. Ri, X. Shi, Y. Wang, G. Li, Z. Tang, *Angew. Chem., Int. Ed. Engl.* **2020**, 59, 3650.
- [60] Y. Yun, H. Sheng, K. Bao, L. Xu, Y. Zhang, D. Astruc, M. Zhu, *J. Am. Chem. Soc.* **2020**, 142, 4126.
- [61] T. Y. Luo, C. Liu, X. Y. Gan, P. F. Muldoon, N. A. Diemler, J. E. Millstone, N. L. Rosi, *J. Am. Chem. Soc.* **2019**, 141, 2161.
- [62] G. Lee, S. Lee, S. Oh, D. Kim, M. Oh, *J. Am. Chem. Soc.* **2020**, 142, 3042.
- [63] O. Kwon, J. Y. Kim, S. Park, J. H. Lee, J. Ha, H. Park, H. R. Moon, J. Kim, *Nat. Commun.* **2019**, 10, 3620.
- [64] X. Yang, S. Yuan, L. Zou, H. Drake, Y. Zhang, J. Qin, A. Alsalmeh, H. C. Zhou, *Angew. Chem., Int. Ed. Engl.* **2018**, 57, 3927.
- [65] J. W. M. Osterrieth, D. Wright, H. Noh, C. W. Kung, D. Vulpe, A. Li, J. E. Park, R. P. Van Duyne, P. Z. Moghadam, J. J. Baumberg, O. K. Farha, D. Fairen-Jimenez, *J. Am. Chem. Soc.* **2019**, 141, 3893.
- [66] H. He, L. Li, Y. Liu, M. Kassymova, D. Li, L. Zhang, H.-L. Jiang, *Nano Res.* **2020**, 14, 444.
- [67] S. Dai, F. Nouar, S. Zhang, A. Tissot, C. Serre, *Angew. Chem., Int. Ed. Engl.* **2021**, 60, 4282-4288.
- [68] Z.-W. Zhao, X. Zhou, Y.-N. Liu, C.-C. Shen, C.-Z. Yuan, Y.-F. Jiang, S.-J. Zhao, L.-B. Ma, T.-Y. Cheang, A.-W. Xu, *Catal. Sci. Technol.* **2018**, 8, 3160.
- [69] Q. Gao, S. Xu, C. Guo, Y. Chen, L. Wang, *ACS Appl. Mater. Interfaces* **2018**, 10, 16059.
- [70] W. Zhang, Y. Wang, H. Zheng, R. Li, Y. Tang, B. Li, C. Zhu, L. You, M.-R. Gao, Z. Liu, S.-H. Yu, K. Zhou, *Acs Nano* **2020**, 14, 1971.
- [71] N. Wang, Q. Sun, J. Yu, *Adv. Mater.* **2019**, 31, e1803966.
- [72] Z. G. Wang, R. Chen, Y. Xiong, K. Cepe, J. Schneider, R. Zboril, C. S. Lee, A. L. Rogach, *Part. Part. Syst. Charact.* **2017**, 34.

- [73] N. Ogiwara, H. Kobayashi, P. Concepcion, F. Rey, H. Kitagawa, *Angew. Chem., Int. Edi.* **2019**, 58, 11731.
- [74] J. D. Xiao, Q. C. Shang, Y. J. Xiong, Q. Zhang, Y. Luo, S. H. Yu, H. L. Jiang, *Angew. Chem., Int. Edi.* **2016**, 55, 9389.
- [75] N. Ogiwara, H. Kobayashi, M. Inukai, Y. Nishiyama, P. Concepcion, F. Rey, H. Kitagawa, *Nano Lett.* **2020**, 20, 426.
- [76] K. M. Choi, K. Na, G. A. Somorjai, O. M. Yaghi, *J. Am. Chem. Soc.* **2015**, 137, 7810.
- [77] D. P. Schrag, *Science* **2007**, 315, 812.
- [78] J. H. Wu, Y. Huang, W. Ye, Y. G. Li, *Adv. Sci.* **2017**, 4, 1700194
- [79] Y. Han, H. Xu, Y. Su, Z.-l. Xu, K. Wang, W. Wang, *J. Catal.* **2019**, 370, 70.
- [80] X. Zhao, H. T. Xu, X. X. Wang, Z. Z. Zheng, Z. L. Xu, J. P. Ge, *ACS Appl. Mater. Interfaces* **2018**, 10, 15096.
- [81] H. Xu, X. Luo, J. Wang, Y. Su, X. Zhao, Y. Li, *ACS Appl. Mater. Interfaces* **2019**, 11, 20291.
- [82] R. Reske, H. Mistry, F. Behafarid, B. Roldan Cuenya, P. Strasser, *J. Am. Chem. Soc.* **2014**, 136, 6978; B. An, Z. Li, Y. Song, J. Zhang, L. Zeng, C. Wang, W. Lin, *Nat. Catal.* **2019**, 2, 709.
- [83] Y. Dou, J. Zhou, A. Zhou, J.-R. Li, Z. Nie, *J. Mater. Chem. A* **2017**, 5, 19491.
- [84] D. W. Flaherty, W. Y. Yu, Z. D. Pozun, G. Henkelman, C. B. Mullins, *J. Catal.* **2011**, 282, 278.
- [85] J. D. Xiao, H. L. Jiang, *Acc. Chem. Res.* **2019**, 52, 356; J. H. Qiu, X. G. Zhang, Y. Feng, X. F. Zhang, H. T. Wang, J. F. Yao, *Appl. Catal. B-Environ.* **2018**, 231, 317.
- [86] B. Wu, H. Huang, J. Yang, N. Zheng, G. Fu, *Angew. Chem., Int. Ed. Engl.* **2012**, 51, 3440.
- [87] Z. Tian, X. Xiang, L. Xie, F. Li, *Ind. Eng. Chem. Res.* **2012**, 52, 288.
- [88] N. Zhang, Q. Shao, P. Wang, X. Zhu, X. Huang, *Small* **2018**, 14, e1704318.
- [89] R. T. Tung, *Appl. Phys. Rev.* **2014**, 1, 54; Y. Liu, J. Guo, E. B. Zhu, L. Liao, S. J. Lee, M. N. Ding, I. Shakir, V. Gambin, Y. Huang, X. F. Duan, *Nature* **2018**, 557, 696.
- [90] N. Tsumori, L. Chen, Q. Wang, Q.-L. Zhu, M. Kitta, Q. Xu, *Chem.* **2018**, 4, 845.
- [91] V. R. Bakuru, B. Velaga, N. R. Peela, S. B. Kalidindi, *Chemistry* **2018**, 24, 15978.
- [92] J. Li, H. Gao, L. Tan, Y. Luan, M. Yang, *Eur. J. Inorg. Chem.* **2016**, 30, 4906.
- [93] H. Gao, Y. Luan, K. Chaikittikul, W. Dong, J. Li, X. Zhang, D. Jia, M. Yang, G. Wang, *ACS Appl. Mater. Interfaces* **2015**, 7, 4667.
- [94] J. Wang, H. Xu, C. Ao, X. Pan, X. Luo, S. Wei, Z. Li, L. Zhang, Z. L. Xu, Y. Li, *iScience* **2020**, 23, 101233.
- [95] H. Zhang, H. Xu, Y. Li, Y. Su, *Appl. Mater. Today* **2020**, 19, 100609.
- [96] F. Zhang, X. Hu, E. W. Roth, Y. Kim, S. T. Nguyen, *Chem. Mater.* **2020**, 32, 4292.
- [97] X. Li, Z. Zhang, W. Xiao, S. Deng, C. Chen, N. Zhang, *J. Mater. Chem. A* **2019**, 7, 14504.
- [98] Y. Wang, L. Ling, W. Zhang, K. Ding, Y. Yu, W. Duan, B. Liu, *ChemSusChem* **2018**, 11, 666.
- [99] M. Zeng, Z. Chai, X. Deng, Q. Li, S. Feng, J. Wang, D. Xu, *Nano Res.* **2016**, 9, 2729.
- [100] Y. Gong, Y. Yuan, C. Chen, P. Zhang, J. Wang, A. Khan, S. Zhuiykov, S. Chaemchuen, F. Verpoort, *J. Catal.* **2019**, 375, 371.
- [101] A. Zhou, Y. Dou, J. Zhou, J. R. Li, *ChemSusChem* **2020**, 13, 205.
- [102] Y. Gong, Y. Yuan, C. Chen, P. Zhang, J. Wang, S. Zhuiykov, S. Chaemchuen, F. Verpoort, *J. Catal.* **2019**, 371, 106.
- [103] L. Li, W. Yang, Q. Yang, Q. Guan, J. Lu, S.-H. Yu, H.-L. Jiang, *ACS Catal.* **2020**, 10, 7753.
- [104] R. Ma, P. Yang, Y. Ma, F. Bian, *ChemCatChem* **2018**, 10, 1446.

- [105] L. Chen, W. Zhan, H. Fang, Z. Cao, C. Yuan, Z. Xie, Q. Kuang, L. Zheng, *Chemistry* **2017**, 23, 11397.
- [106] Y. Long, S. Song, J. Li, L. Wu, Q. Wang, Y. Liu, R. Jin, H. Zhang, *ACS Catal.* **2018**, 8, 8506.
- [107] L. Chen, H. Li, W. Zhan, Z. Cao, J. Chen, Q. Jiang, Y. Jiang, Z. Xie, Q. Kuang, L. Zheng, *ACS Appl. Mater. Interfaces* **2016**, 8, 31059.
- [108] K. Sun, M. Liu, J. Pei, D. Li, C. Ding, K. Wu, H. L. Jiang, *Angew. Chem., Int. Ed.* **2020**, 59, 22749-22755.
- [109] F. Asadi, S. N. Azizi, M. J. Chaichi, *Mater. Sci. Eng. C* **2019**, 105, 110058.
- [110] Y. Li, J. Tang, L. He, Y. Liu, Y. Liu, C. Chen, Z. Tang, *Adv. Mater.* **2015**, 27, 4075-4080.
- [111] W. Shang, C. Zeng, Y. Du, H. Hui, X. Liang, C. Chi, K. Wang, Z. Wang, J. Tian, *Adv. Mater.* **2017** 2017, 29.
- [112] K. M. Choi, J. H. Park, J. K. Kang, *Chem. Mater.* **2015**, 27, 5088.
- [113] L. Zhang, J. Wang, X. Ren, W. Zhang, T. Zhang, X. Liu, T. Du, T. Li, J. Wang, *J. Mater. Chem. A* **2018**, 6, 21029.
- [114] Y. He, M. Sun, Q. Zhao, J. Shang, Y. Tian, P. Xiao, Q. Gu, L. Li, P. A. Webley, *ACS Appl. Mater. Interfaces* **2019**, 11, 30234.
- [115] J. Tang, R. R. Salunkhe, J. Liu, N. L. Torad, M. Imura, S. Furukawa, Y. Yamauchi, *J. Am. Chem. Soc.* **2015**, 137, 1572.
- [116] C. Carrillo-Carrion, R. Martinez, M. F. N. Poupard, B. Pelaz, E. Polo, A. Arenas-Vivo, A. Olgiati, P. Taboada, M. G. Soliman, U. Catalan, S. Fernandez-Castillejo, R. Sola, W. J. Parak, P. Horcajada, R. A. Alvarez-Puebla, P. del Pino, *Angew. Chem., Int. Ed.* **2019**, 58, 7078.
- [117] K. Adil, Y. Belmabkhout, R. S. Pillai, A. Cadiau, P. M. Bhatt, A. H. Assen, G. Maurin, M. Eddaoudi, *Chem. Soc. Rev.* **2017**, 46, 3402.
- [118] S. Furukawa, K. Hirai, K. Nakagawa, Y. Takashima, R. Matsuda, T. Tsuruoka, M. Kondo, R. Haruki, D. Tanaka, H. Sakamoto, S. Shimomura, O. Sakata, S. Kitagawa, *Angew. Chem., Int. Ed. Engl.* **2009**, 48, 1766.
- [119] Z. Song, F. Qiu, E. W. Zaia, Z. Wang, M. Kunz, J. Guo, M. Brady, B. Mi, J. J. Urban, *Nano Lett.* **2017**, 17, 6752.
- [120] M. G. Campbell, D. Sheberla, S. F. Liu, T. M. Swager, M. Dinca, *Angew. Chem., Int. Ed.* **2015**, 54, 4349.
- [121] K. Wang, N. Li, J. Zhang, Z. Zhang, F. Dang, *Biosens. Bioelectron.* **2017**, 87, 339.
- [122] F. Cao, E. Ju, C. Liu, W. Li, Y. Zhang, K. Dong, Z. Liu, J. Ren, X. Qu, *Nanoscale* **2017**, 9, 4128.
- [123] J. Cravillon, R. Nayuk, S. Springer, A. Feldhoff, K. Huber, M. Wiebcke, *Chem. Mater.* **2011**, 23, 2130; Y. C. Pan, Y. Y. Liu, G. F. Zeng, L. Zhao, Z. P. Lai, *Chem. Comm.* **2011**, 47, 2071.

Chapter 2

This chapter is adapted to the following publication:

Monodispersed MOF-808 nanocrystals synthesized via scalable room-temperature approach for efficient heterogeneous peptide bond hydrolysis

Chem. Mater. **2021**, 33, 17, 7057–7066

Shan Dai et al.

Table of Contents

Contributions to this research.....	89
Article	90
1. Introduction	90
2. Results and discussion.....	92
3. Conclusion.....	101
References	102
Supporting information	105

Contributions to this research

In this project, I conducted the literature survey and the experimental attempts at the beginning of my PhD. I carefully explored the synthetic parameters of the room temperature synthesis of MOF-808 to improve both the quality and the yield of this benchmark MOF synthesis. In a second step, I tried to controllably prepare nano-MOF-808, which was not reported in the literature. I characterized the synthesized materials by using many different techniques, such as PXRD, TGA, FT-IR and NMR spectroscopies, SEM-EDX, N₂ sorption isotherms, *in-situ* X-ray diffraction, and DLS. Dr. Gilles Patriarche performed the HRTEM measurements. I have performed all the data analysis and discussed the results with my supervisors and colleagues. The peptide hydrolysis tests were performed by Mrs Charlotte Simms and Prof. Tatjana N. Parac-Vogt, Katholieke Universiteit Leuven, Belgium. During the collaboration, I frequently discussed with Charlotte. I did the post-catalysis stability check. Finally, I plotted the figures and wrote the first manuscript draft with the help of Charlotte.

Monodispersed MOF-808 nanocrystals synthesized via scalable room-temperature approach for efficient heterogeneous peptide bond hydrolysis

Abstract:

Zr(IV)-based metal-organic frameworks (MOFs) such as the Zr(IV) trimesate MOF-808 are promising materials for catalytic applications. In this work, we report an aqueous solution-based room temperature strategy to produce well-defined monodispersed MOF-808 nanocrystals down to 35 nm with a high space-time yield, up to 2516 g/ m³/ day, and an excellent crystallinity and porosity. The resulting nanocrystals show remarkable colloidal dispersion during one day in a wide range of nanoparticles concentrations. As a result, 35 nm MOF-808 colloidal-level nanocrystals exhibit the highest rate of selective peptide bond and protein hydrolysis among reported Zr(IV)-based MOFs. This result may open new opportunities for highly efficient peptide or protein hydrolysis using scalable nano-catalyst.

1. Introduction

In the past decades, nanotechnology has generated interest in many fields, including bio-applications,¹ sensing² and catalysis.³ Metal-Organic Frameworks (MOFs) are ordered hybrid porous materials that are promising for a wide scope of potential applications,⁴⁻⁷ including new properties upon downsizing.⁸⁻¹⁰ Nano-MOFs are particularly appealing in catalysis for their highly tunable porosity and reactivity (presence of acid/basic sites, redox active cations...) that can even sometimes surpass previously studied nanomaterials.¹¹ However, formulation of MOFs as high quality nanomaterials has been relatively underdeveloped despite a few well-developed strategies (e.g., microwave,¹² modulating chemical,¹³ spray-drying¹⁴). Often, the produced nano-MOFs are lacking in uniformity, crystallinity/porosity and even more frequently, are obtained without size control.^{15,16} Thus, the development of new high quality MOF nanomaterials with controllable size may open some new perspectives for catalysis. For example, one emerging application for MOFs is their potential use as artificial nanozymes for middle down proteomics. For accurate protein fragment identification via mass spectrometry, proteins require partial breakdown into smaller fragments, which is achieved through hydrolysis of the highly stable peptide bond (t_{1/2} ~ 400 years).¹⁷ It has been shown that peptide bond hydrolysis can be catalyzed by some metal salts that

can however be prone to hydro-gel formation when used in physiological conditions.¹⁸⁻²² This problem can be overcome through incorporation of the active metal salts into soluble complexes or MOF materials. A few MOFs have already been proven to be active towards hydrolysis of peptide bonds in a range of dipeptides and proteins.²³⁻²⁵ In addition, they are more cost effective than traditional enzymatic methods due to their stability and reusability. Therefore, nanoMOFs are highly promising for the development of extremely efficient catalysts to produce peptides suitable for middle down proteomics.

Zr(IV)-carboxylate based MOFs are known as a subclass of MOFs that usually provide high chemical robustness.²⁶ A prominent example, UiO-66 (University of Oslo), was first reported in 2008 by Lillerud and co-workers and later studied for many potential applications.²⁷⁻²⁹ MOF-808 is another benchmark solid that is promising for catalytic applications, where the trimesate linker is used to bridge Zr₆ oxoclusters with a molar-ratio of 2:1 to give a cubic structure with potentially unsaturated coordination sites, high BET surface area (2060 m²/g) and a large pore size (18.4 Å).³⁰⁻³² Synthesizing Zr(IV)-based MOFs mostly relies on solvothermal strategies using toxic solvents (e.g. DMF), which is not an environmentally-friendly method and is not suitable for some applications such as the synthesis of host-guest architectures using the bottle-around-ship approach.^{33,34} Nonetheless, a few pioneering works have reported the room temperature (RT) synthesis of Zr(IV)-carboxylate based MOFs but most of these attempts were dedicated to 12-connected (each metal cluster coordinated to 12 organic linkers) UiO-type MOFs and the use of DMF was often inevitable.³⁵⁻⁴¹ Considering the appealing properties of MOF-808 and its use in several well-documented advanced applications,³¹ developing an approach to produce MOF-808 nanocrystals at room temperature using environmentally friendly conditions appears really promising.

Herein, we report a two-step, room temperature approach for the synthesis of MOF-808 in environmentally friendly conditions. The MOF nucleation-growth kinetics was investigated by in-situ powder X-ray diffraction (PXRD), which facilitated the understanding of the MOF synthesis. Tuning the synthesis conditions allowed us to obtain monodisperse MOF crystals from sub-micron scale (850 nm) down to the nanoscale (35 nm) via a concentration-induced method, which simultaneously enabled a space-time yield (STY) reaching 2516 kg/m³/day for the smallest nano-MOF-808. To the best of our knowledge, this is the first study tuning the crystal size of MOF-808 with such a high yield at room temperature. Finally, we demonstrated not only the high long-term colloidal stability of the synthesized nano-MOF-808 in a large concentration range but also the effect of particle's size on the efficiency of the highly selective peptide bond hydrolysis in a Hen Egg White Lysozyme (HEWL) protein by MOF-808. Notably, the remarkable catalytic efficiency of nano-MOF-808 allows us to obtain protein fragments of suitable size, which are in the range for the analysis in the emerging middle-down proteomic applications.

2. Results and discussion

In the MOF-808 framework, Zr_6 -nodes are at the vertices and trimesate linkers at the faces of a tetrahedral cage with internal pore size of 4.8 Å. Ten contiguous tetrahedral cages are assembled to form a large adamantane cage with an inner diameter of 18.4 Å (**Figure 1a**) assembled in a *spn* topology. The room temperature synthesis of MOF-808 was performed using preformed octahedral Zr_6 oxoclusters, which is the most common SBU (secondary building unit) in the family of Zr(IV)-carboxylate based MOFs. The synthesis of the Zr_6 oxoclusters was carried out by using a scalable reflux method in a mixture of isopropyl alcohol and acetic acid at 100 °C during 1 h. In order to confirm the composition of the obtained species, ESI-MS (electrospray ionization mass spectroscopy) was applied. As shown in Figure S3, the spectrum pattern observed from solution evidenced the presence of Zr_6 oxoclusters, with an average formula of $Zr_6O_4(OH)_4(C_2H_3O_2)_8(H_2O)_2Cl_3$ that is consistent with the atomic ratio (67% /33%) between Zr/Cl obtained from EDX (Energy-dispersive X-ray spectroscopy, see Figure S1). The efficient preparation of Zr_6 oxoclusters was performed with a high space-time yield (~ 5340 kg/ m³/ day) compatible with up-scaled synthesis (>100 g). From a lab-scale point of view, we demonstrated (Figure S2) that these Zr_6 acetate oxoclusters can be synthesized either on a small or large scale (100 g) without any drop in yield and quality. This new environmentally friendly preparation of Zr_6 oxoclusters with high STY surpassed the previously reported ones that were either performed in toxic solvents or present limited scalability.^{36, 40} MOF-808 synthesis was then performed by simply mixing Zr_6 oxoclusters with formic acid, water and BTC (trimesic acid) under stirring at 600 rpm. The alternative use of acetic acid led to completely clear solution without any product after 7 days at room temperature and therefore, formic acid was used for all the synthesis in this work. After 18 h of stirring, the appearance of a white slurry indicated the formation of MOF-808-RT (RT: Room Temperature). The synthesis yield was calculated based on the amount of ligand, reaching almost 100 %. After washing with water and ethanol once respectively, powder X-ray diffraction (PXRD) (**Figure 1b**) demonstrated the successful synthesis of highly crystalline MOF-808 by comparison to the simulated diffraction pattern. Taking into account the ease of the washing step, this water-based green synthesis has a great advantage in comparison to the DMF-based one, where 10 days are needed to fully activate the MOF.^{30, 42}

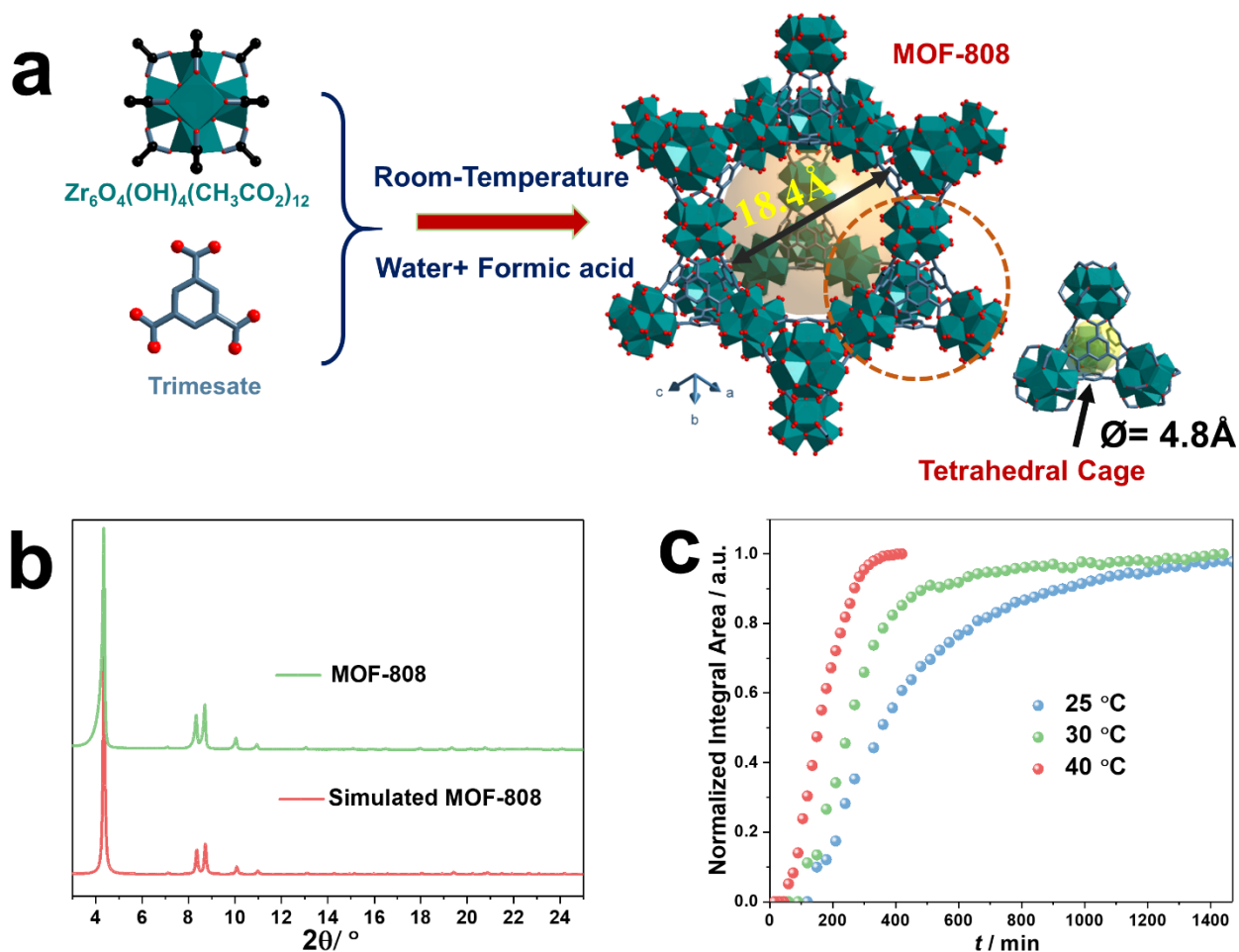


Figure 1. (a) Structures of $Zr_6O_4(OH)_4(CH_3CO_2)_{12}$ nodes, trimesate linker, and the MOF-808 (tetrahedral and adamantane-shaped cages); (b) PXRD ($\lambda_{Cu} = 1.5406 \text{ \AA}$) pattern of MOF-808 and the corresponding simulated PXRD pattern; (c) Normalized integral intensities of (3 1 1) Bragg reflection as a function of time (t) for different temperatures.

MOF-808-RT displayed a typical N_2 sorption isotherm at 77 K (Figure S4) with a high N_2 adsorption capacity of $512 \text{ cm}^3/\text{g}$ along with a high Brunauer-Emmett-Teller (BET) surface area ($2090 \pm 17 \text{ m}^2/\text{g}$), which matches very well with the reported value ($2060 \text{ m}^2/\text{g}$).³⁰ The pore size of MOF-808-DMF, which was calculated using density functional theory (DFT) on a sample prepared using the reported synthesis in DMF, showed two types of apertures at ca. 6.5 \AA and 15.5 \AA , corresponding to the windows of the tetrahedral and adamantane-shaped cages respectively (Figure S5). In the case of MOF-808-RT, the peak at 6.5 \AA was not observed, whereas the large pore shifted to 18.6 \AA and an additional new peak at 12.5 \AA was detected, suggesting very likely the presence of low temperature-induced defects (LTID).⁴¹ Infrared spectra (IR) (Figure S6) evidenced the absence of a C=O stretching band at around 1700 cm^{-1} -corresponding to uncoordinated COOH groups- in the washed MOF-808-RT solid, suggesting that the compound does not present missing nodes. Thermogravimetric analysis (TGA) (Figure S7) proved that each Zr_6 node of MOF-808-RT is connected to 1.82 trimesate ligands, compared to 2 for the defectless

structure, suggesting that 9% of linkers are missing, which might explain the slightly increased pore size compared to the ideal structure.

In order to shed light on the crystallization process, we performed in-situ diffraction measurements using a laboratory X-ray powder diffractometer in order to get a quantitative insight into the nucleation kinetics (e.g., activation energy, reaction rate).^{43, 44} The reaction kinetics has been studied at 25 °C, 30 °C and 40 °C, respectively. Notably, such temperature-dependent in-situ kinetic studies were usually restricted to hydro/ solvo-thermal synthesis and therefore relying on the use of synchrotron pressure-resistant systems. Here, the ambient conditions and relatively fast kinetics allowed us to investigate the thermal kinetics of a MOF material using a laboratory diffractometer. Figure S8 evidenced the direct formation of MOF-808 without any other phase or impurity. The integrated intensity of the (3 1 1) reflection was monitored as a function of crystallization time (**Figure 1c**), evidencing that even a slight increase in temperature from 25 °C to 40 °C induces a much faster reaction. One could therefore imagine multiplying by 5 the space-time yield by a temperature increase of 15 °C (Figure S9 and Table S2). The estimated Arrhenius activation energy of 34.5 kJ·mol⁻¹ is in good agreement with the activation energies measured for the crystallization of other MOFs using mild temperature conditions.^{45, 46}

As low temperature synthesis can be effective to produce nano-MOFs,^{47, 48} our protocol with low activation energy is appealing to prepare size-controlled MOF-808 nanocrystals. Indeed, homogeneously tuning the crystal size while maintaining high product yield and quality is an interesting but still challenging topic in MOF chemistry. For example, one very recent effort with MOF-808 produced nanoparticles with low BET surface area (622 m²/g) and poor crystallinity.⁴⁹ In our case, we control the crystal size via a concentration-induced method (illustrated in **Figure 2a**), where the volume of water and formic acid are kept constant and the concentration of Zr₆ oxoclusters and BTC linker simultaneously tuned. The MOF-808-RT synthesized with BTC concentration of 18.75 mg/ mL exhibits a uniform crystal size of 850 (±10) nm (labeled “850 nm MOF-808” in the following) according to scanning electron microscopy (SEM) images (Figure 2b). By increasing the concentration of reactants by 6, the nucleation-growth kinetics of MOF-808 was significantly accelerated, which shortened the synthesis time to 5 h in comparison to the 14 h for 850 nm MOF-808. As shown in Figure S10, PXRD patterns evidenced the high crystallinity and purity of all the materials with a progressive peak broadening (FWHM from 0.126° to 0.26° in 2θ) that is consistent with the formation of nanocrystals. SEM and High-resolution transmission electron microscope (HRTEM) measurements in **Figure 2b-e** further revealed that this concentration-induced method produced well-defined cubic crystals from sub-micron (850 nm) to nanoscale (35 nm). These samples display very narrow size distribution with a low coefficient of variation (CV) (Figure S13). The statistical analysis also confirms the strong dependence of crystal sizes on the concentration of precursor (**Figure 2f**). The monodispersity of the synthesized MOF-808 could be tentatively attributed to the use of Zr₆ oxoclusters as the metal source that bypasses the formation of Zr₆ from Zr(IV) salts, therefore facilitating the MOFs nucleation. In addition, the syntheses were performed under stirring, which allows the reactants to be mixed in a homogeneous way. Indeed, the absence of stirring in the synthesis of 850 nm MOF-808 resulted not only in prolonged synthesis duration (> 5 days) but also in a more polydispersed sample (see Figure S14).

Additional N₂ porosimetry experiments were carried out to evaluate the impact of the particle size on the surface areas and pore sizes of MOF-808. All values were consistent with the literature (**Figure 2g**), with only slight differences in surface areas following the relationship: 850 nm MOF-808 (2090± 17 m²/g) > 210 nm MOF-808 (2010± 20 m²/g) > 60 nm MOF-808 (1920± 20 m²/g) ≈ 35 nm MOF-808 (1920±20 m²/g). The pore size distributions followed the same trend (Figure S15), 850 nm MOF-808 (18.6 Å) > 210 nm MOF-808 (17.4 Å) > 60 nm MOF-808 (16.0 Å) ≈ 35 nm MOF-808 (16.2 Å), which may be explained by small variation of the defect content in the structure according to the TGA (Figure S16 and Table 1). Indeed, the drop in size is accompanied by a decrease of the modulator (formic acid) to substrate ratio, which can lead to a lower number of defects, as commonly observed in Zr(IV)-based MOF chemistry. Owing to the very low amount of solvents used in the synthesis of 35 nm MOF-808 (1.5g MOF precursors vs 2.67 mL solvent) and the high reaction yield (98 %), the compound showed a gel-like feature (Figure S17) and was obtained with a high STY at 2516 kg/ m³/ day, suggesting possible applications in aerogels^{50, 51} and possible up-scaling (Figure S18, synthesis of 10g of 35nm MOF-808 particles) of the green synthesis. To the best of our knowledge, this value is comparable to a few commercialized MOF examples, which are commonly synthesized through conventional solvothermal approaches. It should be noted that the reaction cannot be performed when the concentration of the BTC is above 112.5 mg/ mL due to the very limited solvent volume that does not allow reactants be fully dispersed.

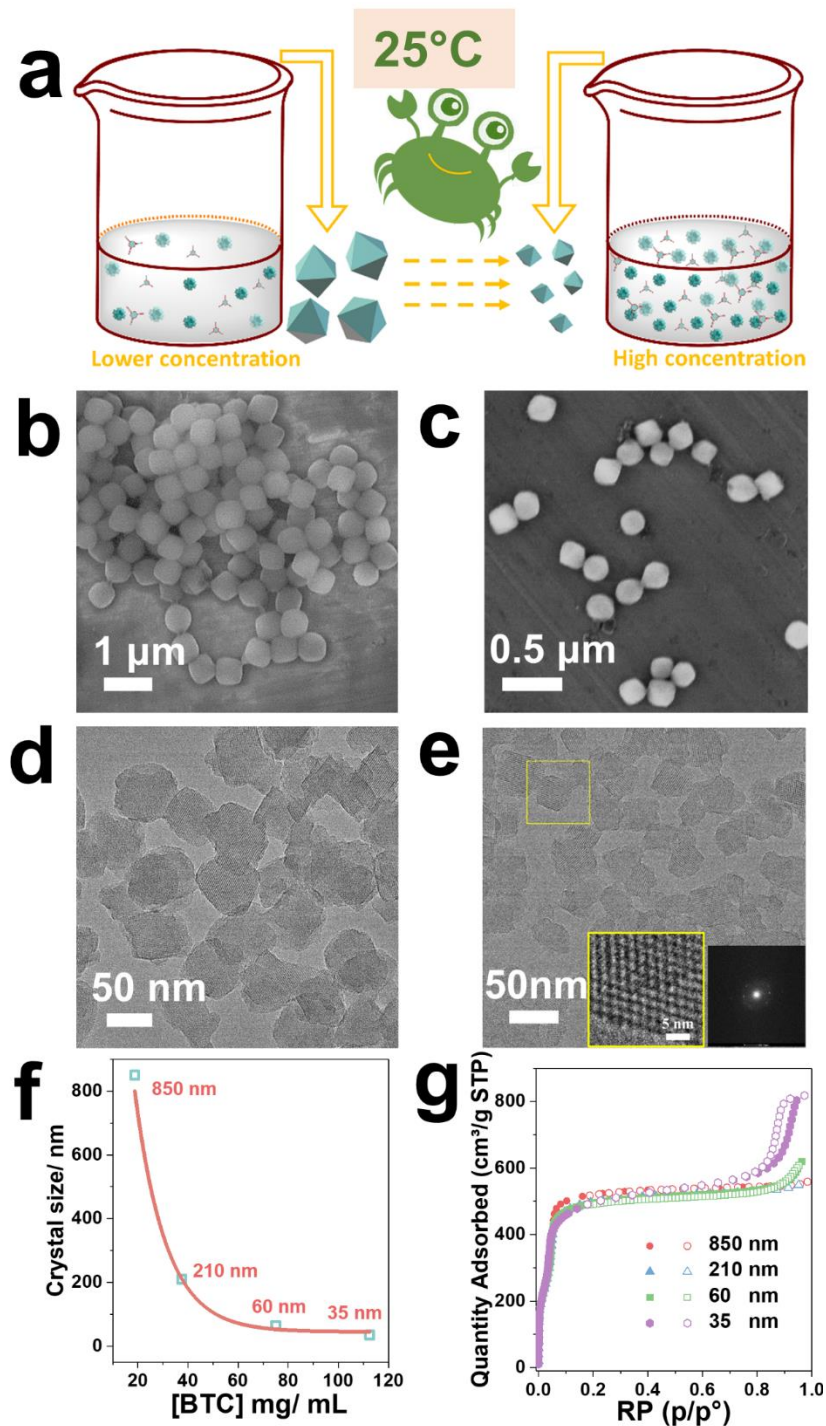


Figure 2. (a) Schematic representation of the concentration-induced method to tune the MOF-808 size; SEM images of (b) 850 nm MOF-808 and (c) 210 nm MOF-808; HRTEM image of (d) 60 nm MOF-808, (e) 35 nm MOF-808, Insets: Fast Fourier transform (FFT), cropped at the predominant lattice fringes and enlarged image inside the yellow square; (f) Statistical mean size of the synthesized MOF-808 in different reactants concentrations; (g) 77 K N_2 adsorption-desorption of 850 nm MOF-808, 210 nm MOF-808, 60 nm MOF-808, and 35 nm MOF-808, RP= Relative pressure.

The size reduction might be explained by the faster reaction kinetics associated with the lower formic acid to MOF precursor ratio. It is common in MOF carboxylate chemistry to use monocarboxylic acids -called modulators- to competitively coordinate with metal sites. In such cases, the more modulator used in the synthesis, the slower the synthesis is, which usually results in larger crystals. In order to confirm this hypothesis, additional experiments were carried out. As the increase in the concentration of reactants leads to a decrease of the modulator/ reactant ratio, we changed the relative ratio between the volume of formic acid and the mass of Zr₆ oxoclusters while keeping constant the concentration of reactants as in the 60 nm MOF-808 synthesis. For example, when this volume to mass ratio (VTMR) was 1.93 (1.93 mL formic acid per gram of Zr₆ clusters) instead of the value 1.25 for 60 nm MOF-808, we observed a clear deceleration of the kinetics, confirming that the amount of modulator influences the reaction kinetics. The obtained well-crystalline product was collected and analyzed with SEM (Figure S19), evidencing the presence of 170 nm MOF-808 crystals. This experiment shows that increasing the amount of modulator leads to an increase in particle size and that therefore, the concentration-induced size tuning effect is related to modulator-induced methods. As further proof, we used the parameters of the 850 nm MOF-808 synthesis but decreased the VTMR to 1.93. The SEM image in Figure S20 indicated that the obtained MOF-808 exhibited a smaller mean size of 175 nm, very close to the MOF-808 particle size synthesized under the same VTMR but with much higher reactant concentrations. However, when the VTMR was further decreased in order to produce nano-MOF-808, a significant drop in reaction yield (12% after 5 days with VTMR= 1.1) and quality (amorphous gel) was observed. We hypothesized this might be due to solubility issues because a lower formic acid content decreases the quantity of BTC dissolved in solution as BTC has a very low solubility in pure H₂O at room-temperature, therefore requiring a much longer synthesis duration associated with a dramatically lower yield. Notably, this can be circumvented by a slight heating (to 60 °C, see Figure S21) or addition of another organic solvent (e.g., Methanol, see Figure S22) that enhance the solubility of BTC to form smaller crystals with reasonable product yield (92%).

Table 1. Main properties of the MOF-808 nanocrystals.

MOF-808 particle size [nm]	BET Surface area [m ² /g]	External Surface area [m ² /g] ^a	Total Pore volume [cm ³ /g]	Pore size [Å]	Connectivity ^b	Space-time yield [kg/m ³ /day]
850	2090	47	0.85	18.6	1.82	102
210	2008	51	0.84	17.4	1.92	420
60	1920	452	0.83	16.0	1.98	1491
35	1920	775	0.83	16.2	1.98	2518

^{a)} External surface area was determined through t-plot method; ^{b)} Connectivity refers to the bridging ligands per Zr₆ oxoclusters.

NanoMOFs are suitable candidates for heterogeneous catalysis, sensing or bio-applications,⁵²⁻⁵⁴ mainly due to their easy processability and fast diffusion kinetics. However, when using heterogeneous catalysts in liquid phase, a high colloidal stability is required. Hence, Dynamic Light Scattering (DLS) was performed on MOF-808 in deionized water. As shown in **Figure 3a** (distribution in number) and Figure S23 (distribution in intensity), 35 nm MOF-808 displayed a constant hydrodynamic size at around 53 (± 13) nm and 91 (± 27) nm, respectively, in a wide range of particle concentrations (from 0.17 mg/mL to 7 mg/mL, pH from 3.63-3.82), which provided a flexible set of conditions to investigate their catalytic activity. Subsequently, time-dependent DLS measurements were carried out (**Figure 3b**) and demonstrated the excellent dispersion stability of this nano-MOF during 24h with an extremely low polydispersity index (0.05-0.1), indicating that no additive or treatment is needed to stabilize the dispersion. The satisfying colloidal stability and dispersion can be attributed to 1) the highly positive surface charge of the MOF-808 nanoparticles (+32 mV, Figure S24), and 2) the well-defined monodispersed nanoparticles.

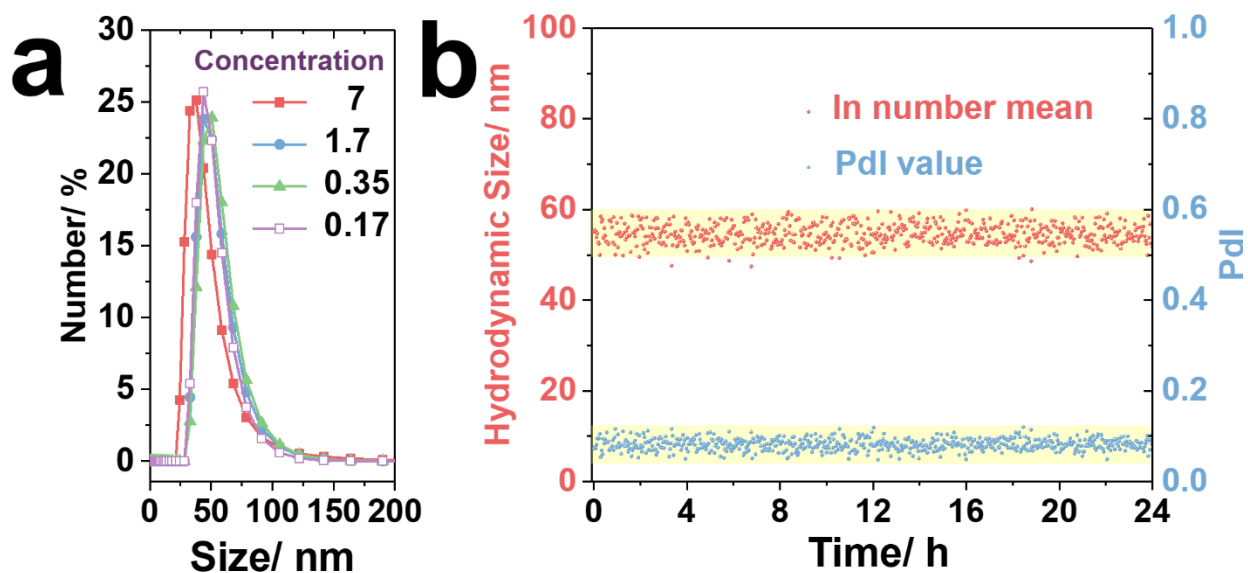


Figure 3. (a) Hydrodynamic sizes of the 35 nm large MOF-808 nanocrystals in aqueous solution with varying concentrations of 7, 1.7, 0.35, 0.17 mg/mL. (b) Time-resolved hydrodynamic size and polydispersity index (PDI) of the 35 nm MOF-808 in aqueous solution.

In order to investigate the effect of particle size on the catalytic activity of MOF-808, the rate of peptide bond hydrolysis at physiological pH was followed with both the model dipeptide glycylglycine (GG) and with the protein Hen Egg White Lysozyme (HEWL) which consists of 129 amino acids. Previous studies have shown that several Zr_6O_8 -based MOFs, including MOF-808, were highly efficient catalysts for peptide bond hydrolysis.²³ Conversion of GG to glycine (G) was followed by quantitative 1H -NMR spectroscopy over 20 h (Figure S25). Noteworthy, after 20 h hydrolysis the MOFs did not suffer from any significant loss of crystallinity under these reaction conditions (Figure S28). **Figure 4a** shows the conversion of GG with time, in addition to the formation of cyclic glycylglycine (cGG), consistent with previous reports involving GG and Zr_6O_8 -carboxylate based MOFs.^{24, 25} Hydrolysis followed first order rate kinetics (Figure S26),

from which, k_{obs} was calculated for each MOF used in the study (Figure 4b). After 20 h, 35 nm MOF-808 hydrolyzed 94.0% of the GG substrate, compared with 91.3%, 80.0% and 70.6% respectively for the 60, 210 and 850 nm MOF-808 crystals. This resulted in k_{obs} that ranged from $3.87 \times 10^{-5} \text{ s}^{-1}$ to $1.73 \times 10^{-5} \text{ s}^{-1}$ depending on the particle size (Figure 4b), showing that smaller particles are the most efficient. Such differences might be due to the external surface area of the MOF. 850 nm MOF-808, with external surface area of $47 \text{ m}^2/\text{g}$ is significantly less efficient at peptide bond hydrolysis than 35 nm MOF-808, which has an external surface area of $775 \text{ m}^2/\text{g}$, while both compounds present relatively similar BET surface areas (Figure S27). This supports the notion that the hydrolysis is likely to occur on the external surface of the MOFs, as external surface area has the most significant influence on the efficiency of peptide bond hydrolysis.

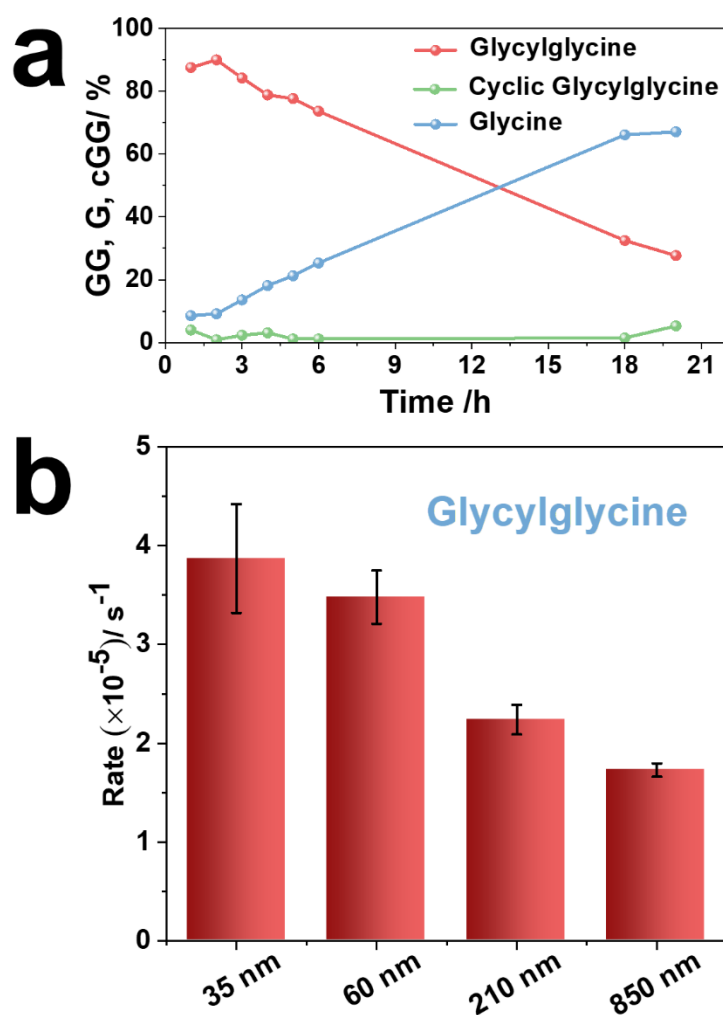


Figure 4. (a) Conversion of glycylglycine (GG) to glycine (G) and the side product cGG with time in the presence of 850 nm MOF-808. (b) k_{obs} of GG hydrolysis with different MOF-808 particle sizes.

Hydrolysis of HEWL was analyzed with Coomassie stained 18 % SDS-PAGE gels (**Figure 5a** and S29). After 72 h of HEWL incubation with 850 nm MOF-808, new fragments appear at 12.7, 11.3, 8.3, 5.8 and 4.7 kDa in addition to the intact protein at 14.3 kDa. The four fragments with the largest molecular weight (MW) were previously observed in HEWL hydrolysis with MOF-80823 and NU-1000,²⁵ suggesting that the new MOF synthesis protocol described here does not affect the selectivity of the MOF catalysts. The MW of the fragments observed in SDS PAGE indicates that they are most likely generated through hydrolysis of the peptide bonds at Asp18 (12.7 kDa), Asp52 (8.3 kDa), and Asp66 (5.8 kDa), as well as sequential hydrolysis of the 12.7 kDa fragment at Asp 119, to give the 11.3 kDa fragment, in analogy with the previously reported HEWL hydrolysis by metal complexes.⁵¹ The lightest fragment (4.7 kDa) was not observed before in MOF catalyzed hydrolysis of HEWL but it corresponds well to the MW of a fragment previously observed in HEWL hydrolysis by an Hf(IV)-Polyoxometalate,⁵⁵ resulting from hydrolysis at the Asp101 site. In addition to these 6 Asp residues, there are two additional Asp residues in HEWL (Asp48 and Asp87) that are located on short stretches of random coils in between larger regions of secondary structure (Figure S30). They most likely remain buried in the tertiary structure of the protein and as such are inaccessible to the active metal sites of the MOF even after partial hydrolysis of the intact protein. The rate of peptide bond hydrolysis in HEWL showed the same trend as with GG hydrolysis, with an increase in the rate observed as particle size decreases (**Figure 5b**).

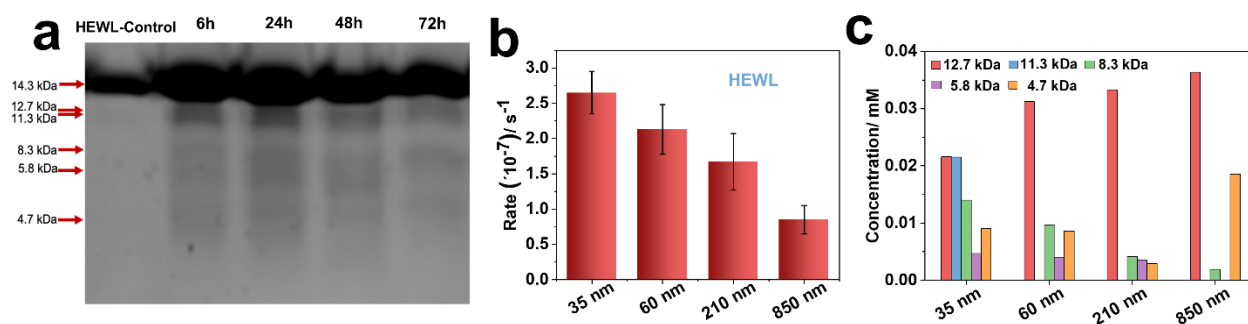


Figure 5. (a) Hydrolysis of HEWL by 850 nm MOF-808 followed by Coomassie blue stained SDS-PAGE. Native weight of protein – 14.3 kDa (b) k_{obs} of HEWL hydrolysis with all MOFs. (c) Concentration of HEWL hydrolysis fragments after 72 h incubation with all MOFs, from SDS-PAGE band analysis.

In addition, as demonstrated in **Figure 5c**, the number of resulting polypeptide fragments and their concentration can be tuned by changing the MOF particle size. While MOFs with smaller particle size produce more fragments within comparable range of concentrations, the larger particle sizes appear to be more efficient at hydrolyzing the Asp18 site, and show limited hydrolysis at Asp52 and Asp66 residues. Furthermore, these MOFs exhibited higher activity towards the secondary hydrolysis at the Asp119 site, which resulted in higher concentration of the lightest fragment at 4.7 kDa. With 35 nm MOF-808, the fragment coming from the hydrolysis at Asp18 bond is likely further hydrolyzed at Asp119 to give the 11.3 kDa fragment, which has not been detected for other

MOFs. Taking into account the dimensions of HEWL (35 x 25 x 45 Å), it is unlikely that the protein is able to diffuse into the MOFs pores without some degree of unfolding as the maximum pore size is 18.6 Å. Such unfolding has been reported previously for the incorporation of the smaller cytochrome c protein into NU-1000 and Tb-meso MOF.^{56, 57} Therefore, we propose that the initial hydrolysis occurs on the surface exposed Zr-nodes present within the half-spherical pockets on the surface of particles that are of similar size to HEWL, after which, subsequent hydrolysis of smaller fragments may also occur to a limited extent, within the pores, as the parent fragments are small enough to diffuse through the pore windows.²³ As was proposed for GG hydrolysis, the external surface area of the MOFs contributes significantly to the observed hydrolysis patterns. For 210 nm MOF-808 and 850 nm MOF-808, which have similar external surface areas (51 and 47 m²/g respectively) the hydrolysis patterns are similar, with the major HEWL fragment being 12.7 kDa. However, as the external surface area increases to 775 m²/g for 35 nm MOF-808, the efficiency of HEWL hydrolysis and number of resulting fragments increase in line with the increase in number of active metal sites present on the external surface of the MOF. The more efficient protein hydrolysis could also be due to the more effective MOF-protein interaction on the structure of the protein as smaller size nanoMOFs with a significantly larger external surface area may induce a substantial structural change in HEWL, causing a greater degree of protein unfolding over the surface of the nanoMOF. This in turn may expose more Asp residues to come into contact with the active metal sites, promoting hydrolysis at more sites on the protein surface.

3. Conclusion

This article reports for the first time an efficient room-temperature synthesis of the benchmark 6-connected MOF-808 under environmentally-friendly conditions. The novel synthesis conditions allowed us to achieve a size tuning from sub-micron range (850 nm) to the nanoscale (35 nm) while maintaining high crystallinity, porosity, homogeneity and a high space-time yield. In addition, we showed the high quality of the colloidal dispersion of the nano-MOF-808, reaching a nearly monodispersed suspension both at various concentrations (from 7 mg/ mL to 0.17 mg/ mL) and long-time-scale (24h). Such ambient conditions are particularly appealing for the incorporation of temperature sensitive species (e.g. small nanoparticles, enzymes, etc.) inside MOFs. Subsequently, the nano-MOF-808 exhibited a remarkable size-dependent catalytic efficiency towards a challenging peptide bond hydrolysis, with the smallest nanoMOF showing the highest catalytic potential. The trend is directly proportional to the external surface area of the MOF particles, thus suggesting that the catalytic reaction is likely to occur on the MOF external surface. The nanoMOF-808 was also able to selectively hydrolyze HEWL protein, efficiently producing fragments with MW that are suitable for the analysis in the emerging middle-down proteomics applications. Additionally, varying the particle size gives control over the specific protein fragments produced. This shows that MOFs can be synthesized with a specific particle size to produce desired fragments, proving these MOFs can act as superior artificial protease nanozymes for use in the field of proteomics. Finally, we hope this work can pave the way for efficient heterogeneous catalysis applications but also for applications that require colloidal-level nano-MOF-808.

References

1. Shang, L.; Nienhaus, K.; Nienhaus, G. U., *J. Nanobiotechnology* **2014**, *12*, 1-11.
2. Jain, P. K.; Huang, X. H.; El-Sayed, I. H.; El-Sayed, M. A., *Acc. Chem. Res.* **2008**, *41* (12), 1578-1586.
3. Cao, S.; Tao, F. F.; Tang, Y.; Li, Y.; Yu, J., *Chem. Soc. Rev.* **2016**, *45* (17), 4747-65.
4. Simon-Yarza, T.; Mielcarek, A.; Couvreur, P.; Serre, C., *Adv. Mater.* **2018**, *30* (37), 1707365.
5. Xiao, X.; Zou, L. L.; Pang, H.; Xu, Q., *Chem. Soc. Rev.* **2020**, *49* (1), 301-331.
6. Sindoro, M.; Yanai, N.; Jee, A. Y.; Granick, S., *Acc. Chem. Res.* **2014**, *47* (2), 459-469.
7. Dang, S.; Zhu, Q. L.; Xu, Q., *Nat. Rev. Mater.* **2018**, *3* (1), 1-14.
8. Bachman, J. E.; Smith, Z. P.; Li, T.; Xu, T.; Long, J. R., *Nat. Mater.* **2016**, *15* (8), 845-849.
9. Sakata, Y.; Furukawa, S.; Kondo, M.; Hirai, K.; Horike, N.; Takashima, Y.; Uehara, H.; Louvain, N.; Meilikhov, M.; Tsuruoka, T.; Isoda, S.; Kosaka, W.; Sakata, O.; Kitagawa, S., *Science* **2013**, *339* (6116), 193-196.
10. Doherty, C. M.; Buso, D.; Hill, A. J.; Furukawa, S.; Kitagawa, S.; Falcaro, P., *Acc. Chem. Res.* **2014**, *47* (2), 396-405.
11. Aguado, S.; Canivet, J.; Farrusseng, D., *J. Mater. Chem.* **2011**, *21* (21), 7582-7588.
12. Khan, N. A.; Kang, I. J.; Seok, H. Y.; Jhung, S. H., *Chem. Eng. J.* **2011**, *166* (3), 1152-1157.
13. Morris, W.; Wang, S. Z.; Cho, D.; Auyeung, E.; Li, P.; Farha, O. K.; Mirkin, C. A., *Acs Appl. Mater. & Interfaces* **2017**, *9* (39), 33413-33418.
14. Zhang, A. J.; Li, X. Y.; Zhang, S. Y.; Yu, Z. K.; Gao, X. M.; Wei, X. R.; Wu, Z. X.; Wu, W. D.; Chen, X. D., *J. Colloid and Interface Sci.* **2017**, *506*, 1-9.
15. Majewski, M. B.; Noh, H.; Islamoglu, T.; Farha, O. K., *J. Mater. Chem. A* **2018**, *6* (17), 7338-7350.
16. Wang, S.; McGuirk, C. M.; d'Aquino, A.; Mason, J. A.; Mirkin, C. A., *Adv. Mater.* **2018**, *30* (37), 1800202.
17. Radzicka, A.; Wolfenden, R., *J. Am. Chem. Soc.* **1996**, *118* (26), 6105-6109.
18. Clearfield, A., *J. Mater. Res.* **1990**, *5* (1), 161-162.
19. Yashiro, M.; Takarada, T.; Miyama, S.; Komiyama, M., *J. Chem. Soc., Chem. Commun.* **1994**, (15), 1757-1758.
20. Milinkovic, S. U.; Parac, T. N.; Djuran, M. I.; Kostic, N. M., *J. Chem. Soc., Dalton Trans.* **1997**, (16), 2771-2776.
21. Kopera, E.; Krezel, A.; Protas, A. M.; Belczyk, A.; Bonna, A.; Wyslouch-Cieszynska, A.; Poznanski, J.; Bal, W., *Inorg. Chem.* **2010**, *49* (14), 6636-6645.
22. Krezel, A.; Kopera, E.; Protas, A. M.; Poznanski, J.; Wyslouch-Cieszynska, A.; Bal, W., *J. Am. Chem. Soc.* **2010**, *132* (10), 3355-3366.
23. Ly, H. G. T.; Fu, G. X.; Kondinski, A.; Bueken, B.; De Vos, D.; Parac-Vogt, T. N., *J. Am. Chem. Soc.* **2018**, *140* (20), 6325-6335.
24. Ly, H. G. T.; Fu, G. X.; de Azambuja, F.; De Vos, D.; Parac-Vogt, T. N., *Acs Appl. Mater. & Interfaces* **2020**, *3* (9), 8931-8938.
25. Loosen, A.; de Azambuja, F.; Smolders, S.; Moons, J.; Simms, C.; De Vos, D.; Parac-Vogt, T. N., *Chem. Sci.* **2020**, *11* (26), 6662-6669.

26. Bai, Y.; Dou, Y. B.; Xie, L. H.; Rutledge, W.; Li, J. R.; Zhou, H. C., *Chem. Soc. Rev.* **2016**, *45* (8), 2327-2367.
27. Cavka, J. H.; Jakobsen, S.; Olsbye, U.; Guillou, N.; Lamberti, C.; Bordiga, S.; Lillerud, K. P., *J. Am. Chem. Soc.* **2008**, *130* (42), 13850-13851.
28. Wu, H.; Chua, Y. S.; Krungleviciute, V.; Tyagi, M.; Chen, P.; Yildirim, T.; Zhou, W., *J. Am. Chem. Soc.* **2013**, *135* (28), 10525-10532.
29. Vermoortele, F.; Bueken, B.; Le Bars, G.; Van de Voorde, B.; Vandichel, M.; Houthoofd, K.; Vimont, A.; Daturi, M.; Waroquier, M.; Van Speybroeck, V.; Kirschhock, C.; De Vos, D. E., *J. Am. Chem. Soc.* **2013**, *135* (31), 11465-11468.
30. Furukawa, H.; Gandara, F.; Zhang, Y. B.; Jiang, J. C.; Queen, W. L.; Hudson, M. R.; Yaghi, O. M., *J. Am. Chem. Soc.* **2014**, *136* (11), 4369-4381.
31. Moon, S. Y.; Liu, Y. Y.; Hupp, J. T.; Farha, O. K., *Angew. Chem. Int. Ed.* **2015**, *54* (23), 6795-6799.
32. Trickett, C. A.; Popp, T. M. O.; Su, J.; Yan, C.; Weisberg, J.; Huq, A.; Urban, P.; Jiang, J. C.; Kalmutzki, M. J.; Liu, Q. N.; Baek, J.; Head-Gordon, M. P.; Somorjai, G. A.; Reimer, J. A.; Yaghi, O. M., *Nat. Chem.* **2019**, *11* (2), 170-176.
33. Osterrieth, J. W. M.; Wright, D.; Noh, H.; Kung, C. W.; Vulpe, D.; Li, A.; Park, J. E.; Van Duyne, R. P.; Moghadam, P. Z.; Baumberg, J. J.; Farha, O. K.; Fairen-Jimenez, D., *J. Am. Chem. Soc.* **2019**, *141* (9), 3893-3900.
34. Lu, G.; Li, S. Z.; Guo, Z.; Farha, O. K.; Hauser, B. G.; Qi, X. Y.; Wang, Y.; Wang, X.; Han, S. Y.; Liu, X. G.; DuChene, J. S.; Zhang, H.; Zhang, Q. C.; Chen, X. D.; Ma, J.; Loo, S. C. J.; Wei, W. D.; Yang, Y. H.; Hupp, J. T.; Huo, F. W., *Nat. Chem.* **2012**, *4* (4), 310-316.
35. Guillerm, V.; Gross, S.; Serre, C.; Devic, T.; Bauer, M.; Ferey, G., *Chem. Commun.* **2010**, *46* (5), 767-769.
36. DeStefano, M. R.; Islamoglu, T.; Hupp, J. T.; Farha, O. K., *Chem. Mat.* **2017**, *29* (3), 1357-1361.
37. Sang, X.; Zhang, J.; Xiang, J.; Cui, J.; Zheng, L.; Zhang, J.; Wu, Z.; Li, Z.; Mo, G.; Xu, Y.; Song, J.; Liu, C.; Tan, X.; Luo, T.; Zhang, B.; Han, B., *Nat. Commun.* **2017**, *8* (1), 1-7.
38. Avci-Camur, C.; Perez-Carvajal, J.; Imaz, I.; Maspocho, D., *ACS Sustain. Chem. Eng.* **2018**, *6* (11), 14554-14560.
39. Pakamoré, I.; Rousseau, J.; Rousseau, C.; Monflier, E.; Szilágyi, P. Á., *Green Chem.* **2018**, *20* (23), 5292-5298.
40. Noh, H.; Kung, C.-W.; Islamoglu, T.; Peters, A. W.; Liao, Y.; Li, P.; Garibay, S. J.; Zhang, X.; DeStefano, M. R.; Hupp, J. T.; Farha, O. K., *Chem. Mat.* **2018**, *30* (7), 2193-2197.
41. Dai, S.; Nouar, F.; Zhang, S.; Tissot, A.; Serre, C., *Angew. Chem. Int. Ed.* **2021**, *60* (8), 4282-4288.
42. Jiang, J. C.; Gandara, F.; Zhang, Y. B.; Na, K.; Yaghi, O. M.; Klemperer, W. G., *J. Am. Chem. Soc.* **2014**, *136* (37), 12844-12847.
43. Ragon, F.; Horcajada, P.; Chevreau, H.; Hwang, Y. K.; Lee, U. H.; Miller, S. R.; Devic, T.; Chang, J. S.; Serre, C., *Inorg. Chem.* **2014**, *53* (5), 2491-2500.
44. Millange, F.; Serre, C.; Guillou, N.; Ferey, G.; Walton, R. I., *Angew. Chem. Int. Ed.* **2008**, *47* (22), 4100-4105.
45. Haque, E.; Khan, N. A.; Park, J. H.; Jung, S. H., *Chemistry* **2010**, *16* (3), 1046-1052.
46. Zahn, G.; Zerner, P.; Lippke, J.; Kempf, F. L.; Lilienthal, S.; Schröder, C. A.; Schneider, A. M.; Behrens, P., *CrystEngComm* **2014**, *16* (39), 9198-9207.

47. Xia, W.; Zhu, J. H.; Guo, W. H.; An, L.; Xia, D. G.; Zou, R. Q., *J. Mater. Chem. A* **2014**, *2* (30), 11606-11613.
48. Chalati, T.; Horcajada, P.; Gref, R.; Couvreur, P.; Serre, C., *J. Mater. Chem.* **2011**, *21* (7), 2220-2227.
49. Thur, R.; Van Velthoven, N.; Lemmens, V.; Bastin, M.; Smolders, S.; De Vos, D.; Vankelecom, I. F. J., *ACS Appl. Mater. Interfaces* **2019**, *11* (47), 44792-44801.
50. Li, L.; Xiang, S.; Cao, S.; Zhang, J.; Ouyang, G.; Chen, L.; Su, C. Y., *Nat. Commun.* **2013**, *4*, 1-9.
51. Xia, W.; Zhang, X.; Xu, L.; Wang, Y.; Lin, J.; Zou, R., *RSC Adv.* **2013**, *3* (27), 11007-11013.
52. Cai, X.; Xie, Z.; Li, D.; Kassymova, M.; Zang, S.-Q.; Jiang, H.-L., *Coord. Chem. Rev.* **2020**, *417*, 213366.
53. Marshall, C. R.; Staudhammer, S. A.; Brozek, C. K., *Chem. Sci.* **2019**, *10* (41), 9396-9408.
54. Dalstein, O.; Gkaniatsou, E.; Sicard, C.; Sel, O.; Perrot, H.; Serre, C.; Boissiere, C.; Faustini, M., *Angew. Chem. Int. Ed.* **2017**, *56* (45), 14011-14015.
55. Vandebroek, L.; De Zitter, E.; Ly, H. G. T.; Conic, D.; Mihaylov, T.; Sap, A.; Proost, P.; Pierloot, K.; Van Meervelt, L.; Parac-Vogt, T. N., *Chem. Eur. J.* **2018**, *24* (40), 10099-10108.
56. Chen, Y.; Lykourinou, V.; Vetromile, C.; Hoang, T.; Ming, L. J.; Larsen, R. W.; Ma, S. Q., *J. Am. Chem. Soc.* **2012**, *134* (32), 13188-13191.
57. Chen, Y.; Jimenez-Angeles, F.; Qiao, B.; Krzyaniak, M. D.; Sha, F.; Kato, S.; Gong, X.; Buru, C. T.; Chen, Z.; Zhang, X.; Gianneschi, N. C.; Wasielewski, M. R.; Olvera de la Cruz, M.; Farha, O. K., *J. Am. Chem. Soc.* **2020**, *142*(43), 18576-18582.

Supporting information

Monodispersed MOF-808 nanocrystals synthesized via scalable room-temperature approach for efficient heterogeneous peptide bond hydrolysis

Experimental

Ambient Powder X-ray Diffraction (PXRD) data were recorded on a high-throughput Bruker D8 Advance diffractometer working on transmission mode and equipped with a focusing Göbel mirror producing CuK α radiation ($\lambda = 1.5418 \text{ \AA}$) and a LynxEye detector. In situ kinetics PXRD data were collected using Malvern Panalytical Empyrean diffractometer (CuK α radiation, $\lambda = 1.5418 \text{ \AA}$), equipped with GaliPIX^{3D} detector and temperature-controlled HTK-1200N furnace. The data were collected within $7.5\text{-}11.5^\circ$ 2θ range and the temperatures were fixed at 25, 30 and 40 °C. The obtained time-dependent PXRD patterns were analyzed using sequential Le Bail refinement of the integrated intensities using Fullprof software.¹ Nitrogen porosimetry data were collected on a Micromeritics Tristar/ Triflex instrument at 77 K (pre-activating samples at 100 °C under vacuum, 5 hours). Scanning Electron Microscopy coupled with energy-dispersive X-ray spectroscopy (SEM-EDX) results were recorded with FEI Magellan 400 scanning electron microscope. Thermogravimetric analysis (TGA) data were collected on Mettler Toledo TGA/DSC 2, STAR System apparatus with a heating rate of 5 °C/min under the oxygen flow. Infrared spectra were measured with a Nicolet iS5 FTIR ThermoFisher spectrometer. Zeta potential and DLS size measurements of hydrodynamic radii were made on a Malvern Zetasizer Nano-ZS (Malvern Instruments).

High resolution TEM images (HRTEM) were acquired on a Titan Themis 200 microscope operating at 200 kV. This microscope is equipped with a Ceta 16M hybrid camera from ThermoFischer Scientific capable of working under low electron irradiation conditions. The HRTEM images are obtained in low dose condition with an irradiation current between 100 and 250 electrons per square angstroms. For the TEM grid preparation, a 2 μL drop of the solution is placed on a 200 mesh copper grid covered with a pure carbon membrane (from Ted Pella). The MS analyses were performed on 10 μL of sample each on a Tribrid Eclipse mass spectrometer (ThermoFisher Scientific) equipped with a nanoESI source (Triversa Nanomate Advion), at a resolution 120K (m/z 200) for both MS and MS/MS modes. MS2 acquisition was performed in

HCD mode (NCE 30). The solution sample was diluted x100 in of methanol/Aqueous acetic acid 1%, 1/1 (v/v) before analysis.

Chemicals:

All chemicals were purchased from commercial suppliers and used as received without further purification. Trimesic acid, 98%, Alfa Aesar. $ZrCl_4$ anhydrous, 98%, Acros. Zirconyl chloride octahydrate, 98%, Acros. Isopropyl alcohol, 99+%, Sigma. Formic acid, 98%, Acros. Acetic acid, 99+%, Fisher. Acetone, 99%, Acros. Ethanol absolute, $\geq 99\%$, Acros. Distilled water, Millipore system.

Synthesis of Zr_6 oxo-clusters:

Gram-scale synthesis of Zr_6 oxo-clusters: $ZrCl_4$ (2g, 0.84 mmol) was added in the mixture of 3 mL Acetic acid and 5mL isopropanol, while under stirring at 500 rpm at 120 °C for 60 min. The product can be collected either through suction filtration or centrifuge (at the speed of 10,000 rpm). The collected white solid was subsequently washed with acetone twice and dried under room-temperature vacuum. The

Hundred gram-scale synthesis of Zr_6 oxo-clusters: $ZrCl_4$ (200g, 0.84 mol) was added in the mixture of 300 mL Acetic acid and 500 mL isopropanol, while under stirring at 500 rpm at 120 °C for 60 min. The product can be collected either through suction filtration or centrifuge (at the speed of 10,000 rpm). The collected white solid was subsequently washed with acetone twice and dried under room-temperature vacuum. The mass of dry powder was 175 g, corresponding to 98% of product yield (calculation based on the Zr), indicating space-time yield at 5340 kg/m³/day.

Synthesis of MOF-808:

MOF-808-DMF: MOF-808 was obtained via solvothermal synthesis in N,N-dimethylformamide (DMF) at 110°C for 48 hours. The method was adapted from literature. Typically, 1,3,5-Benzenetricarboxylic acid (1.49 g, 7 mmol) was added to N,N-dimethylformamide (128 mL) in a thick glass jar with stirring at 600 rpm. $ZrOCl_2 \cdot 8H_2O$ (2.16 g, 6.7 mmol) and formic acid (133 mL) were added and the reaction mixture was stirred at room temperature over 20 minutes. The jar was heated at 110 °C for 48 hours. A white solid was collected by centrifugation at 14 500 rpm for 5 minutes and washed in N,N-dimethylformamide (250 mL) at 100 °C overnight with stirring at 350 rpm. The solid collected again, was further washed in acetone (250 mL) at 60 °C overnight at 600 rpm. The solid was obtained by filtration and dried in air. Activation before gas adsorption was performed on samples of ca. 120 mg by heating to 180°C for 5 hours.

850 nm MOF-808: Zr_6 oxoclusters (0.6 g) was dispersed in formic acid (3 mL) at 600 rpm. H_2O (5 mL) was subsequently added until the reaction mixture was completely colorless. 1,3,5-Benzenetricarboxylic acid (150 mg, 0.7 mmol) was added and the reaction was stirred overnight.

The solid was collected by centrifugation at 14 500 rpm for 5 minutes. The solid was then simply washed with 40 mL H₂O and 40 mL EtOH, once, respectively. The collected solid was dried in vacuum for 3 hours afforded a white powder. Activation before gas adsorption was performed on samples of ca. 120 mg by heating to 180°C for 5 hours.

210 nm MOF-808: Zr₆ oxoclusters (0.6 g) was dispersed in formic acid (1.5 mL) at 600 rpm. H₂O (2.5 mL) was subsequently added until the reaction mixture was completely colorless. 1,3,5-Benzenetricarboxylic acid (150 mg, 0.7 mmol) was added and the reaction was stirred overnight. The solid was collected by centrifugation at 14 500 rpm for 5 minutes. The solid was then simply washed with 40 mL H₂O and 40 mL EtOH, once, respectively. The collected solid was dried in vacuum for 3 hours afforded a white powder. Activation before gas adsorption was performed on samples of ca. 120 mg by heating to 180°C for 5 hours.

60 nm MOF-808: Zr₆ oxoclusters (0.6 g) was dispersed in formic acid (0.75 mL) at 600 rpm. H₂O (1.25 mL) was subsequently added until the reaction mixture was completely colorless. 1,3,5-Benzenetricarboxylic acid (150 mg, 0.7 mmol) was added and the reaction was stirred overnight. The solid was collected by centrifugation at 14 500 rpm for 30 minutes. The solid was then simply washed with 40 mL H₂O and 40 mL EtOH, once, respectively. The collected solid was dried in vacuum for 3 hours afforded a white powder. Activation before gas adsorption was performed on samples of ca. 120 mg by heating to 180 °C for 5 hours.

35 nm MOF-808: Zr₆ oxoclusters (1.2 g) was dispersed in formic acid (1 mL) at 600 rpm. H₂O (1.67 mL) was subsequently added until the reaction mixture was completely colorless. 1,3,5-Benzenetricarboxylic acid (300 mg, 1.4 mmol) was added and the reaction was stirred for 5 h. The solid was collected by centrifugation at 14 500 rpm for 60 minutes. The solid was then simply washed with 40 mL H₂O and 40 mL EtOH, once, respectively. The collected solid was dried in vacuum for 3 hours afforded a white powder. Activation before gas adsorption was performed on samples of ca. 120 mg by heating to 180°C for 5 hours.

MOF activation for hydrolysis reaction: Prior to being used as catalyst for peptide and protein hydrolysis, MOFs were activated in batches of 50 mg, in 0.5 M HCl - acetone solution for 72 h (3 x 2 mL) and methanol for 24 h (2 x 2 mL). After that the MOFs were dried at 70 °C for 2 h and activated at 160 °C for 24 h at atmospheric pressure.

Glycylglycine Hydrolysis: For each experiment, 2 μmol MOF and 2 mM glycylglycine (GG) (1 mL) in D₂O were mixed and pD was adjusted with NaOD and DCl to pD 7.6. Each sample was incubated at 60 °C for 20 h. 600 μL aliquots were taken at different time points, centrifuged and the resulting supernatant, to which internal standard TMSP-d₄ was added, was analysed with ¹H NMR (Bruker 300 MHz, 32 scans, Topspin 4.0.8 software).

Protein Hydrolysis: 0.1 mM protein solution (1 mL) was mixed with 2 μmol MOF and incubated at 60 °C and pH 7.2 for 72 h. 100 μL aliquots were taken for each time point, and analysed with sodium dodecyl sulfate polyacrylamide gel electrophoresis (SDS-PAGE).

Electrophoresis: SDS-PAGE was performed with a 0.5 M Tris - HCl buffer (pH 6.8) 4% (w/v) polyacrylamide stacking gel and a 1.5 M Tris - HCl buffer (pH 8.8) 16% (w/v) polyacrylamide

resolving gel. 15 μL of reaction mixture and 5 μL of buffer were combined and incubated at 95 $^{\circ}\text{C}$ for 5 min prior to the loading of 10 μL into gel wells. Page Ruler unstained low range protein ladder was used as the molecular weight standard, and gels were run at 200 V for 2 h. Subsequently, the gels were stained with Coomassie Blue and imaged with a Gel Doc EZ Imager and Bio-Rad Image Lab software.

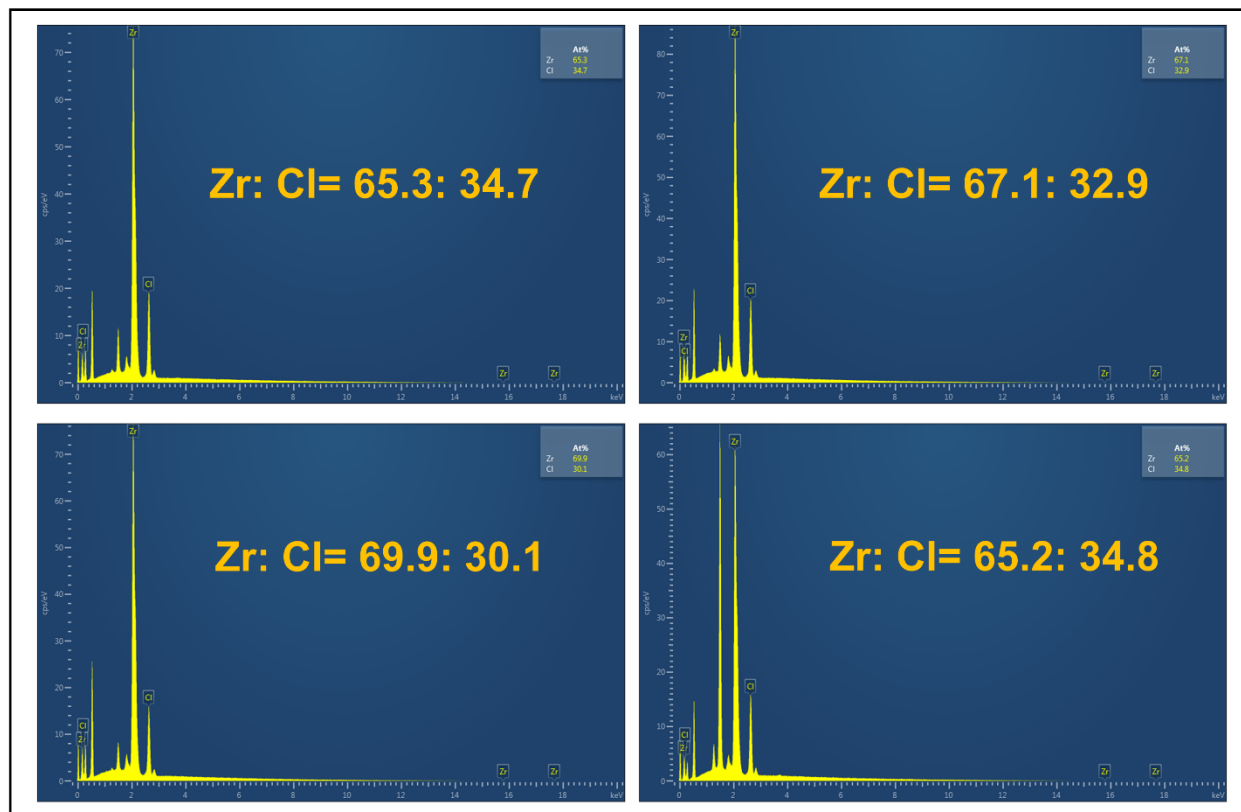


Figure S1. EDX scanning patterns of Zr_6 oxoclusters (four individual scanning regions). (normalized atomic ratio between Zr and Cl)

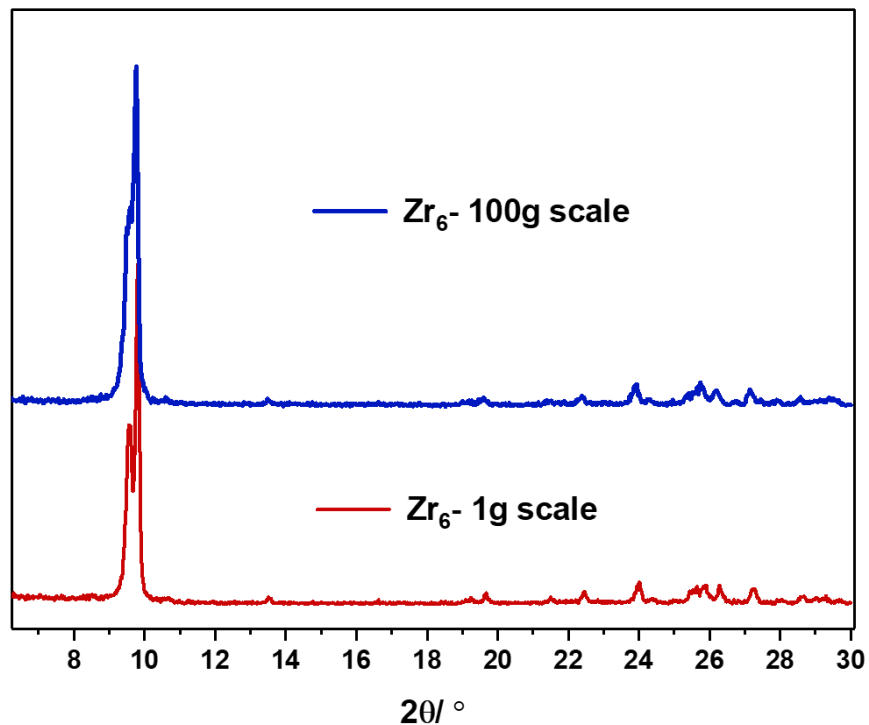


Figure S2. PXRD patterns of as-synthesized Zr_6 oxoclusters in small scale and large scale

Table S1. Synthesis duration, yield and space-time yield of Zr_6 oxoclusters and MOF-808 in varying sizes.

Entry	Synthesis Conditions	Time (h)	Yield (%)	SPY# (kg/m ³ /day)
Zr_6 clusters	Isopropanol +Acetic acid	1	98%	5340
MOF-808	H ₂ O+Formic acid	18/ 10/ 5*	97%	101/ 420/ 2516

*, 18/ 10/ 5 indicate the synthesis time for MOF-808 with the sizes in 800 nm, 210 nm, 30 nm respectively.

#, SPY= space time yield

zirconio soluzione #41-692 RT: 0.32-5.47 AV: 652 NL: 1.02E6
T: FTMS + p NSI Full ms [500.0000-8000.0000]

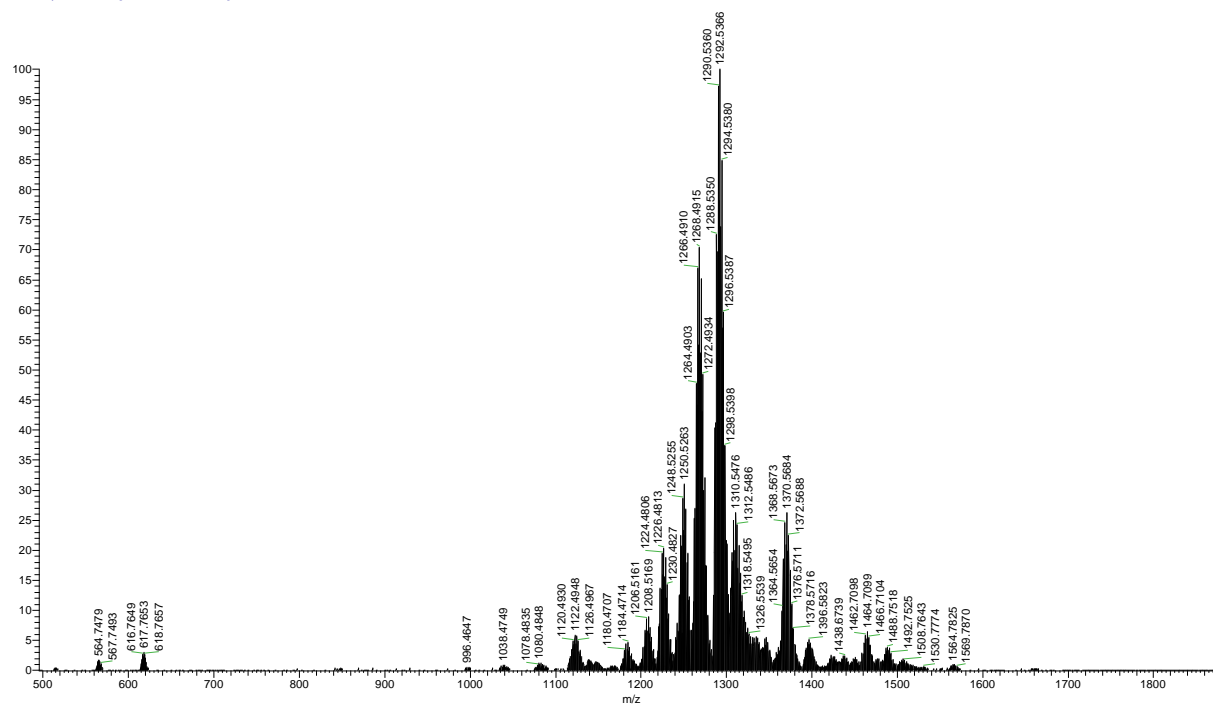


Figure S3. MS spectra of the synthesized $Zr_6O_4(OH)_4(C_2H_3O_2)_8(H_2O)_2Cl_3$.

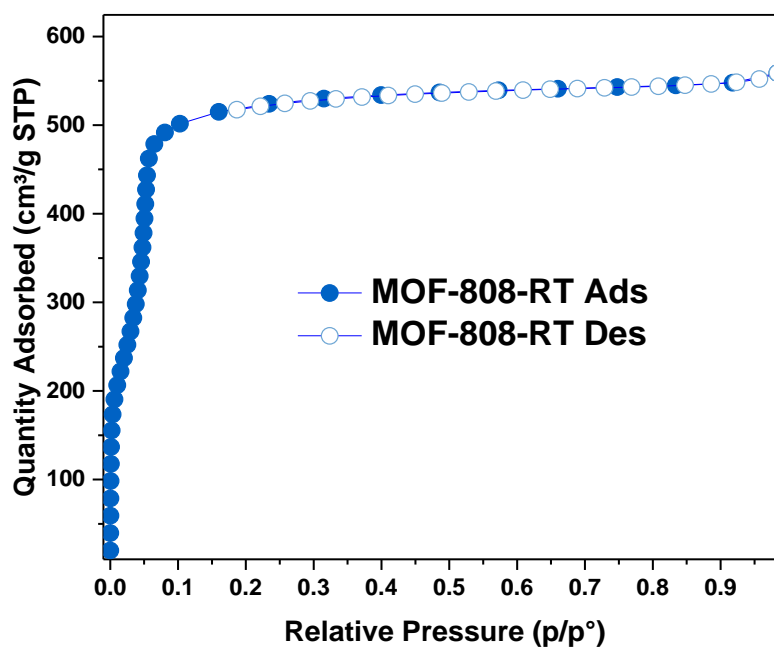


Figure S4. N_2 adsorption-desorption isotherms of MOF-808-RT.

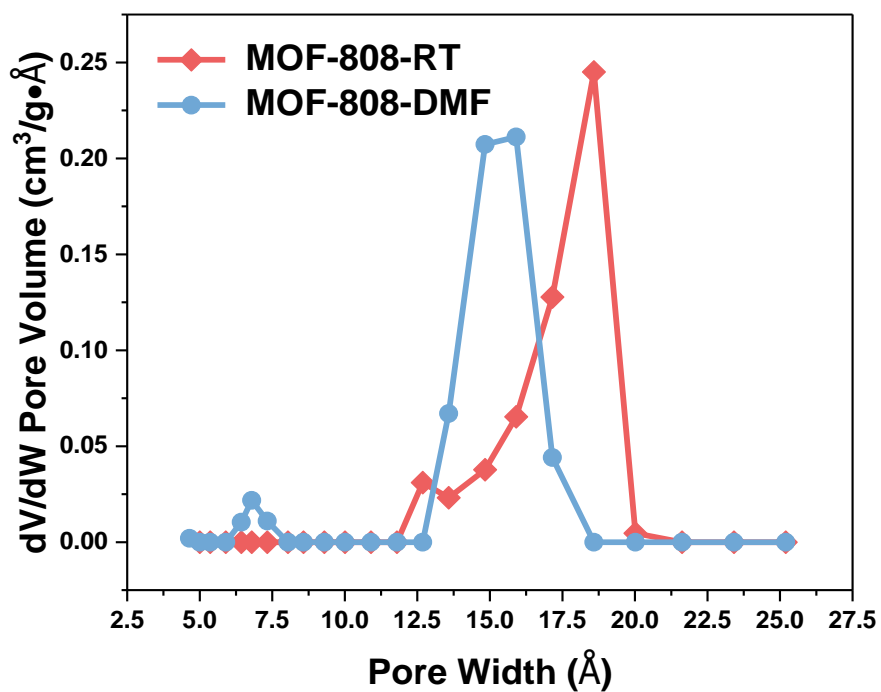


Figure S5. Pore size distributions of MOF-808-DMF and MOF-808-RT from N₂ DFT models. MOF-808-DMF represents the conventional synthesis method (Blue sphere), MOF-808-RT represents the MOF-808 synthesized through the proposed method in this article (red squares).

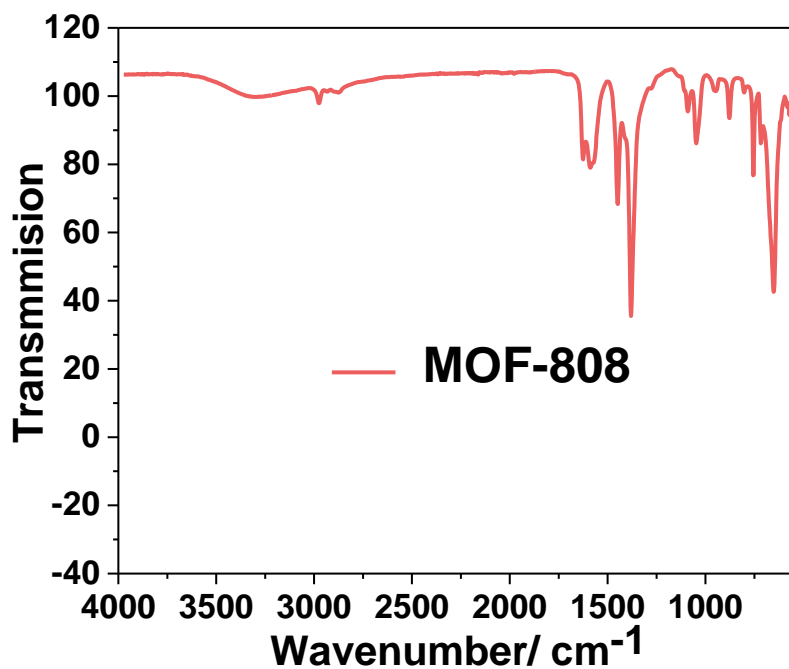


Figure S6. FT-IR analysis of MOF-808-RT.

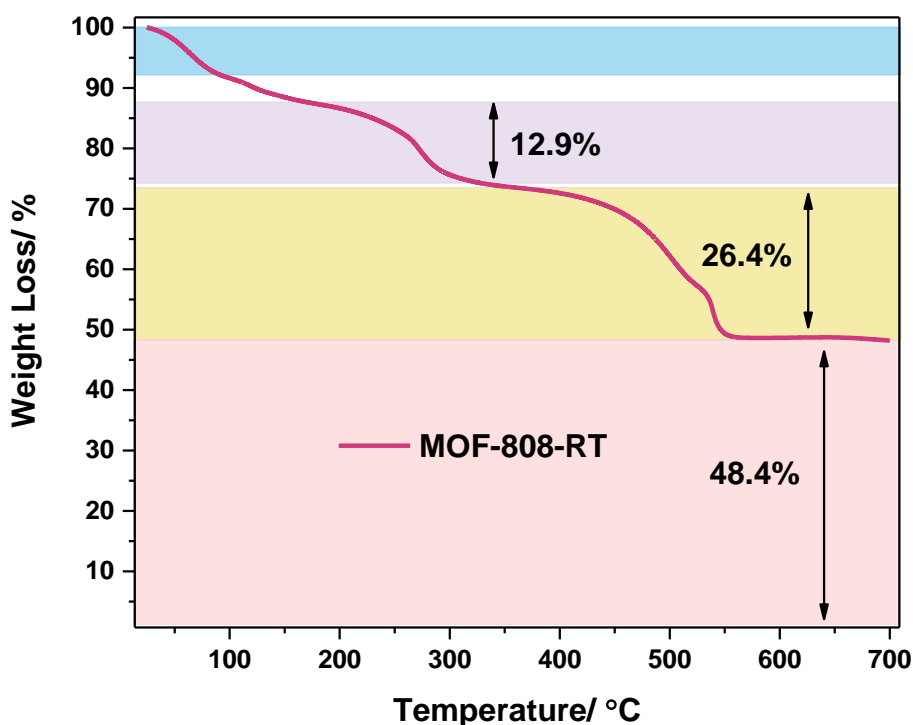


Figure S7. TG analysis of MOF-808-RT under 40 ml/min oxygen flow with 5 °C /min heating rate.

The first step observed on the thermogravimetric analysis (TGA) happened at around 100 °C and is due to the loss of adsorbed H₂O/ Acetic acid. The second step started from 200°C to 320°C and could be attributed to the loss of the coordinated modulators, which is very common in the modular-assisted synthesized MOFs. The last step (350°C to 550°C) was caused by the decomposition of organic linker that involved in the MOF. The plateau after 550°C can be fully regarded as the residue ZrO₂ and allowed us to determine the connectivity of the obtained MOF-808.

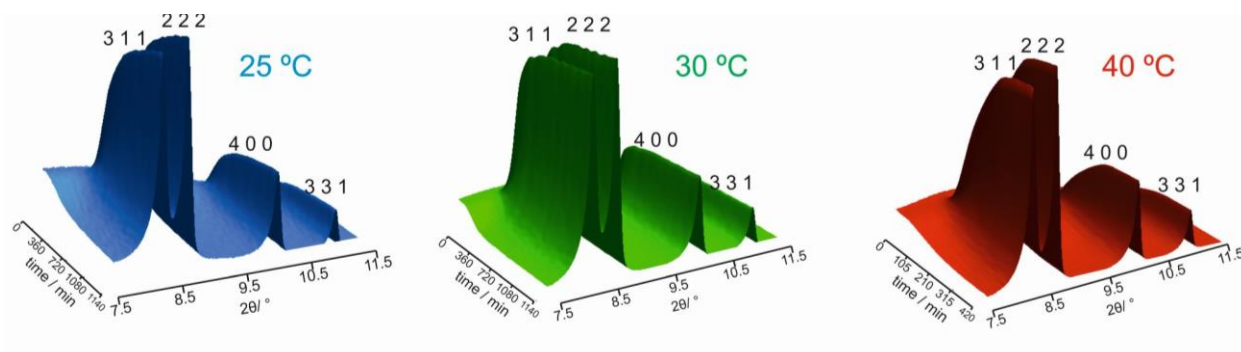


Figure S8. The kinetics plots of MOF-808 time-dependent powder diffraction patterns at various temperatures.

For the kinetics of crystallization, we take into account only the following powder patterns, where time-dependent intensities of the strongest (3 1 1) reflection was integrated. The kinetics of crystallization in such case can be described by the Johnson-Mehl-Avrami-Kolmogorov (JMAK) relation:

$$I_t = 1 - \exp(-(kt)^n) \quad (1)$$

The equation (1) is also known as a fractional order kinetic model, where $I_t \leq 1$ are normalized intensities at time t , k is an Avrami kinetic constant and n is an order of crystallization. These parameters of the equation (1) can be obtained using Sharp-Hancock plot of $\ln[-\ln(1/(1 - I_t))]$ vs. $\ln(t)$.¹⁻² The linear section of the Sharp-Hancock plot yields the Avrami exponent for each temperature.

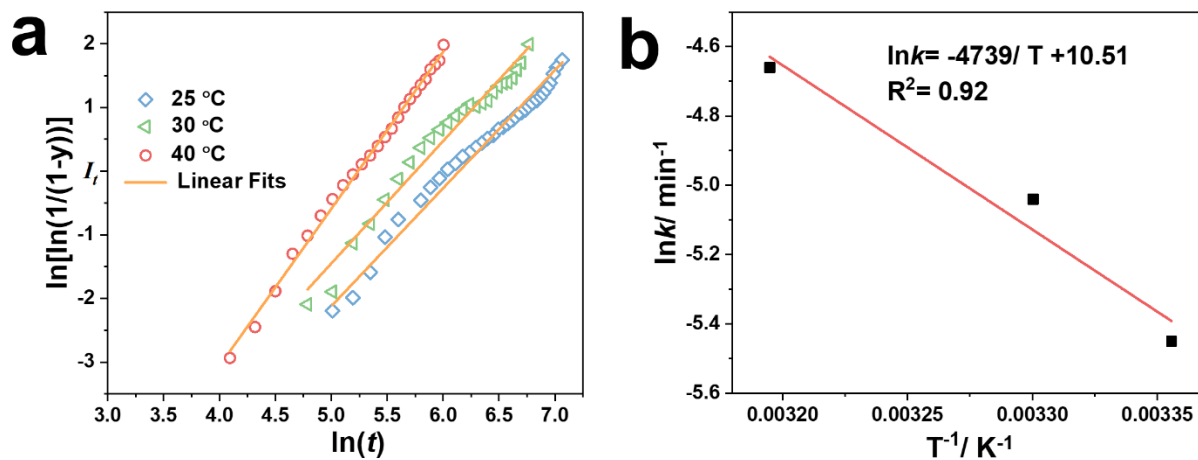


Figure S9. (a) Sharp-Hancock plots for the *in situ* synthesis of MOF-808 at varying temperature. (b) Arrhenius plots for the temperature-dependent rate constants.

Table S2. Kinetic parameters obtained by fitting of the crystallisation curves at different temperature with the Sharp-Hancock equation.

$T/ ^\circ\text{C}$	Sharp-Hancock plot		Constant		$E_a/ \text{kJ}\cdot\text{mol}^{-1}$
	n	R^2	k	R	
25	1.86	0.98	0.0043	8.314	
30	1.93	0.97	0.0065	8.314	33.4
40	2.47	0.99	0.0095	8.314	

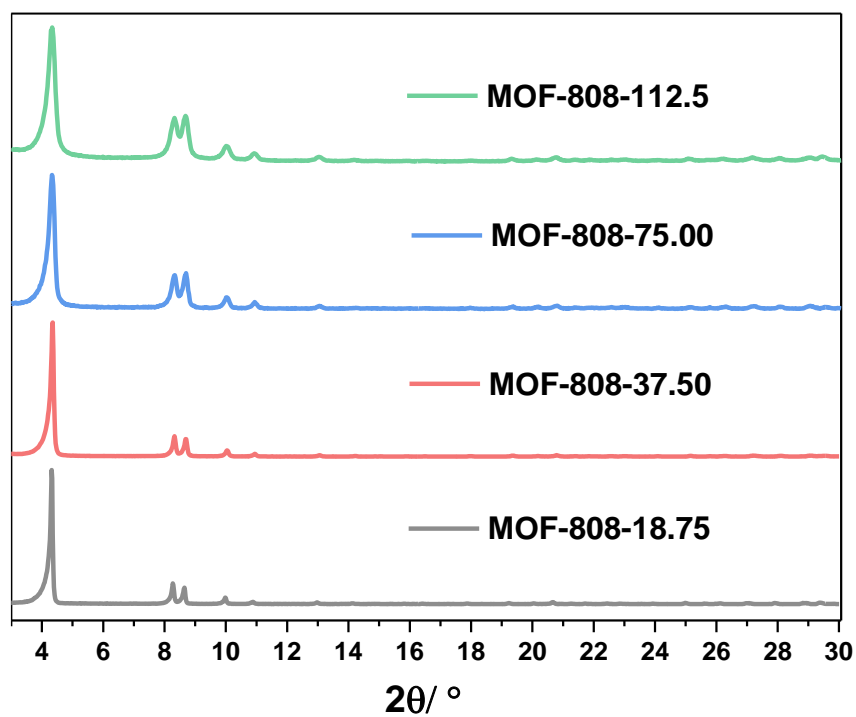


Figure S10. PXRD patterns of MOF-808 with different size.

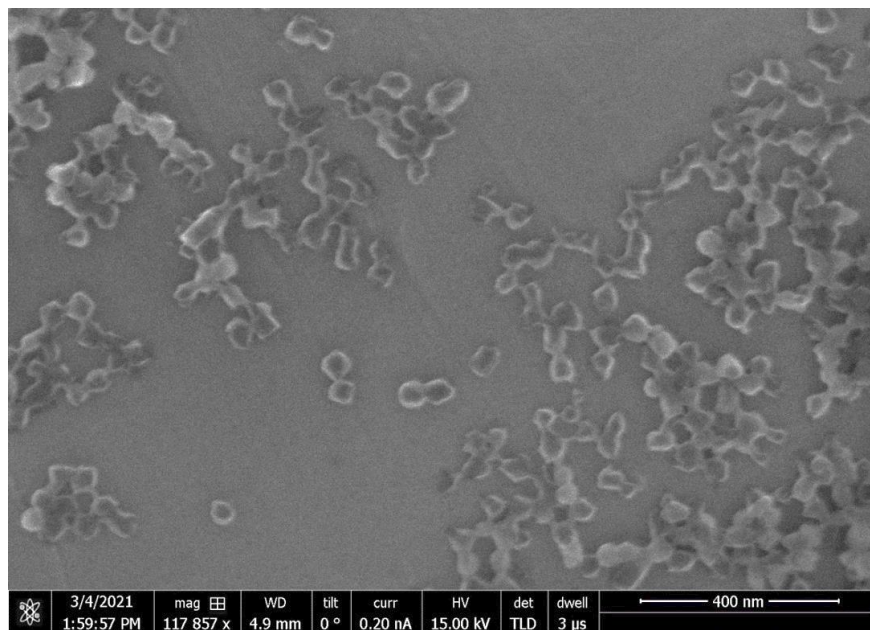


Figure S11. SEM image of 60 nm MOF-808.

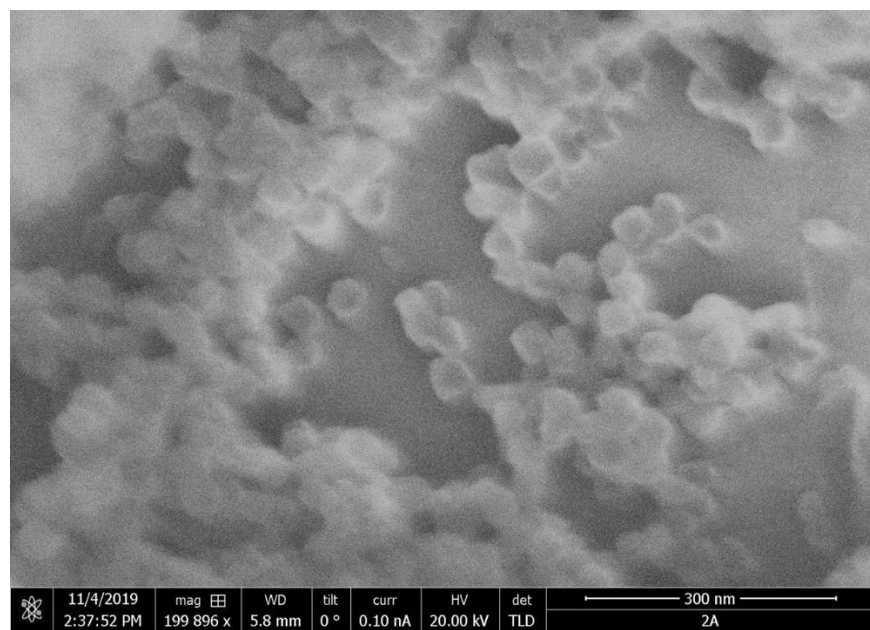


Figure S12. SEM image of 35 nm MOF-808.

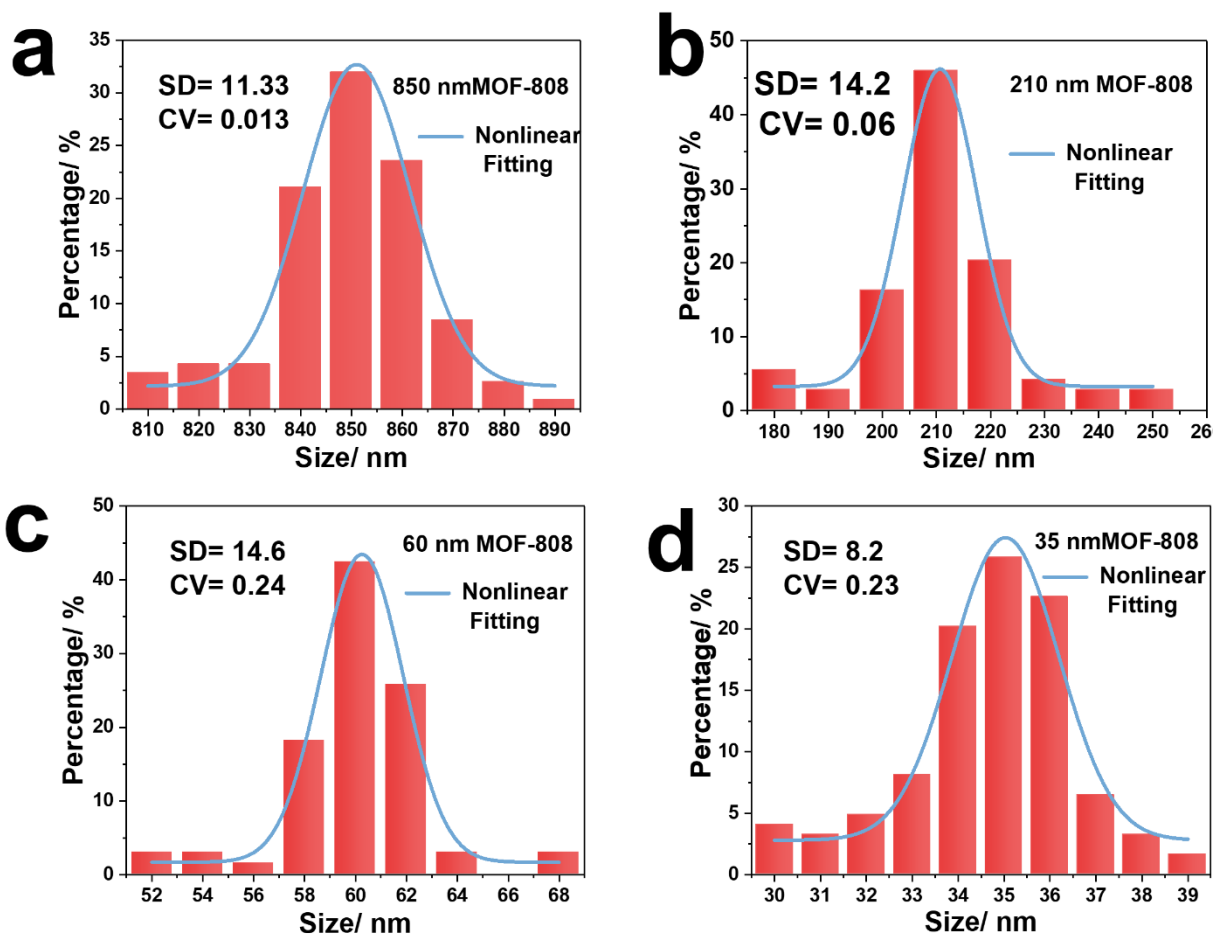


Figure S13. The statistical analyses of 50-100 crystals in (a) 850 nm MOF-801, (b) 210 nm MOF-808, (c) 60 nm MOF-808, (d) 35 nm MOF-808.

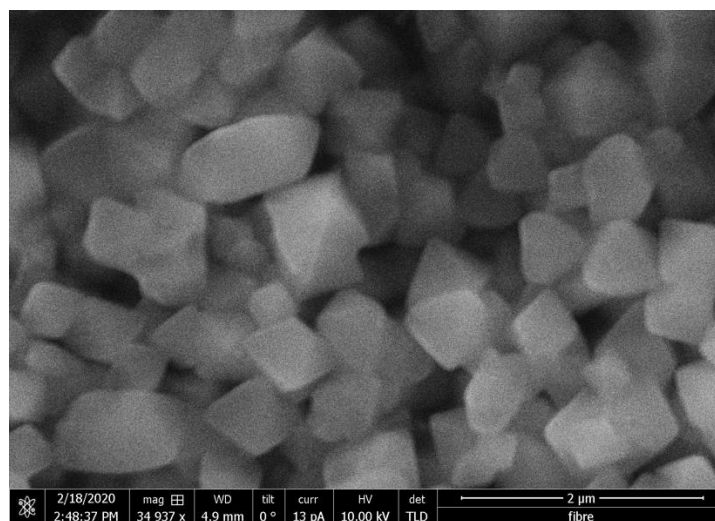


Figure S14. MOF-808 synthesized without stirring (the synthetic parameters come from 850 nm MOF-808)

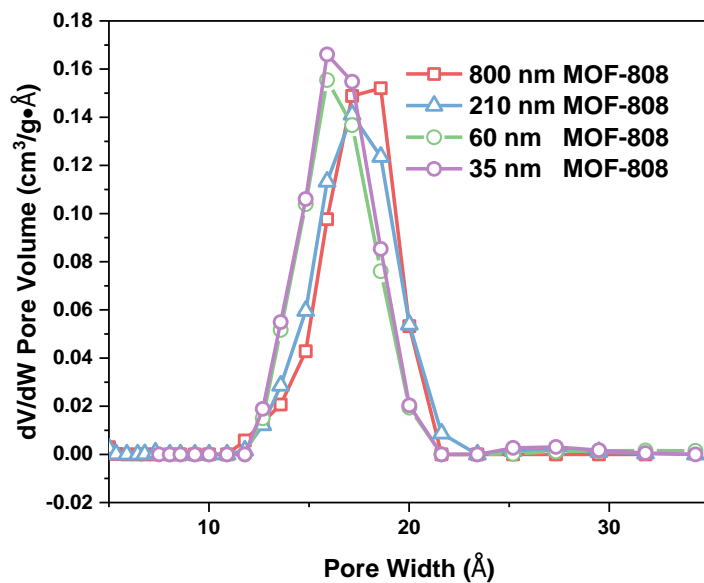


Figure S15. Size distribution analysis based on the DFT-model.

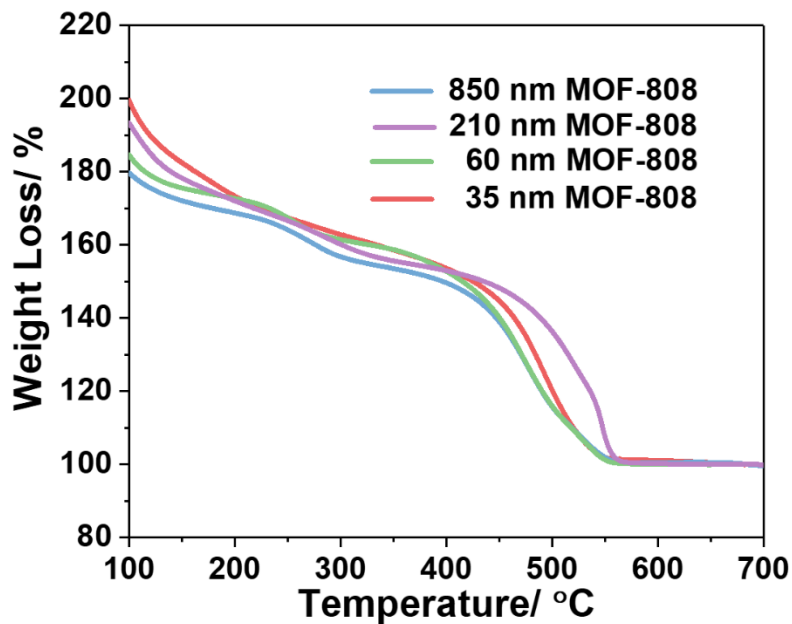


Figure S16. TGA analysis of 850 nm MOF-808, 210 nm MOF-808, 60 nm MOF-808, and 35 nm MOF-808, all under 40 mL/min oxygen flow with 5 °C/min heating rate.

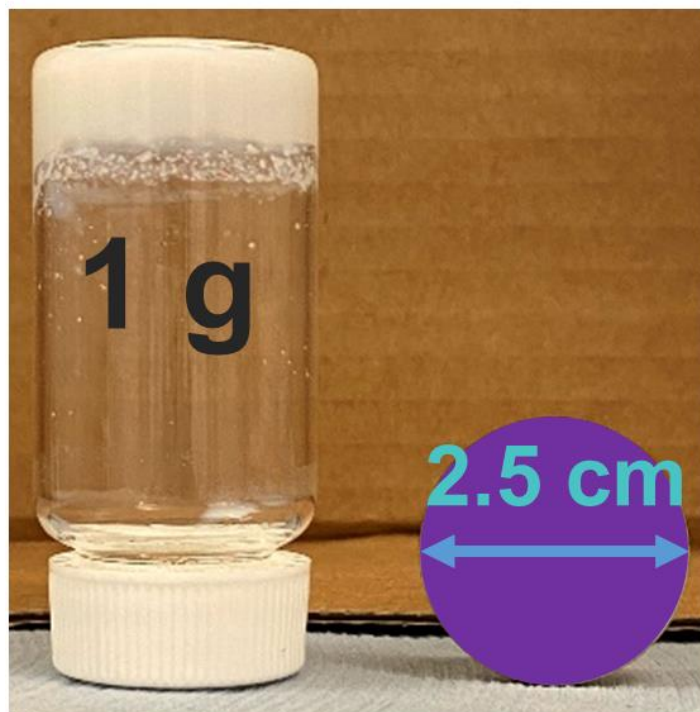


Figure S17. Photograph of the as-synthesized 2 mL 35 nm MOF-808 slurry in comparison to 2 Euro coin.

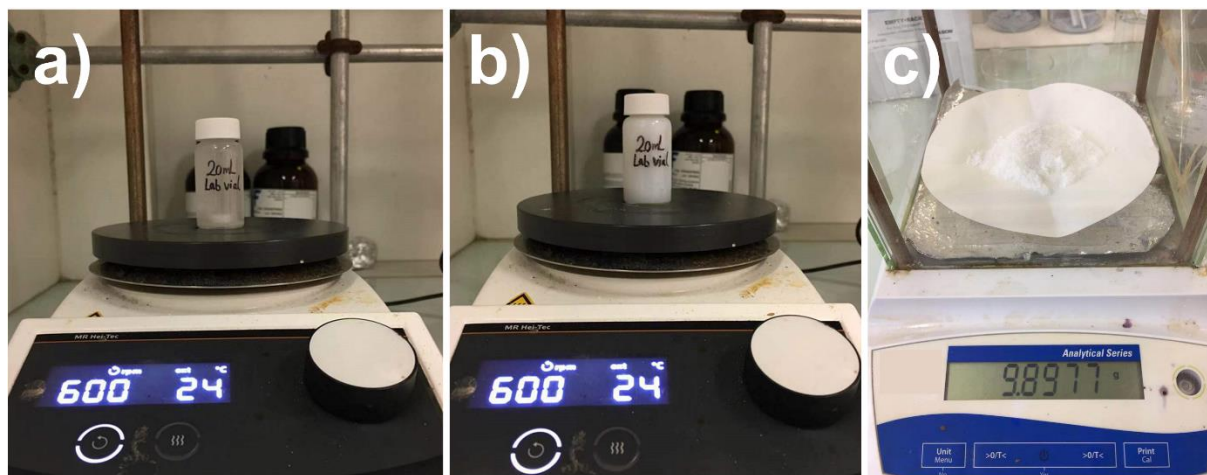


Figure S18. Photograph of the 10 gram MOF-808 synthesis at room temperature using a 20 mL glass vial, (a) initial precursors in glass vial, (b) synthesis batch after 5 h, (c) the isolated product after washing and drying.

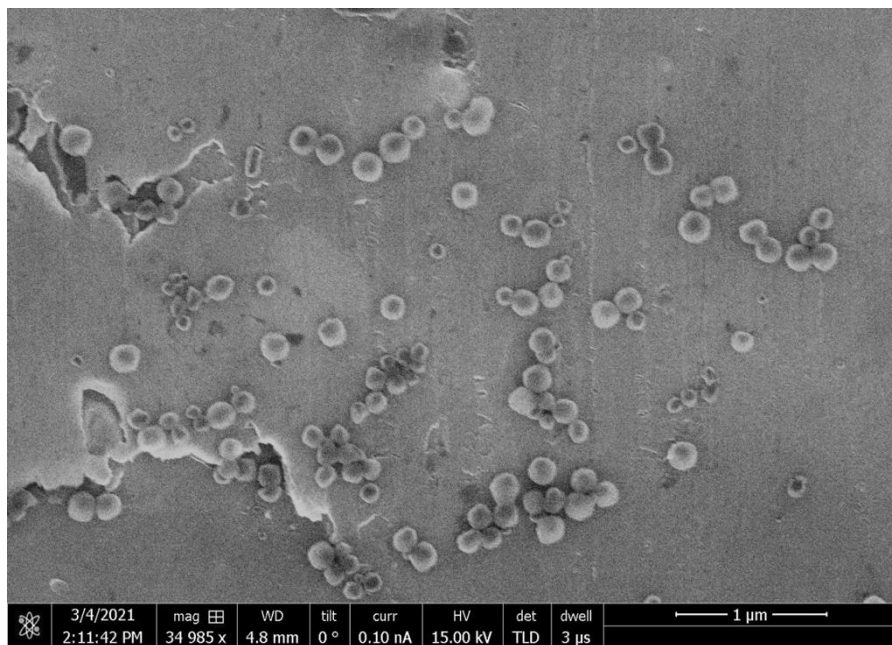


Figure S19. SEM image of MOF-808 synthesized with the same concentration of reactants as 850 nm MOF-808, while changing the Formic acid to Zr_6 oxo-clusters ratio from 1.25 to 1.93 (mL/ g).

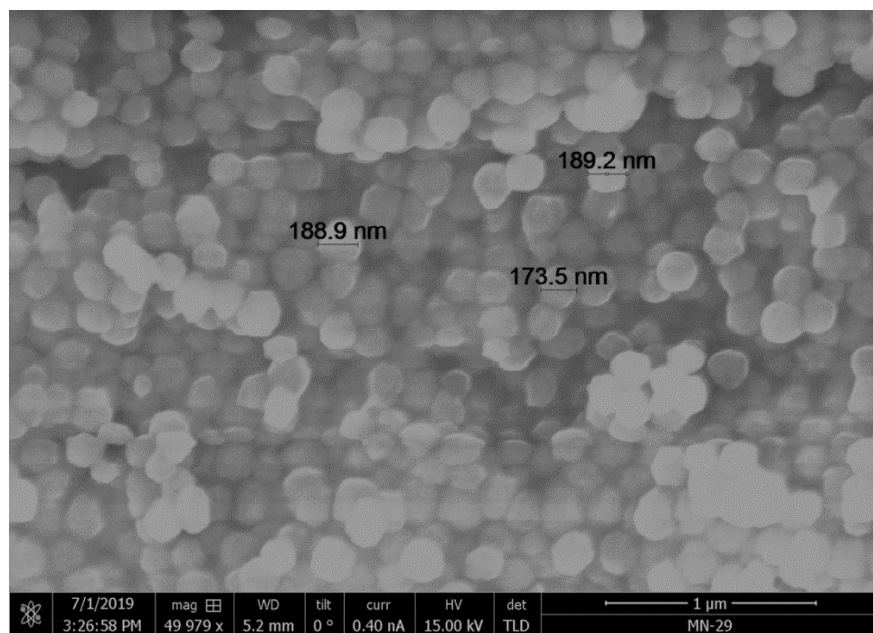


Figure S20. SEM image of MOF-808 synthesized with the same parameters as 850 nm MOF-808 except with decreased VTMR to 1.93.

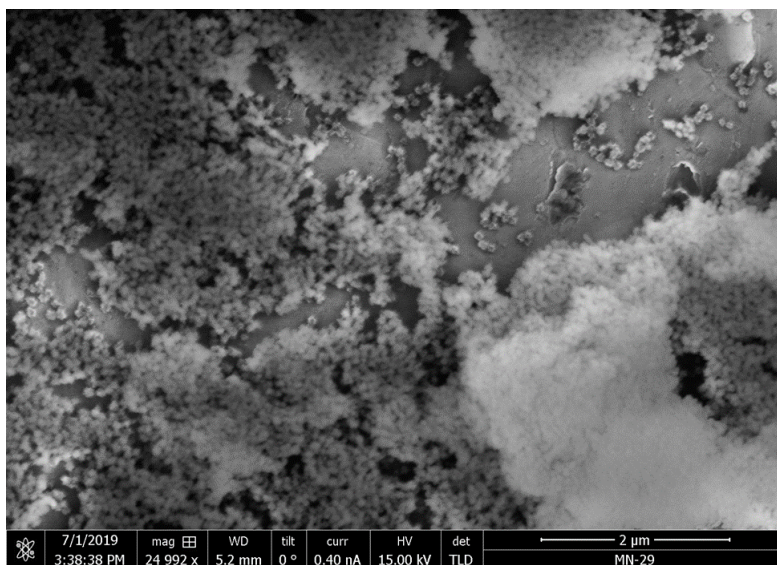


Figure S21. SEM image of MOF-808 synthesized with the parameters of 850 nm MOF-808 while changing the VTMR to 0.83 and at 60 °C.

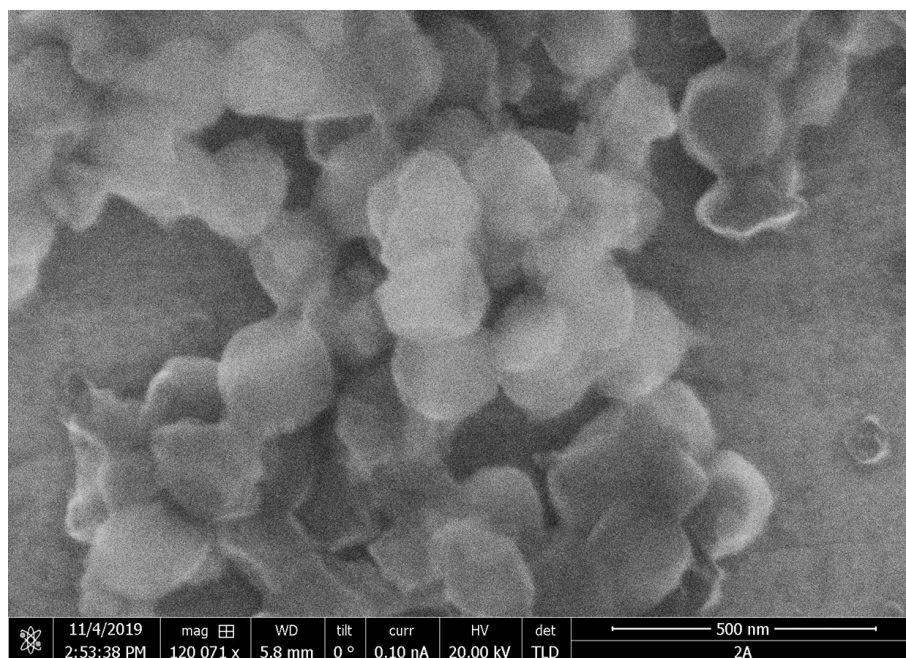


Figure S22. SEM image of MOF-808 synthesized with the parameters of 850 nm MOF-808 while changing the VTMR to 0.83 and adding MeOH.

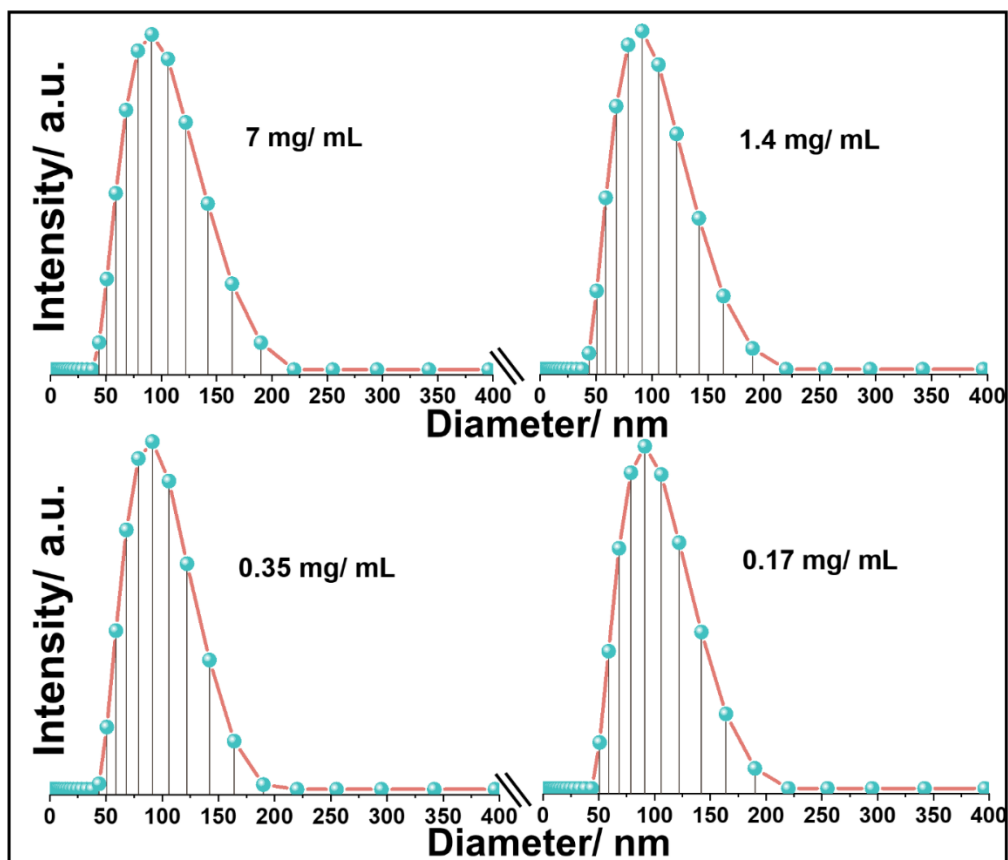


Figure S23. Hydrodynamic sizes of the 35 nm large MOF-808 nanocrystals in aqueous solution with varying concentrations of 7, 1.7, 0.35, 0.17 mg/ mL (in intensity mean).

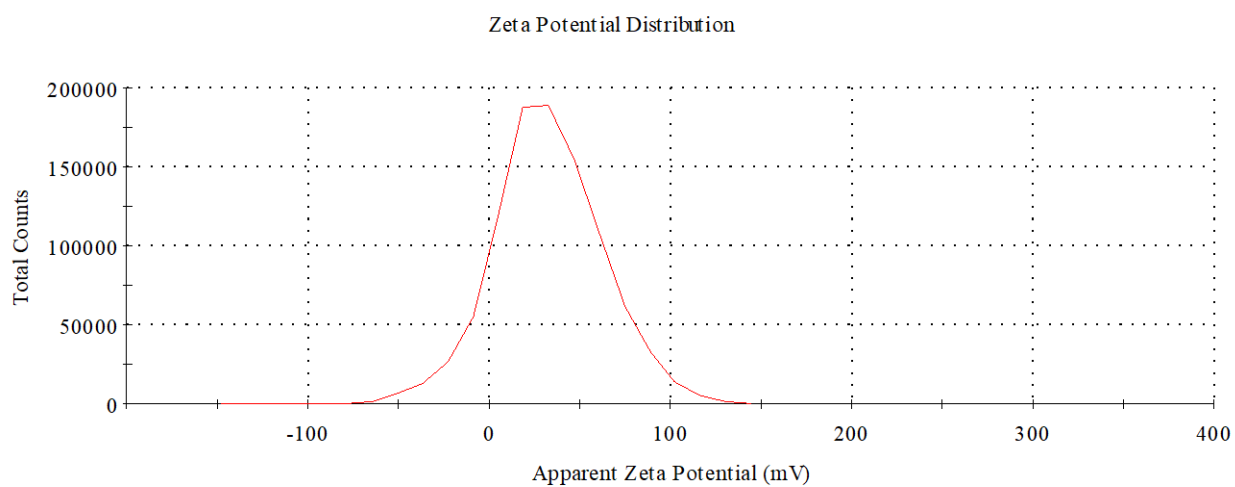


Figure S24. Zeta potential distribution of 35 nm MOF-808. (measured in H₂O, pH= 3.82)

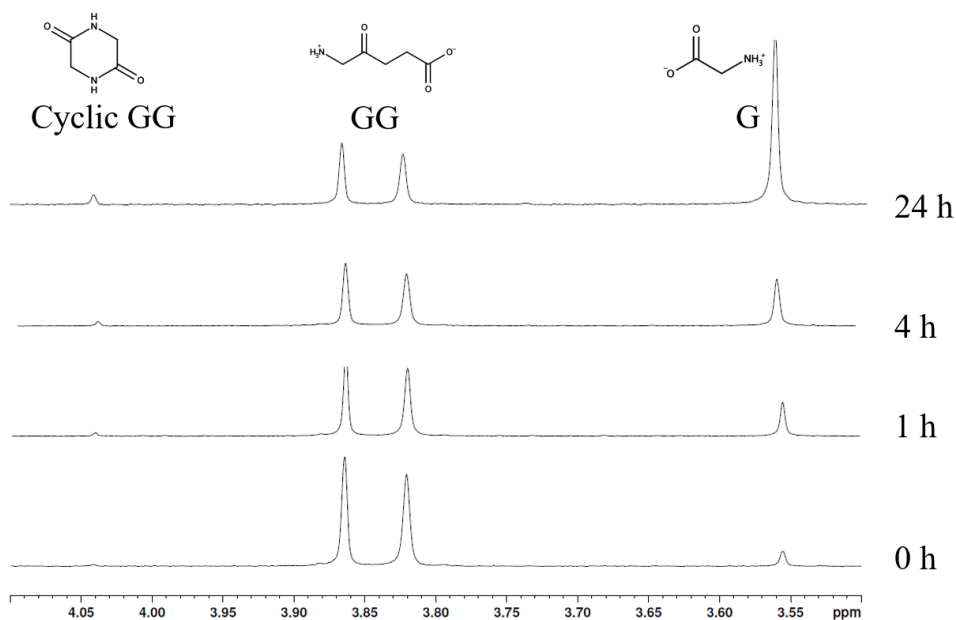


Figure S25: ^1H NMR spectra of glycylglycine (GG) hydrolysis by 35 nm MOF-808 at different reaction times, at 60 °C, pD 7.6. With structures of glycylglycine substrate (GG), cyclic glycylglycine intermediate and glycine(G) product associated with each signal.

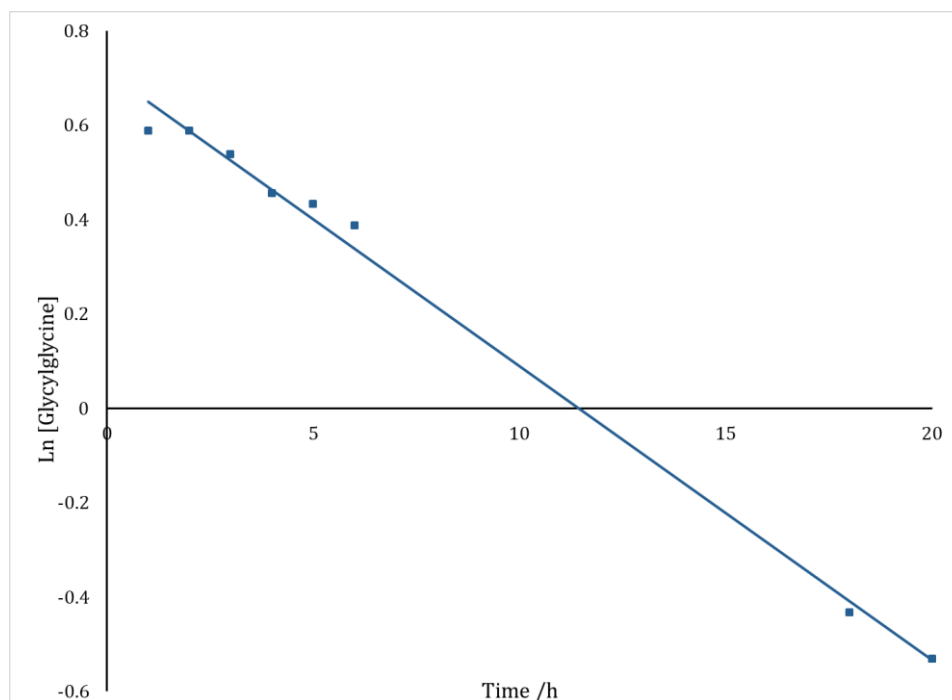


Figure S26: Representative first order rate plot of glycylglycine hydrolysis over time with 800 nm MOF-808.

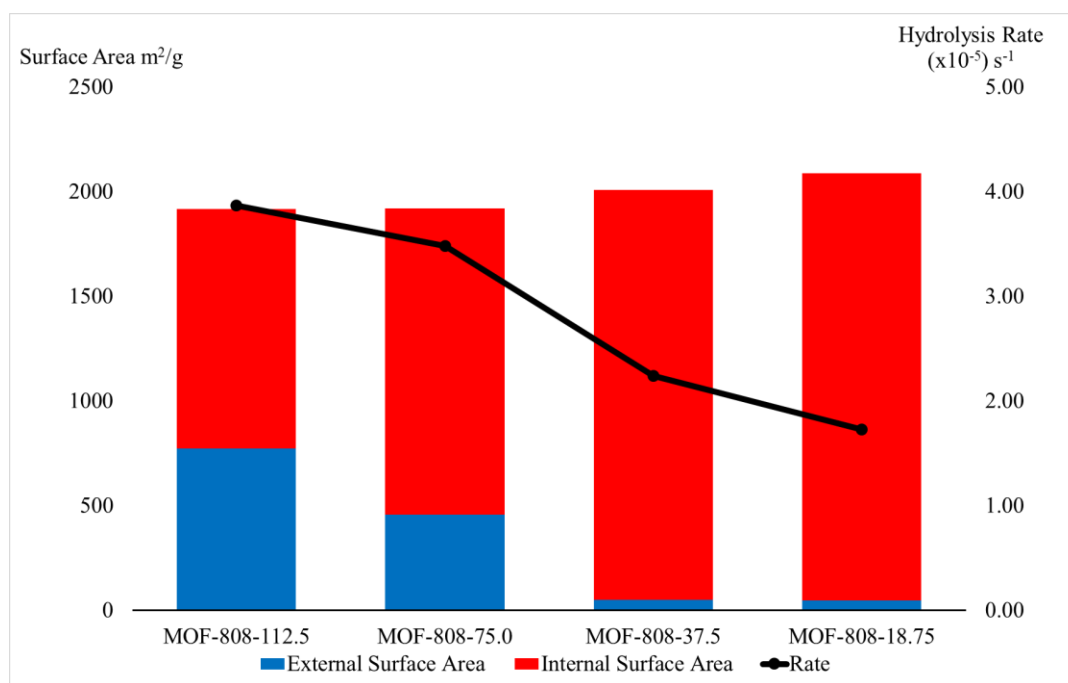


Figure S27: Rate of Glycylglycine hydrolysis in relation to internal and external surface areas of each MOF

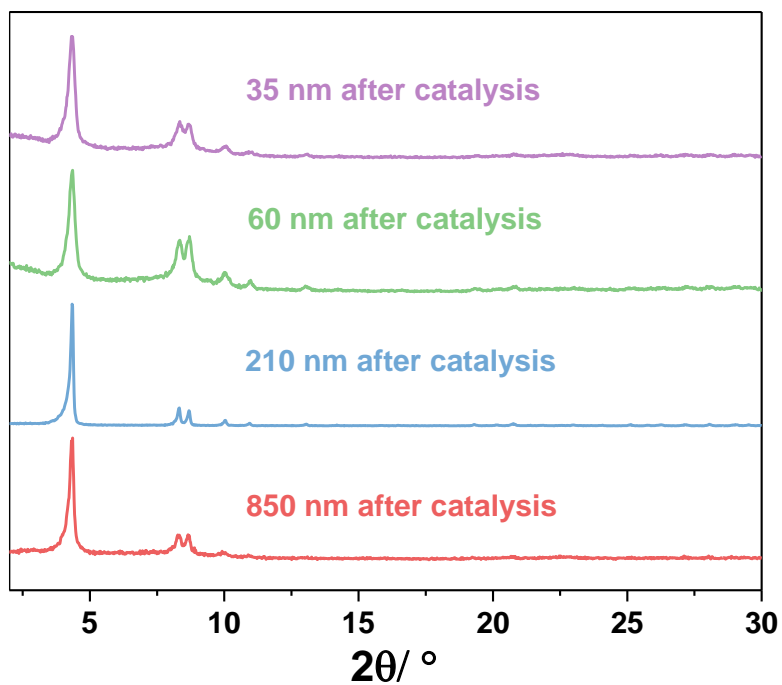


Figure S28: PXRD patterns of MOF-808 in different sizes after 24 h hydrolysis reaction.

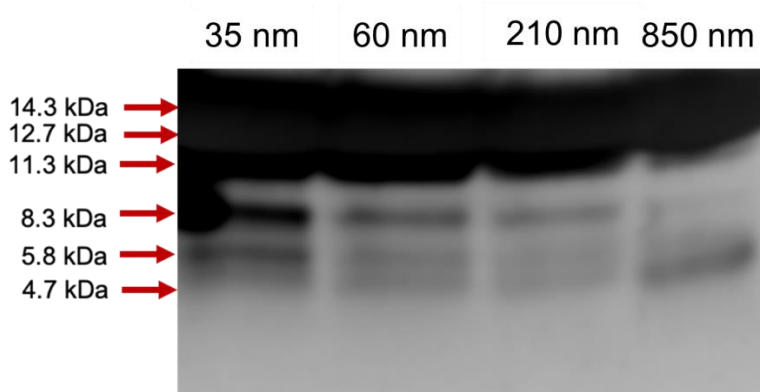


Figure S29: Coomassie stained SDS-PAGE gel of HEWL hydrolysis by all MOFs after 72h. Intact protein at 14.3 kDa.

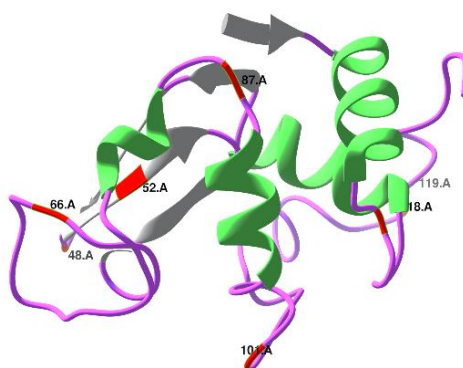


Figure S30: Location of Asp residues in HEWL in red. Random coil in purple, Beta sheets in grey and alpha helices in green.

References:

- [1] Rodríguez-Carvajal, J., *Phys. B Condens. Matter* **1993**, 192 (1–2), 55–69.
- [2]. Hancock, J. D., and J. H. Sharp., *J. Am. Ceram. Soc.* **1972**, 55.2: 74-77.

Chapter 3

This chapter is partially adapted to the following publication and manuscript:

One-step versatile room temperature synthesis of metal(IV) carboxylate MOFs

Angew. Chem. Int. Ed. **2021**, 60, 4282–4288

Shan Dai et al.

Direct preparation of highly crystalline Ce-UiO-66-NH₂ and other benchmark Ce(IV)-MOFs at room temperature

Shan Dai et al.

Table of Contents

Contributions to this research.....	127
Article	128
1. Introduction	128
2. Results and discussion	131
3. Conclusion	136
References	137
Supporting information	140
Article	156
1. Introduction	156
2. Results and discussion	157
3. Conclusion	161
References	162
Supporting information	164

Contributions to this research

The initial idea was proposed by myself after the EuroMOF2019 conference. I started the all experimental investigation and data analysis by myself. The optimization of the synthesis was tried according to my previous experience on stepwise room temperature synthesis. I used many characterizations in this work, for instance, PXRD, TGA, FT-IR, 77K N₂ isotherms, SEM, and *in-situ* PXRD. Dr. Xiangzhen Xu helped to do the TEM. Farid taught me how to perform the scale-up system in ESPCI, Paris. Dr. Shyamapada Nandi helped to perform the vapor adsorption tests. Finally, I analyzed all the data and wrote the manuscript by myself. My supervisors discussed with me throughout the project.

In the second part of this chapter, I conceptualized the synthesis of temperature-sensitive Ce(IV)-UiO-66-NH₂ at room temperature in green solvents. The generality of this synthesis was demonstrated by myself. Ce-UiO-66-X (X= H, -NO₂, -COOH, -Br), Ce-DUT-67(PDA), and Ce-MOF-808 were all synthesized and characterized by me. Routine techniques as abovementioned were similarly applied. The collaboration on the water-splitting evaluation by using Ce-MOFs is still in progress with Dr. Sergio Navalón Oltra, Universidad Politécnica de Valencia, Spain. The initial manuscript was written by me and corrected by my supervisors.

One-step room-temperature synthesis of Metal(IV) carboxylate metal—organic frameworks

Abstract:

The development of room temperature green syntheses of robust MOFs is of great interest to meet the demand of the sustainable chemistry and is a pre-requisite for the incorporation of functional but fragile compounds in water stable MOFs. However, only few ambient conditions routes to produce metal(IV) based MOFs have been reported and most of them suffer from a very low yield and/or multiple steps that preclude their use for most applications. We report here a new versatile one-step synthesis of a series of highly porous M₆ oxoclusters based MOFs (M= Zr, Hf, Ce) at room temperature, including 8 or 12-connected micro/mesoporous solids with different functionalized organic ligands. The resulting compounds show varying degrees of defectivity, particularly for 12-connected phases, while maintaining the chemical stability of the parent MOFs. We propose first insights for the efficient MOF preparation based on In-situ kinetics observations. Remarkably, the synthetic versatility not only allows an efficient room temperature synthesis with a high space-time yield, but also gives possibility to tune the particle size, which therefore paves the way for their practical use.

Introduction:

Room temperature (RT) green-synthesis of Metal-organic frameworks (MOFs) have generated interest in last two decades.^[1] In addition to the interest of industry for lower energy cost and safer conditions, the ambient conditions synthesis could also lead to some property enhancements (e.g. catalysis, gas adsorption) including the use of fragile compounds.^[2] Most low temperature routes reported to date deal with divalent metals based carboxylate MOFs. However, these solids strongly suffer from their poor chemical stability, particularly upon exposure to moisture, which prevents their practical use.^[3] With the more chemically robust Zeolitic Imidazolate Frameworks (ZIFs), low temperature synthesis allows however to construct core-shell materials through the direct formation of ZIFs in the presence of pre-formed functional molecules or nanoparticles in a view of several potential applications (sensing, catalysis, biomedicine...)^[4] Additionally, it is a convenient method to introduce low temperature-induced defects (LTID), as illustrated recently with the RT synthesis of ZIF-67 that led to the improvement of the catalytic activity for the synthesis of cyclic carbonates. It also allows using techniques that requires ambient conditions, such as the investigation of the MOF nucleation-growth kinetics at RT using in-situ Transmission-Electron-Microscope coupled with a liquid cell.^[5]

Trivalent metals (e.g. Fe, Al, Cr) based carboxylate MOFs are generally more chemically robust than the aforementioned divalent ones, particularly with Al(III) and Cr(III).^[6] In such case, the chemistry in play is more complex and developing versatile and easy room temperature synthesis routes is an old but still highly challenging objective.^[7] For example, despite efforts devoted to the sustainable synthesis of Trivalent-MOFs from the MIL family (MIL stands for Materials from Institut Lavoisier), only few of them can be so far synthesized using green solvents at room temperature, including MIL-53(Al), MIL-88A(Fe) and MIL-100(Fe).^[8]

Zr(IV) carboxylate based MOFs are considered as one of the most promising sub-class of MOFs due to their low toxicity and high chemical stability, making them appealing candidates for applications such as heterogeneous catalysis, gas/liquid separation and bio-applications.^[9] These MOFs are typically synthesized using solvothermal conditions with toxic solvents such as DMF. Alternatively, one can synthesize these solids at ambient pressure using conventional^[10] or microwave-assisted heating.^[11]

In 2010, some of us reported a room temperature synthesis of UiO-66 type MOFs, starting from preformed Zr_6 oxoclusters and dicarboxylic acids in DMF.^[12] Since this pioneer study, the reaction of preformed Zr_6 / Zr_{12} oxoclusters with carboxylic acid linkers at room temperature using both solvent and solvent-free reactions has been explored.^[13] However, this strategy relies on the preparation of non-commercially available oxoclusters and in some cases gives rise to poorly crystalline solids with a relatively low yield. Despite the complexity of this RT method, it has been used to incorporate thermally sensitive compounds into Zr-MOFs. For example, Farha et al. reported the RT preparation of the 8-connected Zr-MOF NU-901 via a two steps approach, allowing the formation of core-shell Pd Nanorods@NU-901 for selective surface-enhanced Raman spectroscopy.^[14] RT routes to prepare metal(IV) MOFs is also of interest to produce LTID and tune their properties, including porosity, Lewis acidity and hydrophilicity.^[15]

Few recent reports describe one-step RT synthetic approaches of UiO-type MOFs.^[8b, 16] However, they rely on specific reactants or additives to promote nucleation, associated to cost issues and/or to the presence of impurities in the resulting products. Therefore, despite promises, there is still a

strong need to develop a versatile simple higher yield and environmentally friendly RT approach to produce robust metal(IV) MOFs.

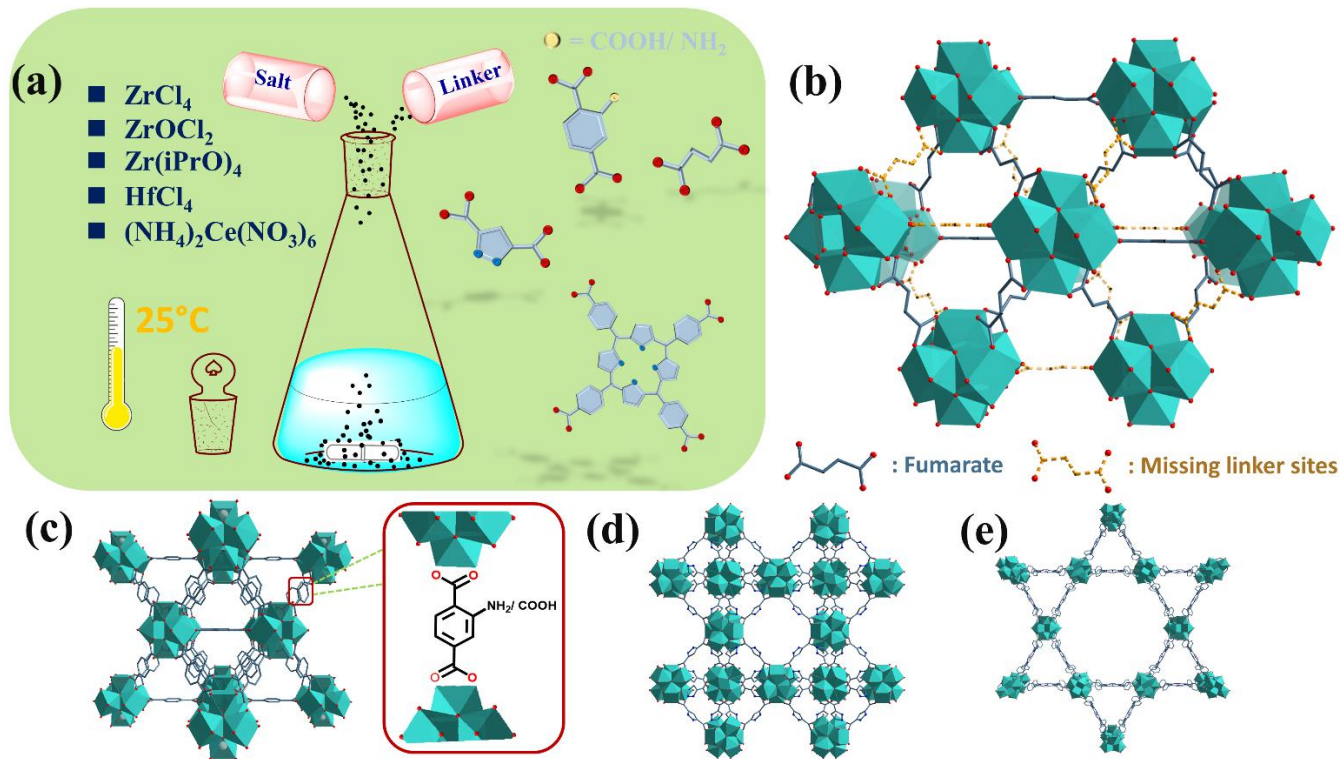


Figure 1. Schematic diagram of the room temperature one-step approach (a). Representative of the crystal structures of MOF-801(Zr, Hf, Ce) viewed along (101) plane and the illustration of existing defects (b), UiO-66-COOH/ NH_2 (c), DUT-67(PDA) (d) and PCN-222 (e). Metal polyhedra, carbon and oxygen atoms are in cyan, black and red, respectively (hydrogen atoms have been omitted for the sake of clarity).

Here, we report a new more efficient one-step environmentally friendly route for the synthesis of metal(IV)-based MOFs at room temperature, including archetypical MOFs based either on 12-connected (MOF-801, UiO-66- NH_2 , UiO-66-COOH) and 8-connected (DUT-67, PCN-222) M_6 oxoclusters ($\text{M}=\text{Zr}$, Hf , Ce). MOF-801 is used as a representative example in order to demonstrate the broad scope of available synthetic conditions, including the use of organic or inorganic Zr(IV) salts, of several tetravalent metal ions (Zr(IV), Hf(IV) or Ce(IV)) and of different types of modulators. In a second step, the extension of this strategy to several other benchmark MOFs is described. *In-situ* PXRD technique is finally considered to shed light on the nucleation/growth process, revealing the importance of the concentration on the synthetic efficiency. Finally, we demonstrate how our findings enable the successful laboratory pilot scale production of MOF-801, with a space-time yield (STY) of $168 \text{ kg/m}^3/\text{day}$, among the highest for the RT synthesis of Zr-MOFs. We believe such novel green ambient conditions synthesis routes of Zr(IV)-carboxylate based MOFs could not only be extended to series of benchmark MOFs on a larger scale, paving the way towards their industrial production, but also be applied to combine MOFs with temperature sensitive species to develop new functional MOFs based composites.

Results and Discussion

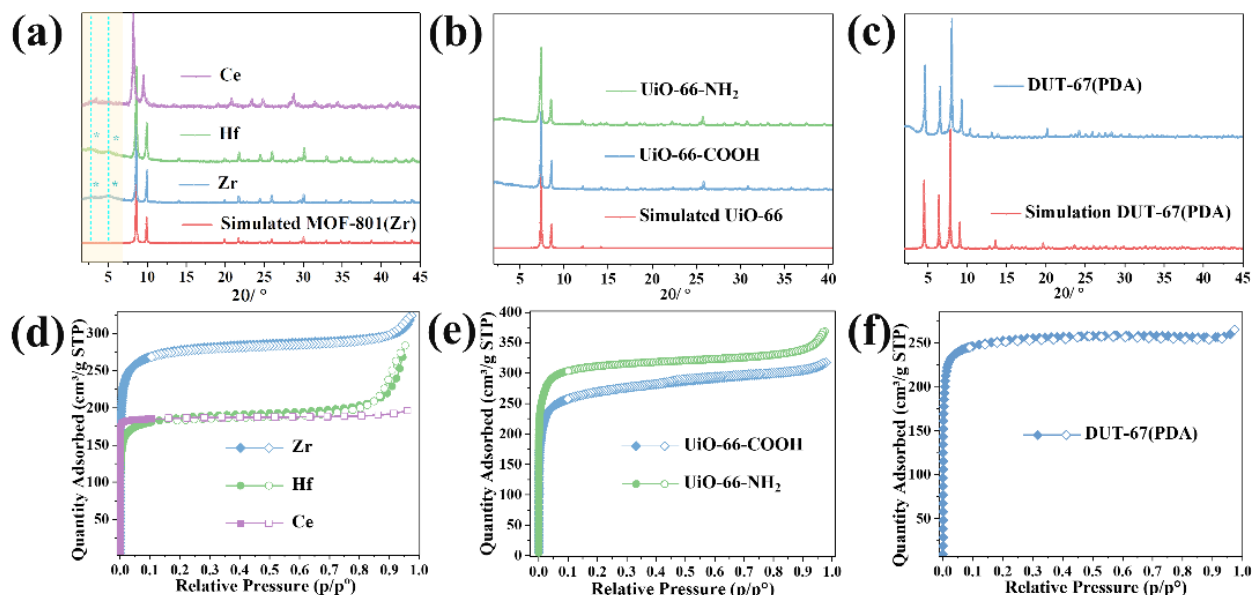
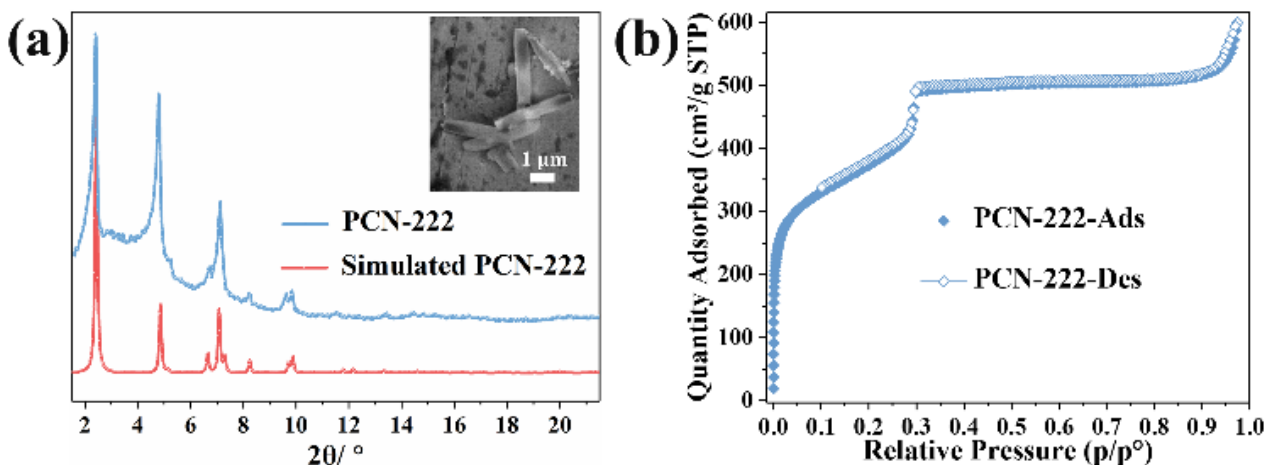


Figure 2. PXRD patterns ($\lambda_{Cu}=1.5406\text{\AA}$) of: (a) MOF-801(Zr), MOF-801(Hf), MOF-801(Ce), (b) UiO-66-NH₂ and UiO-66-COOH, (c) DUT-67(PDA) and the corresponding simulated PXRD patterns. N₂ adsorption-desorption isotherms (adsorption, filled symbols; desorption, empty symbols) at 77K (P₀=1 atm) of: (d) MOF-801(Zr), MOF-801(Hf), MOF-801(Ce), (e) UiO-66-NH₂ and UiO-66-COOH, (f) DUT-67(PDA).

MOF-801 or Zr-fumarate was selected as a prototypical example for our investigation due to the good solubility of fumaric acid in H₂O and the low price of the reactants. It presents a similar structure as UiO-66 with fumaric acid as linker instead of terephthalic acid. As illustrated in Figure 1(b), each Zr₆ oxocluster is coordinated to 12 fumaric acids, giving rise to a cubic 3D structure with two 5.6Å and 4.8Å types of tetrahedral cages and one 7.4Å type of octahedral cage. PXRD patterns evidenced the successful synthesis of well-crystallized MOF-801 with Zr(IV), Hf(IV) and Ce(IV) in water at room temperature using formic acid as modulator (Figure 2(a)). Hf(IV)-based and Ce(IV)-based MOF analogues are usually less investigated comparing to Zr(IV) ones, despite their unique advantages in terms of high acidity and/or redox properties.^[17] A slight shift of the diffraction peaks was observed for MOF-801(Ce) due to the larger atomic radius of Ce(IV) compared to Zr(IV). Additionally, as formic acid is usually considered as a less favorable inhibitor due to its higher acidic character, we also demonstrated the possibility (see Figure S15) to synthesize MOF-801(Zr) using acetic acid as inhibitor. The successful use of diverse metal salts in this approach, such as ZrOCl₂ and Zr(iPrO)₄ for the synthesis of MOF-801(Zr) was also demonstrated (Figure S16). This is of interest particularly if one wants to minimize any corrosion or moisture stability issues when using ZrCl₄. N₂ adsorption-desorption isotherms at 77K (Figure 2(d) and Table 1) evidenced that these materials are highly porous, with Brunauer-Emmett-Teller (BET) surface area of 1035(±5) m²/g (MOF-801(Zr)), 735(±6) m²/g (MOF-801(Hf)) and 780(±5) m²/g (MOF-801(Ce)) respectively. These values are slightly larger than the pristine MOF-801(Zr)

(680 m²/g), which suggests that these MOFs present a significant amount of defects, as reported previously using other synthesis conditions.^[18] In order to determine the defect nature (missing nodes or linkers), FT-IR analysis was carried out (Figure S1). All the materials showed only vibrations associated to COO⁻ groups coordinated to Zr(IV), without traces of uncoordinated fumaric acid, suggesting that missing linkers are more plausible than missing nodes. Thermogravimetric analysis (TGA) further provided the evidence of the lower connectivity of the Zr₆ nodes compared to the ideal structure. According to the ratio of decomposed content of ligands and remaining metal oxide calculated from TGA (Table 1, Figure S2(a)-(c)), a connectivity between 7 and 10 is obtained depending on the samples, while a connectivity of 12 is expected for the perfect structure. Finally, in the case of MOF-801(Zr) and MOF-801(Hf), two low-intensity peaks at low angle (marked with blue dash line) appeared, in agreement with the presence of missing-linker defects in the body-centered initial *fcu* structure.^[19]

In a second step, we extended our strategy to a broader scope of Zr(IV)-based MOFs with different organic ligands and topologies to highlight the versatility of the approach. As shown in Figure 2(b, c), PXRD patterns evidenced that highly crystalline UiO-66-NH₂, UiO-66-COOH (*fcu* topology, see structure in Figure 1(c)) and DUT-67(PDA) (*reo* topology, see structure in Figure 1(d)) were synthesized successfully following a similar synthesis protocol. Notably, synthesizing the functionalized UiO-66-COOH at room temperature is not straightforward due to the lower pK_a of Trimellitic acid in comparison to other derivatives (e.g. -NH₂, -H) that usually favors the formation of amorphous compounds.^[8b, 13c] The room temperature obtained MOFs presented higher surface areas (UiO-66-NH₂ (1255(±5) m²/g), UiO-66-COOH (1050(±6) m²/g) and DUT-67(PDA) (1020(±6) m²/g)) than the theoretical values (see Figure 2(e, f)), in agreement with the presence of defects, as mentioned above for MOF-801 (see Table 1). Pore size distribution for UiO-type MOFs (see Figure S10(a), (b)) revealed indeed the defect-engineering pore size expansion, showing a wide pore size distribution from 0.6 to 1.6 nm, which is much larger than the one deduced from the crystal structures^[20]. In the latter case, DUT-67(PDA) showed a similar



77K N₂ adsorption capacity than the reported one obtained on a compound prepared using solvothermal synthesis. This is in agreement with TGA, which indicates that only 0.2 linker per metal nodes are missing in this case.^[21]

Figure 3. (a) Experimental and simulated PXRD patterns ($\lambda_{\text{Cu}}=1.5406\text{\AA}$) of PCN-222, (b) N_2 adsorption-desorption isotherm at 77K of PCN-222 ($P_0=1\text{ atm}$).

In addition to the use of short dicarboxylic ligands described above, PCN-222, a highly chemically stable MOF based on a 4,8-connected framework (see structure in Figure 1(e)) comprising Zr_6 oxoclusters and TCPP (tetrakis(4-carboxyphenyl)porphyrin), was synthesized at room temperature.^[22] Due to the poor solubility of TCPP in many solvents, including DMF, we used $\text{Zr}(\text{iPrO})_4$ (Zirconium(IV) isopropoxide), a more basic zirconium source than ZrCl_4 and ZrOCl_2 that may enhance the linker solubility via a partial deprotonation of TCPP. Figure 3(a) shows that highly crystalline PCN-222 microcrystals were obtained, confirming that our room temperature synthesis strategy is also suitable for metal(IV) carboxylate MOFs built with large poorly soluble ligands. Even though the product yield (56%) is lower than for the other cases presented in this work, it is still comparable with the reported one using high-temperature synthesis in DMF.^[22] Apart from the low solubility of TCPP in EtOH, the contamination of the product during the synthesis by coordination of TCPP to unsaturated Zr sites in the large hexagonal pores of the MOF can further decrease the product yield. Notably, when one considers the preparation MOFs based on polyphenylene ligands and high valence metal ions, mixed phases are often obtained, which was not the case here as confirmed by PXRD and SEM (Figure S11).^[23] N_2 adsorption-desorption isotherms in Figure 3(b) showed high porosity and a typical shape of isotherm due to the hierarchical pore of PCN-222.

In order to investigate the chemical stability of all these synthesized MOFs, the compounds were soaked in different chemical environments (initial pH= 0, 12, boiling water for 2 days). PXRD measurements in Figure S3-9 proved that all these materials present -as previously reported- a high chemical stability even in presence of a large amount of missing ligands.

The above-mentioned results demonstrated the versatility of this new environmentally friendly synthesis approach. We then investigated the possibility to take benefit from this strategy to produce nanosized MOFs (nanoMOFs). These latter have been extensively studied for their appealing advantages in catalysis, sensing, bio-applications and membrane science.^[24] Usually, the particle size tuning was realized following several strategies such as microwave heating, sonication, fluidics, or the use of emulsions, modulators, shorter reaction time or temperature control.^[25] In spite of diverse synthetic methods, a scalable green synthesis of nanoMOFs with high product yield is still highly demanded and only few examples have been reported so far.^[26] Here, in the case of MOF-801(Zr), decreasing the amount of modulator allowed particle size tuning from ~220 nm to ~45 nm according to SEM, TEM images (Figure S12 and Figure S13) and PXRD (see broadening of the Bragg peaks on Figure S14). Noteworthy, whatever the particle size, a well-crystalline MOF-801(Zr) without any decrease of the yield (89%).

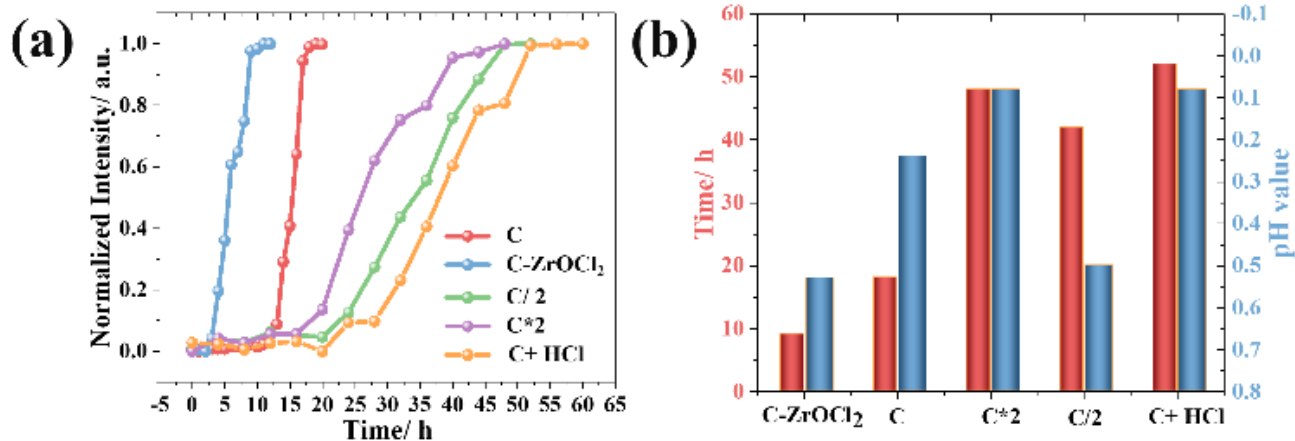


Figure 4. (a) Plot of synthesis time versus the intensities of the strongest (1, 1, 1) reflection of MOF-801 with varying precursors concentrations (the reactions were considered saturated when the intensities did not grow significantly), C represented the MOF-801 synthesized in 0.15 mmol/mL precursors concentration, C*2 represented the 2 times multiple concentration, C/2 represented the 2 times divided concentration, C-ZrOCl₂ represented the MOF-801 synthesized with ZrOCl₂ in 0.15 mmol/mL concentration, C+ HCl represented the MOF-801 synthesized in 0.15 mmol/mL reactant with the presence 0.6 mmol/L of HCl. (b) Correlations between the synthesis time and pH value for samples described in (a).

In order to prepare Zr-MOFs at ambient temperature without any detrimental effect on the kinetics of nucleation, the lowering of activation energies is needed. Previous reports showed that activation energies of nucleation and growth are close for UiO-type MOFs (71 kJ mol⁻¹ vs 66 kJ mol⁻¹).^[27] Few factors have been found to lower down these values, including the addition of HCl,^[28] water and/or the use of more soluble ligands.^[27, 29] In our case, the mixture of ZrCl₄ (or ZrOCl₂) and pure H₂O (~300 equiv H₂O/ Zr) led to relatively low pH values (≈0.24, experimentally) in comparison to the conventional synthesis in DMF but hydrolysis of Zr⁴⁺ species was favored by the excess of water that led to the easier formation of Zr₆ oxoclusters with bridging μ₃-O and μ₃-OH groups. Thus, this might explain why our conditions favor the formation of Zr₆ oxoclusters at room temperature.^[30] Moreover, the Arrhenius activation energies for the MOF growth were expected to be relatively low owing to the reasonable solubility of the chosen linkers in H₂O/ Ethanol. The temperature-dependent *in-situ* nucleation experiments reported previously in the presence of H₂O, ZrCl₄/ ZrOCl₂, HCl, and DMF by some of us indicated that lowering down the temperature had a significantly negative impact on the nucleation time of UiO-66, particularly when the temperature was lower than 90°C.^[28] In a nut-shell, the nucleation time was increased ca. 2 times when decreasing every 10°C. Accordingly, keeping identical the other synthesis parameters, the nucleation time should have reached almost 40 days at room temperature. In our case, the synthesis time was only of 1-2 days (spinning in a capillary). Thus, apart from the synthetic parameters aforementioned, we hypothesize that the use of lower concentrations of Zr precursors here probably compensate the lower temperature due to the less acidic pHs of the solutions. Indeed, higher pH most likely accelerate the nucleation/growth process as the ligands are more easily deprotonated and the formation of Zr oxo-clusters is favored in such conditions.^{[28,}

^{31]} To verify such assumptions, we followed *in-situ* the nucleation-growth processes at room

temperature using PXRD (shown in Figure S17-21) in order to estimate kinetics parameters. It can be concluded that 1) no intermediate states were detected during the synthesis process, 2) nucleation-growth processes of MOF-801 at different concentrations (0.3 mmol/mL and 0.075 mmol/mL) (Figure 4(a-b)) were twice longer (48h, 42h, respectively) than that of MOF-801 at 0.15 mmol/mL. This means that further tuning the concentration, higher or lower, is here not advantageous if one wants to faster the synthesis of MOF-801. When considering a higher concentration (0.3 mmol/mL), the solution becomes more acidic (initial pH=0.08), which may slightly inhibit the MOF growth and slow down its crystallization. To confirm this point, a synthesis was performed with the initial reactant concentrations (0.15 mmol/mL) in presence of 0.6 mmol/mL of HCl. The addition of HCl lowers the initial pH to a value similar to the synthesis performed with 0.3 mmol/mL reactant concentrations. The kinetics showed a similar trend in both cases, strongly evidencing the detrimental effect of low initial pH on the reaction kinetics. When using a lower concentration (0.075 mmol/mL, pH= 0.50), we hypothesize that even if the pH is slightly higher, the high dilution of the reactants may lead to a deceleration of the kinetics. Additionally, when replacing $ZrCl_4$ by the less acidic $ZrOCl_2$ while keeping other parameters unchanged, faster nucleation-growth processes (from 19 h to 9h) were observed as a consequence of the presence of pre-formed Zr-oxo or Zr-OH bonds in $ZrOCl_2$. As a whole, our findings reveal that in addition to the typical parameters investigated so far (temperature, pH, metal source...), the concentration of the reactants is also playing a key role in the synthesis of Zr-MOF, particularly at room temperature.

Room temperature synthesis of Metal (IV) based MOFs, with its lower energy penalty and safer conditions, endows a great potential for a more sustainable industrial production, particularly for more robust Zr-MOFs. However, the previous examples of lab-scale synthesis of MOFs at room temperature led in most cases to very low space-time yields (STY), less than $1 \text{ kg/m}^3/\text{day}$,^[32] which does not meet at all the needs of industry. In the case of Zr-MOFs, this is mainly due to their prolonged synthesis time at room temperature.^[33] Taking benefit from our preliminary crystallization study, we therefore scaled-up the benchmark Zr MOF MOF-801 by using a 5L pilot scale reactor with mechanical stirring (Figure 5(a)).

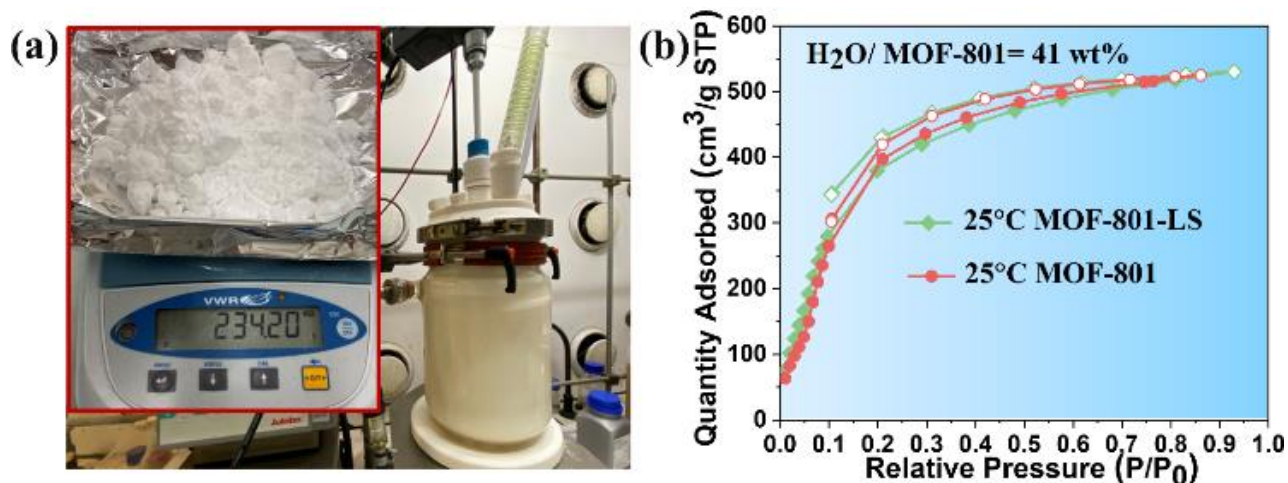


Figure 5. (a) 5L glass reactor laboratory pilot scale system for the upscaling synthesis of MOF-801-LS (large scale), inserted picture: mass of product after synthesis, washing and drying, (b) Water sorption isotherms (adsorption, filled symbols; desorption, open symbols) of MOF-801-LS (large-scale) and MOF-801 (lab-scale) at 25°C.

Table 1. Summary of the properties of room temperature synthesized MOFs presented in this work

				(m ² /g)			TNCL
1	MOF-801(Zr)	12-connected	H ₂ O,	1035	1.2	0.43	4.1/ 6
2	MOF-801(Hf)	12-connected	H ₂ O	737	0.8	0.26	3.5/ 6
3	MOF-801(Ce)	12-connected	H ₂ O	781	0.6	0.3	5.3/ 6
4	UiO-66-NH ₂	12-connected	H ₂ O EtOH	1256	0.7, 1.5	0.5	4.7/ 6
5	UiO-66-COOH	12-connected	H ₂ O	1052	0.8, 1.2	0.4	3.8/ 6
6	DUT-67(PDA)	8-connected	H ₂ O	1018	0.7, 1.2	0.41	3.8/ 4
7	PCN-222	8-connected	H ₂ O EtOH	1394	1.2, 1.6, 3.5	0.86	1.5/ 2

TNCL= Theoretical number of coordinated ligands

The space-time yield of the product was calculated according to the dry solid collected after washing and drying steps, reaching 168 kg/m³/day. To the best of our knowledge, this is the first example of room temperature synthesized Zr-MOF with such a high space-time yield. This quality of a scaled-up material in comparison with a small scale laboratory sample is also a prerequisite for industrial applications. As MOF-801 is a prominent example of sorbent suitable for heat reallocation applications,^[34] we investigated the water sorption properties (Figure 5(b)) of our scaled up material. Noteworthy it led to a consistently highly crystalline solid in comparison to the lab-scale synthesis (see Figure S22), attaining a remarkably high water adsorption capacity of 41 wt% H₂O/ MOF. The isotherm is of a Type-I shape mainly due to the presence of defects in the structure, which on the one hand increases the hydrophilicity due to the increased Coulomb interaction from the hydroxyl terminal group at the defect sites, while on the other hand expands the pore volume of the MOF due to the missing linker effect aforementioned.

Conclusion

In summary, we report here a new facile and versatile approach for the one-step synthesis of a series of highly porous metal(IV) carboxylate MOFs (M=Zr, Hf, Ce) including five 12-connected and two 8-connected MOFs, using greener ambient temperature conditions. Not only this allowed

us to produce high quality crystalline and porous robust metal(IV) carboxylate MOFs with varying metal salts, but also, through a tuning of the synthetic parameters, enabled a control the MOF particle size at the nanoscale. Finally, we evaluated the possibility of scaling-up the synthesis with the use of 5L pilot scale system, evidencing a highest space-time yield for the room temperature synthesis of MOF-801(Zr). As a whole, our method paves the way for the versatile RT synthesis of series of metal(IV)-MOFs that is of strong interest for many applications as well as for their industrial production under sustainable conditions.

Acknowledgements

S. Dai acknowledges the support of CSC scholarship (201706140196).

Keywords: Metal (IV) Metal-organic frameworks • Room temperature synthesis • Defective MOF • Scale-up synthesis

Reference

- [1] S. Yuan, L. Feng, K. C. Wang, J. D. Pang, M. Bosch, C. Lollar, Y. J. Sun, J. S. Qin, X. Y. Yang, P. Zhang, Q. Wang, L. F. Zou, Y. M. Zhang, L. L. Zhang, Y. Fang, J. L. Li, H. C. Zhou, *Adv. Mater.* **2018**, *30*.
- [2] a) P. A. Julien, C. Mottillo, T. Friscic, *Green Chem.* **2017**, *19*, 2729-2747; b) Q. Gao, S. Y. Xu, C. Guo, Y. G. Chen, L. Y. Wang, *Acs Appl. Mater. & Interfaces.* **2018**, *10*, 16059-16065; c) D. S. Sholl, R. P. Lively, *J. Phys. Chem. Lett.* **2015**, *6*, 3437-3444.
- [3] A. J. Howarth, Y. Y. Liu, P. Li, Z. Y. Li, T. C. Wang, J. Hupp, O. K. Farha, *Nat. Rev. Mater.* **2016**, *1*, 15.
- [4] G. Lu, S. Li, Z. Guo, O. K. Farha, B. G. Hauser, X. Qi, Y. Wang, X. Wang, S. Han, X. Liu, J. S. DuChene, H. Zhang, Q. Zhang, X. Chen, J. Ma, S. C. Loo, W. D. Wei, Y. Yang, J. T. Hupp, F. Huo, *Nat. Chem.* **2012**, *4*, 310-316.
- [5] a) J. P. Patterson, P. Abellan, M. S. Denny, C. Park, N. D. Browning, S. M. Cohen, J. E. Evans, N. C. Gianneschi, *J. Am. Chem. Soc.* **2015**, *137*, 7322-7328; b) J. W. Hou, P. D. Sutrisna, Y. T. Zhang, V. Chen, *Angew. Chem., Int. Ed.* **2016**, *55*, 3947-3951; c) C. X. Duan, Y. Yu, P. F. Yang, X. L. Zhang, F. E. Li, L. B. Li, H. X. Xi, *Ind. Eng. Chem. Res.* **2020**, *59*, 774-782; d) B. Q. Yuan, X. Wang, X. Zhou, J. Xiao, Z. Li, *Chem. Eng. J.* **2019**, *355*, 679-686.
- [6] a) G. Férey, C. Mellot-Draznieks, C. Serre, F. Millange, J. Dutour, S. Surble, I. Margiolaki, *Science* **2005**, *309*, 2040-2042; b) C. Serre, F. Millange, C. Thouvenot, M. Nogues, G. Marsolier, D. Louer, G. Férey, *J. Am. Chem. Soc.* **2002**, *124*, 13519-13526.
- [7] S. J. Wang, C. Serre, *Acs Sustainable Chem. Eng.* **2019**, *7*, 11911-11927.
- [8] a) M. Sanchez-Sanchez, N. Getachew, K. Diaz, M. Diaz-Garcia, Y. Chebude, I. Diaz, *Green Chem.* **2015**, *17*, 1500-1509; b) C. Avci-Camur, J. Perez-Carvajal, I. Imaz, D. Maspoch, *Acs Sustainable Chem. Eng.* **2018**, *6*, 14554-14560; c) K. Guesh, C. A. D. Caiuby, A. Mayoral, M. Diaz-Garcia, I. Diaz, M. Sanchez-Sanchez, *Cryst. Growth & Des.* **2017**, *17*, 1806-1813; d) C. Serre, F. Millange, S. Surblé, G. Férey, *Angew. Chem.* **2004**, *116*, 6445-6449.
- [9] a) C. C. Cao, C. X. Chen, Z. W. Wei, Q. F. Qiu, N. X. Zhu, Y. Y. Xiong, J. J. Jiang, D. W. Wang, C. Y. Su, *J. Am. Chem. Soc.* **2019**, *141*, 2589-2593; b) G. D. Pirngruber, L. Hamon, S. Bourrelly, P. L. Llewellyn, E. Lenoir, V. Guillermin, C. Serre, T. Devic, *ChemSusChem* **2012**, *5*, 762-776; c) M. H. Teplerisky, M. Fantham, P. Li, T. C. Wang, J. P. Mehta, L. J. Young, P. Z. Moghadam,

- J. T. Hupp, O. K. Farha, C. F. Kaminski, D. Fairen-Jimenez, *J. Am. Chem. Soc.* **2017**, *139*, 7522-7532.
- [10] a) S. Rapti, A. Pournara, D. Sarma, I. T. Papadas, G. S. Armatas, Y. S. Hassan, M. H. Alkordi, M. G. Kanatzidis, M. J. Manos, *Inorg. Chem. Front.* **2016**, *3*, 635-644; b) Q. Y. Yang, S. Vaesen, F. Ragon, A. D. Wiersum, D. Wu, A. Lago, T. Devic, C. Martineau, F. Taulelle, P. L. Llewellyn, H. Jovic, C. L. Zhong, C. Serre, G. De Weireld, G. Maurin, *Angew. Chem., Int. Ed.* **2013**, *52*, 10316-10320.
- [11] H. Reinsch, S. Waitschat, S. M. Chavan, K. P. Lillerud, N. Stock, *Eur. J. Inorg. Chem.* **2016**, 4490-4498.
- [12] V. Guillerm, S. Gross, C. Serre, T. Devic, M. Bauer, G. Ferey, *Chem. Commun. (Camb)* **2010**, *46*, 767-769.
- [13] a) B. Karadeniz, A. J. Howarth, T. Stolar, T. Islamoglu, I. Dejanović, M. Tireli, M. C. Wasson, S.-Y. Moon, O. K. Farha, T. Friščić, K. Užarević, *Acs Sustainable Chem. Eng.* **2018**, *6*, 15841-15849; b) A. M. Fidelli, B. Karadeniz, A. J. Howarth, I. Huskic, L. S. Germann, I. Halasz, M. Etter, S. Y. Moon, R. E. Dinnebier, V. Stilinovic, O. K. Farha, T. Friscic, U. Z. K., *Chem. Commun. (Camb)* **2018**, *54*, 6999-7002; c) M. R. DeStefano, T. Islamoglu, J. T. Hupp, O. K. Farha, *Chem. Mater.* **2017**, *29*, 1357-1361.
- [14] a) H. Noh, C.-W. Kung, T. Islamoglu, A. W. Peters, Y. Liao, P. Li, S. J. Garibay, X. Zhang, M. R. DeStefano, J. T. Hupp, O. K. Farha, *Chem. Mater.* **2018**, *30*, 2193-2197; b) J. W. M. Osterrieth, D. Wright, H. Noh, C. W. Kung, D. Vulpe, A. Li, J. E. Park, R. P. Van Duyne, P. Z. Moghadam, J. J. Baumberg, O. K. Farha, D. Fairen-Jimenez, *J. Am. Chem. Soc.* **2019**, *141*, 3893-3900.
- [15] a) X. Feng, J. Hajek, H. S. Jena, G. B. Wang, S. K. P. Veerapandian, R. Morent, N. De Geyter, K. Leyssens, A. E. J. Hoffman, V. Meynen, C. Marquez, D. E. De Vos, V. Van Speybroeck, K. Leus, P. Van Der Voort, *J. Am. Chem. Soc.* **2020**, *142*, 3174-3183; b) J. Choi, L.-C. Lin, J. C. Grossman, *J. Phys. Chem. C* **2018**, *122*, 5545-5552; c) C. A. Clark, K. N. Heck, C. D. Powell, M. S. Wong, *Acs Sustainable Chem. Eng.* **2019**, *7*, 6619-6628.
- [16] X. Sang, J. Zhang, J. Xiang, J. Cui, L. Zheng, J. Zhang, Z. Wu, Z. Li, G. Mo, Y. Xu, J. Song, C. Liu, X. Tan, T. Luo, B. Zhang, B. Han, *Nat. Commun.* **2017**, *8*, 175.
- [17] a) S. Rojas-Buzo, P. García-García, A. Corma, *Green Chem.* **2018**, *20*, 3081-3091; b) M. Lammert, M. T. Wharmby, S. Smolders, B. Bueken, A. Lieb, K. A. Lomachenko, D. De Vos, N. Stock, *Chem. Commun.* **2015**, *51*, 12578-12581.
- [18] J. Choi, L. C. Lin, J. C. Grossman, *J. Phys. Chem. C* **2018**, *122*, 5545-5552.
- [19] G. C. Shearer, S. Chavan, J. Ethiraj, J. G. Vitillo, S. Svelle, U. Olsbye, C. Lamberti, S. Bordiga, K. P. Lillerud, *Chem. Mater.* **2014**, *26*, 4068 – 4071.
- [20] a) J. H. Cavka, S. Jakobsen, U. Olsbye, N. Guillou, C. Lamberti, S. Bordiga, K. P. Lillerud, *J. Am. Chem. Soc.* **2008**, *130*, 13850-13851; b) G. R. Cai, H. L. Jiang, *Angew. Chem., Int. Ed.* **2017**, *56*, 563-567.
- [21] a) V. Bon, I. Senkovska, I. A. Baburin, S. Kaskel, *Cryst. Growth & Des.* **2013**, *13*, 1231-1237; b) J. Jacobsen, H. Reinsch, N. Stock, *Inorg. Chem.* **2018**, *57*, 12820-12826.
- [22] D. Feng, Z. Y. Gu, J. R. Li, H. L. Jiang, Z. Wei, H. C. Zhou, *Angew. Chem., Int. Ed.* **2012**, *51*, 10307-10310.
- [23] H. Q. Xu, K. Wang, M. Ding, D. Feng, H. L. Jiang, H. C. Zhou, *J. Am. Chem. Soc.* **2016**, *138*, 5316-5320.
- [24] a) M. Sindoro, N. Yanai, A. Y. Jee, S. Granick, *Accounts Chem. Res.* **2014**, *47*, 459-469; b) O. Shekhah, J. Liu, R. A. Fischer, C. Woll, *Chem. Soc. Rev.* **2011**, *40*, 1081-1106.

- [25] a) W. Morris, S. Z. Wang, D. Cho, E. Auyeung, P. Li, O. K. Farha, C. A. Mirkin, *Acs Appl. Mater. & Interfaces*. **2017**, *9*, 33413-33418; b) H. Bunzen, M. Grzywa, M. Hambach, S. Spirkl, D. Volkmer, *Cryst. Growth & Des.* **2016**, *16*, 3190-3197; c) S. H. Jhung, J. H. Lee, J. W. Yoon, C. Serre, G. Ferey, J. S. Chang, *Adv. Mater.* **2007**, *19*, 121-124; d) S. Dang, Q. L. Zhu, Q. Xu, *Nat. Rev. Mater.* **2018**, *3*, 14.
- [26] a) X. Xiao, L. L. Zou, H. Pang, Q. Xu, *Chem. Soc. Rev.* **2020**, *49*, 301-331. b) M. Panchal, F. Nouar, C. Serre, M. Benzaqui, S. Sene, N. Steunou, M.G. Marques, EP 17305119.4, **2017**.
- [27] G. Zahn, P. Zerner, J. Lippke, F. L. Kempf, S. Lilienthal, C. A. Schröder, A. M. Schneider, P. Behrens, *CrystEngComm* **2014**, *16*, 9198-9207.
- [28] F. Ragon, P. Horcajada, H. Chevreau, Y. K. Hwang, U. H. Lee, S. R. Miller, T. Devic, J. S. Chang, C. Serre, *Inorg. Chem.* **2014**, *53*, 2491-2500.
- [29] F. Ragon, H. Chevreau, T. Devic, C. Serre, P. Horcajada, *Chem. Eur. J.* **2015**, *21*, 7135-7143.
- [30] H. Xu, S. Sommer, N. L. N. Broge, J. Gao, B. B. Iversen, *Chem. Eur. J.* **2019**, *25*, 2051-2058.
- [31] M. Taddei, N. Casati, D. A. Steitz, K. C. Dümbgen, J. A. van Bokhoven, M. Ranocchiari, *CrystEngComm* **2017**, *19*, 3206-3214.
- [32] P. Silva, S. M. F. Vilela, J. P. C. Tome, F. A. A. Paz, *Chem. Soc. Rev.* **2015**, *44*, 6774-6803.
- [33] A. U. Czaja, N. Trukhan, U. Muller, *Chem. Soc. Rev.* **2009**, *38*, 1284-1293.
- [34] X. Liu, X. Wang, F. Kapteijn, *Chem. Rev.* **2020**, *120*, 8303-8377.

Supporting information

Chemicals.

All chemicals were purchased from commercial suppliers and used as received without further purification. Fumaric acid, 99%, Alfa Aesar. 2-Aminoterephthalic acid(BDC-NH₂), 99+%, Acros. 1,2,4-Benzenetricarboxylic acid(BDC-COOH), 98%, Acros. 1H-Pyrazole-3,5-dicarboxylic acid(PDA), 97%, FluoroChem. Tetrakis(4-carboxyphenyl)-porphyrin(TCPP), 97%, TCI. Zirconium(IV) propoxide, ca. 70%, solution in 1-Propanol, Acros. ZrCl₄ anhydrous, 98%, Acros. ZrOCl₂•8H₂O, 98%, Alfa Aesar. HfCl₄, 99%, Acros. Ammonium Cerium(IV) nitrate, 99%, Acros. Formic acid, 98+%, Acros. Ethanol absolute, >=99%, Acros. Acetic acid, 98+%, Fisher. MilliQ water, Millipore system.

Instruments.

Powder X-ray Diffraction (PXRD) data were recorded on a high-throughput Bruker D8 Advance diffractometer working on transmission mode and equipped with a focusing Göbel mirror producing CuK α radiation ($\lambda = 1.5418 \text{ \AA}$) and a LynxEye detector. Nitrogen porosimetry data were collected on a Micromeritics Tristar/ Triflex instrument at 77K (pre-activating samples at 100°C under vacuum, 5 hours). SEM images were recorded with FEI Magellan 400 scanning electron microscope. TGA data were collected on Mettler Toledo TGA/DSC 2, STAR System apparatus with a heating rate of 5 °C/min under the oxygen flow. Mettler Toledo FiveEasy™ Plus pH / mV bench meter. Infrared spectra were measured with a Nicolet iS5 FTIR ThermoFisher spectrometer. In-situ PXRD patterns were collected at room temperature from Bruker D8 Advance diffractometer with a Debye-Scherrer geometry, in the 2 θ range of 6-15°.

Synthesis of MOFs.

Synthesis of MOF-801(Zr): 1.5 mmol (350mg) of ZrCl₄ was weighted in a glass vial, 2 mL of formic acid and 8 mL of distilled water was stepwisely introduced in the reactor, following by 1 minute of stirring at 600 rpm. 1.5 mmol (175 mg) of fumaric acid was subsequently added in the solution. The solution became very cloudy within 12h, indicating the formation of MOF-801(Zr). The product was collected by centrifugation, washed with water and ethanol and finally dried under vacuum. The product yield was 92% based on the Zr(IV) salt due to the excess of ligand.

Synthesis of MOF-801(Hf): The synthesis protocol follows the one of MOF-801-ZrCl₄ except 1.5 mmol (480mg) of HfCl₄ was used instead of ZrCl₄. The product yield was 88% based on the Hf(IV) salt due to the excess of ligand.

Synthesis of MOF-801(Ce): The synthesis protocol follows the one of MOF-801-ZrCl₄ except 1.5 mmol (822 mg) of (NH₄)₂Ce(NO₃)₆ was used instead of ZrCl₄. The product yield was 82% based on the Ce(IV) salt due to the excess of ligand.

Synthesis of UiO-66-COOH: The synthesis protocol follows the one of MOF-801-ZrCl₄ except 3 mL formic acid, 1.5 mmol (350mg) of BDC-COOH and 72h reaction time were used. The product yield was 84% based on the Zr(IV) salt due to the excess of ligand.

Synthesis of DUT-67(PDA): The synthesis protocol follows the one with UiO-66-COOH except 1 mmol (176mg) PDA were used instead. The product yield was 87% based on the Zr(IV) salt due to the excess of ligand.

Synthesis of UiO-66-NH₂: 2 mmol (470 mg) of ZrCl₄ was weighted in a glass vial, 7 mL of formic acid and 16 mL of distilled water were stepwisely introduced in the reactor, following by 1 minute of stirring at 600 rpm. 2 mmol (362 mg) of 2-aminoterephthalic acid (BDC-NH₂) and 20 mL ethanol were subsequently added in solution. The solution became very cloudy solution after 12h, indicating the formation of UiO-66-NH₂. The product was collected by centrifugation, washed with ethanol and acetone and finally dried under vacuum. The product yield was 96% based on the Zr salt due to the excess of ligand.

Synthesis of PCN-222: 0.5 mmol (200 mg) of a 70%wt zirconium isopropoxide solution was weighted in a glass vial, 6 mL of formic acid and 5 mL of distilled water were stepwisely introduced in the reactor, following by 1 minute of stirring at 600 rpm. 0.26 mmol (205 mg) tetrakis(4-carboxyphenyl)porphyrin acid (TCPP) was subsequently added in solution. The color of the solution turned from green to brown after 2 days, indicating the formation of PCN-222. The product was collected by centrifugation and intensively washed with 1M HCl DMF for 5 times. Finally, the solvent was exchanged with acetone and the solid was dried under vacuum. The product yield was 56% based on the Zr salt due to the excess of ligand.

Synthesis of MOF-801-Zr(iPrO)₄: 1.8 mmol (1 g) of a 70%wt Zirconium isopropoxide solution was weighted in a glass vial. 5 mL of formic acid and 16 mL of distilled water were stepwisely introduced in the reactor, following by 1 min of stirring at 600 rpm. 3.5 mmol (414 mg) fumaric acid was subsequently added in solution. The solution became very cloudy solution after 1h, indicating the formation of MOF-801. The product was collected by centrifugation, washed with water and acetone and finally dried under vacuum. The product yield was 95% based on the Zr salt due to the excess of ligand.

Synthesis of MOF-801-ZrOCl₂: The synthesis protocol follows the one of MOF-801-ZrCl₄ except ZrOCl₂•8H₂O is used instead of ZrCl₄. The product yield was 94% based on the Zr(IV) salt due to the excess of ligand.

Synthesis of MOF-801-LS (larger scale): 1.1 mol (350 g) of ZrOCl₂•8H₂O was weighted and dissolved in 4L of distilled H₂O with a mechanical stirring at room temperature (25°C), 0.9L of formic acid was subsequently added in a 5L reactor. Then, 88.5g of fumaric acid was weighted and introduced in the reactor carefully. The solution became very cloudy solution after 4h and was kept stirring for another 1.5h to finalize the preparation. The product was washed using Ethanol, collected by centrifugation and finally dried under vacuum. The mass of product was 234 g after drying. The product yield was 88% based on the Zr salt due to the excess of ligand.

Synthesis of MOF-801(Zr)-37.5%: 1.5 mmol (483mg) of ZrOCl₂•8H₂O was weighted in a glass vial, 3 mL of formic acid and 8 mL of distilled water was stepwisely introduced in the reactor, following by 1 minute of stirring at 600 rpm. 1.5 mmol (175 mg) of fumaric acid was subsequently added in the solution. The solution became very cloudy within 12h, indicating the formation of MOF-801(Zr)-37.5%. The product was collected by centrifugation, washed with water and ethanol and finally dried under vacuum. The product yield was 94% based on the Zr(IV) salt due to the excess of ligand.

Synthesis of MOF-801(Zr)-12.5%: : The synthesis protocol follows the one of MOF-801-37.5% except the volume of formic acid is 1mL. The product yield was 95% based on the Zr(IV) salt due to the excess of ligand.

Table of contents

Figure S1. FT-IR spectrums of as-synthesized isorecticular MOF-801(Zr, Hf, Ce)

Figure S2. TG analysis of the synthesized MOFs

Figure S3-S9. PXRD of chemical stability of all the MOFs in this work

Figure S10. Pore size distribution analysis

Figure S11-S12. SEM image of PCN-222 and MOF-801-37.5%

Figure S13. TEM image of MOF-801-12.5%

Figure S14. PXRD of MOF-801-37.5% and MOF-801-12.5%

Figure S15. PXRD of MOF-801 synthesized with formic acid and acetic acid

Figure S16. PXRD of MOF-801 synthesized with different Zr salts

Figure S17-S21. *In-situ* crystallographic kinetics of MOF-801

Figure S22. PXRD of MOF-801 synthesized at lab-scale and large-scale

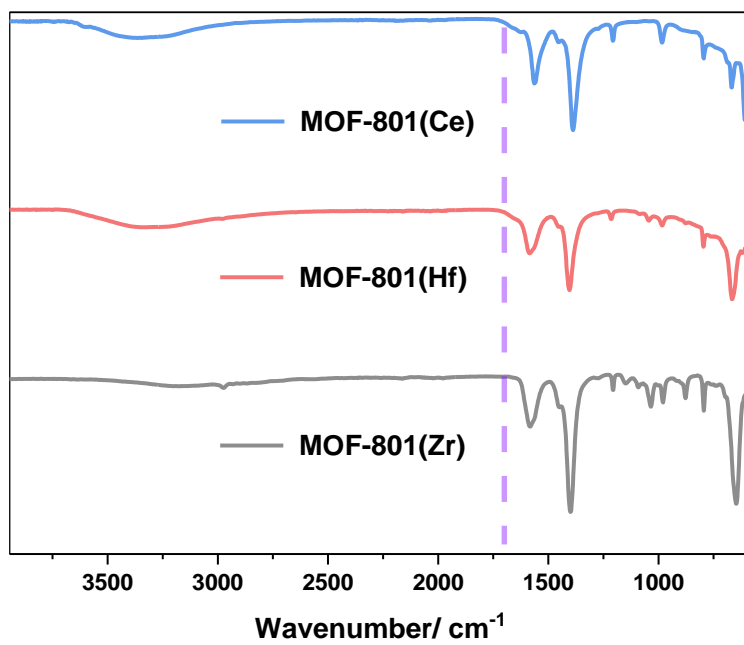


Figure S1, FT-IR spectrums of MOF-801(Zr, Hf, Ce); dotted line indicates the vibration of the uncoordinated carboxylate acid group.

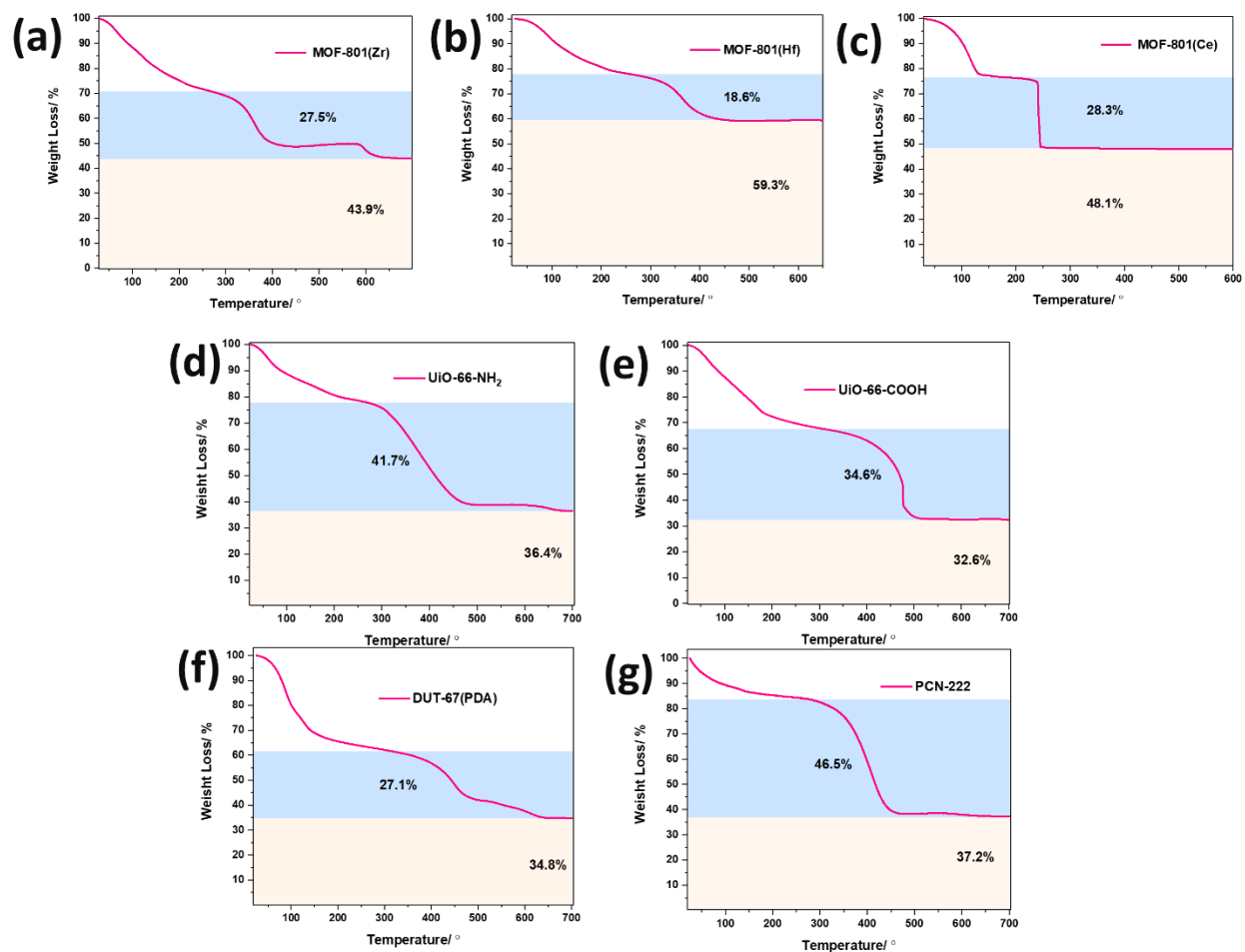


Figure S2. TG analysis of the as-synthesized MOFs: (a) MOF-801(Zr), (b) MOF-801(Hf), (c) MOF-801(Ce), (d) UiO-66-NH₂, (e) UiO-66-COOH, (f) DUT-67(PDA), (g) PCN-222, under oxygen flow with a measuring speed at 5°C/min.

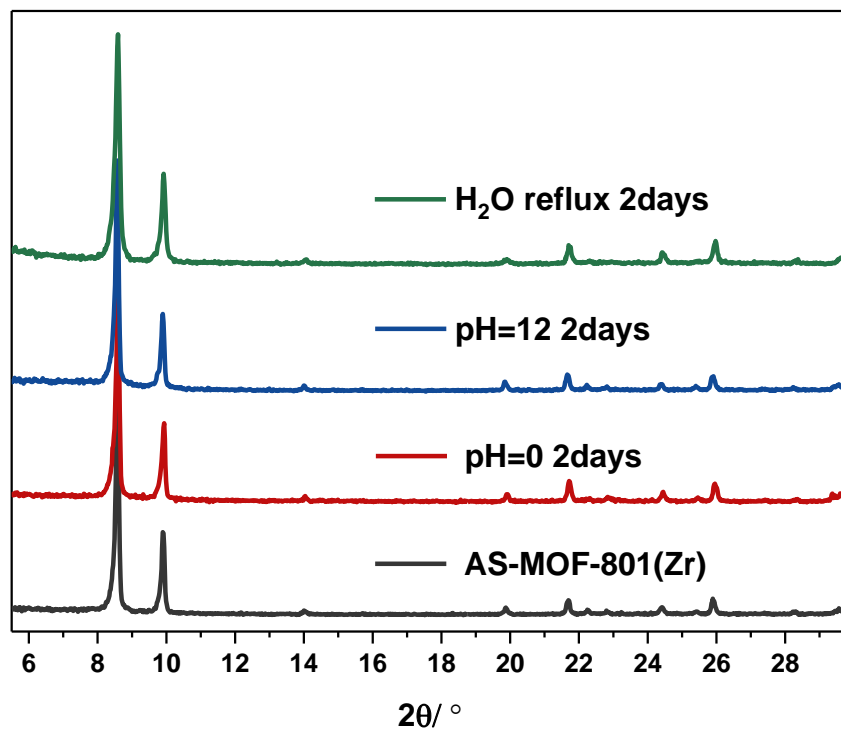


Figure S3. PXRD patterns of MOF-801-ZrCl₄ soaked in extreme chemical conditions, pH=0, pH=12 and boiling water for 2 days.

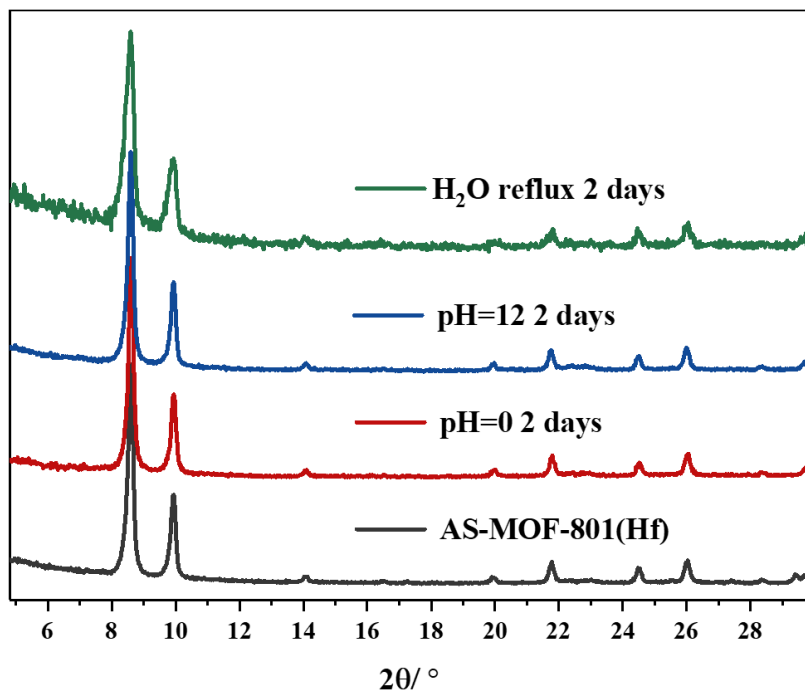


Figure S4. PXRD patterns of MOF-801(Hf) soaked in extreme chemical conditions, pH=0, pH=12 and boiling water for 2 days.

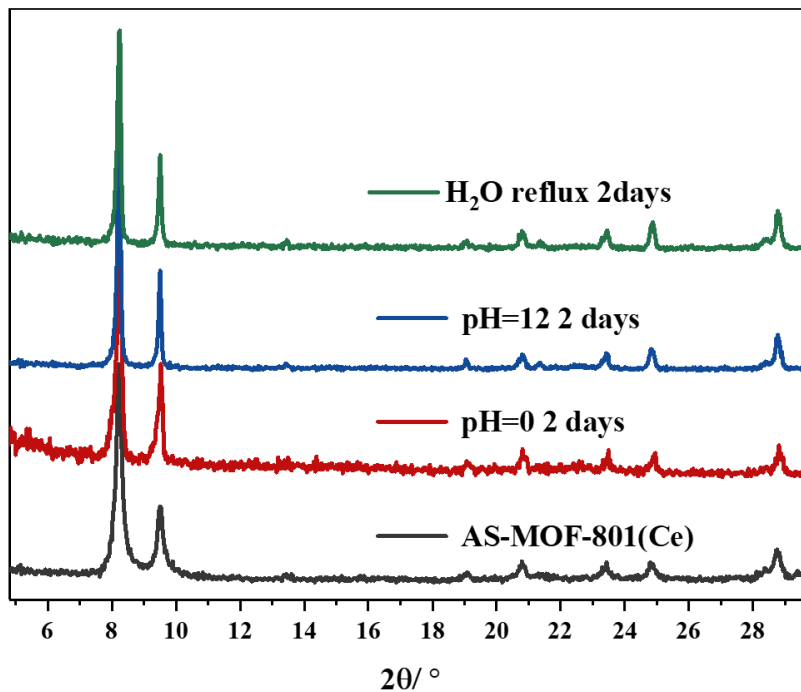


Figure S5. PXRD patterns of MOF-801(Ce) soaked in extreme chemical conditions, pH=0, pH=12 and boiling water for 2 days.

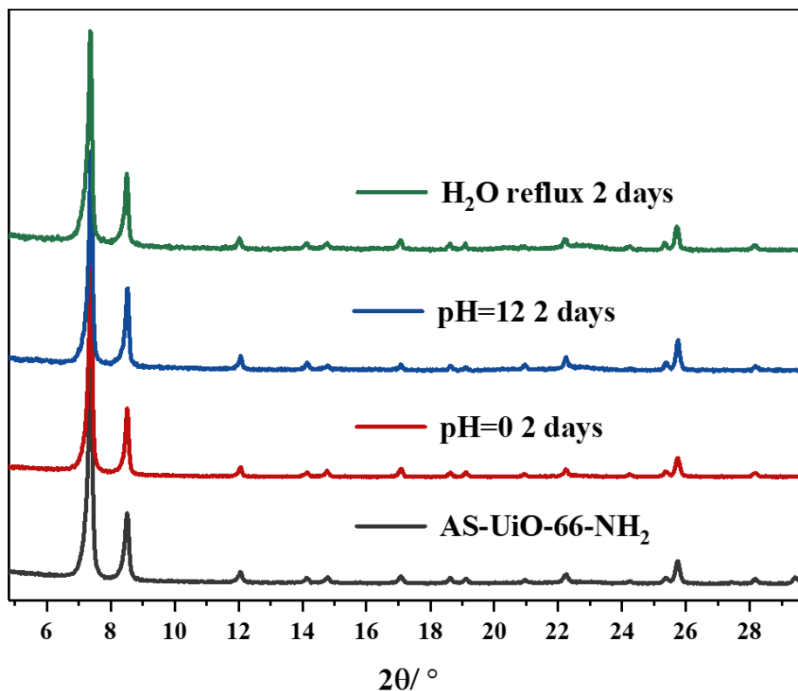


Figure S6. PXRD patterns of UiO-66-NH₂ soaked in extreme chemical conditions, pH=0, pH=12 and boiling water for 2 days.

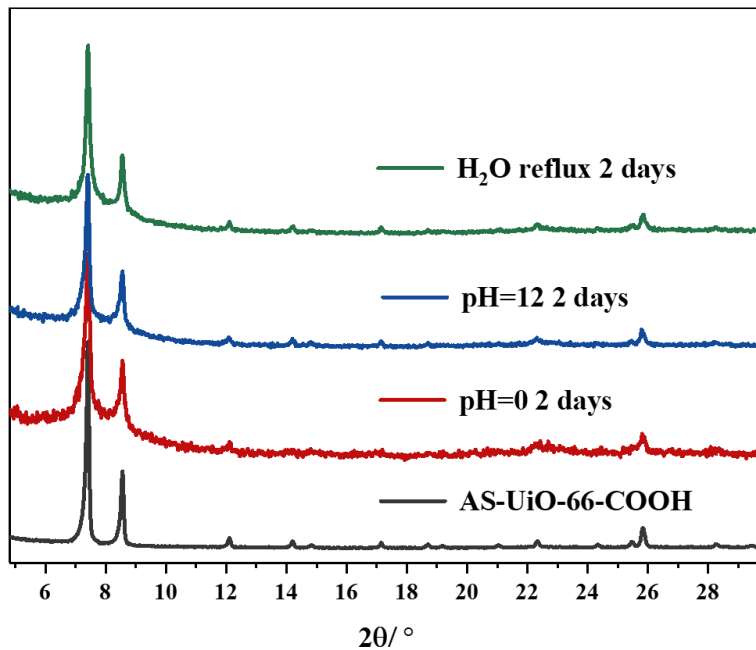


Figure S7. PXRD patterns of UiO-66-COOH soaked in extreme chemical conditions, pH=0, pH=12 and boiling water for 2 days.

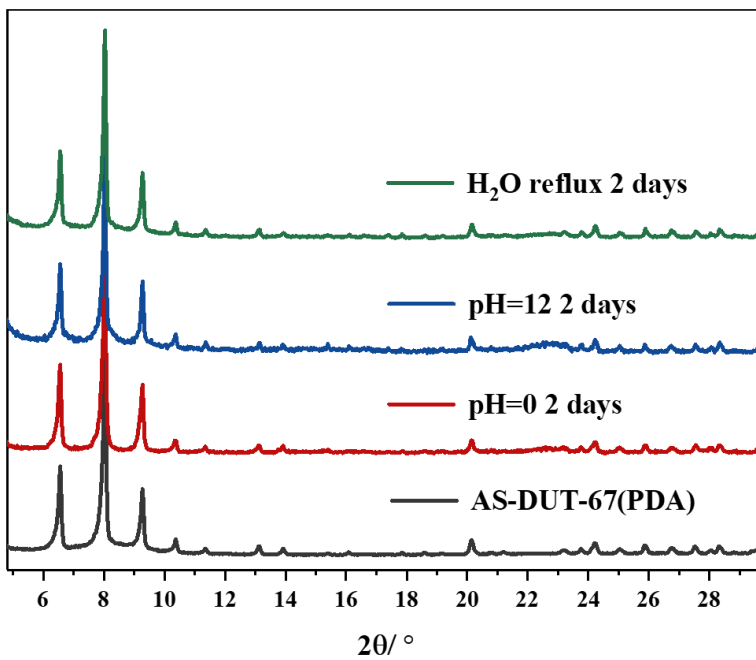


Figure S8. PXRD patterns of DUT-67(PDA) soaked in extreme chemical conditions, pH=0, pH=12 and boiling water for 2 days.

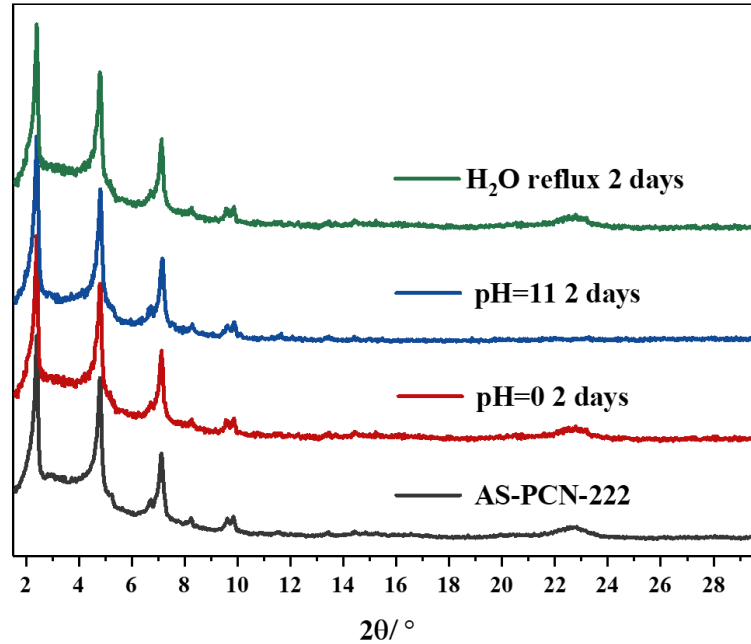


Figure S9. PXRD patterns of PCN-222 soaked in extreme chemical conditions, pH=0, pH=11 and boiling water for 2 days.

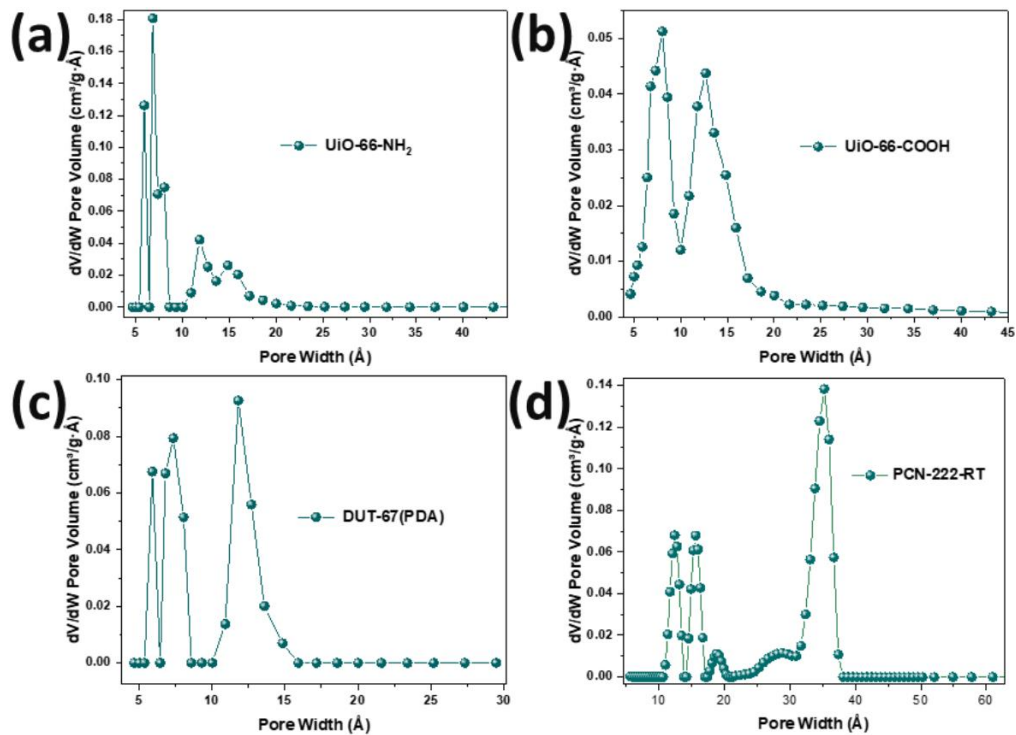


Figure S10. Pore size distribution simulations of (a) UiO-66-NH₂, (b) UiO-66-COOH, (c) DUT-67(PDA) through N₂-DFT model and the Geometry of slit, (d) Pore size distribution simulation of PCN-222 through N₂-DFT model and the Geometry of cylinder.

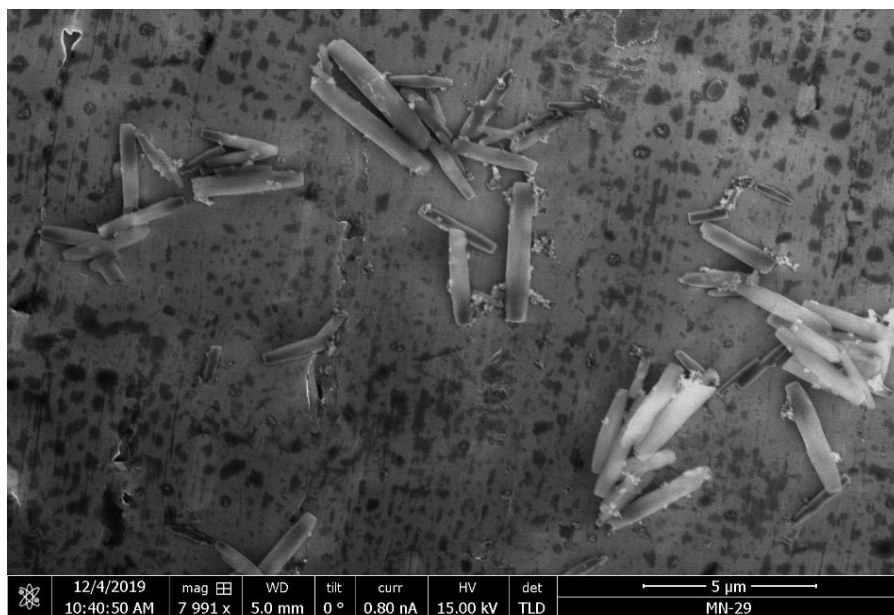


Figure S11. SEM image of room temperature synthesized PCN-222.

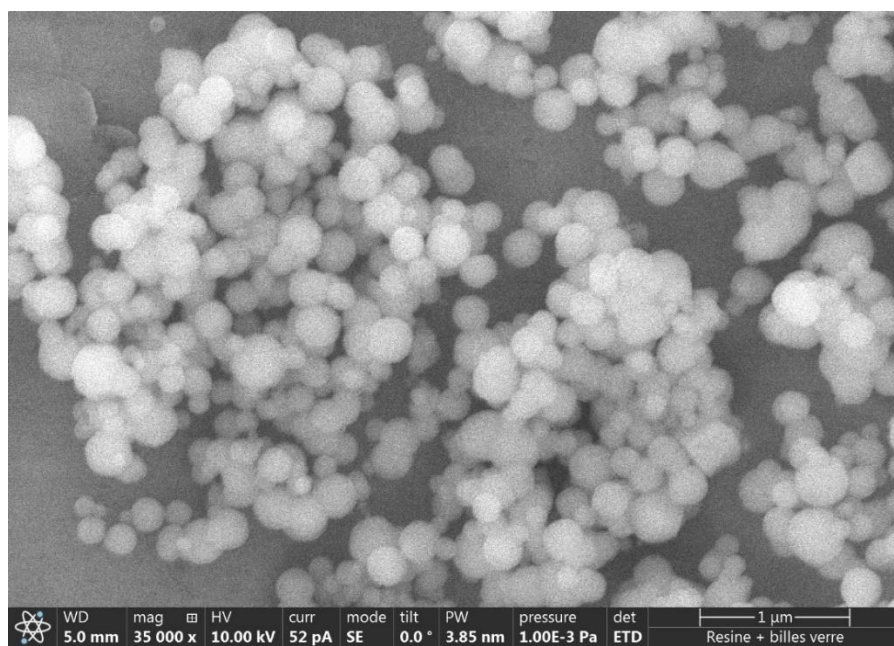


Figure S12. Scanning electron microscope image of room temperature synthesized MOF-801(Zr)-37.5%.

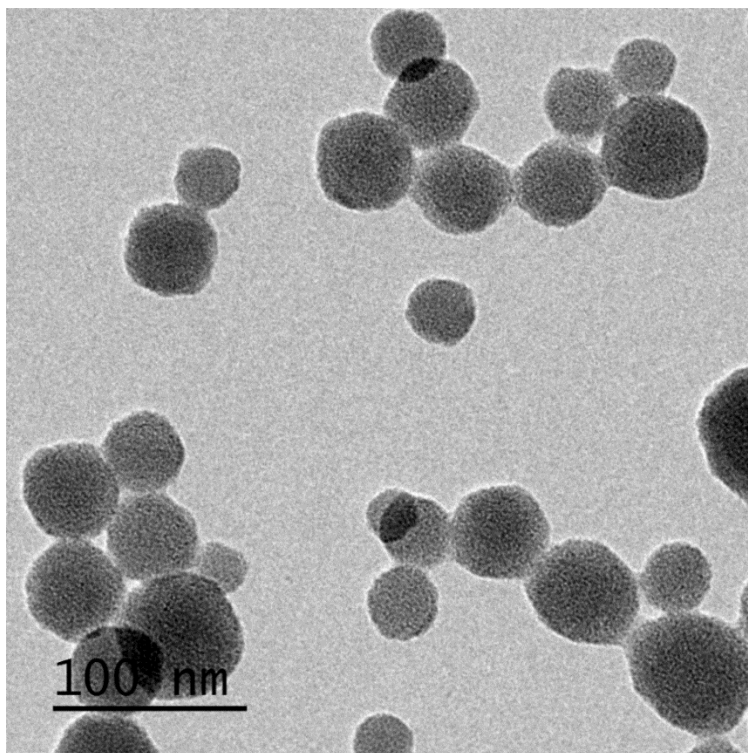


Figure S13. TEM image of room temperature synthesized MOF-801(Zr)-12.5%.

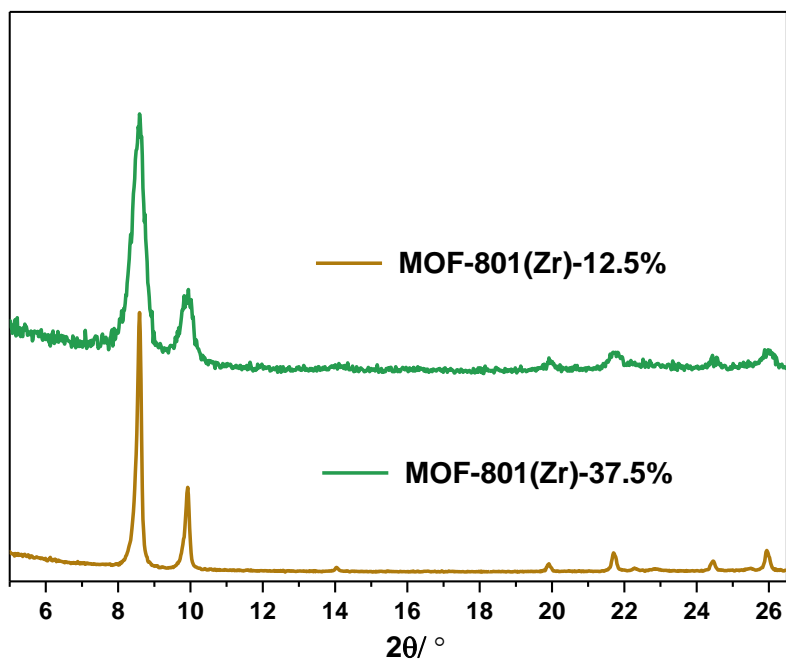


Figure S14. Modulator-induced size tuning of MOF-801(Zr).

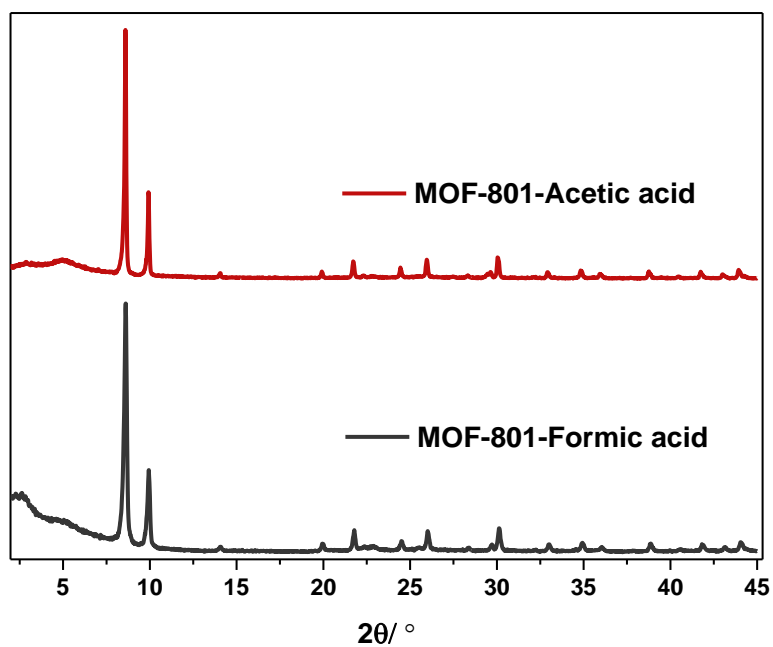


Figure S15. Equal-volume of formic acid and acetic acid in the syntheses of MOF-801(Zr).

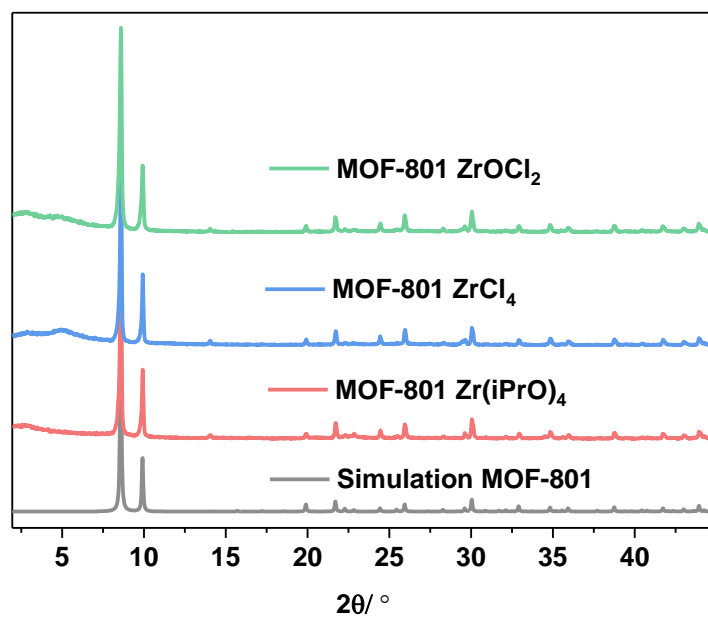


Figure S16. MOF-801 derived from various Zr salts, Zr(iPrO)₄, ZrCl₄, ZrOCl₂.

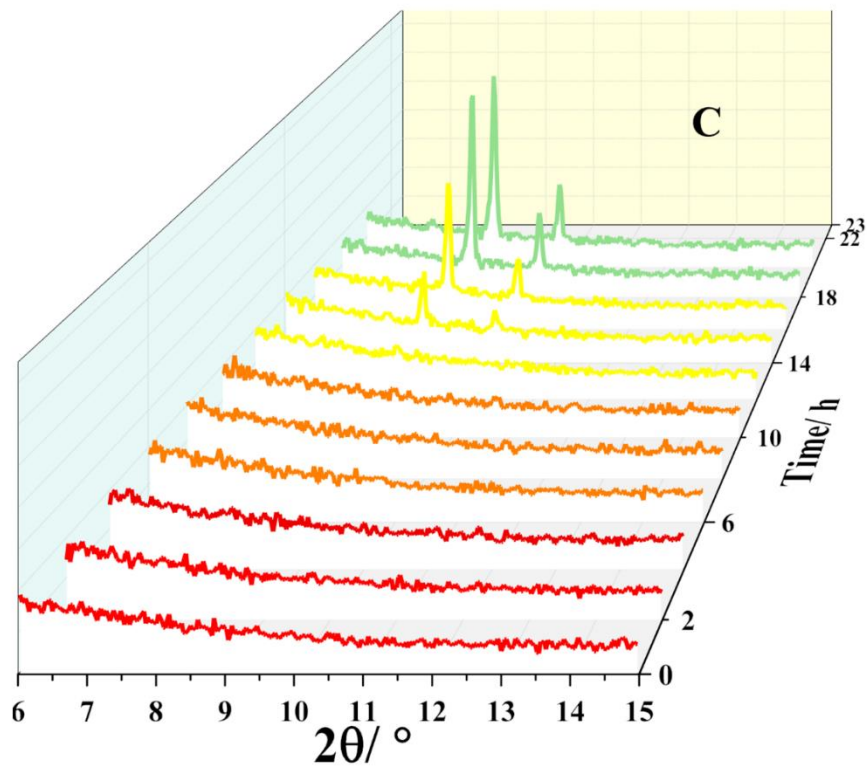


Figure S17. *In-situ* PXRD of MOF-801 synthesized in 0.15 mmol precursors (ZrCl_4) concentration. ($\lambda_{\text{Cu}} \approx 1.5406 \text{ \AA}$)

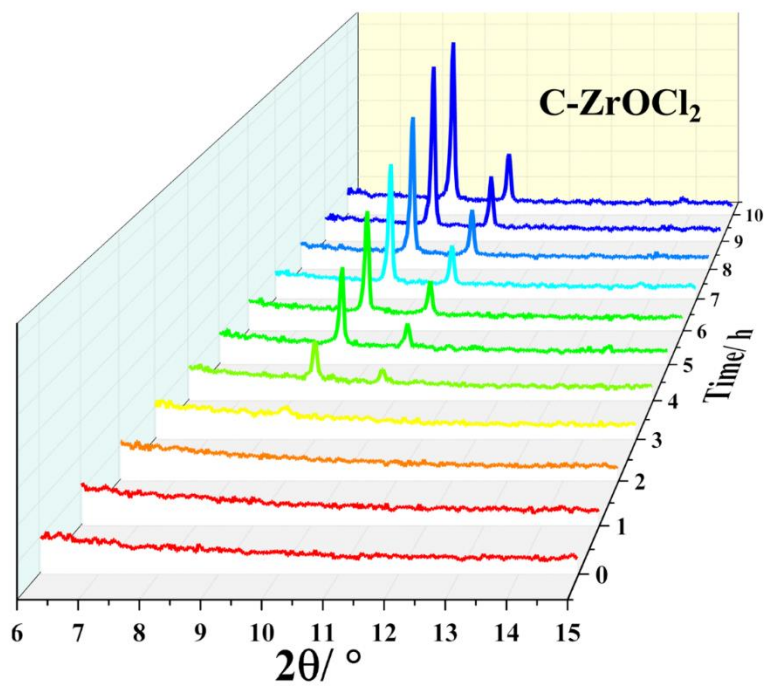


Figure S18. *In-situ* PXRD of MOF-801 synthesized in 0.15 mmol ZrOCl₂ and fumaric acid. ($\lambda_{\text{Cu}} \approx 1.5406\text{\AA}$)

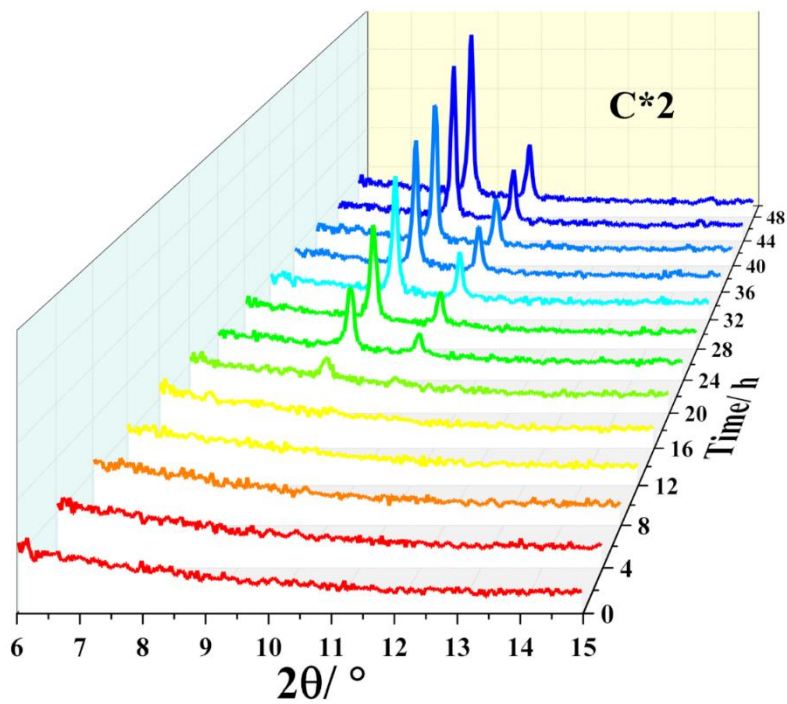


Figure S19. *In-situ* PXRD of MOF-801 synthesized in 0.3 mmol precursors (ZrCl₄) concentration. ($\lambda_{\text{Cu}} \approx 1.5406\text{\AA}$)

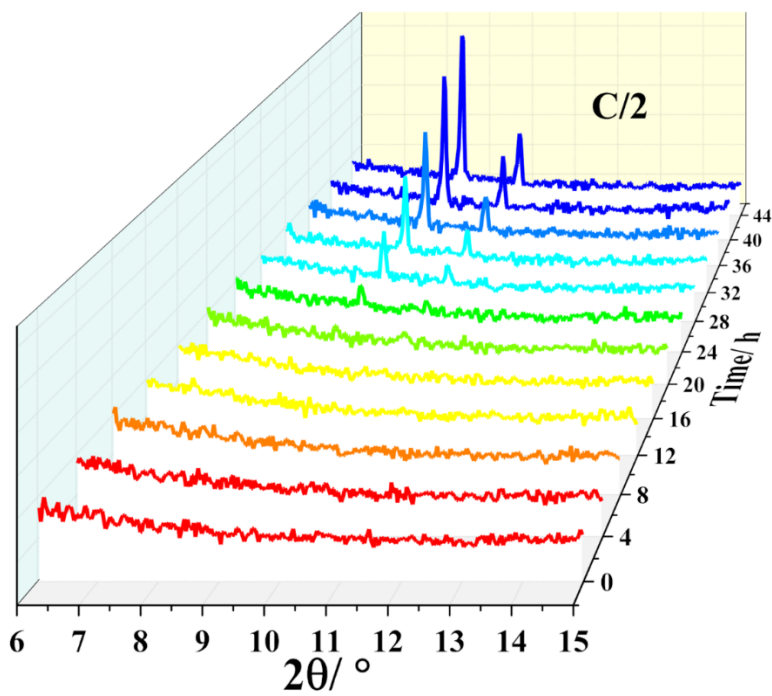


Figure S20. *In-situ* PXRD of MOF-801 synthesized in 0.075 mmol (ZrCl_4) precursors concentration. ($\lambda_{\text{Cu}} \approx 1.5406 \text{ \AA}$)

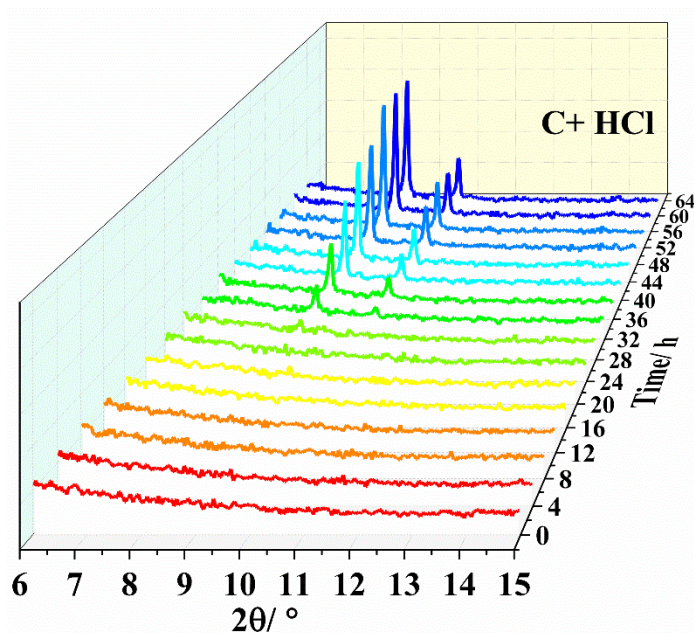


Figure S21. *In-situ* PXRD of MOF-801 synthesized in 1.5 mmol (ZrCl_4) precursors concentration with additional 6 mmol HCl, all other parameters were fixed. ($\lambda_{\text{Cu}} \approx 1.5406 \text{ \AA}$)

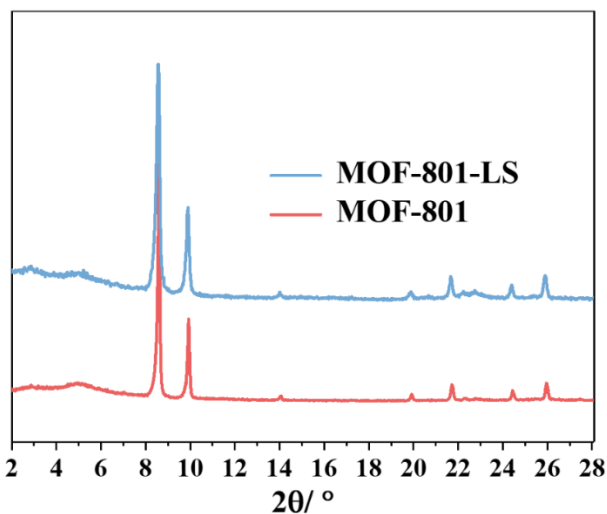


Figure S22. PXRD patterns of MOF-801 synthesized at large scale (MOF-801-LS) and lab-scale (MOF-801). ($\lambda_{\text{Cu}} \approx 1.5406 \text{ \AA}$)

Direct preparation of highly crystalline Ce-UiO-66-NH₂ and other benchmark Ce(IV)-MOFs at room temperature

Introduction

The ever-increasing energy crisis and its environmental impact has brought about the need to seek alternative renewable energy sources that neither rely on the consumption of fossil fuels nor emit carbon dioxide.^{1, 2} Solar-driven water splitting is considered as one very promising candidate for future energy supply. The approach involves the sustainable and inexpensive production of hydrogen, hence paving a way towards carbon neutrality.³ To obtain high solar energy conversion efficiency, incorporating noble metals as cocatalysts and designing complex composites is often inevitable, which implies high price, limited availability, and scalability.⁴ Thus, it is of great importance to design highly efficient scalable catalysts, without exploiting noble metals.

Metal-organic frameworks (MOFs) are emerging porous crystalline materials that consist of metal oxoclusters/ ions connected by organic ligands (e.g., di/ tri/ tetra carboxylic acid or N-based linkers), which display almost infinite structural diversity and functionality.⁵⁻⁷ The partial/ full substitution of inorganic nodes and organic linkers can bring controllable desired properties, especially in the field of catalysis. Ce-carboxylate-based MOFs are attractive for their relatively low cost, redox activity, and tailorable functions.^{8, 9} Ce-UiO-66 is a recent benchmark MOF built with Ce₆O₄(OH)₄¹²⁺ inorganic oxoclusters and 1,4-benzene-dicarboxylate (BDC) linkers, sharing many similarities with the isostructural Zr(IV)-UiO-66.^{10, 11} The high redox potential of Ce(IV) (1.61 V) brings a uniqueness to Ce(IV)-MOFs, mainly differentiating them from Zr(IV) analogs in photo-physical properties due to the low energy 4f orbitals, making them more competitive in some photo-related applications like photocatalysis.¹²⁻¹⁵ More recently, Truhlar et al. reported a computational investigation on the photo-reactivity of Ce-based UiO-66-X (X refers to the functional groups) by using the Kohn-Sham DFT method, predicting the high performance of Ce-UiO-66-X for application in overall water splitting.¹⁶

The typical synthesis method for most MOFs relies on the solvothermal route in highly toxic solvent (e.g. DMF) for long reaction time (12-96h).¹⁷ In terms of sustainability, synthesizing MOFs in green solvent under mild conditions (ideally in water at room temperature) is required to broaden the scope of possible applications and future industrialization.¹⁸ So far, green syntheses have been developed with some benchmark MOFs (e.g., MOF-5, HKUST-1, ZIFs).¹⁹⁻²¹ However, these divalent metals-based MOFs suffer from their poor chemical stability, particularly when exposed to humidity or water.¹⁸ Trivalent and tetravalent metals (e.g. Al, Cr, Zr) carboxylate based MOFs are usually more chemically robust than the aforementioned divalent ones. However, the room temperature green route to prepare these high valence-based MOFs are challenging and only few successful examples have been reported so far.¹⁸ Ce(IV) based MOFs, such as Ce-UiO-66, are often showing excellent stability in H₂O due to the strong Ce(IV)-carboxylate bond. The synthesis of Ce-UiO-66 often follows a solvothermal route in DMF similar to the one of Zr-UiO-66.⁹ An efficient and straightforward synthesis of Ce(IV)-MOFs in green solvent at room temperature (RT) is thus highly sought after. Even though tentative exploration reported that high concentration of

additive (NaClO₄) can help to form Ce-UiO-66 at room temperature,²² the subsequent cost and impurity issues may prevent the use of this synthesis for practical applications. We recently reported an efficient green/ RT synthesis of Zr-based MOFs and its extension to Ce-Fumarate (Ce-MOF-801).²³ However, more versatile synthesis of Ce(IV)-based MOFs is worth further research, particularly given the scope of available functionalities and topologies in MOF chemistry.¹⁵

In this work, we report an efficient strategy for the synthesis of highly crystalline Ce-UiO-66-X (X= H, Br, NO₂, COOH) in aqueous solution at room temperature. For the first time, RT strategy has been demonstrated as a useful method to reconcile the contradiction between redox active metal nodes and redox active ligands, preventing the formation of Ce(IV)-MOFs due to the reduction of Ce(IV) to Ce(III) at elevated temperature. As a consequence, highly crystalline Ce-UiO-66-NH₂ was obtained for the first time with green *de novo* route. The efficient preparation conditions (1-2 h) allows to reach space time yields (STY) ranging from 300 kg/ m³/ day to 900 kg/ m³/ day, comparable to that of hydro/ solvothermal strategies of other benchmark MOFs^{24, 25} and fulfilling the requirements of industrial-scale applications. Apart from the above-mentioned 12-connected UiO-type Ce-MOFs, the synthesis of other benchmarks Ce(IV) MOFs with varying connectivity modes such as the 8-connected Ce-DUT-67²⁶ and 6-connected Ce-MOF-808²⁷ are also reported using similar aqueous solution-based room temperature conditions.

Results and Discussion

Ce(IV)-MOFs, have shown extraordinary advances in photocatalysis due to their advantageous physiochemical features. These include distinct surface redox potential, much higher surface area in comparison with conventional ceria, and the relatively low price of metal (e.g., CeO₂, 6 USD/ Kilo²⁸). The Ce(IV)-UiO-66-X (X= functional groups) is built up by Ce₆(μ₃-O)₄(μ₃-OH)₄ clusters that are connected by BDC²⁻ or its derivatives to give 3D cubic structure, usually with high porosity and satisfying stabilities (Figure 1A). Encouraged by our previous findings, where an appropriate acidity of the synthesis solution could notably influence the nucleation kinetics, we extend our RT synthesis to several Ce-MOFs. The standard synthesis reported in this work is performed by mixing (NH₄)₂Ce(NO₃)₆ and the corresponding equivalent of linkers (Figure 1A) at room temperature for 1-2 hours using water and acetic acid (4:1, vol%) as solvents instead of conventionally used highly toxic solvent (e.g., DMF). Applying a similar synthesis route while using BDC-based functional ligands (-H, -NO₂, -COOH, -Br) leads to the corresponding frameworks with identical crystal structures (Figure 1B). These results are evidencing the versatility of the proposed synthetic strategy in synthesizing a large number of Ce-UiO-66-X with high crystallinity (SEM images, Figure S2-5). Of note, due to the very limited solubility of the BDC linker in pure H₂O, ethanol is needed as an assistant solvent in order to form Ce-UiO-66 efficiently.

Ce(IV) exhibits inherent photo-activity due to the low-lying 4f orbitals that can conceivably accept electrons from reduced species. For instance, the use of BDC-NH₂ in the solvothermal synthesis of Ce(IV)-MOFs always lead to the efficient reduction of Ce(IV) to Ce(III), making the desired structures not accessible. Despite very recent efforts including solvent-assisted linker exchange in DMF (SALE, up to 85% linker exchange), where the BDC-NH₂ was replacing the original BDC

ligand from the framework and the fabrication of Ce-UiO-66-NH₂ through the use of pre-formed Ce₆ oxoclusters in DMF,²⁹ the direct, green, and scalable approach is still required. As shown in Figure 1C, a brownish solution with pronounced solid product appears in the glass via standard synthesis using ethanol as co-solvent due to the poor solubility of the ligand in water. The powder X-ray diffraction (PXRD) pattern demonstrates the crystallinity and the high quality of the prepared Ce-UiO-66-NH₂. The Scanning electron microscope (SEM) image in Figure S1 evidences that Ce-UiO-66-NH₂ crystallizes as ca. 80nm nanocrystals, which is concordant with the slight broadening PXRD peaks. Notably, even a slightly elevated synthesis temperature (40 °C) leads to a much worse quality of solids. Moreover, the same synthesis performed at 60 °C results in a clear dark solution without any solid, highlighting the fact that the higher temperature impedes the nucleation of MOF crystals, likely due to the efficient reduction of Ce(IV) while at room temperature, we suppose this oxidation process is, to some extent, inhibited. Despite these promising results, the relatively low product yield of Ce-UiO-66-NH₂ (42%) reveals the inevitable partial reduction of Ce(IV) even at RT. This can be overcome by using Ce salt in excess (2.5 mmol instead of 1.5 mmol), giving rise to a significantly higher product yield (86%) based on the ligand. To the best of our knowledge, this is the first conceptual study that revealed the excellent applicability of room temperature synthesis used in forming novel phases. The simple preparation procedure, as far as we know, is the first reported Ce-UiO-66-NH₂ through a green *de novo* synthesis.

The stability of a given MOF is paramount for their efficacy in a vast array of the practical applications. Considering the infeasible preparation of Ce-UiO-66-NH₂ at elevated temperature in H₂O, we investigate the chemical stability of the as-synthesized Ce-UiO-66-NH₂ by soaking this MOF in boiling water for 24h. The PXRD pattern (Figure 1D) supports the hydrolytic robustness of Ce-UiO-66-NH₂. This substantiates the robustness of Ce-UiO-66-NH₂ towards hot water after the formation of the crystalline solid. Additionally, it confirms that the reduction of Ce(IV) at the beginning of the reaction hinders the formation of crystalline MOF, while once the MOF is synthesized, it remains water stable as the Zr analogue.

From an industrial development point of view, minimizing the energy input and maximizing the space-time yield (STY) is of critical importance. In this regard, RT synthesis often lead to moderate to low STY due to the low energy input that lead to slow crystal formation. While benefiting from the efficient preparation in our case, the space-time-yield (STY) for all these UiO-66-X reaches high regime, 351-900 kg/m³/day (summarized in Table 1), verifying the high synthesis efficiency of all these RT prepared MOFs.

The N₂ adsorption-desorption isotherms at 77K were conducted to investigate the porosity of the prepared Ce-UiO-66-X and are shown in Figure 1E. All the prepared Ce-UiO-66-X display archetypal Type-I isotherms, indicating the microporous feature of these materials. The specific surface area, pore size distribution and micropore volume were calculated from Brunauer–Emmett–Teller (BET) analyses of the adsorption data (shown in Table 1). The high specific BET surface areas and micropore volumes, further exemplify the high quality of the synthesized MOFs, which is also in agreement with the values reported from the conventional synthesis in DMF.¹¹ The variations within surface area values of the functionalized Ce-UiO-66 can be attributed to the introduced functional groups, which increase the density of porous solids, as well as their slightly distinct defect content (summarized in Table S1). As previously mentioned,

despite the successful preparation of Ce-UiO-66-NH₂ through solvothermal synthesis using pre-synthesized Ce₆ oxoclusters, the relatively poor crystallinity led to a much lower 446 m²/g BET surface area (819 m²/g, in this work).

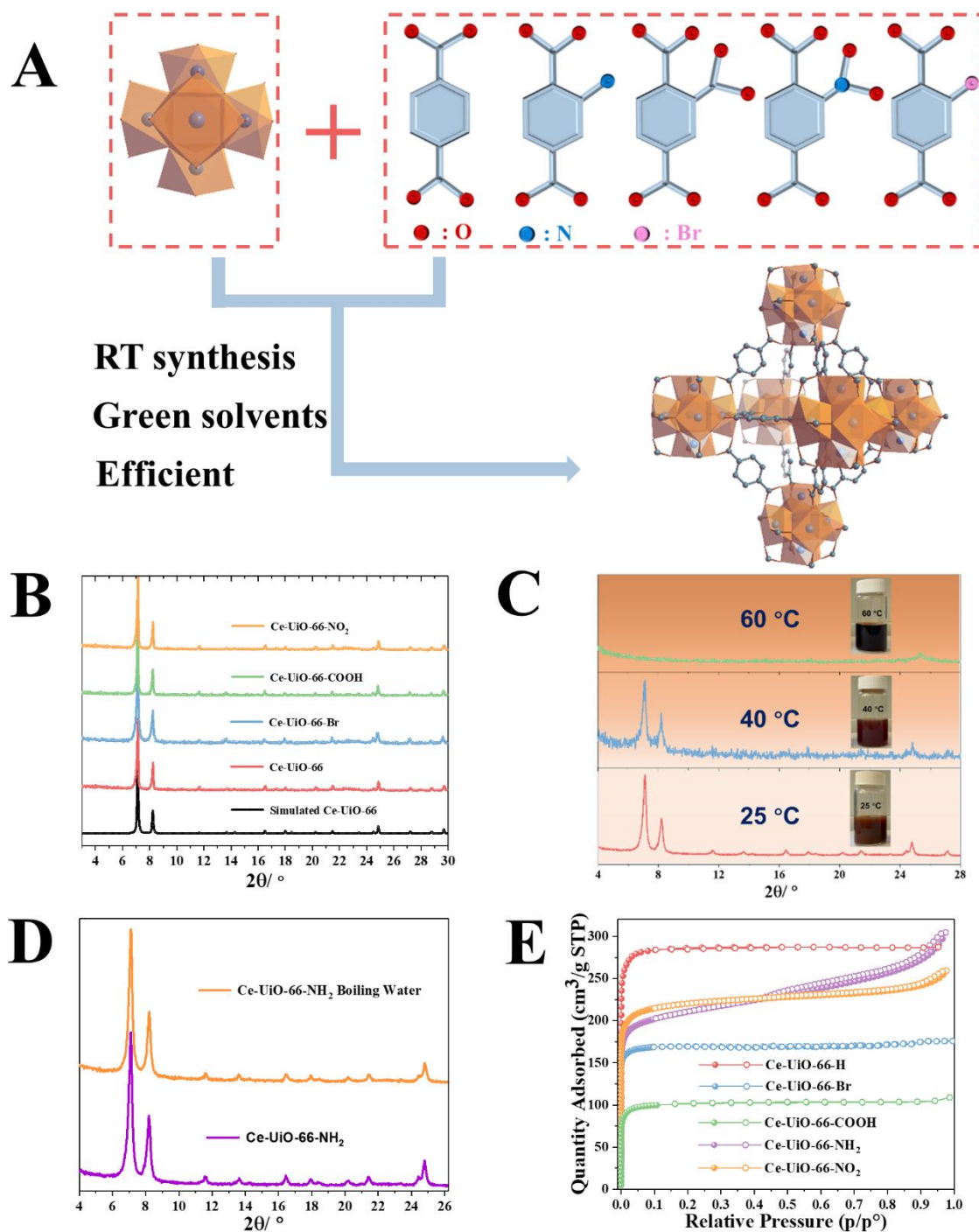


Figure 1. Illustration and Characterization of Ce-UiO-66-X

(A) Structures of Zr₆ oxo-cluster, linkers, and Ce-UiO-66.

(B) PXRD ($\lambda_{Cu}=1.5406\text{\AA}$) patterns of the RT synthesized Ce-UiO-66-X (X= -H, -NO₂, -COOH, -Br).

(C) PXRD patterns of the Ce-UiO-66-NH₂ synthesized at varying temperature (25 °C, 40°C, 60 °C), insert image: photography of the resulting solution.

(D) PXRD patterns of the Ce-UiO-66-NH₂ sample before and after boiling water treatment.

(E) 77K N₂ adsorption-desorption isotherms of the RT synthesized Ce-UiO-66-X.

Table 1. The room-temperature synthesized Ce-MOFs in this work.

Entry	Material	Solvent	Modulator	Connectivity	BET surface area (m ² /g)	Pore volume (cm ³ /g)	STY (kg/m ³ /day)
1	Ce-UiO-66	H ₂ O, Ethanol	Acetic Acid	(2, 12)	1182	0.44	425
2	Ce-UiO-66-NH ₂	H ₂ O, Ethanol	Acetic Acid	(2, 12)	819	0.38	311
3	Ce-UiO-66-NO ₂	H ₂ O	Acetic Acid	(2, 12)	878	0.36	886
4	Ce-UiO-66-Br	H ₂ O	Acetic Acid	(2, 12)	698	0.26	923
5	Ce-UiO-66-COOH	H ₂ O	Acetic Acid	(2, 12)	418	0.16	839
6	Ce-DUT-67(PDA)	H ₂ O	Acetic Acid	(2, 8)	495	0.22	435
7	Ce-MOF-808	H ₂ O	Formic Acid	(3, 6)	1802	0.65	769

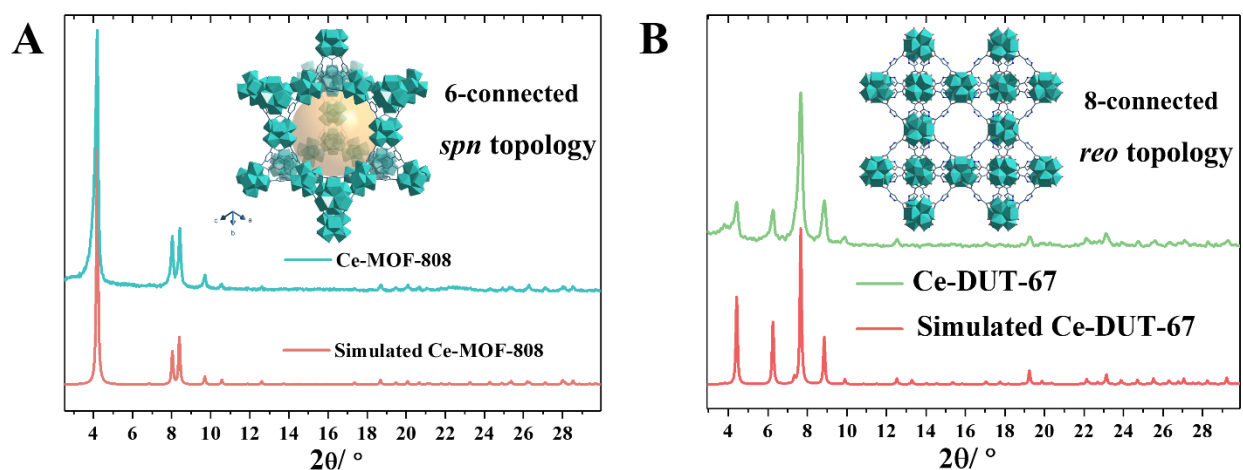


Figure 2. PXRD pattern of synthesized Ce-MOF-808 in comparison to simulated pattern.

The immense library of organic linkers offers great potential to obtain MOFs with distinct dimensionality and porosity. For example, 1,3,5-Benzenetricarboxylic acid (BTC) and 1H-Pyrazole-3,5-dicarboxylic acid (PDA) are two commonly used organic ligands while with tritopic and ditopic (angled coordination sites) geometries, respectively. As a consequence, 6-connected and 8-connected Ce_6 oxocluster based MOFs can be prepared, therefore offering fully distinct porous features and chemical affinities. By applying the standard synthesis conditions developed in this paper while decreasing the ligand stoichiometry, due to the lower connectivity of the corresponding frameworks, highly crystalline Ce-MOF-808 and DUT-67(PDA) were synthesized (Figure 2a, b). Notably, the synthesis of MOF-808 needs the presence of one equivalent of formic acid instead of acetic acid. Otherwise, only amorphous products can be collected. This is probably due to the lower pK_a of BTC, which requires more acidic modulator ($\text{pK}_{a\text{formic acid}} = 3.7$ vs $\text{pK}_{a\text{acetic acid}} = 4.7$) to effectively control the crystallization kinetics.

With the motivation of the ideal bandgaps of Ce-MOFs, particularly for UiO-66-X due to its tunable energy gap, we systematically investigate the overall water splitting performance based on UiO-66-X. The corresponding works are done in collaboration with Dr. Sergio Navalón, Spain.

Conclusion

As a whole, we report a versatile room-temperature synthesis strategy to prepare a series of 12-connected, 8-connected, and 6-connected Ce_6 -based benchmark MOFs in green solvents. Unlike most of the MOFs synthesized at ambient, our approach enables a very high space-time yield, ranging from $300 \text{ kg}/\text{m}^3/\text{day}$ to $900 \text{ kg}/\text{m}^3/\text{day}$. More importantly, ambient synthesis strategy has been demonstrated by the first time, as a useful method to reconcile the contradiction between

redox-active metal nodes and redox-active ligands, allowing *de novo* formation of novel Ce-UiO-66-NH₂, which has been regarded as a conflictive phase. It is worth noting, amino-functionalized ligands are often very interesting linkers for many applications, especially in catalysis due to the shortened band gap. Finally, we use overall water splitting to investigate the catalytic performance of the prepared Ce-UiO-66-X due to their tailorable electronic band structures. The relevant studies are in progress.

References

1. Song, C. S., Global challenges and strategies for control, conversion and utilization of CO₂ for sustainable development involving energy, catalysis, adsorption and chemical processing. *Catal. Today* **2006**, *115* (1-4), 2-32.
2. Lewis, N. S.; Nocera, D. G., Powering the planet: Chemical challenges in solar energy utilization. *PNAS*. **2006**, *103* (43), 15729-15735.
3. Wang, Q.; Domen, K., Particulate Photocatalysts for Light-Driven Water Splitting: Mechanisms, Challenges, and Design Strategies. *Chem. Rev.* **2020**, *120* (2), 919-985.
4. Li, Y. J.; Sun, Y. J.; Qin, Y. N.; Zhang, W. Y.; Wang, L.; Luo, M. C.; Yang, H.; Guo, S. J., Recent Advances on Water-Splitting Electrocatalysis Mediated by Noble-Metal-Based Nanostructured Materials. *Adv. Energy Mater.* **2020**, *10* (11).
5. Yaghi, O. M.; O'Keeffe, M.; Ockwig, N. W.; Chae, H. K.; Eddaoudi, M.; Kim, J., Reticular synthesis and the design of new materials. *Nature* **2003**, *423* (6941), 705-714.
6. Kitagawa, S.; Kitaura, R.; Noro, S., Functional porous coordination polymers. *Angew. Chem. Int. Ed.* **2004**, *43* (18), 2334-2375.
7. Ferey, G., Hybrid porous solids: past, present, future. *Chem. Soc. Rev.* **2008**, *37* (1), 191-214.
8. Lomachenko, K. A.; Jacobsen, J.; Bugaev, A. L.; Atzori, C.; Bonino, F.; Bordiga, S.; Stock, N.; Lamberti, C., Exact Stoichiometry of Ce_xZr_{6-x} Cornerstones in Mixed-Metal UiO-66 Metal-Organic Frameworks Revealed by Extended X-ray Absorption Fine Structure Spectroscopy. *J. Am. Chem. Soc.* **2018**, *140* (50), 17379-17383.
9. Jacobsen, J.; Ienco, A.; D'Amato, R.; Costantino, F.; Stock, N., The chemistry of Ce-based metal-organic frameworks. *Dalton Trans.* **2020**, *49* (46), 16551-16586.
10. Cavka, J. H.; Jakobsen, S.; Olsbye, U.; Guillou, N.; Lamberti, C.; Bordiga, S.; Lillerud, K. P., A new zirconium inorganic building brick forming metal organic frameworks with exceptional stability. *J. Am. Chem. Soc.* **2008**, *130* (42), 13850-13851.
11. Lammert, M.; Wharmby, M. T.; Smolders, S.; Bueken, B.; Lieb, A.; Lomachenko, K. A.; Vos, D. D.; Stock, N., Cerium-based metal organic frameworks with UiO-66 architecture: synthesis, properties and redox catalytic activity. *Chem. Commun.* **2015**, *51* (63), 12578-81.
12. Nouar, F.; Breeze, M. I.; Campo, B. C.; Vimont, A.; Clet, G.; Daturi, M.; Devic, T.; Walton, R. I.; Serre, C., Tuning the properties of the UiO-66 metal organic framework by Ce substitution. *Chem. Commun.* **2015**, *51* (77), 14458-61.
13. Hendrickx, K.; Joos, J. J.; De Vos, A.; Poelman, D.; Smet, P. F.; Van Speybroeck, V.; Van Der Voort, P.; Lejaeghere, K., Exploring Lanthanide Doping in UiO-66: A Combined Experimental and Computational Study of the Electronic Structure. *Inorg. Chem.* **2018**, *57* (9), 5463-5474.

14. Campanelli, M.; Del Giacco, T.; De Angelis, F.; Mosconi, E.; Taddei, M.; Marmottini, F.; D'Amato, R.; Costantino, F., Solvent-Free Synthetic Route for Cerium(IV) Metal-Organic Frameworks with UiO-66 Architecture and Their Photocatalytic Applications. *ACS Appl. Mater. Interfaces* **2019**, *11* (48), 45031-45037.
15. Lu, W. G.; Wei, Z. W.; Gu, Z. Y.; Liu, T. F.; Park, J.; Park, J.; Tian, J.; Zhang, M. W.; Zhang, Q.; Gentle, T.; Bosch, M.; Zhou, H. C., Tuning the structure and function of metal-organic frameworks via linker design. *Chem. Soc. Rev.* **2014**, *43* (16), 5561-5593.
16. Wu, X. P.; Gagliardi, L.; Truhlar, D. G., Cerium Metal-Organic Framework for Photocatalysis. *J. Am. Chem. Soc.* **2018**, *140* (25), 7904-7912.
17. Yuan, S.; Feng, L.; Wang, K. C.; Pang, J. D.; Bosch, M.; Lollar, C.; Sun, Y. J.; Qin, J. S.; Yang, X. Y.; Zhang, P.; Wang, Q.; Zou, L. F.; Zhang, Y. M.; Zhang, L. L.; Fang, Y.; Li, J. L.; Zhou, H. C., Stable Metal-Organic Frameworks: Design, Synthesis, and Applications. *Adv. Mater.* **2018**, *30* (37).
18. Wang, S. J.; Serre, C., Toward Green Production of Water-Stable Metal-Organic Frameworks Based on High-Valence Metals with Low Toxicities. *ACS Sustain. Chem. Eng.* **2019**, *7* (14), 11911-11927.
19. Tranchemontagne, D. J.; Hunt, J. R.; Yaghi, O. M., Room temperature synthesis of metal-organic frameworks: MOF-5, MOF-74, MOF-177, MOF-199, and IRMOF-0. *Tetrahedron* **2008**, *64* (36), 8553-8557.
20. Pan, Y. C.; Liu, Y. Y.; Zeng, G. F.; Zhao, L.; Lai, Z. P., Rapid synthesis of zeolitic imidazolate framework-8 (ZIF-8) nanocrystals in an aqueous system. *Chem. Commun.* **2011**, *47* (7), 2071-2073.
21. Zhuang, J. L.; Ceglarek, D.; Pethuraj, S.; Terfort, A., Rapid Room-Temperature Synthesis of Metal-Organic Framework HKUST-1 Crystals in Bulk and as Oriented and Patterned Thin Films. *Adv. Funct. Mater.* **2011**, *21* (8), 1442-1447.
22. Li, K.; Yang, J.; Gu, J., Salting-in species induced self-assembly of stable MOFs. *Chem Sci* **2019**, *10* (22), 5743-5748.
23. Dai, S.; Nouar, F.; Zhang, S. J.; Tissot, A.; Serre, C., One-Step Room-Temperature Synthesis of Metal(IV) Carboxylate Metal-Organic Frameworks. *Angew. Chem. Int. Ed.* **2021**, *60* (8), 4282-4288.
24. Garzon-Tovar, L.; Carne-Sanchez, A.; Carbonell, C.; Imaz, I.; Maspoch, D., Optimised room temperature, water-based synthesis of CPO-27-M metal-organic frameworks with high space-time yields. *J. Mater. Chem. A* **2015**, *3* (41), 20819-20826.
25. Rubio-Martinez, M.; Batten, M. P.; Polyzos, A.; Carey, K. C.; Mardel, J. I.; Lim, K. S.; Hill, M. R., Versatile, High Quality and Scalable Continuous Flow Production of Metal-Organic Frameworks. *Sci. Rep.* **2014**, *4*.
26. Lammert, M.; Glissmann, C.; Reinsch, H.; Stock, N., Synthesis and Characterization of New Ce(IV)-MOFs Exhibiting Various Framework Topologies. *Cryst. Growth Des.* **2017**, *17* (3), 1125-1131.
27. Ji, P. F.; Sawano, T.; Lin, Z. K.; Urban, A.; Boures, D.; Lin, W. B., Cerium-Hydride Secondary Building Units in a Porous Metal-Organic Framework for Catalytic Hydroboration and Hydrophosphination. *J. Am. Chem. Soc.* **2016**, *138* (45), 14860-14863.
28. Prices of metals. <https://www.argusmedia.com/en/metals>.
29. Son, F. A.; Atilgan, A.; Idrees, K. B.; Islamoglu, T.; Farha, O. K., Solvent-assisted linker exchange enabled preparation of cerium-based metal-organic frameworks constructed from redox active linkers. *Inorg. Chem. Front.* **2020**, *7* (4), 984-990.

Supporting information

Direct preparation of highly crystalline Ce-UiO-66-NH₂ and other benchmark Ce(IV)-MOFs at room temperature

Chemicals.

All chemicals were purchased from commercial suppliers and used as received without further purification. Terephthalic acid, 99%, Alfa Aesar. 2-Aminoterephthalic acid (BDC-NH₂), 99+%, Acros. 1,2,4-Benzenetricarboxylic acid (BDC-COOH), 98%, Acros. 1H-Pyrazole-3,5-dicarboxylic acid (PDA), 97%, FluoroChem. Ammonium Cerium(IV) nitrate, 99%, Acros. Acetic acid, 99%, Acros. Formic acid, 98+%, Acros. Ethanol absolute, >=99%, Acros. MilliQ water, Millipore system.

Instruments.

Powder X-ray Diffraction (PXRD) data were recorded on a high-throughput Bruker D8 Advance diffractometer working on transmission mode and equipped with a focusing Göbel mirror producing CuK α radiation ($\lambda = 1.5418 \text{ \AA}$) and a LynxEye detector. Nitrogen porosimetry data were collected on a Micromeritics Tristar/ Triflex instrument at 77K (pre-activating samples at 80°C under vacuum, 12 hours). SEM images were recorded with FEI Magellan 400 scanning electron microscope. TGA data were collected on Mettler Toledo TGA/DSC 2, STAR System apparatus with a heating rate of 5 °C/min under the oxygen flow. Infrared spectra were measured with a Nicolet iS5 FTIR ThermoFisher spectrometer. The optical spectra of solids have been measured using a Varian Cary 300 Bio UV-Vis spectrometer equipped with an integration sphere in diffuse reflectance mode.

Synthesis of MOFs.

Standard synthesis strategy (SSS) for Ce-UiO-66: 1.5 mmol (820 mg) of (NH₄)₂Ce(NO₃)₆ was weighted in a glass vial, 3 mL of acetic acid and 8 mL of distilled water was stepwisely introduced in the reactor, following by 1 minute of stirring at 600 rpm. 1.5 mmol of corresponding ligand (2-Bromoterephthalic acid/ 2-Nitroterephthalic acid/ 1,2,4-Benzenetricarboxylic acid) was subsequently added in the solution. The solution became very cloudy within 1-2h, indicating the formation of the corresponding MOF. The product was collected by centrifugation, washed with water and ethanol and finally dried under vacuum. The product yield was 89% for Ce-UiO-66-Br, 82% for Ce-UiO-66-NO₂, 80% for Ce-UiO-66-COOH based on the Ce(IV) salt due to the excess of ligand.

Synthesis of Ce-UiO-66 and Ce-UiO-66-NH₂: the synthesis of these two kinds of MOFs followed the SSS while adding 20 mL Ethanol in the solution before the introduction of the corresponding ligands (Terephthalic acid/ 2-aminoterephthalic acid). The product yield was 92% for Ce-UiO-66, 42% for Ce-UiO-66-NH₂ based on the Ce(IV) salt due to the excess of ligand.

Synthesis of Ce-DUT-67 (PDA): the synthesis of Ce-DUT-67(PDA) followed the SSS while using 1 mmol of 1H-Pyrazole-3,5-dicarboxylic acid monohydrate (PDA). The product yield was 65% based on the Ce(IV).

Synthesis of Ce-MOF-808: the synthesis of Ce-MOF-808 followed the SSS while using 0.5 mmol of Benzene-1,3,5-tricarboxylic acid (BTC) and 3 mL formic acid. The product yield was 86% based on the Ce(IV).

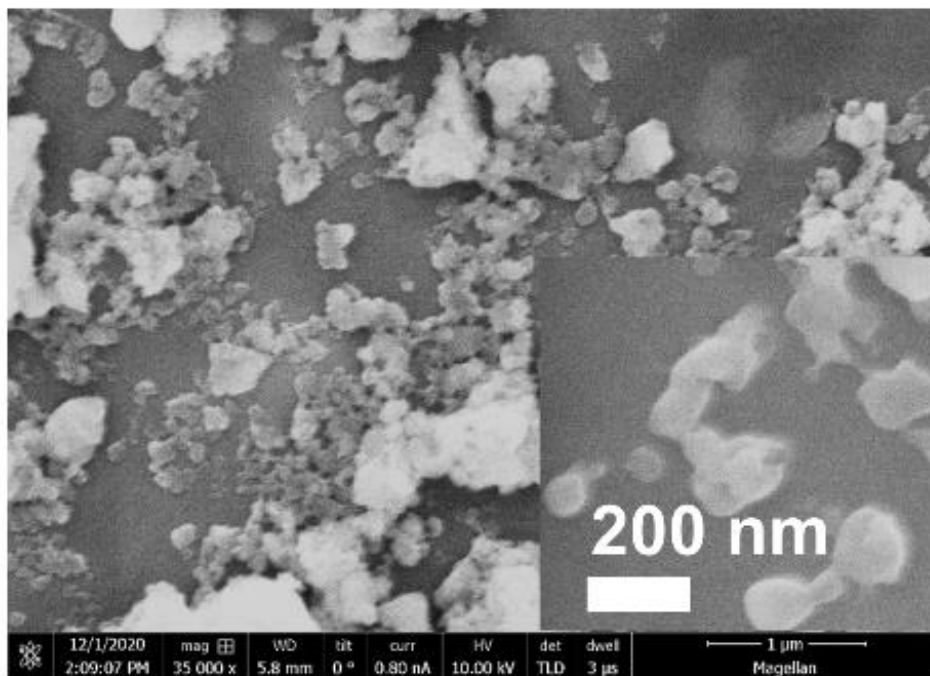


Figure S1. SEM image of Ce-UiO-66-NH₂ in large and small magnification.

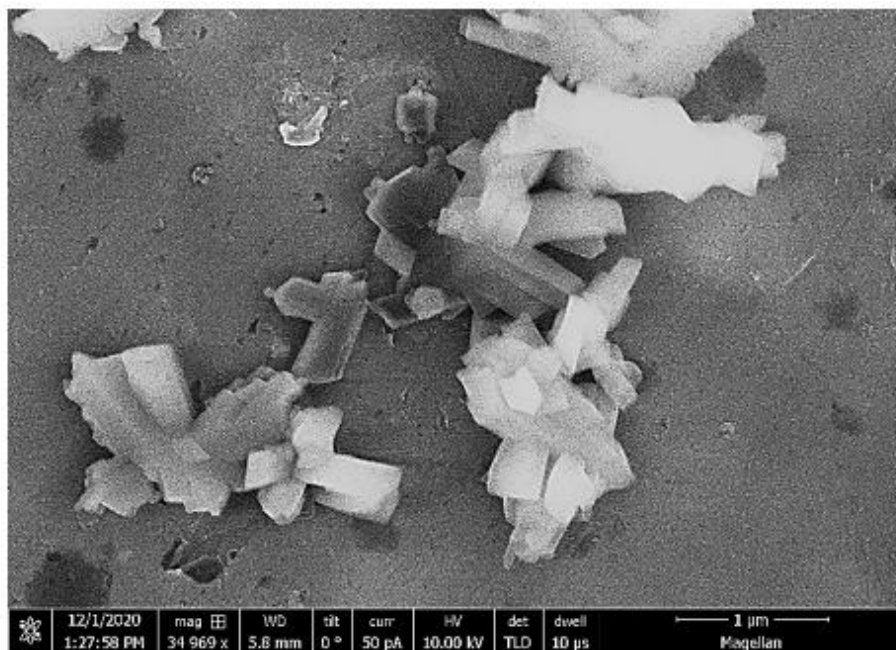


Figure S2. SEM image of Ce-UiO-66.

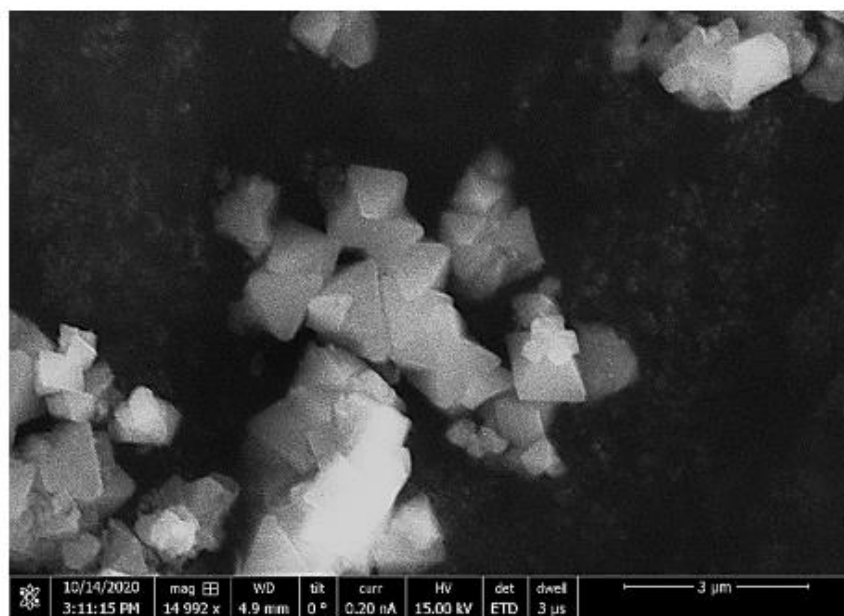


Figure S3. SEM image of Ce-UiO-66-Br.

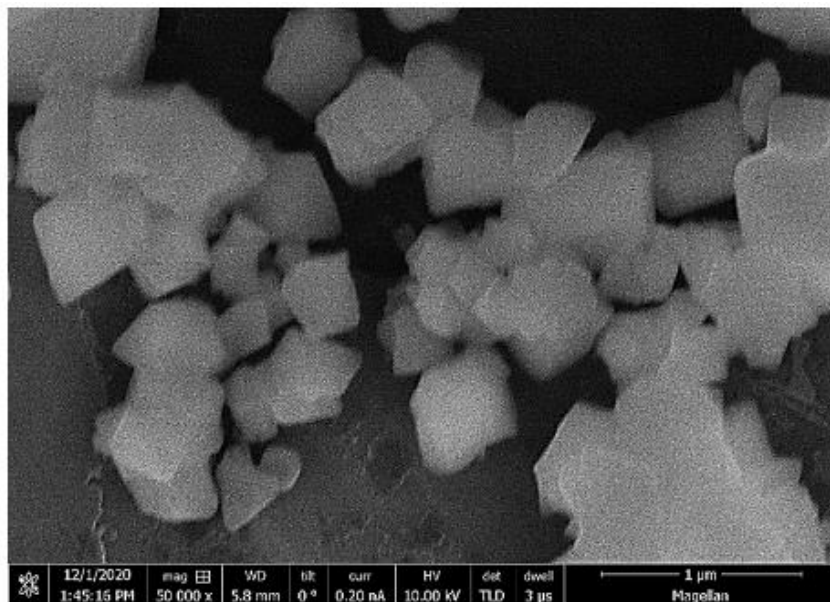


Figure S4. SEM image of Ce-UiO-66-COOH.

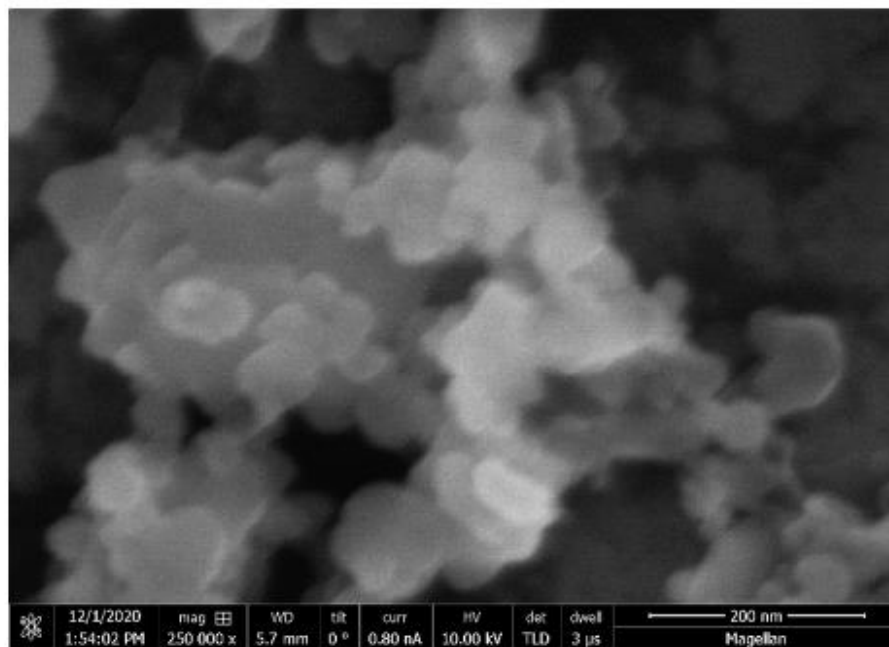


Figure S5. SEM image of Ce-UiO-66-NO₂.

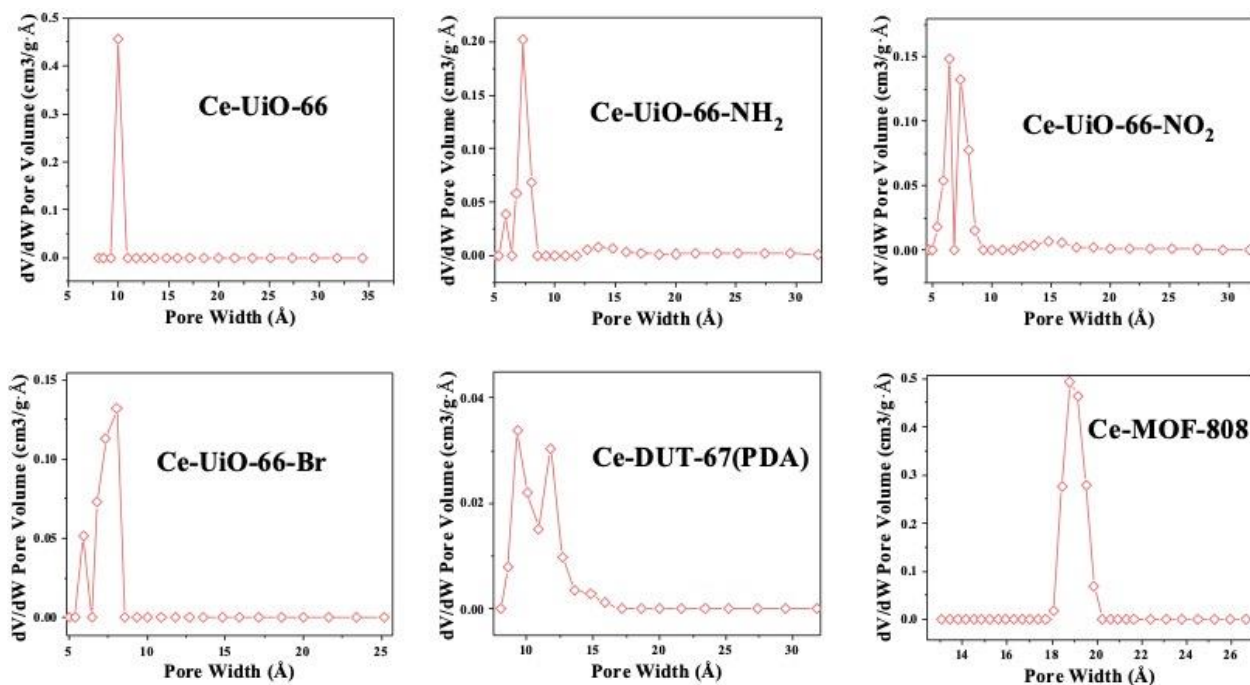


Figure S6. Pore size distribution patterns of the MOFs in this work. (DFT model)

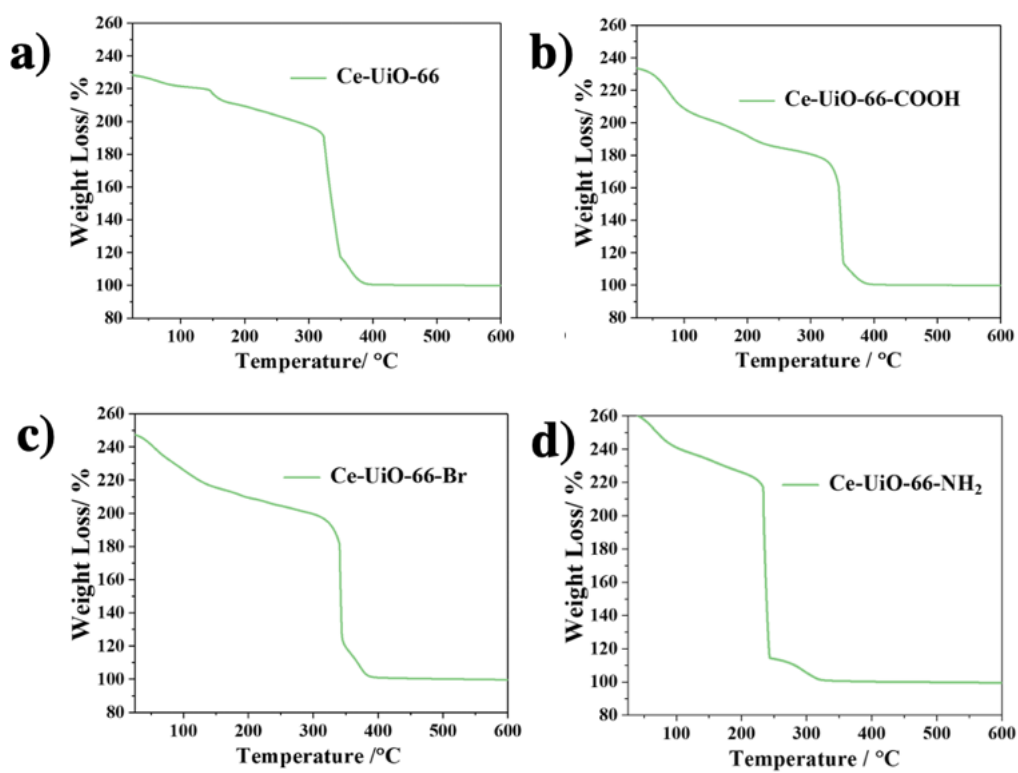


Figure S7. TG analysis of Ce-UiO-66-X (X= NH₂, H, Br, COOH).

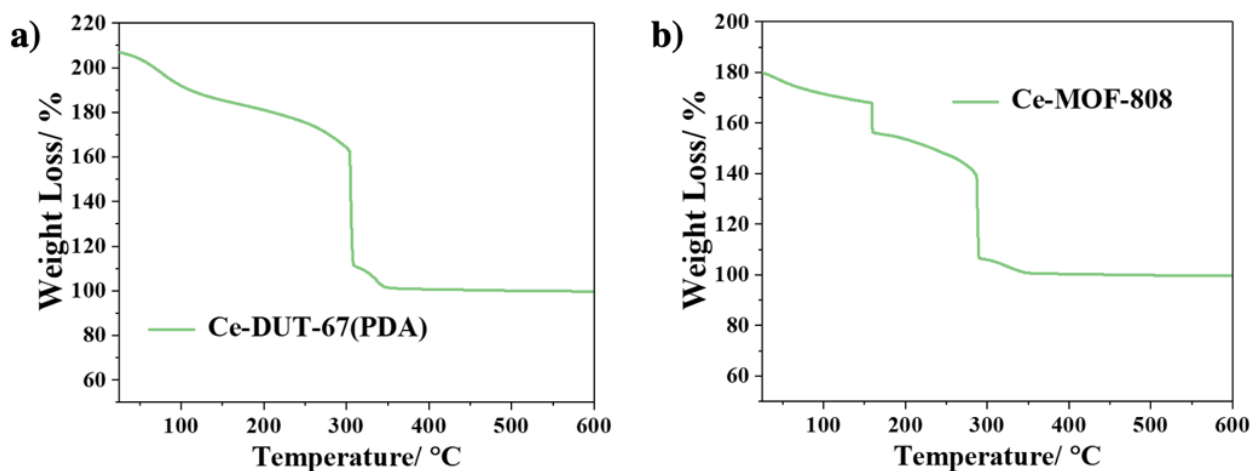


Figure S8. TG analysis of Ce-DUT-67(PDA) and Ce-MOF-808.

Table S1. Comparison of the theoretical mass loss and measured mass loss of Ce-MOFs in this work. (extracted from TGA)

Entry	Materials	T/ °C	Measured wt%	Theoretical wt%
1	Ce-UiO-66	325	192	195
2	Ce-UiO-66-NH ₂	225	220	204
3	Ce-UiO-66-NO ₂	295	--	213
4	Ce-UiO-66-Br	325	198	237
5	Ce-UiO-66-COOH	320	180	220
6	Ce-DUT-67(PDA)	300	170	160
7	Ce-MOF-808	280	140	140

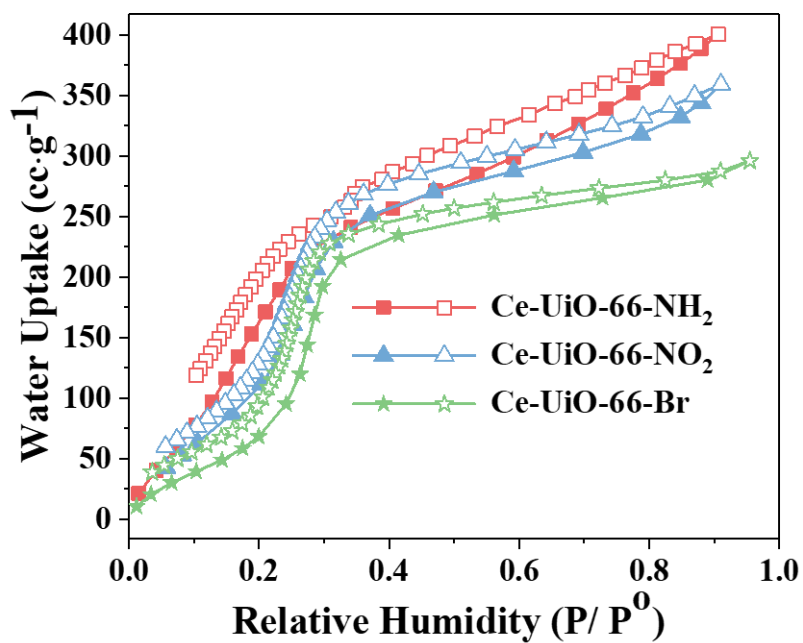


Figure S9. Water isotherms of Ce-UiO-66-NH₂/ NO₂/ Br at 25°C.

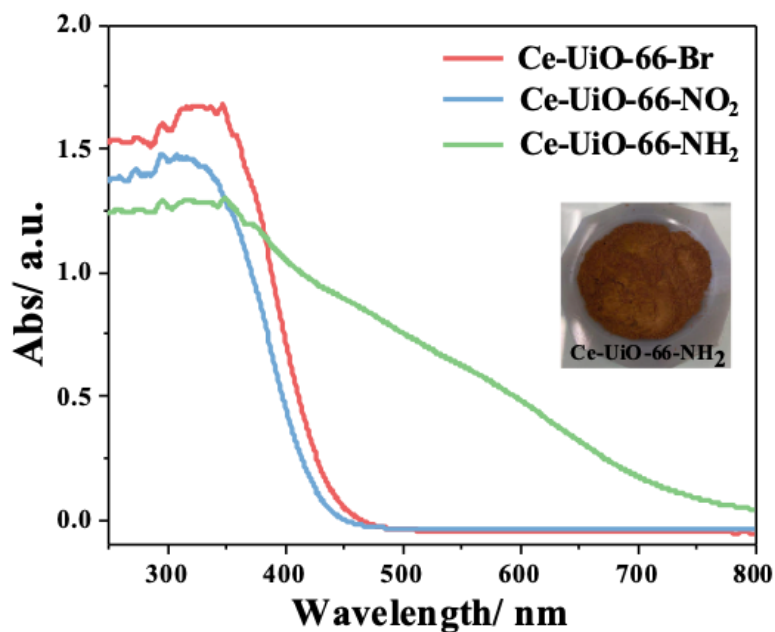


Figure S10. Diffuse reflectance spectra of UiO-66-Br, UiO-66-NO₂, and UiO-66-NH₂.

Chapter 4

This chapter is adapted to the following manuscript:

Investigation of the removal of capping agents from core-shell Au NPs@MOF-808: A facile synergetic route

Shan Dai et al.

Table of Contents

Contributions to this research.....	173
Article	174
1. Introduction	174
2. Results and discussion.....	175
3. Conclusion.....	181
References	182
Supporting information	183

Contributions to this research

I synthesized Au NPs as the first step and subsequently used a bottle-around-ship approach to grow a MOF-808 shell on the surface of Au NPs. The formed Au NPs and core-shell Au NPs@MOF-808 were fully characterized by myself except the TEM were done by Dr. Xiangzhen Xu. The investigation of the removal of the capping agent was done by me and my intern, Kieu Phung Ngoc. Dr. Laurence Grimaud discussed us for the project. I plotted all the figures and wrote the manuscript.

Motivation

This chapter deals with the construction and application of ultra-small Au NPs@MOF-808 composites using the synthetic approach I described in Chapter 2, where the room temperature/low acidity synthesis of Zr(IV)-based MOFs was systematically investigated. Ultra-small Au NPs are well-known for their potential catalytic performance. However, they often tend to aggregate upon harsh conditions, such as strong acidity and high temperature, which are typically used in the synthesis of Zr-MOFs. Room temperature synthesis of tetravalent MOFs has been applied accordingly. The mild synthetic conditions successfully prevent the aggregation of ultra-small Au NPs during the core-shell synthesis, after the capping agent removal and during catalytic tests.

Investigation of the removal of capping agents from core-shell Au NPs@MOF-808: A facile synergetic route

Abstract:

Metal nanoparticles encased in MOF shell have shown remarkable properties in catalysis due to potential synergistic effects. However, capping agents, commonly used to prepare these nanoparticles, lower their reactivity once embedded into the MOF. Here we present a new route to prepare PVP-capped Au NPs@MOF composites where the capping PVP can easily be removed by chemical treatment while maintaining the integrity of MOF shell. We finally show how this leads to an enhancement of the reactivity of Au nanoparticles for oxidation reactions.

Introduction

Metal nanoparticles (MNPs, e.g., Au, Pt, Pd NPs. etc) are often used to bring new functions to hybrid structures including chemical sensing,^{1, 2} catalysis,^{3, 4} and bioimaging^{5, 6} thanks to their tailorable properties. The preparation of MNPs with a well-defined particle size distribution often requires their stabilization by the adhesion of organic surfactant or other organic species at their surface. In addition, this can prevent the targeting NPs from aggregation.⁷ However, these molecules attached to the particle surface usually block the active sites of NPs, making the charge transfer between substrates and NPs difficult. Thus, removing the surface stabilizer is of importance, particularly for applications in catalysis.⁸

Zr-carboxylate Metal-organic frameworks (MOFs) are a subclass of solids in MOFs chemistry, being regarded as very promising in catalysis due to their notable chemical and thermal stability.⁹ For example, MOF-808 is a benchmark robust Zr-MOF comprised of Zr₆ oxoclusters and trimesate ligand with a molar ratio in 1: 2, giving rise to a 6-connected-nodes-based 3D framework with a 1.8 nm large pore.¹⁰ The large aperture size of MOF-808, as well as the abundant open metal sites (when the coordinated species are removed), make it very promising for organic-phase heterogeneous catalysis applications.¹¹

Incorporating MNPs into MOFs often endows novel functions for multi-applications, especially for catalysis due to the potential synergetic host-guest effect.¹² Bottle-around-ship strategy refers to the method where a MOF shell is built on preformed core materials (e.g., MNPs) regardless of their shape, size, morphology. The resulting core-shell composites exhibit “empty” MOF pores, therefore making the overall surface area accessible, in sharp contrast to the conventional loading MNPs in the pores of the pre-synthesized and activated MOFs.¹³ A major challenge still remains in synthesizing core-shell composites due to the fast intrinsic nucleation of MOFs.¹³ As such, to construct core-shell composites, the use of capping agents on the surface of NPs is often inevitable to counterbalance the mismatched lattice parameters and/or surface chemistry. To the best of our knowledge, the study of the removal of capping agents of MOF-based core-shell composites is still an unexplored topic. This is probably due to the limited chemical stability of the shell materials

used (ZIF-8, HKUST-1) and/or the difficulty in tracing stabilizers in a complex chemical environment.

Here, we report the first core-shell MNPs@MOF structure based on benchmark MOF-808 and ultra-small Au NPs via a room temperature assembly strategy. The resulting Au NPs@MOF-808 displays a uniform Au NPs distribution. We subsequently show for the first time how the PVP can be removed from an Au@MOF core-shell, here the Au NPs@MOF-808, using various chemical treatments. The catalytic efficiency of the double solvent method and hydrochloric acid (HCl) washing, was then evaluated by using a model reaction (oxidation of benzyl alcohol). A promising impact on the removal of PVP with a boosted reaction efficiency was observed, in agreement with a better accessibility to the Au surface sites. This discovery will pave the way for the preparation of capping free MNP@MOF composite with a better reactivity and selectivity.

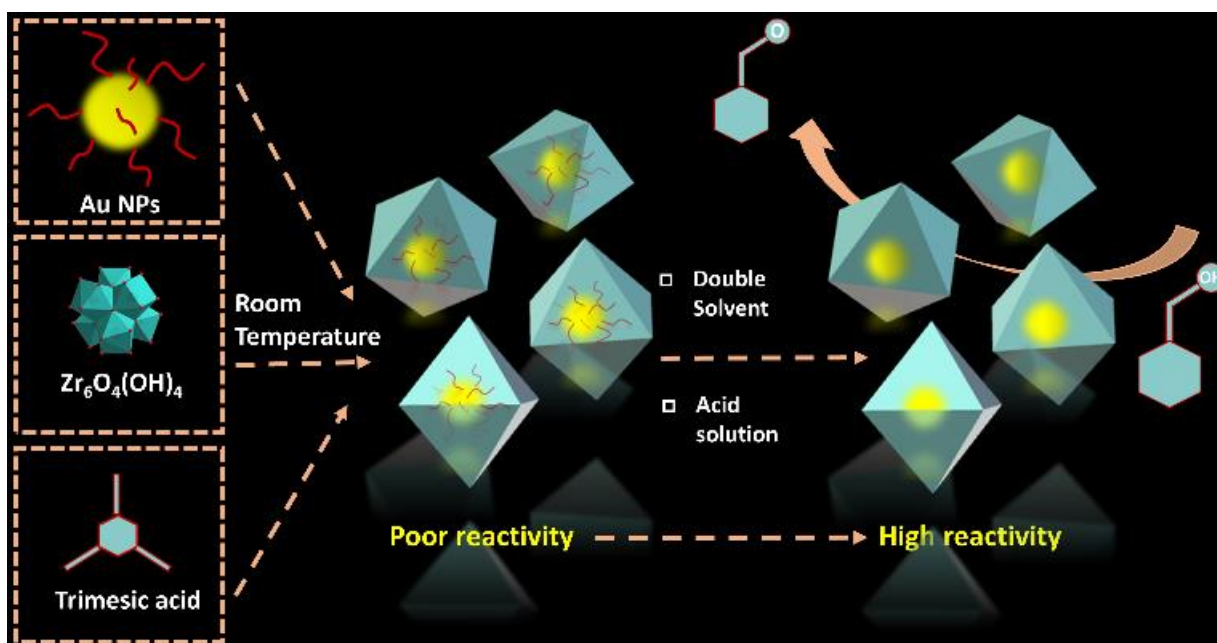


Figure 1. Schematic diagram for the assembly and PVP-removal of Au NPs@MOF-808 composite.

Results and discussion

Our strategy for the catalysis fabrication (see Scheme 1) takes the advantage of our previously reported two-steps room temperature synthesis of MOF-808 with small modifications. PVP is a commonly used stabilizer in the preparation of MNPs for its role not only in the control of the size/shape of certain nanoparticles but also in the prevention of their aggregation. Au was used as a model metal to investigate the removal of surface PVP due to its high reactivity for some standard catalytic reactions once the active sites are accessible. To construct the heterostructure of core-shell Au NPs@MOF-808, the PVP on the surface of Au NPs is required to help Au NPs being well-dispersed in solution and efficiently adsorbed on crystal planes. As shown in Figure 1a, the prepared Au NPs displayed a polydispersed size, ranging from 1.2 to 3 nm (Figure S1). Note that

the incorporation of such small-sized nanoparticles within Zr-MOFs is still challenging due to the uncontrollable aggregating of Au NPs, particularly for the conventional solvothermal synthetic conditions that require elevated temperature. Furthermore, the core-shell architecture of Au NPs@MOFs could help to prevent from aggregation of Au NPs when the PVP is removed due to the “compartment effect” from MOFs.

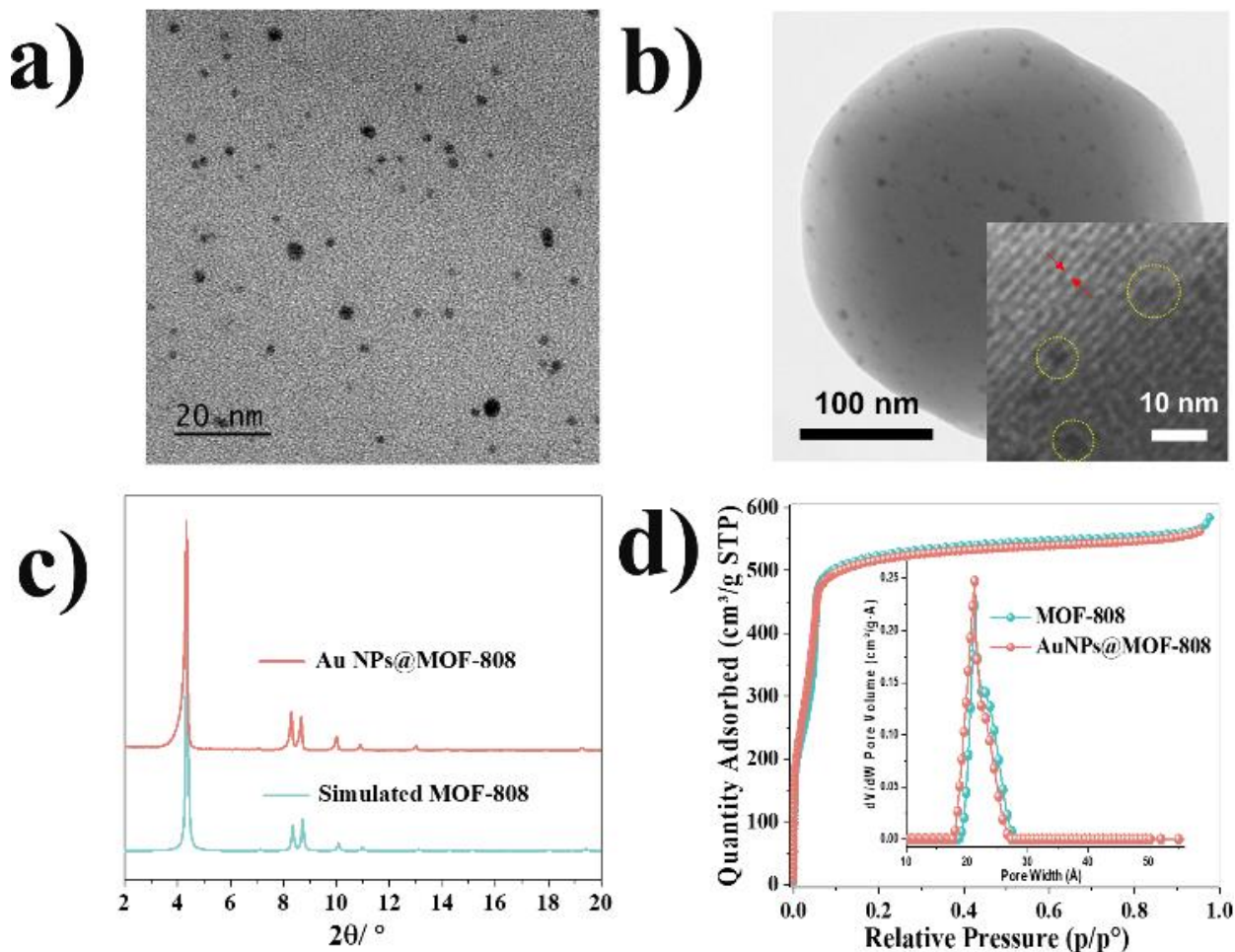


Figure 2. TEM images of a) the synthesized Au nanoparticles, b) the synthesized Au NPs@MOF-808 in large and small magnification; c) PXRD patterns ($\lambda_{\text{Cu}}=1.5406\text{\AA}$) of Au NPs@MOF-808 in comparison with the simulated pattern of MOF-808; (d) 77K N_2 sorption isotherms of Au NPs@MOF (pore size distribution as an inset).

For the synthesis of the composite, a solution of pre-formed Zr_6 oxoclusters in formic acid was added to well-dispersed Au NPs (in excess, 10 mM) in deionized water at ambient conditions, followed by the addition of BTC. After reaction under stirring at room temperature overnight, a well-defined core-shell structure was obtained after intensive washings (Figure 1b). The mean size of the encased Au NPs was 3 nm, which is slightly larger than the initial size. This could be due to the large pore size of MOF-808 (ca. 2 nm) that only allow the successful incorporation of larger-sized Au NPs in the frameworks. Viz., the pore size of any given MOFs should be smaller than

the guests in order to effectively block the guests. EDX analysis (Figure S2) on the obtained composites revealed the incorporated Au content (3.5/ 96.5, Au/ Zr in atomic ratio). The powder X-ray diffraction pattern (PXRD) in Figure 2c is in good agreement with the simulated pattern from the crystal structure, which confirms the crystallinity of Au NPs@MOF-808. As mentioned above, despite intensive H₂O washings (20 times) to remove the excess Au NPs, the elemental mapping, through EDX analysis (see Table S1), demonstrated that only 0.2% of Au was removed during this step, which further proved the formation of well-defined core-shell structure. N₂ porosimetry was conducted to investigate the porosity of the bare MOF-808 and the Au NPs@MOF-808 composites (Figure 1d), giving very close Brunauer-Emmett-Teller (BET) surface areas of 2100 m²/g for both materials, which could be due to the moderate Au content in our case (3.3 atomic%). The pore size distribution analysis (Figure 1d) evidenced almost no change in agreement with the unique feature of the core-shell architecture, where the loaded guest does not occupy the pores of the MOF.¹³

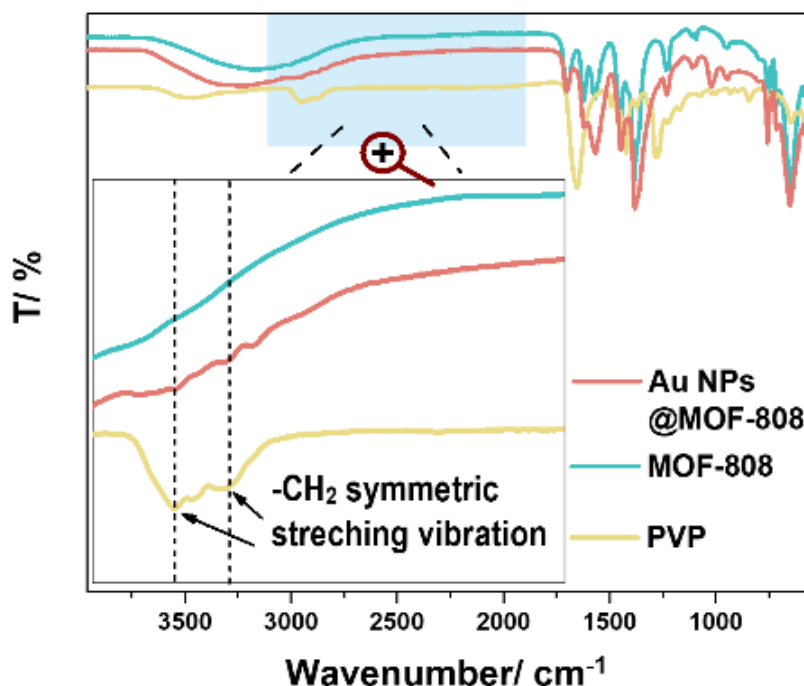


Figure 3. FT-IR spectra (T=298 K) of PVP, Au NPs@MOF-808, and bare MOF-808, the inserted pattern represents the zoom-in blue area.

Owing to the excess amount of PVP used in the synthesis of Au nanoparticles (Au/ PVP= 1: 100 molar ratio), this is expected at this stage that the surface of Au NPs might be quantitatively covered. Figure 3 shows the Fourier-transform infrared spectroscopy (FT-IR) spectra of the water-washed Au NPs@MOF-808, pure PVP, and bare MOF-808 respectively. In the case of Au NPs@MOF-808, the frequency of the –CH₂ symmetric stretching vibrational modes in the region of 3000-2800 cm⁻¹ that corresponds to the PVP reference confirms the existence of a significant amount of PVP left in the composites. Notably, it has been reported so far that capping agents exhibit a negative role in terms of catalytic activity due to the blocking of the accessible surface sites of nanoparticles.¹⁴ Note this is also challenging to analyse traces of PVP in a core-shell MOF-

based composite using usual analytical methods such as NMR, FT-IR/ Raman spectroscopies and TGA. Thus to assess the presence of these residual species, a model catalytic reaction -the oxidation of benzyl alcohol (BA)- was selected to evaluate the accessibility of the Au catalytic sites.¹⁵ Since the size of BA is much smaller than the pore of MOF-808 (0.65 nm vs 1.8 nm), the diffusion of the BA is assumed not to limit the catalytic activity.

The model reaction is described in the Figure 4a. First, the BA oxidation efficiency of the pure MOF-808, pure Au NPs, and Au NPs@MOF-808 catalyst, before and after extensive washing (20 times), was evaluated. As shown in Figure 4b, all these catalysts did not exhibit any reactivity (see the quantification in SI), indicating that i) the pure MOF-808 isn't active for this reaction and ii) the Au sites are inaccessible. Even though the PVP is highly hydrophilic, the washing in water did not allow a successful removal of the capping agent, probably due to the very strong affinity of Au for PVP. It is also interesting to see that no activity was observed for the pure Au nanoparticles, even after 24h under airflow. These results thus demonstrate that the excess of PVP indeed made the active Au sites inaccessible whatever inside the MOF shell or not.

Several studies have been reported regarding the removal of PVP from noble metal nanoparticles based composites but all of them were dealing with much more robust inorganic host matrices (e.g., silica, TiO₂...etc).⁸ Even though Zr-based MOFs like MOF-808 exhibit a relatively strong chemical/ thermal stability compared to other MOFs, it is still not comparable to these inorganic oxides. Therefore, new more gentle ways need to be dedicated to remove PVP from NPs while protecting the MOF structure from degradation.

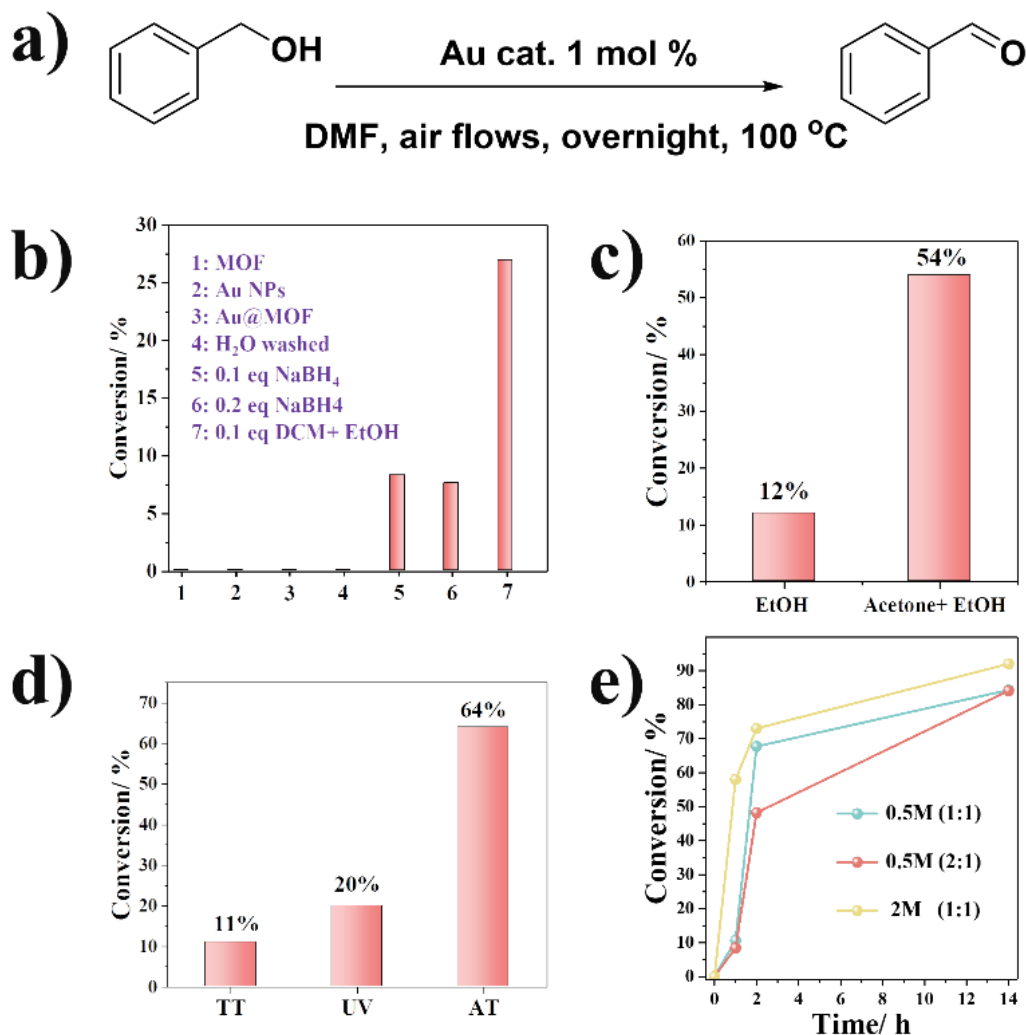


Figure 4. a) Model reaction and its catalytic parameters used in this study b) BA oxidation achieved with different materials, pure MOF-808, pure Au NPs, Au NPs@MOF-808, water washed Au NPs@MOF-808, and Au NPs@MOF-808 treated with 0.1 eq. NaBH₄, 0.2 eq. NaBH₄ in acetone, and 0.1 eq. NaBH₄ in the mixture of DCM and EtOH; BA oxidation achieved with Au NPs@MOF-808 treated with c) EtOH washing and the mixture of Acetone and EtOH washing, d) thermal treatment (TT), UV irradiation, acid washing, e) acid washing in different HCl concentration and solvent ratio.

NaBH₄ was chosen for PVP removal inspired by Jongh et al. that have considered this treatment on dense Au/TiO₂ composites to displace PVP from Au NPs.^{16, 17} Nevertheless, the treatment for Au/TiO₂ used either H₂O or *tert*-butylamine (TBA), which is not suitable for MOF-808 due to the strong alkaline feature of TBA and NaBH₄ once presented in H₂O. Thus, treatments with different amounts of NaBH₄ were investigated preliminarily using an aprotic solvent (acetone). As shown in Figure 4b, the treatment with NaBH₄ (5-6) indeed displayed improved catalytic efficiency as the treatment time increased. However, 0.2 eq NaBH₄ did not show any improved reactivity in comparison with 0.1 eq NaBH₄, indicating that a higher quantity of NaBH₄ did not lead to a satisfying reactivity. The treatment with 0.2 eq NaBH₄ for 2h did also lead to a loss of crystallinity

as evidenced from a slight broadening of the Bragg peaks (see Figure S3) due to a partial degradation of MOF-808 in 0.2eq NaBH₄ solution for longer time. The limited efficiency of varying treatments with NaBH₄ may also be due to a low solubility of NaBH₄ in acetone. Therefore, the treatment was subsequently carried out (with 0.1eq of NaBH₄) in a more protonic solvent (DCM/ ethanol=8.3: 1 in volume). This is also required as acetone was shown to be reduced by NaBH₄ in the presence of alcohol, which might inactivate NaBH₄.¹⁸ After this new reduction assay at room temperature, the PXRD pattern of the composite showed its integrity was kept (see Figure S4). Interestingly, a pronounced catalytic enhancement using the treated catalyst reaching 27% conversion was observed after overnight reaction (Figure 4b (7)). We believe this could be due to a better removal efficiency of PVP associated with its better dissolution through the reported double solvent method (DSM). DSM represents the use of the mixture of good/ poor solvent in an appropriate ratio to remove capping agents. The surface ligands tend to shrink on the surface of NPs to form compact configuration when the poor solvent is added, whilst they can be fully dispersed in the good solvent and therefore easy to detach from the particle surface. This dynamical process offers the opportunity to effectively remove the stabilizer. In order to verify our hypothesis, we treated the catalyst with 0.1eq NaBH₄ in ethanol. The PXRD of the catalyst after the treatment showed a significant decreased crystallinity (Figure S5), while the catalytic activity did not exhibit any improvement, with only 12% of conversion after overnight reaction (Figure 4b). Thus, it is likely that the mixed solvent is responsible for the reactivity improvement in the DCM/EtOH mixture. However, due to the high toxicity of DCM, from a green/ sustainable chemistry point of view, alternative greener solvents shall be considered. According to our hypothesis, one shall select a combination of a solvent that can fully dissolve PVP and another one not compatible with PVP. Accordingly, acetone and H₂O were used instead of DCM and Ethanol. The high-quality PXRD pattern (figure S6) indicated the intact structure of the treated catalyst after xx h of soaking. The subsequent catalytic test on the model reaction gave a remarkable 54% conversion, much higher than the previous tests. This is in good agreement with the previous observation of the solvent effect on the PVP removal from Pt nanoparticles and Pt nanocubes.^{19, 20}

Thus, all the treatments indicated that 1) the catalysts treated with NaBH₄ present a low reactivity and that therefore, this approach was excluded from further study, 2) the DSM indeed displayed competitive advantage in both crystallinity preservation and efficiency enhancement.

Other treatments relying on other strategies were also applied, such have been previously reported such as thermal (TT),²¹ Ultraviolet-visible (UV),²² and acid treatments.²³ Thermal decomposition of PVP is usually performed between 200°C-350 °C. The incorporation of the guest NPs in the MOF structure often decreases the thermal stability of the MOF. Our Au NPs@MOF-808 are thermally stable up to 225°C under air (see Figure S7). We thus considered 200 °C to treat the catalyst for 5h but the conversion of BA was only 11% after 14h reaction, which suggested that thermal treatment is not here sufficient for the removal of PVP. Ultraviolet-visible (UV) treatment represents the decomposition of PVP under UV irradiation. The irradiation produces ozone upon interacting with molecular oxygen, which subsequently induces the oxidation of the carbon-containing compounds into carbon dioxide and water. However, the treatment under 257 nm UV irradiation led to a complete decomposition of the MOF structure even after 2h. This is due to UV-induced linker oxidation.²⁴ Alternatively, we used 365 nm UV irradiation to protect MOF from

degradation. Unfortunately, PXRD (see Figure S8) evidenced a decrease of the crystallinity after the exposure only for 4h, and only 20% of the BA conversion (Figure 4d) was achieved. Considering the fact that the PVP most likely interacts with Au (0) species through Au-O or Au-N bond, therefore one plausible pathway to remove ligands is to use guest molecular to protonate organic stabilizer, which thus makes the coordinating bonds weaker and being more soluble in the solvents. In our case, since MOF-808 has a good stability in acidic media, we used 0.5M HCl acetone solution to treat the catalyst. The subsequently extensive acetone exchange was also used to exclude the remaining species after treatment. Interestingly, BA oxidation experiment demonstrated the enhancement in the reactivity (Figure 3c), which reached 64% conversion. The structure stabilities after treatment and catalysis were evidenced by PXRD (see Figure S9).

These two different DSM and acid treatments routes therefore both showed a very positive impact on the composite reactivity. Notably, both of these methods have excellent compatibility when taking the stability of MOF material into account. In the next step, we combined the DSM and acid treatment using 0.5M HCl in a mixture of acetone and H₂O (in 1: 1 vol%) at room temperature. We then analysed the reaction kinetics and showed that the treated catalyst could further enhance the reactivity up to 80% conversion (Figure 4e). Even though a higher volume ratio of acetone was used in the reference, this is not a significant factor in our case, as the Acetone and H₂O in the volumetric ratio in 2: 1 did not result in promoted efficiency and final conversion in 24h. As the Zr-MOFs are known to be highly stable in acidic media, a 2M HCl solution in acetone and H₂O mixed solution. The catalytic test in Figure 4e exhibited an even higher reactivity as well as a faster kinetics, reaching 73% and 92% conversion in 2h and 14h, respectively. The PXRD measurement (Figure S10) and EDX analysis (Figure S11) both revealed the overall integrity and component of composites were maintained. This indicates that combining an acid treatment with with DSM is an ideal method for the removal of PVP from core-shell Au NPs@MOF-808 composites. Interestingly, no -CH₂ symmetric stretching vibrational peaks were observed in the as-treated composites (Figure S12), indicating the excellent removal of PVP, in good accordance with the catalytic results.

Conclusion

As conclusion, for the first time, a core-shell architecture based on MOF-808 was synthesized with ultra-small Au NPs. The room temperature aqueous solution based synthesis allowed the encapsulation in green manner without Au NPs aggregation. Subsequently, the successful removal of the PVP from the Au NPs@MOF-808 composite was achieved following a double solvent method (DSM) under acidic conditions. This work will guide future works towards the design of new generations of efficient metal nanoparticles@MOF composites for heterogeneous catalysis.

References

1. J. H. Fu, Z. Zhong, D. Xie, Y. J. Guo, D. X. Kong, Z. X. Zhao, Z. X. Zhao and M. Li, *Angew. Chem. Int. Edit.*, 2020, **59**, 20489-20498.
2. M. Weber, J. Y. Kim, J. H. Lee, J. H. Kim, I. Iatsunskyi, E. Coy, P. Miele, M. Bechelany and S. S. Kim, *J. Mater. Chem. A*, 2019, **7**, 8107-8116.
3. D. Munoz-Santiburcio, M. F. Camellone and D. Marx, *Angew. Chem. Int. Edit.*, 2018, **57**, 3327-3331.
4. L. C. Liu and A. Corma, *Chemical Reviews*, 2018, **118**, 4981-5079.
5. Y. Chen, H. R. Chen, D. P. Zeng, Y. B. Tian, F. Chen, J. W. Feng and J. L. Shi, *ACS Nano*, 2010, **4**, 6001-6013.
6. X. H. Huang, P. K. Jain, I. H. El-Sayed and M. A. El-Sayed, *Lasers Med. Sci.*, 2008, **23**, 217-228.
7. X. Wang, J. Zhuang, Q. Peng and Y. D. Li, *Nature*, 2005, **437**, 121-124.
8. Z. Q. Niu and Y. D. Li, *Chem. Mater.*, 2014, **26**, 72-83.
9. Y. Bai, Y. B. Dou, L. H. Xie, W. Rutledge, J. R. Li and H. C. Zhou, *Chem. Soc. Rev.*, 2016, **45**, 2327-2367.
10. H. Furukawa, F. Gandara, Y. B. Zhang, J. C. Jiang, W. L. Queen, M. R. Hudson and O. M. Yaghi, *J. Am. Chem. Soc.*, 2014, **136**, 4369-4381.
11. S. Y. Moon, Y. Y. Liu, J. T. Hupp and O. K. Farha, *Angew. Chem. Int. Edit.*, 2015, **54**, 6795-6799.
12. Q. H. Yang, Q. Xu and H. L. Jiang, *Chem. Soc. Rev.*, 2017, **46**, 4774-4808.
13. S. Dai, A. Tissot and C. Serre, *Adv. Energy Mater.*, DOI: 10.1002/aenm.202100061.
14. T. H. Yang, Y. Shi, A. Janssen and Y. Xia, *Angew. Chem. Int. Edit.*, 2020, **59**, 15378-15401.
15. C. Della Pina, E. Falletta and M. Rossi, *Chem. Soc. Rev.*, 2012, **41**, 350-369.
16. B. Donoeva and P. E. de Jongh, *ChemCatChem*, 2018, **10**, 989-997.
17. M. Luo, Y. Hong, W. Yao, C. Huang, Q. Xu and Q. Wu, *J. Mater. Chem. A*, 2015, **3**, 2770-2775.
18. H. C. Brown, E. J. Mead and B. C. S. Rao, *J. Am. Chem. Soc.*, 1955, **77**, 6209-6213.
19. R. M. Arán-Ais, F. J. Vidal-Iglesias, J. Solla-Gullón, E. Herrero and J. M. Feliu, *Electroanalysis*, 2015, **27**, 945-956.
20. I. A. Safo, C. Dosche and M. Oezaslan, *Z. Phys. Chem.*, 2018, **232**, 1319-1333.
21. C. Prossl, M. Kubler, M. A. Nowroozi, S. Paul, O. Clemens and U. I. Kramm, *Phys. Chem. Chem. Phys.*, 2021, **23**, 563-573.
22. R.-Y. Zhong, K.-Q. Sun, Y.-C. Hong and B.-Q. Xu, *ACS Catal.*, 2014, **4**, 3982-3993.
23. G. Lee, J. H. Shim, H. Kang, K. M. Nam, H. Song and J. T. Park, *Chem. Commun.*, 2009, DOI: 10.1039/b911068b, 5036-5038.
24. D. Mateo, A. Santiago-Portillo, J. Albero, S. Navalón, M. Alvaro and H. García, *Angew. Chem.*, 2019, **131**, 18007-18012.

Supporting information

Investigation of the removal of capping agents from core-shell Au NPs@MOF-808: A facile synergetic route

Shan Dai,^a Kieu Phung Ngoc,^a Laurence Grimaud,^a Sanjun Zhang,^c Antoine Tissot,^{a†} Christian Serre^{a†}

Experimental

Ambient Powder X-ray Diffraction (PXRD) data were recorded on a high-throughput Bruker D8 Advance diffractometer working on transmission mode and equipped with a focusing Göbel mirror producing CuK α radiation ($\lambda = 1.5418 \text{ \AA}$) and a LynxEye detector. Nitrogen porosimetry data were collected on a Micromeritics Tristar/ Triflex instrument at 77 K (pre-activating samples at 150 °C under vacuum, 12 hours). Scanning Electron Microscopy coupled with energy-dispersive X-ray spectroscopy (SEM-EDX) results were recorded with FEI Magellan 400 scanning electron microscope. Infrared spectra were measured with a Nicolet iS5 FTIR ThermoFisher spectrometer. ¹H NMR spectra were recorded on a Bruker Avance 300 spectrometer.

Chemicals:

All chemicals were purchased from commercial suppliers and used as received without further purification. Trimesic acid, 98%, Alfa Aesar. ZrCl₄ anhydrous, 98%, Acros. Zirconyl chloride octahydrate, 98%, Acros. Isopropyl alcohol, 99+%, Sigma. Formic acid, 98%, Acros. Acetone, 99%, Acros. Methanol absolute, $\geq 99\%$, Acros. NaNH₄, $\geq 98\%$, Aldrich. Polyvinylpyrrolidone, average mol wt 10,000, Aldrich. HAuCl₄·3H₂O, 99.99%, Alfa Aesar. Distilled water, Millipore system.

Synthesis of Au NPs :

The synthesis of Au NPs was from the previous work.¹ To a solution of PVP (K-90) (277.85 mg) in 30 mL of H₂O (MiliQ grade) was added an aqueous solution of HAuCl₄ (1 mM) so that the molar ratio of AuCl₄⁻ and monomer unit of PVP was kept at 1:100. The mixture was kept stirring for 30 minutes at 0 °C, followed by the addition of an aqueous solution of NaBH₄ (100 mM, 2.5 mL). The resulted clear dark mixture was kept stirring at 0 °C for 15 more minutes before washing with the mixture of acetone/H₂O (7/1) three times by centrifugation. The final Au NPs was dry in air to remove completely acetone and diluted in H₂O (3.25 mL) and stored in the fridge for further use.

Synthesis of Au NPs@MOF-808:

Zirconium oxocluster ($\text{Zr}_6\text{O}_4(\text{OH})_4(\text{C}_2\text{H}_3\text{O}_2^-)_8\text{Cl}_4$, 120 mg, 0,16 mmol) was stirred in HCOOH (600 μL) until well dissolved. Then, an aqueous solution of Au NPs (1 mL, 10 mM) was added. The mixture was kept stirring for around 15 minutes until observation of clear dark solution. Then, BTC (20 mg, 0.095 mmol) was added and the resulted mixture was kept stirring over night until observation of cloudy purple solution. The solid was collected and washed three times with H_2O , three times with MeOH and three times with acetone. Final purple solids (105 mg) were then dried under vacuum.

PVP removal with thermal treatment:

The well-washed dry composite was heated in the oven for 4 hours at 200 °C. The resulted composite crystallinity was tested/ used directly for other characterizations in this context. Observation showed a slight change in color from dark purple to lighter purple.

PVP removal with UV radiation treatment:

The well-washed dry composite was positioned under the ultraviolet lamp (365 nm) chamber for 24 hours. The resulted composite crystallinity was tested/ used directly for other characterizations in this context.

PVP removal with acid solution treatment:

The well-washed dry composite (17 mg) was dispersed in H_2O (2 mL) by sonification, until all the solid was well dispersed in the solution. Different amount of HCl was then added to the mixture to reach the targeting final HCl concentration (0.5M and 2M), which was kept stirring for 2 hours. The resulted solution was washed with acetone and dried under air.

PVP removal with NaBH_4 treatment:

The well-washed dry composite (17 mg) was suspended in 2 mL acetone followed by the addition of a solution of NaBH_4 (0.04 mg, 0.1 eq or 0.08 mg, 0.2 eq) in acetone. The mixture was kept stirring at room temperature for 0.5 hour. The final catalyst was obtained by centrifugation, then washed with acetone three times and dried under air. Protocol mentioned above was applied for the different treatments with NaBH_4 using various amount of NaBH_4 as well as different reaction times.

PVP removal with NaBH_4 treatment in the co-solvent of DCM and EtOH:

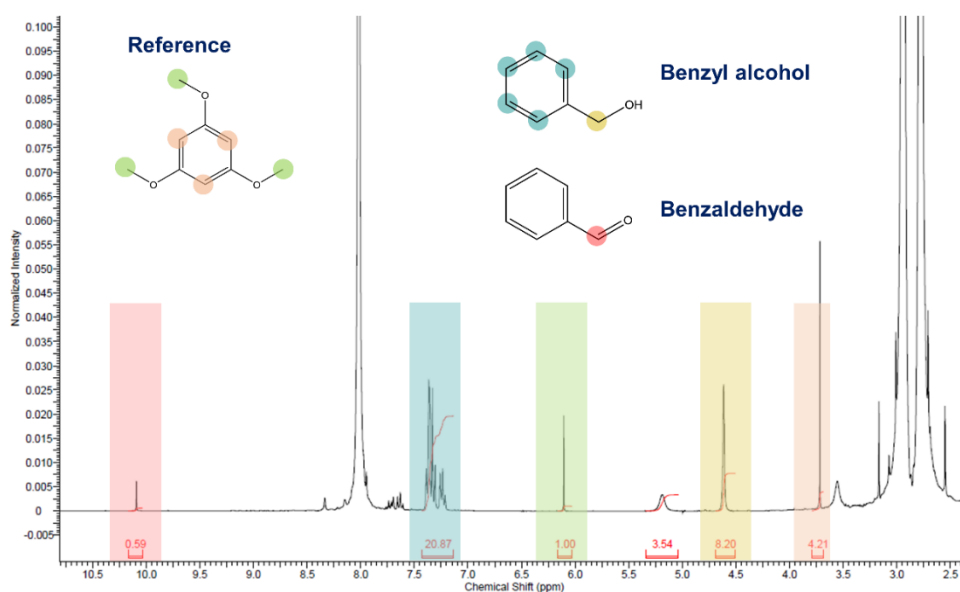
The catalyst (10.1 mg) was dispersed in a mixture of NaBH₄/DCM/EtOH (0.068 mg/ 527 μL/ 63.3 μL) and kept stirring for 30 minutes at room temperature. Final solid was obtained by centrifugation, washed with DCM three times and acetone three times before drying under air.

PVP removal with double solvent treatment:

The well-washed dry composite (35 mg) was dispersed in a H₂O (2 mL) in a round bottom flask, following by the addition of acetone (2 mL). The mixture was refluxed overnight. Final solid was obtained by centrifugation and washed with a mixture of H₂O/acetone (1:1), then three times with acetone followed by drying under air.

Quantitative method:

Quantitative-¹H NMR experiment were performed for the catalyst activity study in the presence of 1,3,5-trimethoxybenzene in a coaxial insert was used a reference. The conversions were calculated according to the integrated area of each peak.



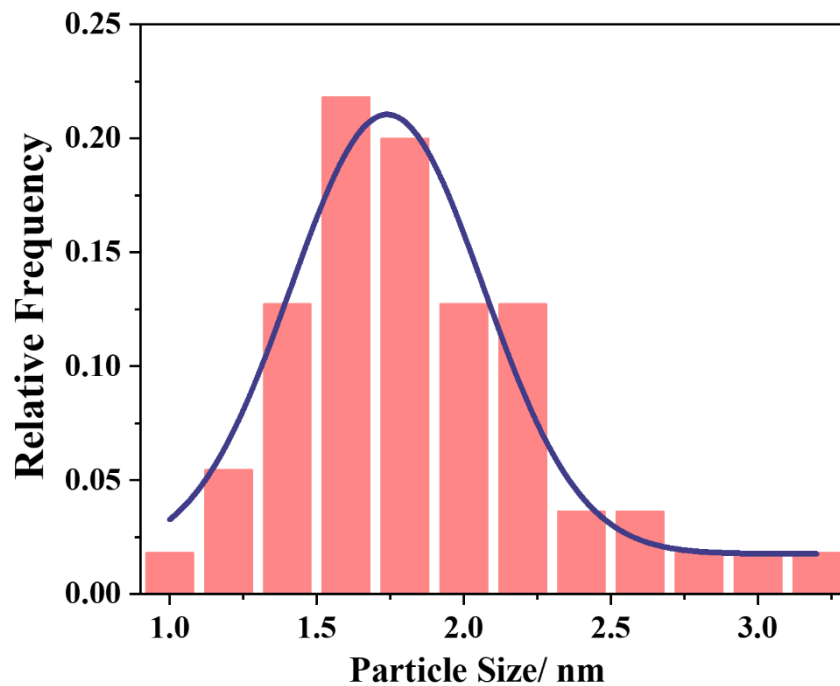


Figure S1. Particle size distribution histogram corresponding to the aqueous prepared Au NPs.

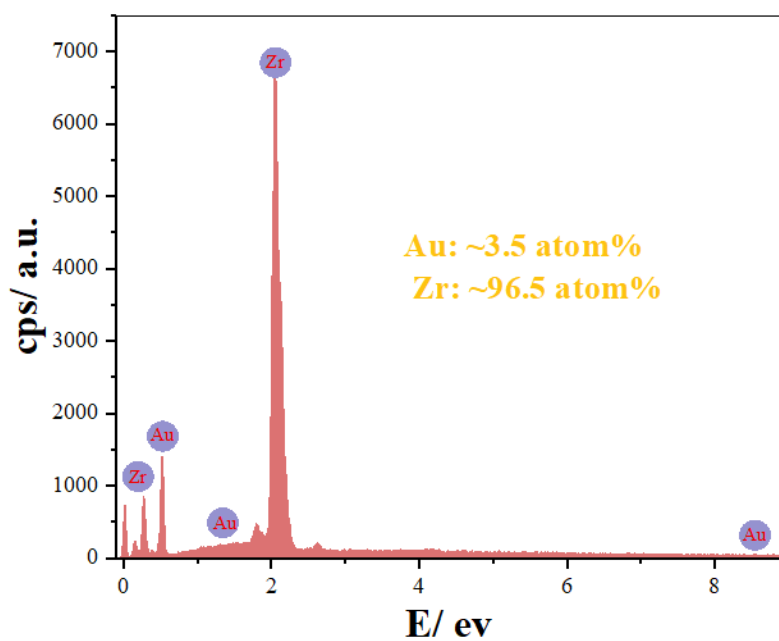


Figure S2. EDX spectra of Au NPs@MOF-808.

Table S1. The EDX characterizations of Au NPs@MOF-808 with different treatments.

	Au/ Zr (atom%)
As-synthesized Au NPs@MOF-808	3.5/ 96.5
20 times water washing	3.3/ 97.7

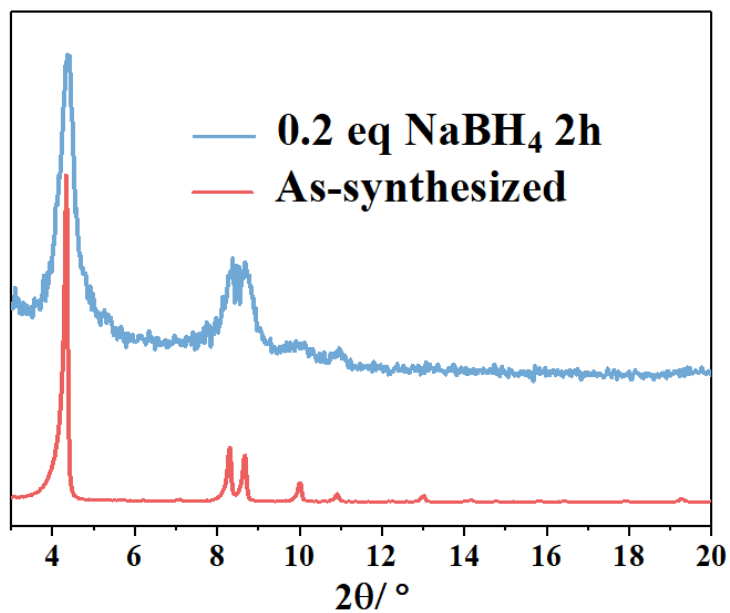


Figure S3. PXR D patterns of the synthesized Au NPs@MOF-808 and the one after treated with 0.2 eq NaBH₄ for 2h.

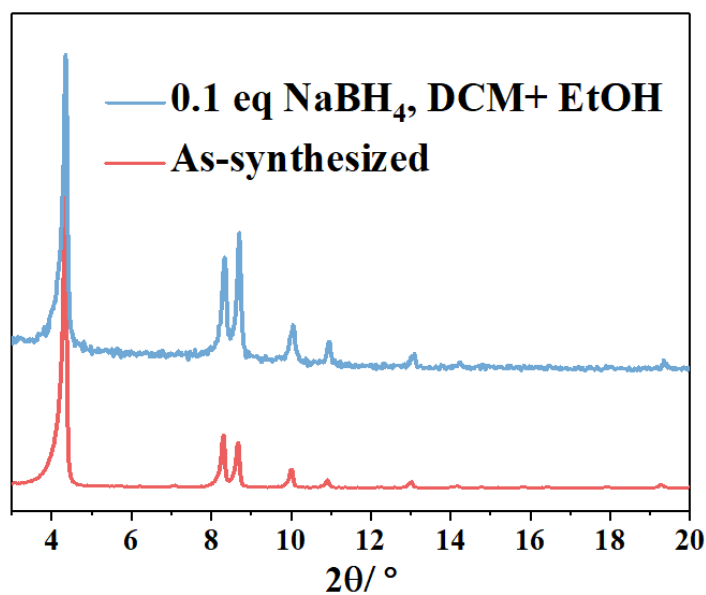


Figure S4. PXR D patterns of the synthesized Au NPs@MOF-808 and the one after treated with 0.1 eq NaBH₄ in the mixture of DCM and EtOH solvent.

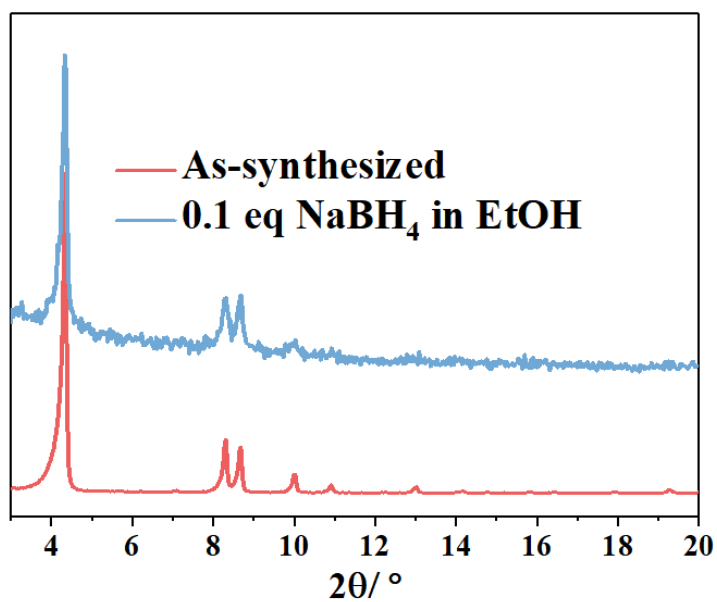


Figure S5. PXRD patterns of the synthesized Au NPs@MOF-808 and the one after treated with 0.1 eq NaBH_4 in EtOH.

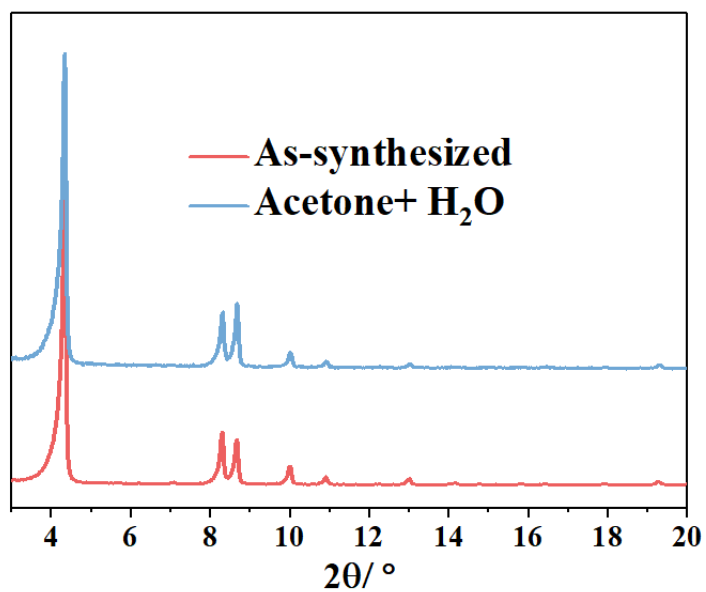


Figure S6. PXRD patterns of the synthesized Au NPs@MOF-808 and the one after mixture solvent washing (acetone+ H_2O).

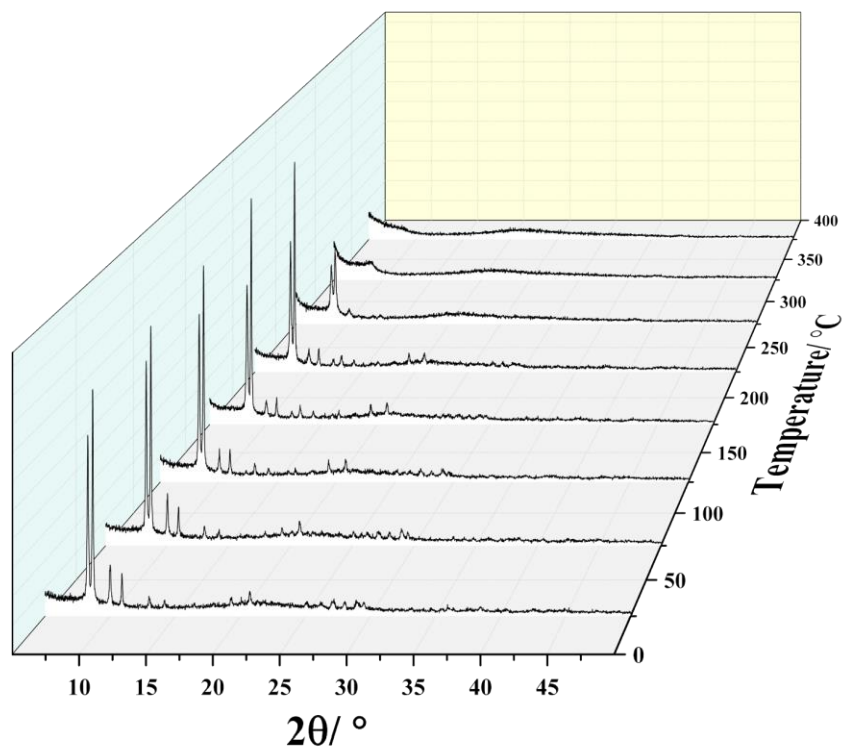


Figure S7. In-situ temperature-dependent PXRD of Au NPs@MOF-808.

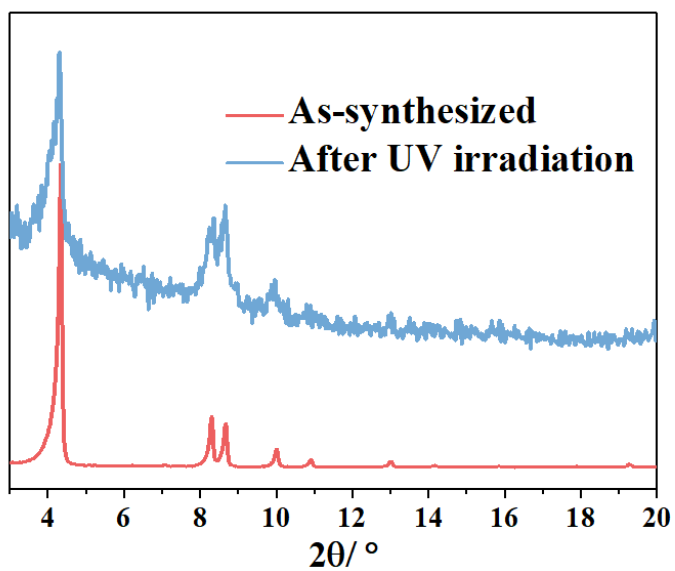


Figure S8. PXRD patterns of the synthesized Au NPs@MOF-808 and the one after 365 nm UV irradiation.

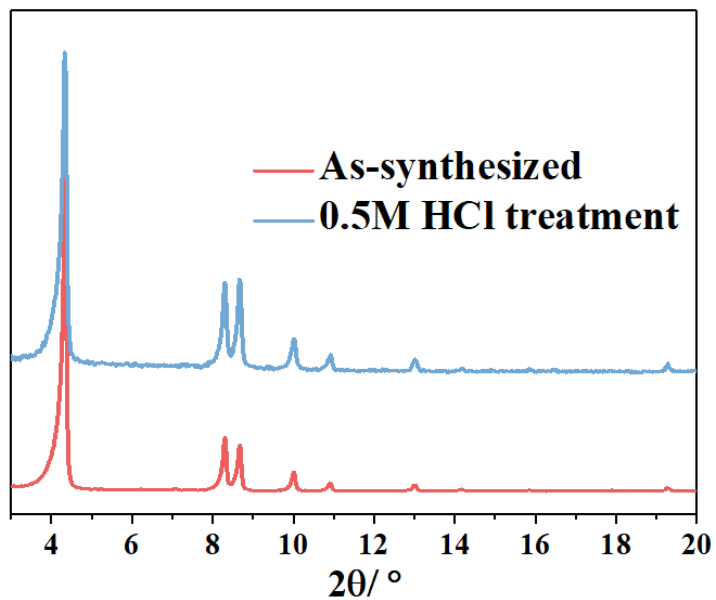


Figure S9. PXRD patterns of the synthesized Au NPs@MOF-808 and the one after 0.5M HCl treatment.

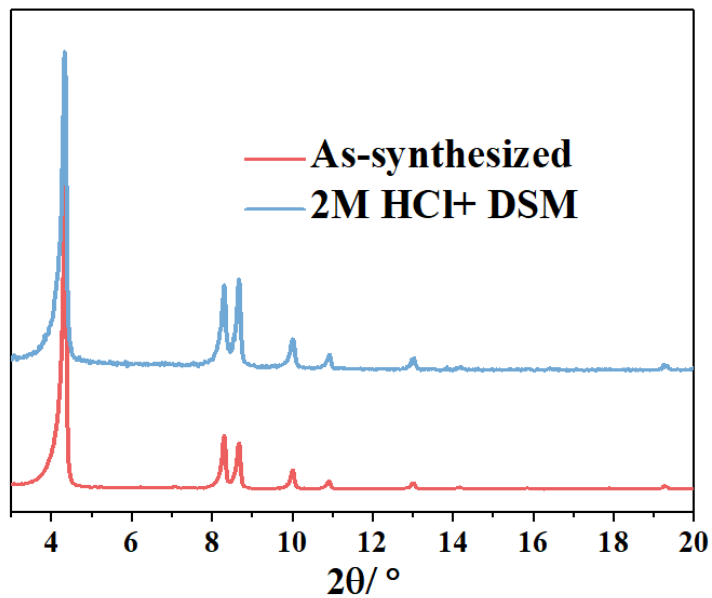


Figure S10. PXRD patterns of the synthesized Au NPs@MOF-808 and the one after 2M HCl treatment in the mixture solvent of Acetone and H₂O (1 : 1).

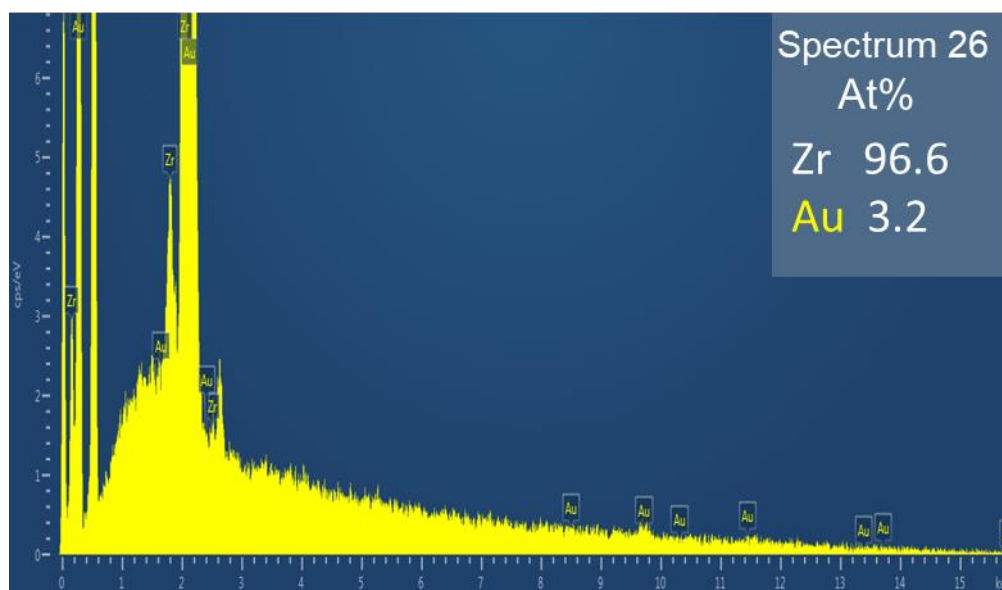


Figure S11. EDX characterization of the Au NPs@MOF-808 after 2M HCl treatment in the mixture solvent of Acetone and H₂O (1 : 1).

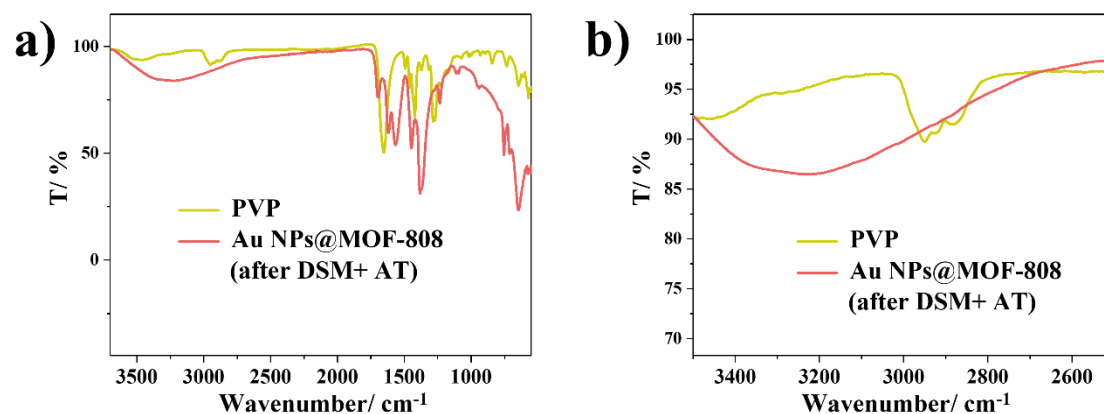


Figure S12. a) FT-IR spectra of PVP, and Au NPs@MOF-808 (after acid treatment in double solvent), b) zoom in figure of a).

1. H. Tsunoyama, H. Sakurai, N. Ichikuni, Y. Negishi and T. Tsukuda, *Langmuir*, 2004, **20**, 11293-11296.

Chapter 5

This chapter is adapted to the following manuscript:

Incorporating ultra-small Cu nanoclusters in Zr Metal-Organic Frameworks: location regulated CO₂ photo-reduction efficiency

Shan Dai et al.

Table of Contents

Contributions to this research.....	194
Article	195
1. Introduction	195
2. Results and discussion.....	196
3. Conclusion.....	201
References	202
Supporting information	205

Contributions to this research

I did the synthesis of Cu nanoclusters and core-shell Cu NCs@MOFs. The corresponding characterizations, including PXRD, SEM, EDX, TGA, N₂/CO₂ isotherms, NMR, and FT-IR, were all done by myself. Mr. Bernard Goetz helped to do ICP and Dr. Gilles Patriarche did the HRTEM and STEM for this work. *In-situ* gas adsorption FT-IR characterizations were done at ENSICAEN, Caen, France, with the help of Dr. Marco Daturi and Dr. Alexandre Vimont. The catalytic application was in collaboration with Dr. Takashi Kajiwara, Dr. Miyuki Ikeda, and Dr. Qiang Xu from Japan. I plotted all the figures and wrote the manuscript by myself.

Motivation

I further took the advantage of the room temperature synthesis strategy from the previous chapters to encapsulate the ultra-small Cu nanoclusters, the latter one has been demonstrated very promising for CO₂ reduction to form C₁/C₂ organic feedstocks. However, the very limited chemical/thermal stability of Cu nanoclusters is one main drawback that prevents their practical applications, as their catalytic activity can be significantly weakened by nanoclusters aggregation. Therefore, using porous solids to stabilize Cu nanoclusters inside core-shell nanocrystals is one effective way to overcome this challenge. Furthermore, potential catalytic synergetic effects might offer more promises in terms of catalytic reactivity and selectivity.

Incorporating ultra-small Cu nanoclusters in Zr Metal-Organic Frameworks: location regulated CO₂ photo-reduction efficiency

▪ Introduction

The massive emission of CO₂ into the atmosphere has been regarded as the main reason for global warming. One of the most promising techniques to overcome this threat is to use catalytically reactive porous materials to trap and convert CO₂ into chemical feedstocks.¹ Previous works have focused on CO₂ reduction by hydrogenation at high temperatures regardless of the additional cost of hydrogen.² Electrocatalytic CO₂ reduction is another promising alternative even though it might give rise to the decomposition of the resulted chemicals due to the commonly required overpotential and additional electricity needs, which is a secondary form of energy.³ Consequently, the photoreduction of CO₂ has been drawing considerable attention due to the abundance and renewability of solar energy.

Cu nanoclusters (NCs) are a class of ultra-small metallic nanoparticles (NPs), typically with a size less than 2 nm.⁴ The well-known size-dependent catalytic effect makes Cu NCs more appealing compared to the larger-size Cu nanoparticles.^{5,6} Moreover, Cu is an inexpensive metal with a large abundance, in contrast with noble metal-based photocatalysts that have been widely studied and can selectively reduce CO₂ to CO.⁷⁻⁹ In addition, Cu can lead to the CO₂ reduction into hydrocarbon products, including C₁ to C₂, which is advantageous from the industrial point of view.^{5,10,11} However, Cu NCs are often very fragile due to their ultra-small size and therefore very high surface energy and the aggregation of Cu NCs is often unavoidable, particularly in harsh conditions (e.g., high temperature).

Metal-organic frameworks (MOFs) are crystalline solids that usually show high porosity, tunable physical/ chemical properties.¹² Zr-based MOFs are a particularly appealing subset of MOFs, presenting a high chemical stability, and almost infinite structural diversity. Encapsulating catalytic inorganic NPs into Zr-MOFs has therefore been intensively studied, particularly for the conventional loading of NPs in the cavity of MOF.^{13,14} However, many problems may occur when using these solids as catalysts such as the leaching of active NPs, the hindered diffusion of substrate, and the undefined spatial distribution of active sites. Constructing a MOF shell around the preformed nanoparticles to form a core-shell structure is one effective way that excludes all the above-mentioned drawbacks.¹⁵ However, a great challenge remains in making core-shell NPs@MOF due to the lattice mismatch between the NPs and MOF. Exciting achievements have been reported dealing with noble metal NPs, such as Au, Pt, Pd.^{13,16} Unfortunately, the attempts on Cu NPs@MOFs remain scarce, which from our understanding is due to the high activity of Cu NPs, making it indeed difficult to form the targeting structures. Motivating efforts have been reported recently about the construction and the superior catalytic performance of the core-shell structures based on large Cu NPs (≥ 18 nm).^{2,17} The study on Cu nanoclusters ($\varnothing \leq 2$ nm)@MOFs is still an unexplored field in spite of greater promises that can arise from the produced composites. Furthermore, preparing any core-shell NPs@MOFs in gram-scale has not yet been investigated regardless of their interest in practical applications.

Herein, we apply a room temperature, aqueous solution-based strategy for the first time to incorporate ultra-small Cu nanoclusters in two benchmark microporous Zr-MOFs (Zr-fumarate, UiO-66-NH₂). The low cost of the raw materials and green synthesis conditions enable us to optimize the synthetic parameters to achieve gram-scale catalyst preparation. The prepared composites display high reactivity and selectivity for the photo-conversion of CO₂ to chemical feedstock at room temperature. In addition, when comparing the catalytic reactivities of Cu NCs on the MOFs, where Cu NCs are mainly on the surface of MOF, much lower reactivities are observed, demonstrating the advantages of core-shell structures in governing the high reactivity of MOF-based catalytical composites. Finally, the origin of active sites is studied by using *In-situ* IR spectroscopy, revealing the importance of the Cu(I) from the surface of Cu NCs.

▪ **Results and discussion**

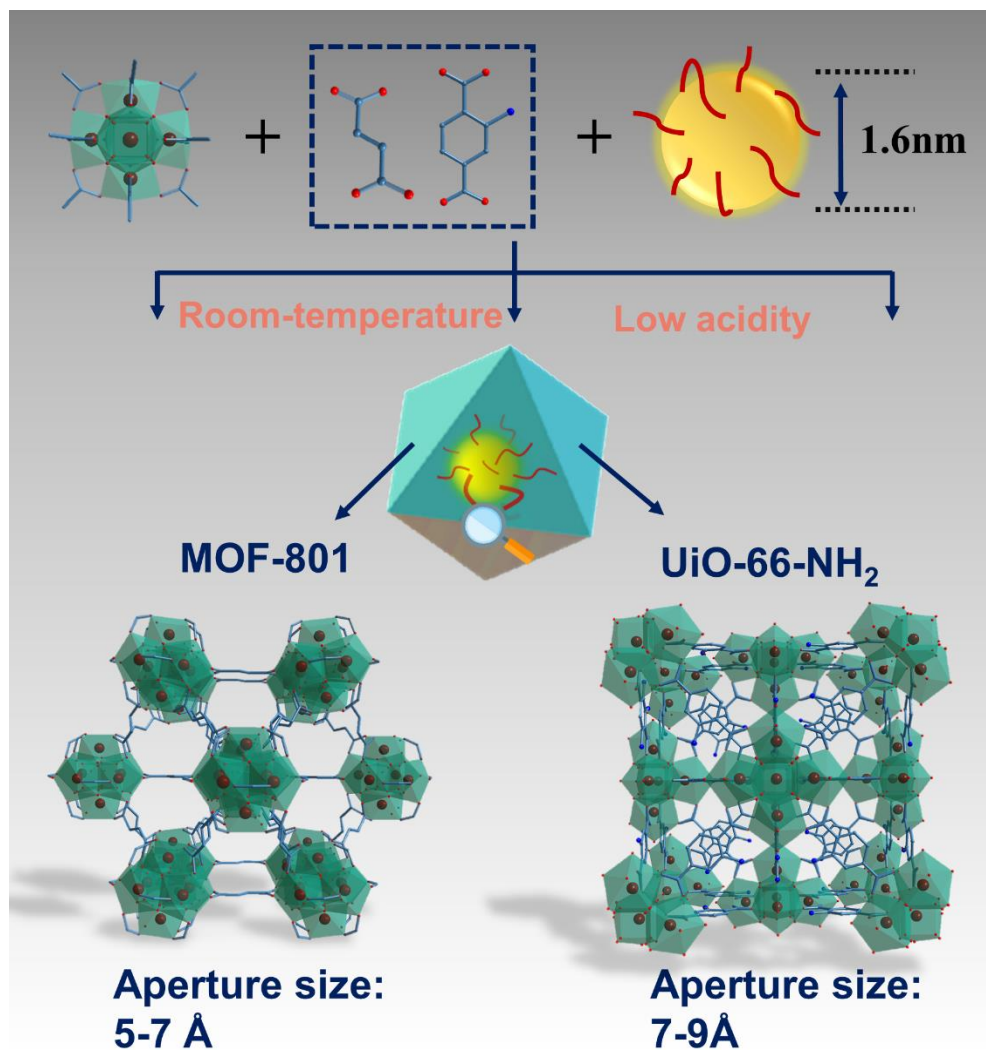


Figure 1. Conceptual scheme of the bottle-around-ship strategy applied in this work, as well as all the involved Cu NCs and Zr-MOFs and their basic information in this work.

The bottle-around-ship strategy relies on the pre-synthesized nanoparticles. The fabrication of the MOF shell around nanoparticles is subsequently carried out to form guest@host composites (illustrated in Figure 1). The synthesis of ultra-small Cu nanoclusters (Cu NCs) was performed using L-ascorbic acid as both reducing and capping agent thanks to its strong affinity with Cu. High-Resolution Transmission electron microscopy (HRTEM) image (Figure 2b) indicated that the yellowish solution obtained after stirring 1h at room temperature contains 1.6 nm monodispersed Cu nanocluster at (Figure 2c). The ultra-small Cu NCs are often much less thermally/ chemically stable than other common nanoclusters (e.g., Ag, Au, Pt NCs) due to their higher reactivity that can lead to aggregation and oxidation at elevated temperatures in solution. As most of the robust MOFs (e.g., Zr-MOFs) are synthesized using solvo/ hydro-thermal methods, we applied a novel room temperature strategy to design Cu NCs@MOF composites without altering the Cu NCs properties. The synthesis required the use of pre-synthesized Zr₆ oxoclusters, which represents a less acidic starting material in comparison to other Zr salts in our previous study.² Indeed, using ZrCl₄ as the starting metal salt for the synthesis of Zr-MOFs led to the dissolution of Cu NCs, in agreement with reported results.² The introduction of Cu NCs in the MOF precursor solution was well comparable to the MOF growth even though the preparation was in gram-scale, which was proved by both PXRD and 77 K N₂ isotherm measurements (see Figure S1-S2). The preservation of porosity suggested that the spatial distribution of Cu NCs is more likely to be core-shell, as opposed to the conventional loading of nanoparticles in the pore space of a given MOF that usually leads to a strong decrease of the solid porosity. Since the size of Cu NCs (1.6 nm) are larger than the aperture size of MOF-801 (5-7 Å), the Cu NCs might also be grafted on the surface of MOF particles due to the affinity between MOF and Cu NCs. In order to check this, we simply mixed the preformed MOF-801 and Cu NCs solution in the same conditions as the bottle-around-ship strategy abovementioned. Inductively coupled plasma (ICP) analysis on the collected sample evidenced the absence of Cu in the sample, indicating that the Cu NCs are unlikely to be on the surface of MOF. Interestingly, after carefully investigating the relationship between the introduced Cu NCs and the nucleation of MOFs, we found a dramatic Cu NCs concentration-dependent Bragg peaks broadening of the obtained composites (Figure 2d), suggesting that the size of Cu NCs@MOF decreased as a function of the introduced Cu NCs quantity (illustrated in Figure 2a). SEM and TEM images in Figure S4-S6 (corresponding to PXRD patterns in Figure 2d (1), (2), and (9)) confirmed our hypothesis. These results revealed the nucleation process followed the seed-mediated crystal growth, where the larger number of small Cu NCs seeds led to the much more binding sites with MOF precursors, making the MOFs stayed in nano-regime rather than further assembly to larger crystals. This observation is in good agreement with the previous reports, where the introduced guest nanoparticles resulted in the downsizing of the MOF shell.^{18, 19} A control experiment using one equivalent L-ascorbic acid in the synthesis without Cu nanocrystals did not result in the similar downsizing (no PXRD peak broadening, Figure S7), further indicating the seeds-mediated crystal growth. UV-vis diffuse reflectance spectroscopy was applied to exclude the agglomeration of ultra-small Cu NCs according to the characteristic localized surface plasmon resonance (LSPR) spectrum of larger-sized Cu NPs. Cu NCs@MOF-801 presents only a pronounced yellowish color (Figure 1e) due to the well-documented quantum size effect usually for inorganic nanoparticles under 3 nm,²⁰ without additional peak in the visible range that exclude the formation of larger Cu NCs. Moreover,

the Cu NCs@MOF-801 after 600 °C annealing under O₂ showed greenish color, distinct from the original yellow color (Figure S8), indicating that the initial Cu was likely to be the reduced rather than Cu(II). The aberration-corrected high-angle annular dark-field scanning TEM (ac-HAADF-STEM) measurements in Figure 2g-j indeed displayed a very uniform distribution of Cu, despite the difficulty to localize Cu NCs due to their low crystallinity and the low atomic number of Cu (Figure 1e) compared to the Zr-MOF shell. The energy dispersive X-ray spectroscopy (EDX) indicated the content of the introduced Cu NCs is 2.8 % in atomic ratio to Zr (97.2%).

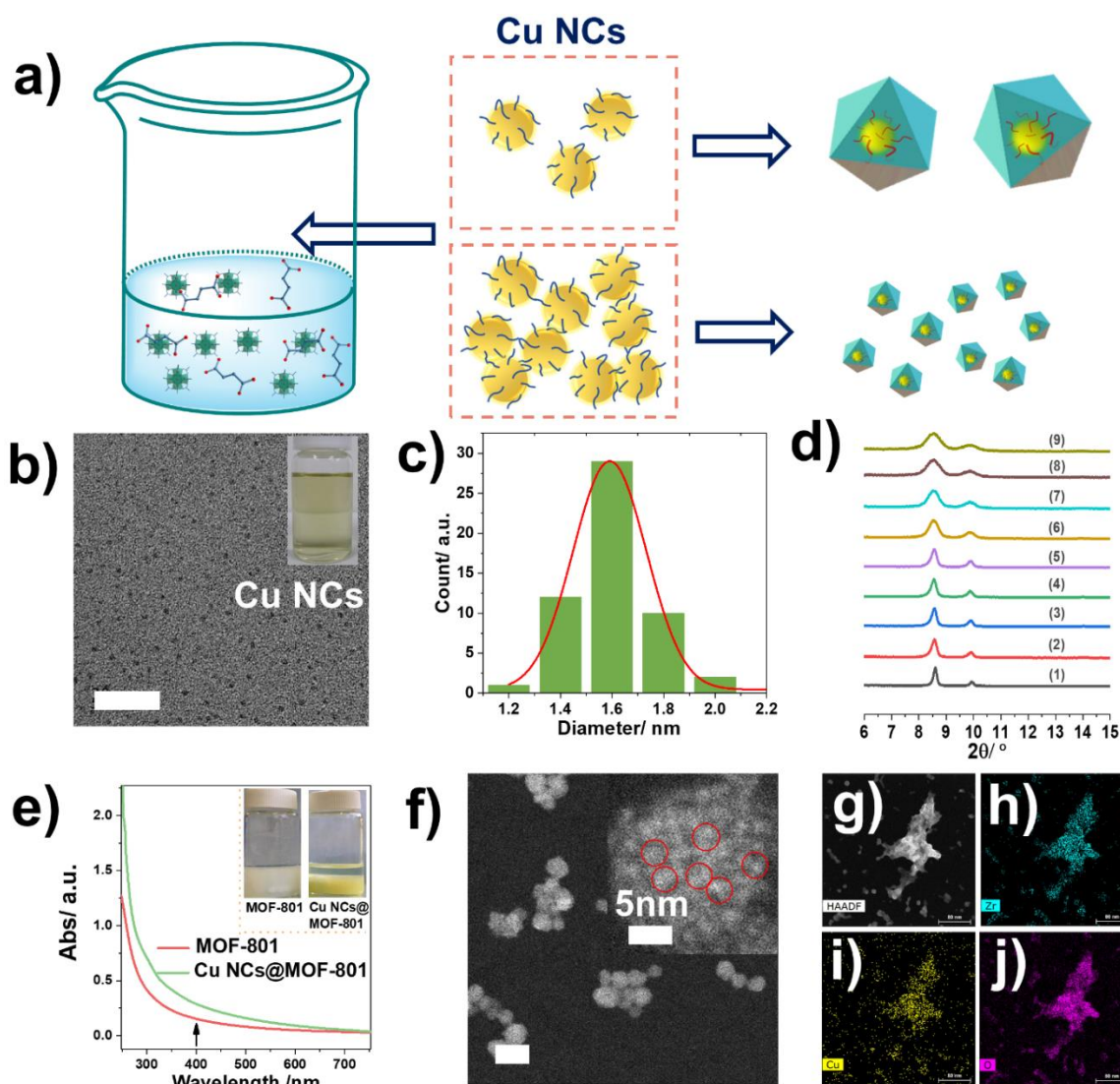


Figure 2. a) Schematic representation of the Cu NCs concentration-dependent size reduction of the prepared Cu NCs@MOF-801, b) TEM images of Cu nanoclusters; insert: the photograph of the synthesized Cu NCs; c) particle size distribution of the synthesized Cu nanoclusters; d) PXRD patterns ($\lambda_{\text{Cu}}=1.5406\text{\AA}$) of synthesized MOF-801(1) and CuNPs@MOF-801 with increasing Cu NPs loading from 64 μmol to 6.4 mmol (labeled with 1-9); e) Solid UV-VIS reflectance spectra of MOF-801 and Cu NCs@MOF-801 synthesized with 6.4 mmol Cu NCs; f) The aberration-corrected high-angle annular dark-field scanning transmission electron microscopy (ac-HAADF-

STEM) image of Cu NCs@MOF-801 synthesized with 6.4 mmol Cu NCs insert: zoomed-in image; g-j) HAADF-STEM images and corresponding EDS elemental (Zr, Cu, O) mapping of Cu NCs@MOF-801 with 6.4 mmol Cu NCs; Scale bar in b) and f)= 20 nm.

The large structural diversity of Zr-MOFs endows many possibilities to tune the functions of the shell MOFs. For instance, UiO-66-NH₂ is an amino-functionalized UiO-type of MOF, where the introduced amino groups can effectively improve the light harvest and the affinity with guest molecules like CO₂. By performing similar room-temperature syntheses, homologous hybrid composites were obtained. As shown in Figure 3a-b, the synthesized Cu NCs@UiO-66-NH₂ displayed identical crystallinity and porosity comparing to pristine UiO-66-NH₂ regardless the loading of 2.5 at% of Cu. The ambient facile synthesis allows us to achieve gram-scale products without quality change (the characterizations mentioned here were all based on gram-scale products). The HAADF-STEM and EDS mapping in Figure 3c-f demonstrated a similar distribution of the Cu NCs. Notably, the seed-mediated MOF growth was also observed in this case and the size of composites particles decreased from ca. 200 nm to ca. 80 nm (Figure S9-S10) in the presence of Cu NCs, which was in good line with Cu NCs@MOF-801.

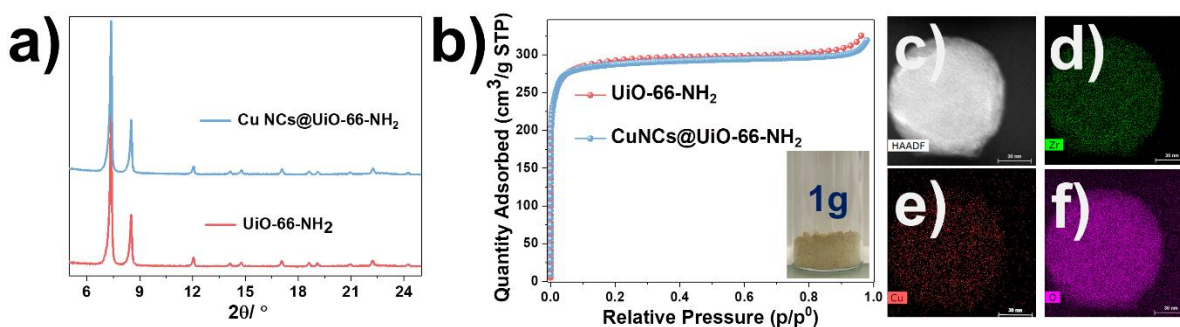


Figure 3. a) PXRD patterns; b) 77K N₂ isotherms of synthesized Cu NCs@UiO-66-NH₂ composites and pristine UiO-66-NH₂; c-f) High-angle annular dark-field scanning transmission electron microscopy (HAADF-STEM) images and corresponding EDS elemental (Zr, Cu, O) mapping of Cu NCs@UiO-66-NH₂.

As Cu nanoparticles hold the unique ability to catalyze challenging CO₂ reduction to organic feedstock, we selected CO₂ reduction as a model reaction to investigate the structure-property relationship. To the best of our knowledge, photoreduction of CO₂ to form organic C1 products while using core-shell Cu NPs@MOFs composites has unfortunately not been reported so far mainly due to the difficulty in synthesizing composites. The photoreduction experiments were carried out by using triethanolamine (TEOA) as a sacrificial agent under UV irradiation (250–385 nm) at room temperature for 18 h. The gas phase and the liquid phase were analyzed by gas chromatography (GC) and liquid chromatography (LC), respectively. In the case of Cu NCs@MOF-801, CO (22.5%) and HCOOH (64.9%) were found as the main products. The evolution rates of CO and HCOOH were about 32 and 94 μmol.h⁻¹.g⁻¹, respectively. The major generation of CO and HCOOH suggested the two-electron reduction of CO₂ by the Cu NCs@MOF-801 catalyst, as either CO or HCOOH only needs two electrons to be produced from CO₂. In contrast, the core-shell Cu NCs@UiO-66-NH₂ showed an enhanced reactivity for formic

acid, with an evolution rate at $128 \mu\text{mol}\cdot\text{h}^{-1}\cdot\text{g}^{-1}$, demonstrating that the use of UiO-66-NH₂ shell can effectively improve the production of formic acid likely due to the boosted affinity of this MOF with CO₂ (NH₂-CO₂ bond). Interestingly, the selectivity of the formation of HCOOH reached 86% due to the much less produced CO (blue block in Figure 4a). At the same time, the other byproducts (CH₃OH, CH₄, HCHO) were minority and did not exhibit much change upon on varying catalysts, which demonstrated that the catalytic centers in these two cases are rather similar. The change in selectivity of CO and HCOOH can be understood by the different surface functionalization of the shell MOF, which has been well-documented in the literature.²¹⁻²³ The high catalytic efficiency here is very comparable to those that were prepared using complex synthesis steps, expensive starting materials, or reducing agents (e.g., H₂).²⁴⁻²⁶ In order to understand how the location of the Cu NCs influence the catalytic performance, we mixed Cu ions with the pre-formed MOF-801 or UiO-66-NH₂ in the solution and subsequently reduced them with the use of L-ascorbic acid. We fixed all the synthetic parameters including solvents and precursors while adjusting the quantity of Cu and L-ascorbic acid to have the same Cu content. The corresponding HRTEM and STEM images in Figure S11 revealed the loaded Cu distributed either on the surface or in the cavity of MOFs without any observable large Cu nanoparticles. Surprisingly, the as-prepared composites (labeled as Cu NCs/ MOF-801, Cu NCs/ UiO-66-NH₂) both showed dramatically lower reactivity in the formation of HCOOH (2.7 and 2.8 times, respectively, Figure 4b). We presume this is probably due to the closer packing of Cu NCs and Zr oxide nodes in the core-shell composite, promoting the charge transfer from MOF to Cu, which is more powerful in driving catalytically synergetic effect between the guest NCs and host MOF. This observation was in good line with the previously reported core-shell composites.^{2, 27} It is clear that core-shell Cu NCs@MOFs architectures outperformed the traditional Cu NCs loaded in the outer surface of the cavity, which demonstrated for the first time in two similar supporting carriers.

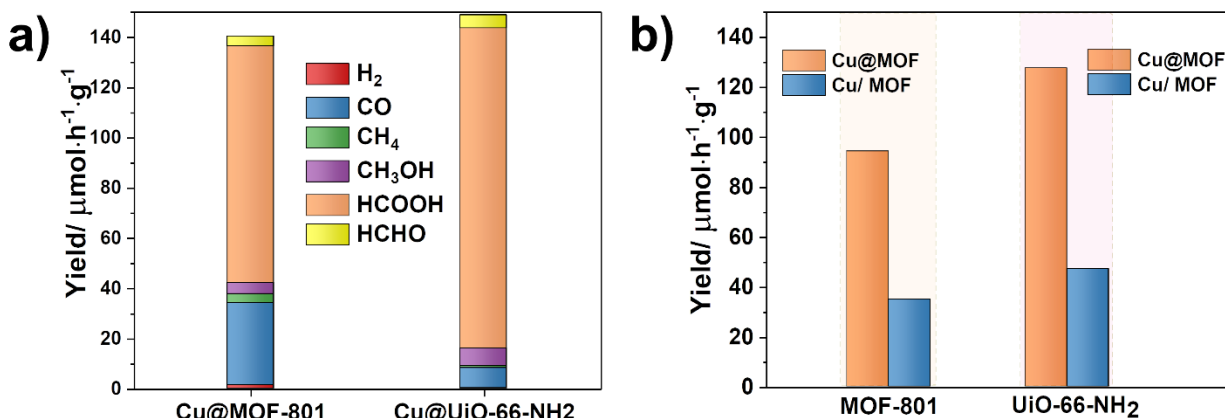


Figure 4. a) Production of the photo-catalyzed CO₂ with Cu NCs@MOF-801 and Cu NCs@UiO-66-NH₂. b) Comparative rates of the HCOOH formation with Cu NCs/ MOFs, and core-shell Cu NCs@MOFs.

To better understand the high reactivity and selectivity of Cu NCs@MOFs, *in-situ* IR spectroscopy was applied in transmission mode on the core-shell composites. NO and CO were used as probe gases to quantify the different accessible metal sites. As well documented in the literature, NO and CO are ideal molecules to selectively detect Cu²⁺, Cu⁺ and Cu(0) sites, respectively, due to their

strong and characteristic interactions with each Cu states.^{28, 29} As shown in Figure S12a,b, no characteristic NO vibration peak can be observed at the range of 1850-1900 cm^{-1} for both of the composites, neither at small dose nor equilibrium pressure, which indicated the absence of Cu^{2+} site. The stepwise dosing of CO into the cell at room temperature was applied subsequently. As shown in Figure 5a, b, peaks appeared and increased upon the introduction and dosing of CO at the range between 2109-2140 cm^{-1} , which are commonly attributed to the interaction between CO- Cu^+ . The slightly distinct FT-IR peaks in the two composites can be understood by the slightly different coordination environments. Therefore, the Cu sites in the two cases are quite similar, suggesting that the introduced Cu NCs have accessible Cu(I) sites rather than neither highly oxidized Cu^{2+} nor Cu(0) sites. This is due to the high sensitivity of Cu(0) upon a trace of oxygen in the solution. Cu(0) nanoclusters were formed initially with the addition of ascorbic acid, while the surface Cu(0) was oxidized to Cu(I) and subsequently protected by ascorbic acid.^{30, 31}

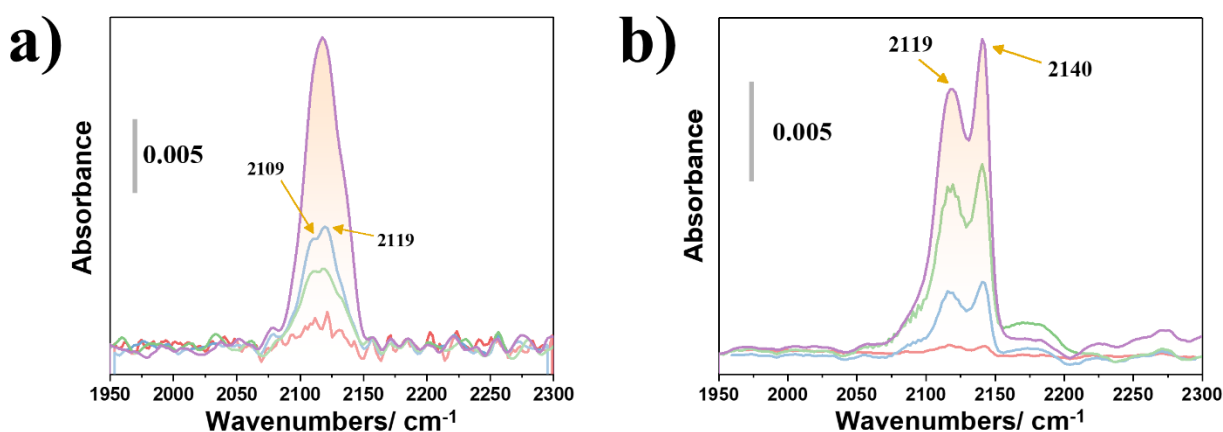


Figure 5. *In-situ* FTIR spectra of CO adsorption at room temperature from small dose to equilibrium on the activated a) Cu NCs@MOF-801 (equilibrium pressure of 5.69 torr), b) Cu NCs@UiO-66-NH₂ (equilibrium pressure of 6.11 torr).

■ Conclusion

In summary, we utilized a sustainable route to prepare ultra-small Cu nanoclusters@MOFs (including MOF-801 and UiO-66-NH₂). The cheap starting materials and facile synthesis approach allow producing both catalysts at gram scale, which is the first time for such kind of MOF-based core-shell composites. The seed-mediated growth mechanism was found in both core-shell cases, enabling us to have an insight into the formation of core-shell structures. Remarkably, Cu NCs@MOF-801 exhibited efficient CO₂ photo-reduction rates of 94 $\mu\text{mol}\cdot\text{h}^{-1}\cdot\text{g}^{-1}$. While Cu NCs@UiO-66-NH₂ showed a 36% higher catalytic rate, as well as improved selectivity towards the formic acid product, which indicated the importance of the introduced photo-reactive functional groups on the MOF linker. In addition, the comparison of catalytic efficiencies between Cu NCs on the surface / in the pores of the host MOFs and the core-shell ones revealed that the core-shell architectures were presenting a 3 times higher catalytic reactivity. This is probably due to the closer packing of the electron acceptors and the electron donors in the case of core-shell structures. Finally, the *in-situ* FT-IR technique helped to understand the origins of active sites.

Cu(I) was found to consistently exist in our cases, revealing Cu(I) sites rather than Cu(II) or Cu(0) can catalyze the photo-reduction of CO₂ efficiently at room temperature. Overall, this study can not only guide the future design of challenging core-shell structures but also offers an excellent avenue to rationally hatch up highly efficient heterogeneous catalysts for critical reactions.

References

1. Kattel, S.; Ramírez, P. J.; Chen, J. G.; Rodriguez, J. A.; Liu, P., Active sites for CO₂ hydrogenation to methanol on Cu/ZnO catalysts. *Science* **2017**, *355* (6331), 1296-1299.
2. Rungtaweeworanit, B.; Baek, J.; Araujo, J. R.; Archanjo, B. S.; Choi, K. M.; Yaghi, O. M.; Somorjai, G. A., Copper Nanocrystals Encapsulated in Zr-based Metal-Organic Frameworks for Highly Selective CO₂ Hydrogenation to Methanol. *Nano Lett.* **2016**, *16* (12), 7645-7649.
3. Zhang, X. D.; Hou, S. Z.; Wu, J. X.; Gu, Z. Y., Two-Dimensional Metal–Organic Framework Nanosheets with Cobalt-Porphyrins for High-Performance CO₂ Electroreduction. *Chem. Eur. J.* **2020**, *26* (7), 1604-1611.
4. Sanchez, A.; Abbet, S.; Heiz, U.; Schneider, W. D.; Hakkinen, H.; Barnett, R. N.; Landman, U., When gold is not noble: Nanoscale gold catalysts. *J. Phys. Chem. A* **1999**, *103* (48), 9573-9578.
5. Reske, R.; Mistry, H.; Behafarid, F.; Roldan Cuenya, B.; Strasser, P., Particle size effects in the catalytic electroreduction of CO₂ on Cu nanoparticles. *J. Am. Chem. Soc.* **2014**, *136* (19), 6978-6986.
6. Campbell, C. T.; Parker, S. C.; Starr, D. E., The effect of size-dependent nanoparticle energetics on catalyst sintering. *Science* **2002**, *298* (5594), 811-814.
7. Zhu, W.; Michalsky, R.; Metin, O. n.; Lv, H.; Guo, S.; Wright, C. J.; Sun, X.; Peterson, A. A.; Sun, S., Monodisperse Au nanoparticles for selective electrocatalytic reduction of CO₂ to CO. *J. Am. Chem. Soc.* **2013**, *135* (45), 16833-16836.
8. Ma, M.; Trzeźniewski, B. J.; Xie, J.; Smith, W. A., Selective and efficient reduction of carbon dioxide to carbon monoxide on oxide-derived nanostructured silver electrocatalysts. *Angew. Chem.* **2016**, *128* (33), 9900-9904.
9. Gao, D.; Zhou, H.; Wang, J.; Miao, S.; Yang, F.; Wang, G.; Wang, J.; Bao, X., Size-dependent electrocatalytic reduction of CO₂ over Pd nanoparticles. *J. Am. Chem. Soc.* **2015**, *137* (13), 4288-4291.
10. Liao, F.; Huang, Y.; Ge, J.; Zheng, W.; Tedsree, K.; Collier, P.; Hong, X.; Tsang, S. C., Morphology-Dependent Interactions of ZnO with Cu Nanoparticles at the Materials' Interface in Selective Hydrogenation of CO₂ to CH₃OH. *Angew. Chem.* **2011**, *123* (9), 2210-2213.
11. Karapinar, D.; Huan, N. T.; Ranjbar Sahaie, N.; Li, J.; Wakerley, D.; Touati, N.; Zanna, S.; Taverna, D.; Galvão Tizei, L. H.; Zitolo, A., Electroreduction of CO₂ on single-site copper-nitrogen-doped carbon material: selective formation of ethanol and reversible restructuring of the metal sites. *Angew. Chem. Int. Edit.* **2019**, *58* (42), 15098-15103.

12. Maurin, G.; Serre, C.; Cooper, A.; Férey, G., The new age of MOFs and of their porous-related solids. *Chem. Soc. Rev.* **2017**, *46* (11), 3104-3107.
13. Chen, D.; Yang, W.; Jiao, L.; Li, L.; Yu, S. H.; Jiang, H. L., Boosting catalysis of Pd nanoparticles in MOFs by pore wall engineering: the roles of electron transfer and adsorption energy. *Adv. Mater.* **2020**, *32* (30), 2000041.
14. Chen, Y.-Z.; Gu, B.; Uchida, T.; Liu, J.; Liu, X.; Ye, B.-J.; Xu, Q.; Jiang, H.-L., Location determination of metal nanoparticles relative to a metal-organic framework. *Nat. Commun.* **2019**, *10* (1), 1-10.
15. Dai, S.; Tissot, A.; Serre, C., Recent Progresses in Metal–Organic Frameworks Based Core–shell Composites. *Adv. Energy Mater.* **2021**, 2100061.
16. Yang, Q.; Xu, Q.; Jiang, H.-L., Metal–organic frameworks meet metal nanoparticles: synergistic effect for enhanced catalysis. *Chem. Soc. Rev.* **2017**, *46* (15), 4774-4808.
17. Yang, J.; Ye, H. L.; Zhao, F. Q.; Zeng, B. Z., A Novel Cu_xO Nanoparticles@ZIF-8 Composite Derived from Core-Shell Metal-Organic Frameworks for Highly Selective Electrochemical Sensing of Hydrogen Peroxide. *ACS Appl. Mater. Interfaces* **2016**, *8* (31), 20407-20414.
18. Osterrieth, J. W.; Wright, D.; Noh, H.; Kung, C.-W.; Vulpe, D.; Li, A.; Park, J. E.; Van Duyn, R. P.; Moghadam, P. Z.; Baumberg, J. J., Core–shell gold Nanorod@ zirconium-based metal–organic framework composites as in situ size-selective Raman probes. *J. Am. Chem. Soc.* **2019**, *141* (9), 3893-3900.
19. Wei, J.; Hu, Y.; Liang, Y.; Kong, B.; Zheng, Z.; Zhang, J.; Zhao, Y.; Wang, H., Graphene oxide/core–shell structured metal–organic framework nano-sandwiches and their derived cobalt/N-doped carbon nanosheets for oxygen reduction reactions. *J. Mater. Chem. A* **2017**, *5* (21), 10182-10189.
20. Jin, R. C., Atomically precise metal nanoclusters: stable sizes and optical properties. *Nanoscale* **2015**, *7* (5), 1549-1565.
21. Guo, J.; Qin, Y.; Zhu, Y.; Zhang, X.; Long, C.; Zhao, M.; Tang, Z., Metal–organic frameworks as catalytic selectivity regulators for organic transformations. *Chem. Soc. Rev.* **2021**.
22. Ye, Y.; Cai, F.; Li, H.; Wu, H.; Wang, G.; Li, Y.; Miao, S.; Xie, S.; Si, R.; Wang, J., Surface functionalization of ZIF-8 with ammonium ferric citrate toward high exposure of Fe-N active sites for efficient oxygen and carbon dioxide electroreduction. *Nano Energy* **2017**, *38*, 281-289.
23. Chughtai, A. H.; Ahmad, N.; Younus, H. A.; Laypkov, A.; Verpoort, F., Metal–organic frameworks: versatile heterogeneous catalysts for efficient catalytic organic transformations. *Chem. Soc. Rev.* **2015**, *44* (19), 6804-6849.
24. Yu, S.; Lv, P.; Xue, P.; Wang, K.; Yang, Q.; Zhou, J.; Wang, M.; Wang, L.; Chen, B.; Tan, T., Light-driven enzymatic nanosystem for highly selective production of formic acid from CO₂. *Chem. Eng. Sci.* **2021**, *420*, 127649.
25. Kuk, S. K.; Ham, Y.; Gopinath, K.; Boonmongkolras, P.; Lee, Y.; Lee, Y. W.; Kondaveeti, S.; Ahn, C.; Shin, B.; Lee, J. K., Continuous 3D titanium nitride nanoshell structure for solar-driven unbiased biocatalytic CO₂ reduction. *Adv. Energy Mater.* **2019**, *9* (25), 1900029.
26. Legrand, U.; Boudreault, R.; Meunier, J., Decoration of N-functionalized graphene nanoflakes with copper-based nanoparticles for high selectivity CO₂ electroreduction towards formate. *Electrochim. Acta* **2019**, *318*, 142-150.
27. Xiao, J. D.; Shang, Q.; Xiong, Y.; Zhang, Q.; Luo, Y.; Yu, S. H.; Jiang, H. L., Boosting Photocatalytic Hydrogen Production of a Metal-Organic Framework Decorated with Platinum

Nanoparticles: The Platinum Location Matters. *Angew. Chem. Int. Ed. Engl.* **2016**, *55* (32), 9389-93.

28. Hadjiivanov, K. I., Identification of neutral and charged N x O y surface species by IR spectroscopy. *Catal. Rev.* **2000**, *42* (1-2), 71-144.

29. Frache, A.; Cadoni, M.; Bisio, C.; Marchese, L.; Mascarenhas, A. J.; Pastore, H. O., NO and CO adsorption on over-exchanged Cu-MCM-22: A FTIR study. *Langmuir* **2002**, *18* (18), 6875-6880.

30. Kuo, C. H.; Chen, C. H.; Huang, M. H., Seed-mediated synthesis of monodispersed Cu₂O nanocubes with five different size ranges from 40 to 420 nm. *Adv. Funct. Mater.* **2007**, *17* (18), 3773-3780.

31. Zhou, P.; Zhang, J.; Zhang, Y.; Liu, Y.; Liang, J.; Liu, B.; Zhang, W., Generation of hydrogen peroxide and hydroxyl radical resulting from oxygen-dependent oxidation of l-ascorbic acid via copper redox-catalyzed reactions. *RSC Adv.* **2016**, *6* (45), 38541-38547.

Supporting Information

Incorporating ultra-small Cu nanoclusters in Z Metal-Organic Frameworks: location regulated CO₂ photo-reduction efficiency

Materials and equipments:

Powder X-ray Diffraction (PXRD) data were recorded on a high-throughput Bruker D8 Advance diffractometer working on transmission mode and equipped with a focusing Göbel mirror producing CuK α radiation ($\lambda = 1.5418 \text{ \AA}$) and a LynxEye detector. Nitrogen porosimetry data were collected on a Micromeritics Tristar/ Triflex instrument at 77 K (pre-activating samples at 100 °C under vacuum, 12 hours). Scanning Electron Microscopy coupled with energy-dispersive X-ray spectroscopy (SEM-EDX) results were recorded with FEI Magellan 400 scanning electron microscope. Thermogravimetric analysis (TGA) data were collected on Mettler Toledo TGA/DSC 2, STAR System apparatus with a heating rate of 5 °C/min under the oxygen flow. Infrared spectra were measured with a Nicolet iS5 FTIR ThermoFisher spectrometer. Zeta potential and DLS size measurements of hydrodynamic radii were made on a Malvern Zetasizer Nano-ZS (Malvern Instruments). High resolution TEM images (HRTEM) were acquired on a Titan Themis 200 microscope operating at 200 kV. This microscope is equipped with a Ceta 16M hybrid camera from ThermoFischer Scientific capable of working under low electron irradiation conditions. The HRTEM images are obtained in low dose condition with an irradiation current between 100 and 250 electrons per square angstroms. In-situ Infrared spectroscopy measurements were conducted in a homebuilt cell, constructed from a 2 and 3/400 stainless steel cube. The powder sample was pressed onto a tungsten grid. The IR spectra were collected in transmission mode using a Bruker Vertex 80 spectrometer equipped with a liquid nitrogen-cooled MCT detector. Spectra was recorded at 4 cm⁻¹ resolution and each spectrum presented was an average of 256 scans.

CO₂ reduction: To a glass test tube was added a catalyst (10 mg), triethanolamine (TEOA, 0.6 mL), and *N,N*-dimethylacetamide (DMA, 9.4 mL). The volumes of gas and liquid phases were 53.5 and 10.0 mL, respectively. The tube was capped with a silicone septum and degassed with CO₂ by bubbling through the reaction mixture (150 mL/min, 15 min). The CO₂-saturated suspension was stirred and irradiated using a 300 W Xe lamp (MAX-303 equipped with UV (250–385 nm) mirror module, Asahi Spectra) at room temperature for 18 h. The amounts of CO, CH₄, and H₂ in the gas phase were determined by a gas chromatograph equipped with a thermal conductivity detector (GC-2014, SHIMADZU). The amount of CH₃OH in the liquid phase was determined by a gas chromatograph mass spectrometer (GCMS-QP2010 Ultra, SHIMADZU). The amount of HCOOH in the liquid phase was determined by a liquid chromatograph equipped with a conductivity detector (Prominence Organic Acid Analysis System, SHIMADZU). The amount of HCHO in the liquid phase was determined by a liquid chromatograph mass spectrometer

equipped with a diode array detector (LCMS-2020, SHIMADZU) after the treatment with 2,4-dinitrophenylhydrazine (DNPH).

All chemicals were purchased from commercial suppliers and used as received without further purification. Fumaric acid, 98%, Alfa Aesar. 2-Aminoterephthalic acid(BDC-NH₂), 99+%, Acros. 1H-Pyrazole-3,5-dicarboxylic acid(PDA), 97%, FluoroChem. ZrCl₄ anhydrous, 98%, Acros. Isopropyl alcohol, 99+%, Sigma. Acetic acid, 99+%, Fisher. Ethanol absolute, >=99%, Acros. L-ascorbic acid, Analytical reagent, Fisher. Copper Nitrate hemipentahydrate, 98%, Acros. Distilled water, Millipore system.

Synthesis of Cu NCs: L-ascorbic acid (880 mg, 5 mmol) was added to Cu(NO₃)₂.2.5H₂O (116 mg, 0.5 mmol) in 55 mL aqueous solution with strong stirring. The solution was allowed to stir at room temperature for 1.5 h. The resulting light yellow solution was used throughout the following experiments.

Synthesis of Cu NCs@MOF-801 (with 6.4 mmol Cu NCs): Zirconium oxocluster (Zr₆O₄(OH)₄(C₂H₃O₂)₈Cl₄, 1 g) was stirred in Acetic acid (20 mL) until well dispersed. Then, an aqueous solution of Cu NCs (50 mL) was added. The mixture was kept stirring for a few minutes until all Zr₆ oxoclusters were dissolved. Then, Fumaric acid (532 mg, 4.6 mmol) was added and the resulted mixture was kept stirring for 3 days until observation of cloudy yellowish solution. The solid was collected and washed 5 times with only H₂O. Final solids were then dried under vacuum.

Synthesis of Cu NCs@UiO-66-NH₂: Zirconium oxocluster (Zr₆O₄(OH)₄(C₂H₃O₂)₈Cl₄, 1.2 g) was stirred in 8 mL Acetic acid until well dispersed. Then, an aqueous solution of Cu NCs (20 mL) was added. The mixture was kept stirring for a few minutes until all Zr₆ oxoclusters were dissolved. Then, 2-Aminoterephthalic acid (400 mg, 2.2 mmol) and 20 mL ethanol were added. The resulted mixture was kept stirring for 3 days until observation of cloudy yellowish solution. The solid was collected and washed 5 times with only H₂O. Final solids were then dried under vacuum.

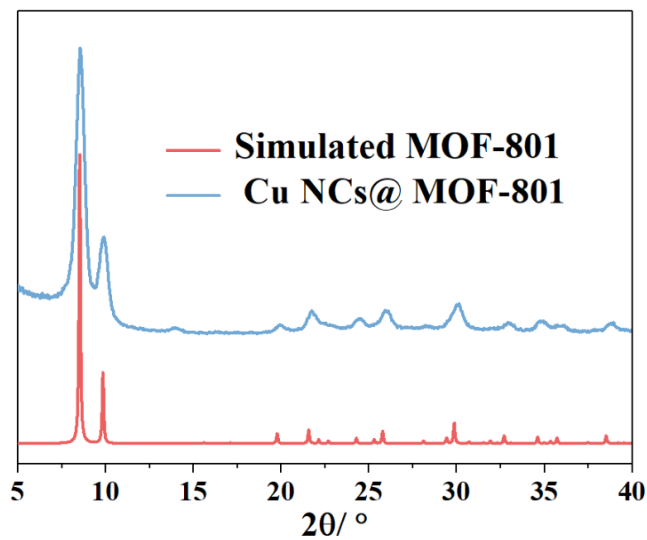


Figure S1. PXRD patterns of Cu NCs@MOF-801 and the simulated one.

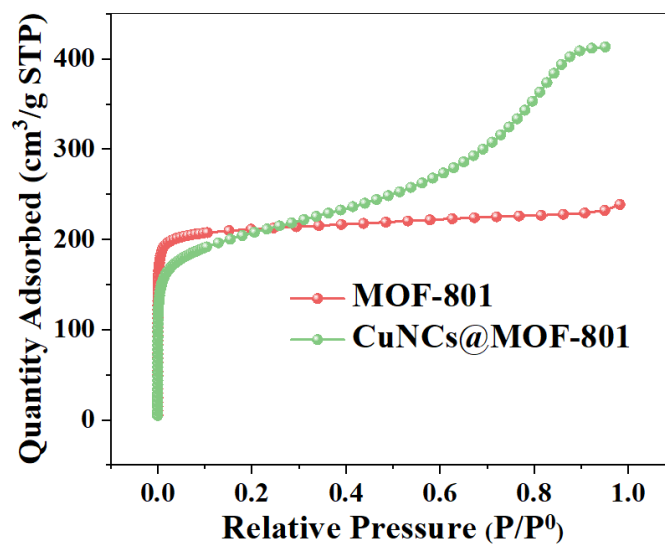


Figure S2. 77 K N_2 isotherms of pristine MOF-801 and Cu NCs@MOF-801.



Figure S3. 1 g of Cu NCs@MOF-801.

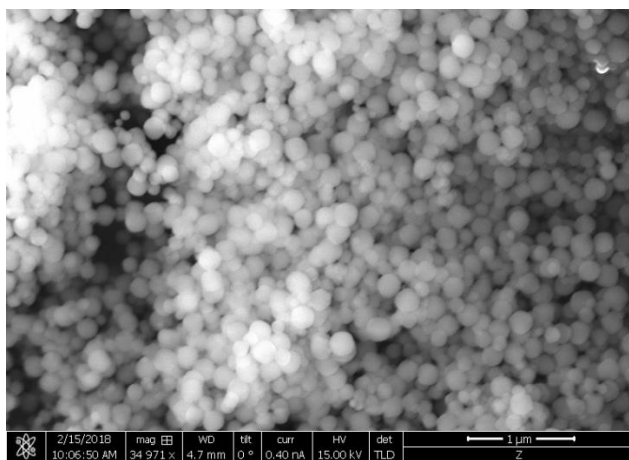


Figure S4. SEM image of MOF-808 prepared without Cu NCs, which corresponds to the PXRD pattern in Figure 2d(1).

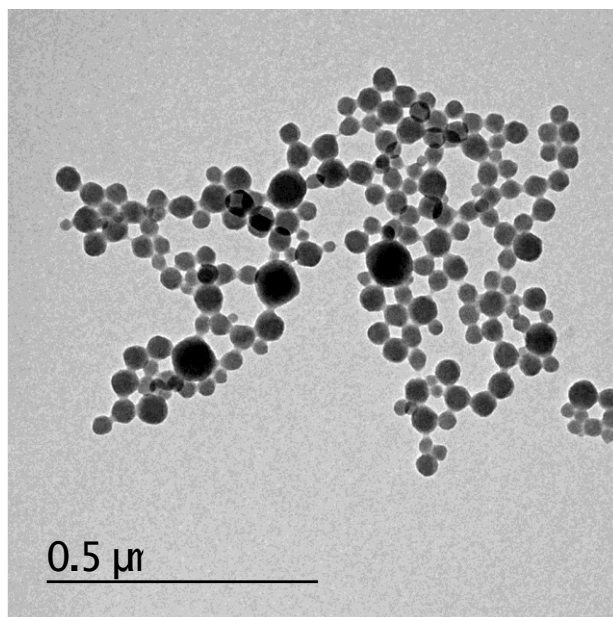


Figure S5. TEM image of Cu NCs@MOF-801 prepared with 64 μmol Cu NCs, which corresponds to the PXRD pattern in Figure 2d(3).

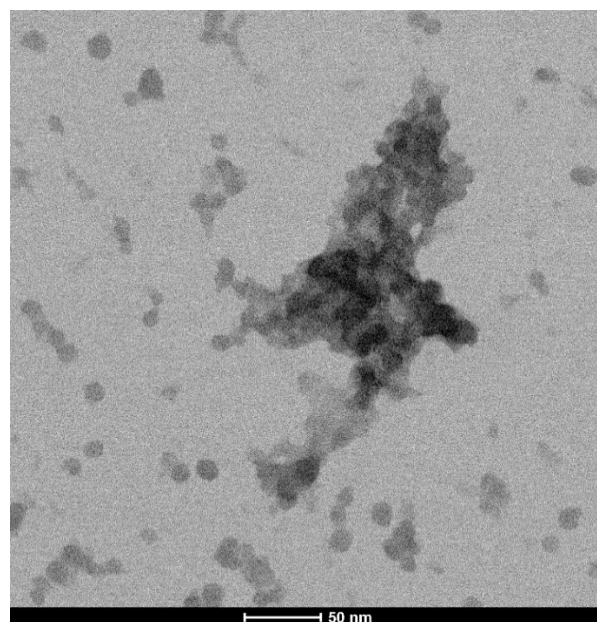


Figure S6. TEM image of Cu NCs@MOF-801 prepared with 6.4 mmol Cu NCs, which corresponds to the PXRD pattern in Figure 2d(9).

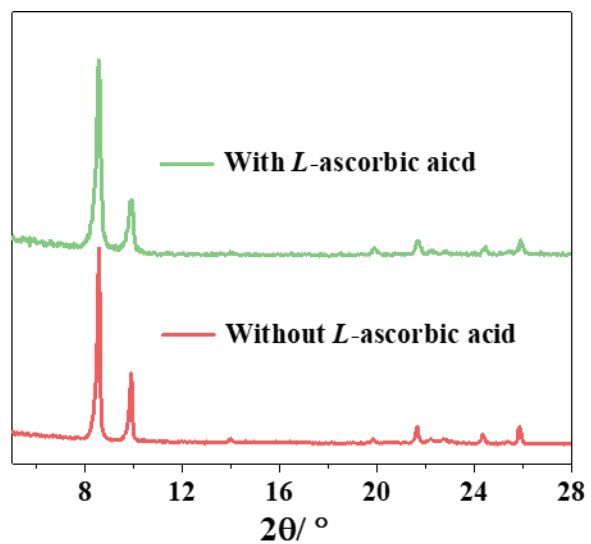


Figure S7. PXR D patterns of MOF-801 synthesized with and without L-Ascorbic acid.

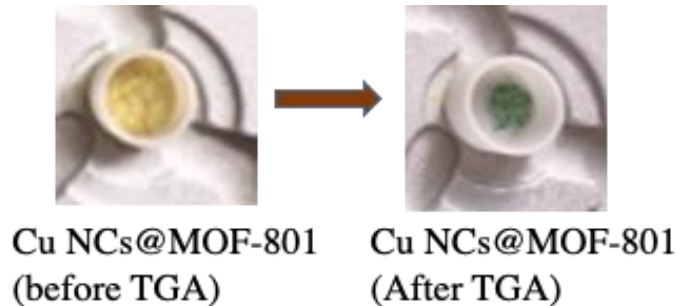


Figure S8. Photograph of Cu NCs@MOF-801 before and after TGA measurements under O_2 .

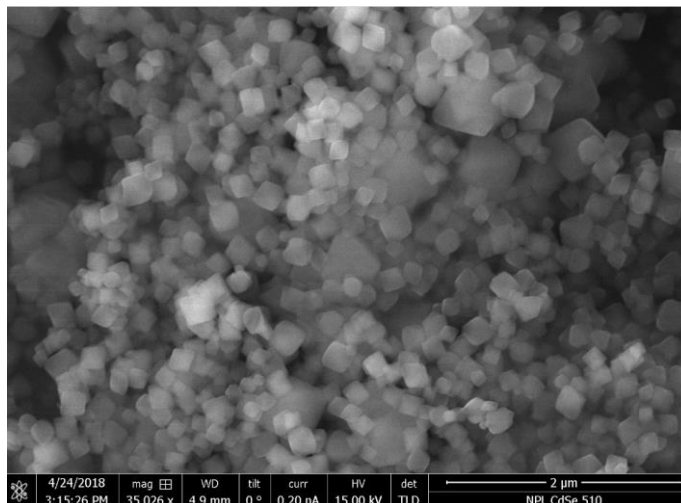


Figure S9. UiO-66-NH₂ synthesized without the addition of Cu NCs.

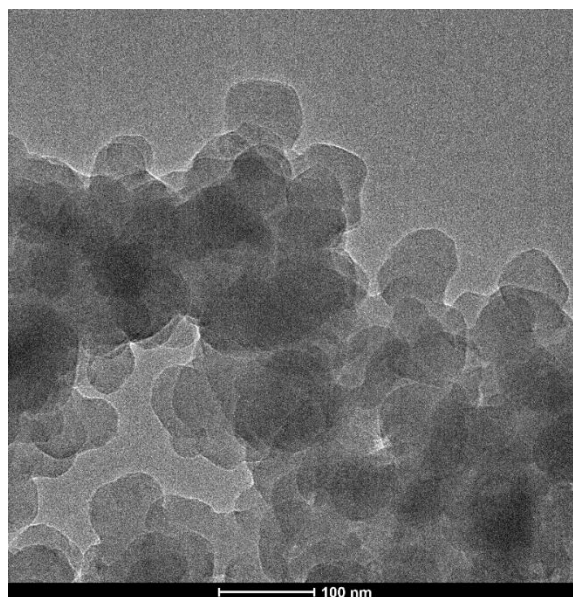


Figure S10. UiO-66-NH₂ synthesized without Cu NCs.

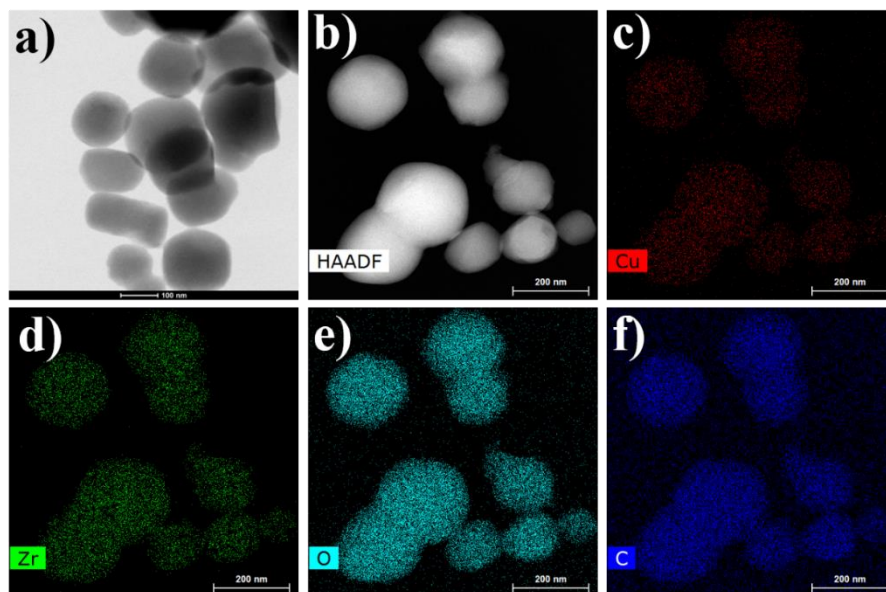


Figure S11. Electron microscope characterizations of Cu NCs/ UiO-66-NH₂, a) high-resolution TEM image, b) HAADF-STEM image, c-f) EDS mapping

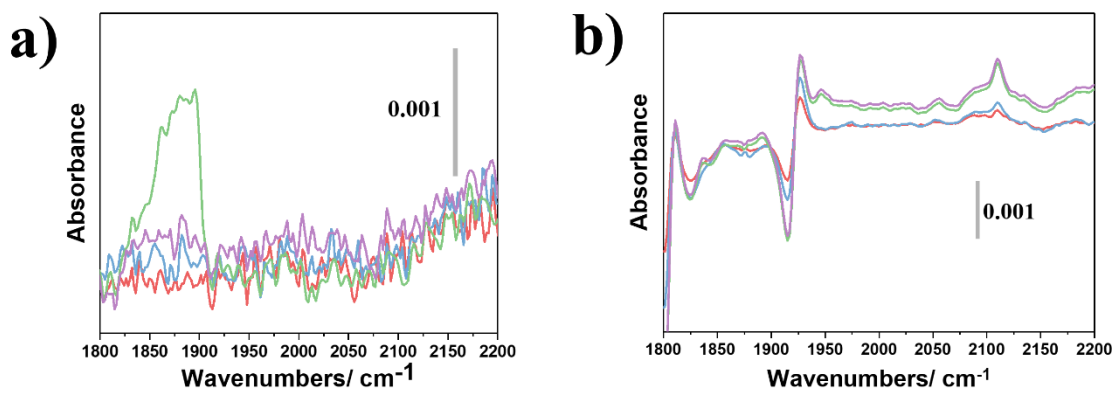


Figure S12. FTIR spectra of NO adsorption at room temperature from small dose to equilibrium on the activated a) Cu NCs@MOF-801 (equilibrium pressure of 5.37 torr), b) Cu NCs@UiO-66-NH₂ (equilibrium pressure of 6.29 torr).

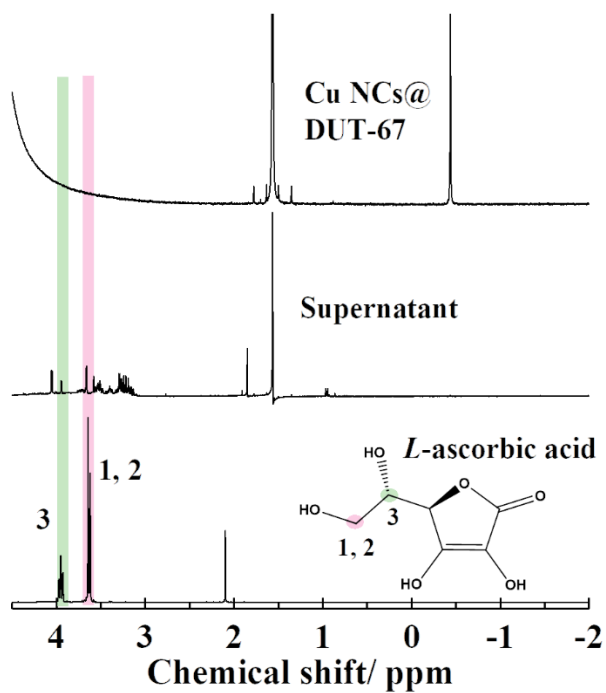


Figure S13. ^1H NMR spectra of L-ascorbic acid, the supernatant of the synthesis batch of Cu NCs@DUT-67(PDA), and the obtained Cu NCs@DUT-67(PDA) product.

General Conclusion and Perspectives

This thesis focuses on the construction of chemically stable core-shell MOF-based composites and their roles in challenging applications.

The main goals in this thesis are:

- 1) developing versatile room temperature (RT) greener synthesis for tetravalent MOFs,
- 2) using RT synthesis to reproducibly encapsulate ultra-small inorganic nanoparticles forming core-shell structures,
- 3) using the prepared MOFs/ composites to address the challenges of catalysis.

Following an introduction to ambient synthesis of MOFs and the synthesis and applications of core-shell composites in Chapter 1, in Chapter 2, I first report the stepwise room temperature synthesis of benchmark Zr- trimesate (MOF-808) and its efficient size tuning preparation from 850 nm to 35 nm. The prepared MOF nanoparticles show very nice monodispersity and quality. More importantly, the resulting 35 nm MOF-808 showed highest efficiency in peptide hydrolysis comparing to the larger sized ones. In Chapter 3, I report another new route to realize one-pot and one-step room temperature synthesis of a series of highly porous metal(IV) carboxylate MOFs (M=Zr, Hf, Ce) including five 12-connected and two 8-connected MOFs mostly in water-based solution. Subsequently, the similar synthesis is extended to a series of highly crystalline Ce-UiO-66-X (X= H, Br, NO₂, COOH, NH₂), Ce-DUT-67, and Ce-MOF-808. The optimal room temperature synthesis enables a very high space-time yield for these MOFs, ranging from 300 kg/ m³/ day to 900 kg/ m³/ day. Ambient synthesis strategy has been demonstrated by the first time, as a useful method to reconcile the contradiction between redox-active metal nodes and redox-active ligands, allowing *de novo* formation of novel Ce-UiO-66-NH₂, which has been regarding as a conflictive phase.

So far, different room temperature green synthesis approaches are well achieved.

In Chapter 4 and 5, I take the advantage of the developed room temperature synthesis strategy to make core-shell NPs@MOF composites. Consequently, ultra-small inorganic nanoparticles are incorporated in the Zr-MOFs, resulting in Au NPs@MOF-808, Cu NCs@MOF-801, Cu NCs@UiO-66-NH₂, and Cu NCs@DUT-67(PDA) are designed. For the Au NPs@MOF-808, I systematically investigate the efficient removal of capping agents from the surface of Au NPs as large amount of capping agents are used in this study to cover Au NPs. Due to the unique catalytic reactivity of the reduced state Cu, we use photo-reduction of CO₂ as a model reaction to demonstrate the ability of prepared Cu NCs@MOFs composites comparing to the Cu NCs simply on the surface of MOFs. As a result, formic acid is found as the main reduced production of CO₂, which is a very important chemical feedstock.

Overall, the main objectives of this thesis are met, and whilst there are still some future works that need to be finished. This work will hopefully have not only a very positive impact on the synthesis of tetravalent MOFs but also facilitation to the future development of core-shell MOF-based composites as well as their promising catalytic applications.

Perspectives:

The green synthesis of MOFs has been drawing more and more interest at both academic and industrial levels. Synthesizing MOFs at room temperature is particularly fascinating not only due to the **minimized energy input and safer conditions** but also for **the incorporation of functional but fragile compounds** in water-stable MOFs via bottle-around-ship strategy. However, there are still many points that need to be considered for novel room-temperature synthesis, such as 1) if the **organic modulator** can be completely gotten rid of, 2) if the versatile synthesis strategies can be extended to other **tetravalent MOFs**, especially those with different inorganic building units (e.g. Ti), 3) can we get insights into the MOF nucleation mechanism by using other **in-situ techniques** which are only operable **at room temperature**, 4) if the room temperature synthesis leads to the **different property** comparing to the conventional ones apart from the observed low-temperature-induced defect (LTID), 5) how to solve the ambient preparation of MOFs that consists of **poorly soluble organic linkers**. Furthermore, benchmark high-valence MOFs that are consistent with cost-effectiveness, functionality, and bio-compatibility raw materials should be more valued than the others as they are practically **more feasible in industrialization**. What is a good point is that industrial research has already been focused to develop sustainable and green methods for MOF production.

Using room temperature synthesis as a method to *in-situ* incorporate the temperature-sensitive compounds bears several important merits. Despite the achievements that have been accomplished in this thesis and other published works, several challenges still exist. For instance, the **synthetic parameters** dominating the resulting core-shell structure often remain unclear, regardless the fact that the key role of some parameters (e.g., capping agent, anion, ratio of metal/ ligand, solvents) have already been identified. More systematical investigation of synthetic conditions shall be performed in a near future to guide the effective designing of these complex composites. Subsequently, the precise **control of the shell thickness**, of the **spatial distribution/ content** of the core remains really challenging, while they are the vital parameters in most application performance-focused works. In terms of applications, the charge transfer behavior between metal nodes and NPs has been regarded as a remarkable feature associated with **synergetic effects**. However, **maximizing this interface interaction** still requires many efforts. Obviously, the increase in the quantity of active compounds is one clear pathway to achieve this goal. Unfortunately, this has not yet been investigated in the literature. Understanding the synergy between host and guest remains unclear while it can guide the design of the composites. Therefore, additional **computational and advanced characterization techniques** are demanded to build up structure-property correlations.

In the end, I hope my thesis can give a leap forward not only the greener synthesis of water-stable MOFs but also the synthesis and understanding of core-shell NPs@MOFs composites for catalytic applications.

Appendix 1 : Résumé

Cette thèse est centrée sur le développement de nouvelles stratégies pour synthétiser des réseaux hybrides poreux cristallisés ou ‘Metal Organic Frameworks’ (MOFs) tétravalents à température ambiante. Ces stratégies nous permettent d’atteindre de nombreux objectifs différents tels que l’ajustement de la taille des particules de MOF afin de maximiser leur activité catalytique, la préparation de nouvelles phases qui ont longtemps été inaccessibles en utilisant des synthèses à température élevée, et la préparation de phases très défectueuses mais relativement stables chimiquement. De plus, la synthèse à température ambiante de MOFs à base de métaux tétravalents constitue la première étape de la formation de composites cœur-coquille à base de MOFs. Ainsi, au cours de cette thèse, les méthodes de synthèse à température ambiante ont été appliquées pour former de nouvelles structures cœur-coquille avec des nanoparticules métalliques (taille < 3 nm). Les composites cœur-coquille obtenus montrent une excellente efficacité catalytique dans des réactions hétérogènes d’intérêt, telles que la photo-réduction du CO₂.

En détail, cette thèse est divisée en cinq chapitres.

Le **chapitre 1** est composé de deux revues publiées qui présentent une introduction aux MOFs et à leur synthèse à température ambiante ainsi que les progrès concernant la synthèse et les applications des composites cœur-coquille à base de MOFs. Ces articles sont intitulés "Metal-organic frameworks: from ambient green synthesis to applications" (*Adv. Energy. Mat.*, 2021), et "Recent Progresses in Metal-Organic Frameworks based core-shell composites" (*Bull. Japan Chem. Soc.*, 2021).

Dans le **chapitre 2**, je me concentre sur un MOF de référence à base d’oxoclusters Zr₆ connectés 6 fois, à savoir le MOF-808. Dans ce travail, j’ai utilisé des oxoclusters de Zr₆ préformés comme source de métal au lieu des sels organiques/inorganiques de zirconium couramment utilisés, en raison de leur état d’hydrolyse plus élevé. L’utilisation d’oxoclusters de Zr₆ préformés permet d’utiliser des conditions de synthèse douces (moins acides qu’avec les sels de zirconium) qui facilitent la déprotonation des ligands et la réaction d’assemblage du MOF. De plus, ces réactifs permettent d’éviter l’étape de formation *in-situ* de Zr₆ à partir de sels de Zr(IV), ce qui favorise la nucléation des MOFs. En conséquence, le MOF-808 est synthétisé à température ambiante dans une solution aqueuse. De plus, la concentration élevée des réactifs rend la synthèse à température ambiante relativement rapide (18 h) et le rendement de synthèse atteint presque 100% (calculé en fonction du ligand). Par la suite, j’ai réalisé que la taille des nanoparticules de MOF-808 dépend fortement de la concentration des réactifs (de 850 nm à 35 nm), où une plus grande concentration de réactifs conduit à une plus petite taille des nanoparticules. Grâce à l’efficacité accrue de la synthèse due à la concentration élevée de réactifs, le rendement spatio-temporel pour les plus petites nanoparticules de MOF-808 atteint 2516 kg/ m³/jour. Les nanocristaux résultants présentent une dispersion colloïdale de haute qualité, quasi monodisperse à la fois à différentes concentrations (de 7 mg/ mL à 0.17 mg/ mL) et sur une longue durée (24h). Ce type de synthèse à partir d’une solution aqueuse à température ambiante est très intéressant pour l’encapsulation de nanoparticules actives thermosensibles en utilisant une stratégie ‘bottle around a ship’. De plus, la série de nano-MOF-808 préparée dans ce travail montre une efficacité catalytique remarquable et dépendant de la taille des nanocristaux pour l’hydrolyse sélective de liaisons peptidiques, à la fois dans un peptide Gly-Gly modèle et dans un substrat protéique composé de 129 acides aminés. Les plus

petits nano-MOFs présentent le potentiel catalytique le plus élevé rapporté jusqu'à présent parmi les MOFs à base de Zr(IV) et la réactivité des nanocristaux est directement proportionnelle à la surface externe des particules de MOF, suggérant ainsi que la réaction catalytique se produit très probablement sur la surface externe du MOF. En outre, la variation de la taille des particules permet de contrôler les fragments de protéines spécifiques produits. Cela montre que les MOF peuvent être synthétisés avec une taille de particule spécifique pour produire les fragments souhaités, ce qui prouve leur potentiel pour agir comme des nanozymes protéases artificielles supérieures aux systèmes existants pour une utilisation dans le domaine de la protéomique. Les travaux en question ont été publiés dans *Chem. Mater.* en 2021.

Dans le **chapitre 3**, une nouvelle approche facile et polyvalente est présentée pour la synthèse en une étape d'une série de cinq MOFs à base de ligands carboxylate et de métaux tétravalents (M=Zr, Hf, Ce) à température ambiante dans des solvants verts. Cette nouvelle synthèse m'a permis de produire des MOFs robustes, cristallins et poreux de haute qualité avec des divers sels métalliques. De plus, l'ajustement des paramètres de synthèse m'a permis de contrôler la taille des particules à l'échelle nanométrique, ce qui indique que cette nouvelle synthèse est également applicable pour produire des nanoMOFs. J'ai ensuite utilisé un système pilote de 5L pour évaluer la possible mise à l'échelle de la synthèse, ce qui m'a permis d'obtenir un rendement spatio-temporel très élevé pour la synthèse à température ambiante du MOF-801(Zr). Ensuite, j'ai réalisé des mesures cinétiques *in-situ* afin de comprendre l'origine de l'efficacité de cette synthèse à température ambiante. J'ai ainsi pu montrer que la concentration des réactifs joue un rôle très important dans l'efficacité de la réaction : une concentration élevée de réactifs conduit à une solution plus acide, ce qui inhibe la croissance du MOF et ralentit la cristallisation, alors qu'avec une faible concentration, la cristallisation du MOF est significativement ralentie même si le pH est également plus élevé par rapport à la synthèse de référence. Par conséquent, j'ai optimisé les conditions de synthèse, en particulier la présence d'eau et la concentration des réactifs, afin de faciliter la synthèse ambiante. Cette nouvelle approche de synthèse a également été appliquée pour synthétiser l'UiO-66-NH₂, l'UiO-66-COOH, le DUT-67 et le PCN-222 à température ambiante dans des solvants verts. Cette étude représente la première synthèse à température ambiante, en une seule étape, polyvalente et sans template, de plusieurs MOFs tétravalents, qui, je l'espère, guidera la synthèse future de ce type de MOFs dans des conditions ambiantes. Les travaux en question ont été publiés dans *Angew. Chem. Int. Ed.* en 2020. Ensuite, j'ai utilisé une stratégie similaire pour synthétiser efficacement une série de Ce-UiO-66-X (X= H, Br, NO₂, COOH) hautement cristallins en solution aqueuse à température ambiante. Les MOFs à base de Ce(IV) présentent des caractéristiques photocatalytiques très intéressantes en raison des orbitales 4f basses en énergie qui peuvent accepter les électrons des espèces réduites. En outre, la bande d'énergie interdite du Ce-UiO-66-X peut être ajustée par la fonctionnalisation du ligand organique de référence (acide benzènedicarboxylique, BDC). Cependant, il est très difficile de synthétiser des phases de Ce(IV) avec des ligands basiques/redox actifs, tels que le BDC-NH₂, en particulier à des températures élevées. Durant ma thèse, j'ai pu démontrer que la synthèse à température ambiante pouvait être une méthode utile pour synthétiser des MOFs à base de Ce(IV) avec des ligands redox-actifs en limitant la réduction *in-situ* du Ce(IV) en Ce(III). Ainsi, j'ai pu obtenir le Ce-UiO-66-NH₂ hautement cristallin pour la première fois via une synthèse verte à température ambiante. J'ai également démontré que ce MOF ne pouvait pas être préparé si la température de réaction est de 60 °C alors que les autres paramètres de synthèse sont fixes. Il est à noter que le rendement du produit Ce-UiO-66-NH₂ est significativement plus faible que celui des autres Ce-UiO-66-X,

probablement en raison de la réduction partielle inévitable du Ce(IV). Ceci peut être surmonté en utilisant un excès de sel de cérium, ce qui permet d'obtenir un rendement de 86% (basé sur le ligand). Les conditions de préparation efficaces (1-2 h) permettent d'atteindre des rendements spatio-temporels allant de 300 à 900 kg/m³/jour, comparables à ceux des stratégies hydro/solvothermales d'autres MOFs de référence et répondant aux exigences de l'industrie. Outre ces MOFs de type UiO-66, j'ai également synthétisés d'autres MOFs de référence au Ce(IV) avec des modes de connectivité variés, tels que le Ce-DUT-67 et le Ce-MOF-808 en utilisant des conditions similaires en solution aqueuse à température ambiante. L'activité catalytique de ces MOFs est en cours d'étude. Une publication sur ce travail est en cours de rédaction.

Dans le **chapitre 4**, le protocole de synthèse à température ambiante du MOF-808 présenté dans le chapitre 2 est appliqué pour construire de nouveaux composites cœur-coquille Au NPs@MOF-808. Les composites obtenus présentent une distribution spatiale uniforme des nanoparticules d'or (taille moyenne de 3 nm) au sein du MOF, ce qui pourrait être très intéressant pour la catalyse hétérogène. Cependant, la grande quantité d'agent complexant (polyvinylpyrrolidone, PVP) utilisé dans cette étude (Au : PVP= 1 : 100) pour stabiliser les nanoparticules d'or rend les composites non traités inactifs pour la catalyse et le PVP doit donc être éliminé post-synthèse afin d'obtenir une activité catalytique intéressante. Dans cette étude, j'ai pu montrer pour la première fois comment le PVP coordonné aux NPs d'or dans les core-shell Au NPs@MOF-808 peut être éliminé en utilisant différents traitements chimiques/physiques. L'accessibilité des sites métalliques d'or a ensuite été évaluée en utilisant une réaction modèle (oxydation de l'alcool benzylique). La méthode du double solvant, basée sur l'utilisation d'un mélange de bons et mauvais solvants dans un ratio approprié, couplée à un lavage à l'acide chlorhydrique (HCl), a montré un effet prometteur sur l'élimination du PVP, qui se traduit par une augmentation de l'efficacité de la réaction. L'élimination efficace de l'agent coordonnant peut s'expliquer par l'effet conjugué de l'acide chlorhydrique qui aide à protoner le PVP, ce qui rend les liaisons de coordination plus faibles et augmente sa solubilité et du lavage optimisé dans un mélange de solvants (acétone et H₂O). Je pense que ces résultats peuvent aider les études futures à obtenir une meilleure réactivité et sélectivité en utilisant des composites cœur-coquille similaires à base de MOFs. Une publication présentant ces résultats sera bientôt soumise.

Dans le **chapitre 5**, j'ai utilisé la stratégie de synthèse à température ambiante de MOFs tétravalents préalablement présentée pour incorporer pour la première fois des nanoclusters de Cu (1,6 nm) dans trois MOF microporeux de référence (MOF-801, UiO-66-NH₂, DUT-67). Les structures cœur-coquille Cu NCs@MOFs formées présentent une porosité, une cristallinité et sont obtenus avec un rendement similaire à leur synthèse originale sans nanoclusters de Cu. L'utilisation de conditions de synthèse douces, notamment à température ambiante et en solution beaucoup moins acide, sont des facteurs très importants pour la réussite de la synthèse de ces composites. De plus, le faible coût des matières premières et les conditions de synthèse vertes m'ont permis d'optimiser les paramètres de synthèse afin d'obtenir une préparation de catalyseurs à l'échelle du gramme. Les composites préparés présentent une réactivité et une sélectivité élevées pour la photo-conversion du CO₂ à température ambiante. De plus, la comparaison entre la réactivité catalytique des composites cœur-coquille avec des solides où les nanoclusters de cuivre sont principalement sur la surface du MOF, pour lesquels une réactivité beaucoup plus faible a été observée, a permis de démontrer les avantages des structures cœur-coquille pour obtenir une haute réactivité catalytique. Enfin, j'ai étudié la nature des sites actifs cuivre en utilisant la spectroscopie

IR in-situ, révélant la présence de Cu(I) à la surface des nanoclusters de cuivre. Une publication sur ce travail est en cours de rédaction.

En conclusion, la synthèse de MOFs tétravalents de référence à température ambiante ainsi que l'ajustement de la taille des nanocristaux, la préparation d'une phase inaccessible à haute température et la construction de composites cœur-coquille NPs@MOF ont été réalisés avec succès. Les solides MOFs/NPs@MOFs préparés à température ambiante présentent une activité catalytique prometteuse pour diverses réactions d'intérêt.

RÉSUMÉ

Les catalyseurs hétérogènes constituent une pierre angulaire de l'industrie chimique et sont l'une des technologies les plus cruciales pour un avenir durable. À cet égard, les matériaux hybrides représentent une direction très excitante pour le développement de catalyseurs innovants. L'incorporation de nanoparticules métalliques (MNPs) dans des réseaux hybrides poreux cristallisés appelés « Metal-Organic Frameworks » (MOFs) est une stratégie prometteuse pour préparer des catalyseurs hétérogènes très efficaces, combinant les propriétés à la fois du MOF hôte et des MNPs invitées. Les composites préparés présentent un grand potentiel pour plusieurs applications en dehors de la catalyse (par exemple, détection, bio-applications) car les matériaux invités encapsulés peuvent introduire de nouvelles propriétés souhaitées qui sont absentes/peu efficaces dans le matériau hôte. Dans cette thèse, les composites MNPs et MOFs ont été préparés grâce à une stratégie dite « bottle-around-ship », dans laquelle les MOFs sont assemblés dans une solution contenant des MNPs préformées pour fabriquer des structures coeur-coquille. Dans un premier temps, plusieurs approches ont été développées pour préparer à température ambiante des MOFs robustes à base de cations tétravalents, basées sur des approches séquentielles ou directes. Par la suite, ces approches de synthèse à température ambiante ont été adaptées pour incorporer des nanoparticules ultra-petites dans les MOFs afin de former de manière reproductible des composites coeur-coquille MNPs@MOF capables de relever plusieurs défis en catalyse hétérogène (réduction de CO₂, hydrolyse de liaison peptidique...).

MOTS CLÉS

Réseaux hybrides poreux cristallisés, nanoparticules métalliques (MNPs), catalyse hétérogène, synthèse à température ambiante

ABSTRACT

Heterogeneous catalysts frame a cornerstone of the chemical industry and are one of the most crucial technologies for a sustainable future. Hybrid materials represent a very exciting direction for developing innovative catalysts. Incorporating guest metal nanoparticles (MNPs) into Metal-Organic Frameworks (MOFs) is an effective route to prepare highly efficient heterogeneous catalysts, which combines the properties of both the host MOF and guest MNPs. The prepared composites present a great potential for several applications apart from catalysis (e.g. sensing, bio-applications), as the encapsulated guest materials can introduce new desired properties that are absent/ poor in the parent material. In this thesis, MNPs and MOFs composites were prepared through challenging bottle-around-ship strategy. As the first step, multiple approaches were developed to prepare robust tetravalent Metal-organic frameworks (MOFs) at room temperature, including conventional stepwise and more facile direct strategies. Subsequently, the new room temperature synthesis approaches were adapted to incorporate ultra-small MNPs into the MOF to reproducibly form core-shell MNPs@MOF composites, prior to addressing several heterogeneous catalysis challenges (e.g., CO₂ reduction, peptide hydrolysis).

KEYWORDS

Metal-organic frameworks (MOFs), metal nanoparticles (MNPs), heterogeneous catalysis, room temperature synthesis